Rikin Trivedi · Luca Saba
Jasjit S. Suri *Editors*

3D Imaging Technologies in Atherosclerosis

Springer

3D Imaging Technologies in Atherosclerosis

Rikin Trivedi • Luca Saba • Jasjit S. Suri
Editors

3D Imaging Technologies in Atherosclerosis

Springer

Editors
Rikin Trivedi
Department of Neurosurgery
Addenbrookes Hospital
Cambridge, UK

Luca Saba
University of Cagliari
Cagliari, Italy

Jasjit S. Suri
AtheroPoint LLC
Roseville, CA, USA

ISBN 978-1-4899-7617-8 ISBN 978-1-4899-7618-5 (eBook)
DOI 10.1007/978-1-4899-7618-5

Library of Congress Control Number: 2015941312

Springer New York Heidelberg Dordrecht London

Printed on acid-free paper

Springer Science+Business Media LLC New York is part of Springer Science+Business Media (www.springer.com)

Preface

Nowadays atherosclerosis represents the leading cause of mortality and morbidity in the world. Two of the most common, severe, diseases that may occur, Acute Myocardial Infarction and Stroke, have their pathogenesis in the atherosclerosis that may affect the coronary arteries as well as the carotid\intra-cranial vessels.

Therefore, in the past there was extensive research in identifying pre-clinical atherosclerotic diseases in order to plan the correct therapeutical approach before the pathological events occur.

In the last 20 years imaging techniques and in particular Computed Tomography and Magnetic Resonance had a tremendous improvement in their potentialities. In the field of the Computed Tomography, the introduction of the multi-detector-row technology and more recently the use of dual energy and multi-spectral imaging allow reaching an exquisite level of anatomic detail. The MR thanks to the use of strength magnetic field and extremely advanced sequences can image very fast the human vessels by offering an outstanding contrast resolution.
In this book our purpose is to offer a synthetic but complete window into the state of the art of the CT\MR imaging application for the study of arteriosclerosis by the means of the most renowned scientist in this field.

Cambridge, UK — Rikin Trivedi
Cagliari, Italy — Luca Saba
Roseville, CA, USA — Jasjit S. Suri

Contents

Principles of Computed Tomography

Michele Porcu, Luca Saba, and Jasjit S. Suri

History and Basic Physics of X-rays [1]

In 1895, Wilhem Röentgen discovered X-rays and opened new ways for medicine, improving diagnosis and therapy.

X-rays are electromagnetic waves (speed: 3×10^9 m/s) with very short wavelength (between 0,1 and 10 nm), high frequency (**f**) between 10^{17} and 10^{19} Hz, and thus high energy (**E**), according to the formula (1):

$$E = \mathrm{hf} \tag{1}$$

where **h** is the Planck constant (value: $4{,}135 \times 10^{-15}$ eVs).

These properties allow X-rays to interact with the different tissues of the human body: once they have been generated from an X-ray source and have crossed the patient's body, emerging X-rays hit a detection system, interact with it and create an image which can be read by radiologists.

Various sources can generate X-rays; in 1913 William David Coolidge, a researcher of General Electric Company, invented the so-called "X-ray Coolidge Tube" which represents still today the model on which are designed modern X-ray sources (Fig. 1).

The general principle of Coolidge Tube is very simple: in a vacuum tube are placed a cathode and an anode (both made of tungsten, an element with high atomic number) with a difference in potential ($\mathbf{\Delta V_1}$) created between them:

M. Porcu, M.D. • L. Saba, M.D. (✉)
University of Cagliari, Cagliari, Italy
e-mail: lucasabamd@gmail.com

J.S. Suri, Ph.D., M.B.A., Fellow AIMBE.
AtheroPoint LLC, Roseville, CA, USA

R. Trivedi et al. (eds.), *3D Imaging Technologies in Atherosclerosis*,
DOI 10.1007/978-1-4899-7618-5_1

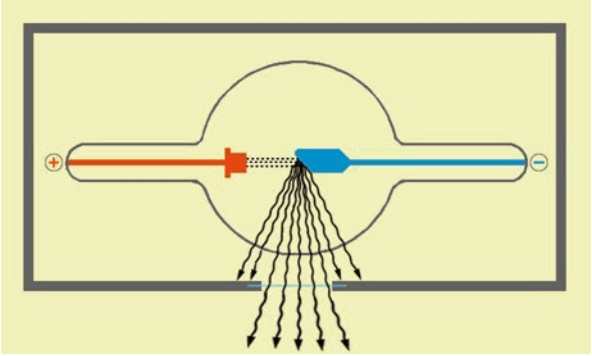

Fig. 1 This picture shows the Coolidge tube model: the electrons created on the cathode (+) for thermionic effect, are accelerated and hit the tungsten plate of the anode (−). An X-rays-beam is generated from this interaction. The X-rays can only goes out from the opening of the tube not covered by the lead

1. The **cathode** consists of a little pigtail wire in which flows an electric current generated by a little potential difference ($\mathbf{\Delta V_2}$). This wire is heated because of the Joule effect.
2. The **anode** consists of a plate of tungsten.

Thanks to the $\mathbf{\Delta V_1}$ between the two electrodes, electrons generated for **thermionic effect** from the pigtail wire are accelerated and an "electron beam" travels through the vacuum from the cathode to the anode with an incredible speed. The kinetic energy of the impact of the "electron beam" is converted into heat for 99 %, the other 1 % as "X-ray beam".

This X-ray beam has its own **intensity** and the X-rays which it consists of have their own average **energy**. It is made of two kinds of X-rays, **bremsstrahlung X-rays** and **characteristic X-rays** (Fig. 2):

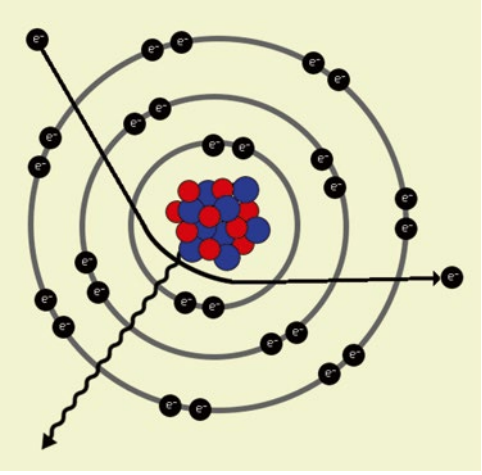

Fig. 2 This picture shows the interaction of an electron with the inner orbitals, characterised by the deceleration of the electron, the deflection of the trajectory, and the emission of an X-ray (Bremsstrahlung X-ray)

- **Bremsstrahlung X-rays**: these are produced by the deceleration and deflection of electrons emitted from the cathode when they hit the crystal lattice of the anode. This kind of X-rays is that produced more during an "electron-beam" collision.

- **Characteristic X-rays**: these are produced after the collision of electrons emitted from the cathode with the electrons of inner orbital of the atoms that constitute the anode (in this case tungsten).

We must point out that the entire process is probabilistic, since a single electron could be decelerated and deflected by outer or inner orbitals of the tungsten atoms of the anode, creating single X-rays with different frequency (and thus energy). Actually the number of electrons and X-rays generated is so great that we consider the average value of energy of every single X-ray of the beam; thus we talk in terms of "**X-ray beam**", "**intensity of the X-ray beam**" and "**energy of X-rays**".

The intensity of the X-ray beam can be considered as "**the number of X-rays**" **emitted from the source**; its value depends on the amount of electrons emitted from the cathode (i.e. the charge of the cathode): we can increase X-rays number, and thus of the intensity of the X-ray beam, increasing the **charge** (**q**) of the cathode, according to the formula (2):

$$q = t\Delta V_2 \tag{2}$$

where **t** is the time and $\mathbf{\Delta V_2}$ is the difference in potential between the two ends of the pigtail wire of the cathode. The unit of measure of the X-rays intensity is **mAs** (**1 mAs = 10^{-3} C** (**Coulomb**)). Greater the total charge, greater the number of electrons emitted for thermionic effect, greater the intensity of X-ray beam, greater the **definition** of the image, greater the **total ionising dose** (**TID**) given to the patient. In daily practice, in order to obtain a greater charge (and thus X-ray beam intensity), we modify in particular the $\mathbf{\Delta V_2}$ value.

The energy (**E**) **is the average** "**strength**" **or the** "**passing ability**" **of the single X-rays of which the beam is made of**; it depends on Eq. (3):

$$E = q\Delta V_1 \tag{3}$$

where **q** is the charge and $\mathbf{\Delta V_1}$ is the potential difference between the electrodes. The unit of measure is **keV** (**1 keV = 1.6×10^{-16} J** (**Joule**)). Since the charge of a single electron is constant and it is 1.6×10^{-19} C (Coulomb), if we want X-rays with greater energy, we have to increase the potential difference $\mathbf{\Delta V_1}$. High energy X-rays (**hard X-rays**) are generated for **high $\mathbf{\Delta V_1}$ values**, whereas low energy X-rays (**soft X-rays**) are generated for **low $\mathbf{\Delta V_1}$ values**. Harder X-rays have greater capability to penetrate through the patient and reach the detection system.

X-rays at different energies interact in different ways with human tissues, depending on their composition.

Radiology technicians can modify these two parameters (intensity of X-ray beam and X-ray energy) to obtain an optimal image, both in traditional radiology and CT (see below).

Once the X-rays emerge from the Coolidge tube, they interact with human tissues, in a probabilistic way. This interaction will be different based on the density and atomic composition of the tissue. Possible interactions are the following:

1. **X-rays scattering**: X-rays are deflected in all the directions by the crystalline lattice of the tissues. This kind of interaction is responsible for the **scattered effect** of the image, the so-called "**noise**" of an image (see below).
2. **Photoelectric effect** (Fig. 3a): an X-ray hits an electron of the inner orbitals of an atom and gives it all his energy; this results in the ejection of the electron from its orbital, and the ionisation of the atom.
3. **Compton effect** (Fig. 3b): an X-ray hits an electron of the outer orbitals of an atom and gives it a part of its energy (less energy is required to eject an electron from outer orbitals than the inner orbitals): this interaction results in the ejection of the electron outside the atom and the deflection and loss of energy of the X-ray.
4. **Couple production**: an X-ray interacts near the atomic nucleus, and this led to a production of a couple which consists of electron and positron (This kind of interaction happens only for high X-ray energy, greater than 1.02 MeV; these energies are not used in traditional radiology and CT).

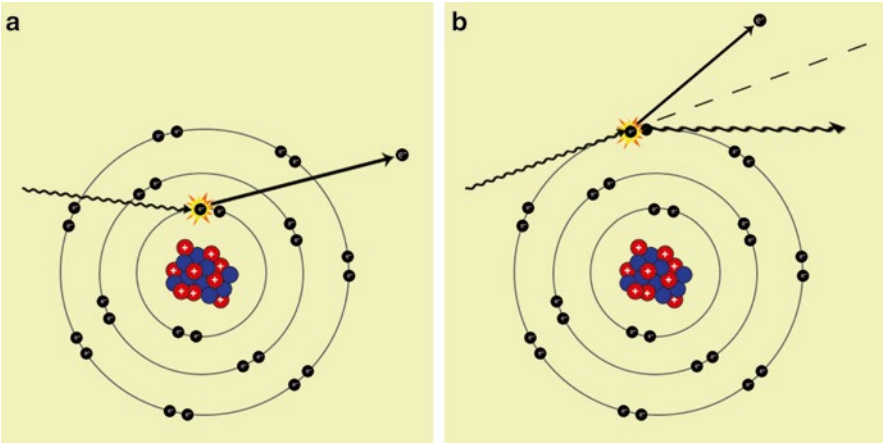

Fig. 3 These pictures show the most important interaction of X-rays with the atoms of the human-body. In (**a**) is shown the "Photoelectric effect", characterised by the fact that the X-ray interact with an electron of the inner orbitals, throwing it out. In (**b**) is shown the "Compton effect" in which the X-ray interacts with an electron of the outer orbital, resulting in a loss of energy and deflection of its trajectory, and in a emission of the electron hit

Photoelectric and Compton effects are important because they explain the **ionising capability of X-rays**, responsible for undesirable effects (teratogenic effects, mutagenic effects) which limit use of X-rays in clinical practice (in particular in pregnancy) according to stochastic and non-stochastic effects on the tissues (see below).

When an X-ray beam crosses a patient's body, it loses its intensity according to the principles just exposed, and reaches a detection system placed over human body, with intensity (**I**) lesser from the original ($\mathbf{I_0}$) as we can see in the formula (4):

$$I = I_0 e^{-\mu x} \tag{4}$$

where **I** is the intensity of X-ray beam emerging from the patient , $\mathbf{I_0}$ the intensity of X-ray beam originated from the source, **e** the Euler number, **μ** the linear attenuation coefficient (different for every tissue based on their composition) and **x** the tissue thickness.

Applications of X-Rays in Clinical Practice [2, 3]

All the concepts exposed before are the basic physical principles that permit to explain how it is possible to obtain an image (a radiograph, a fluoroscopic image or a CT) using X-rays. Now we quickly expose the most important applications of X-rays in clinical practice.

In **traditional radiology** X-rays originated from a Coolidge tube once have crossed human body reach a detection system: this detection system originally was a **photographic film** impressed by X-ray beam, while nowadays it is a **radiographic cassette** made of **photo-stimulate phosphors** read by a laser optic viewer after the execution of a radiograph, or a **plane** made of **digital sensors**, which once has detected the X-rays displays directly digital images on a monitor. The images obtained are two-dimensional (**2D**) static images called **radiographs,** and they do not allow to discriminate the three-dimensional (**3D**) arrangement of body structures.

In **fluoroscopy**, X-rays emerging from human body were detected originally by a fluorescent screen, while nowadays they are detected by an **X-ray image intensifier** and a **CCD camera**; in this way, images are displayed on a monitor in real time. This technique allows to obtain dynamic 2D images, used for such examinations as angiographies in which the operator needs to follow the diffusion of a contrast medium or radiopaque objects (catheters, coils …) along the body structures in diagnostic and, above all, therapeutic procedures.

Computed Tomography (**CT**) allows to obtain sectional axial images of the body and, in modern CT scanners, thanks to the spiral acquisitions, multiplanar sectional and 3D images of the body.

Introduction to CT [4]

In 1970s, thanks to the work of Sir Godfrey N. Hounsfield and Dr. Conmark, winners of the Nobel Prize in 1979, **CT** was introduced in clinical practice. It was a revolution because of its incredible capability in diagnosis and management of patient.

The great **contrast resolution** (the ability to detect in an image two different points with different degrees of intensity—in b/w images, shades of gray), **spatial resolution** (the ability to distinguish two different points next to each other—the lesser the distance between two points, the higher the spatial resolution) and **temporal resolution** (the time for acquisition of a frame) of modern CT scanner,

in particular in the evaluation of soft tissue, make CT an essential instrument for detection and staging of various pathological conditions.

In fact, traditional X-ray radiographs are still important instruments to assess patient condition, but cannot offer a complete evaluation; moreover, CT's intrinsic capability to explore deep organs despite ultrasonography (US) and its very low execution time than Magnetic Resonance (MR) allow us to have many and detailed information in a very little time. Anyway, we must remember CT uses ionising rays that can have mutagenic effects on human tissues (with increased risk of neoplasms and, in pregnant women, of foetal malformations and spontaneous abortions).

How a CT Scanner Is Made [4, 5]

CT uses X-rays to produce a series of images that will be analysed by the radiologist.

Modern CT scanner consists of (Fig. 4):

- **Circular gantry**
- **Moving patient table**
- **Control console**

Fig. 4 This picture shows the parts of which a Modern CT scanner is made: the control console (1), the circular gantry (2) and the moving table (3)

The **circular gantry** consists of a solid structure containing an **X-ray source** (made based on a **Coolidge tube**, see above) and a **detection system**, firmly connected opposite to each other forming a 180° angle between them, and a **rotation system** that rotates the X-ray source and detection system by a 360° angle. Thanks to the "**slip rings**" technology, a wireless electrical connection, the X-ray source-detection system complex can rotate continuously over 360° degrees (allowing the "**helical scanning**", see below). Detection system is connected with a **data-acquisition-system** (**DAS**) which converts X-rays in electric pulses that will be analysed and managed by the computer to create an image series. Moreover, the circular gantry contains a **laser sighting system** to correctly position the patient in the moving patient table, and an important **cooling system** to dissipate the great heat generated by the X-ray source.

The **moving patient table** carries the patient into the gantry hole.

The **control console** is managed by the radiology technician, who controls the whole procedure supported by the radiologist.

General Acquisition Principles [1, 4, 6]

The general principle is very simple: **X-rays, generated from a rotating X-ray source placed in the circular gantry, cross the patient body lying on the moving table in the centre of the gantry and are detected by the detection system placed opposite to the X-ray source** (Fig. 5). The X-ray beam generated at a known intensity value, equal for every degree of rotation, reaches detection system with an intensity value less than that at the source because of the interaction with human body structures, according to the formula (5) derived from the formula (4):

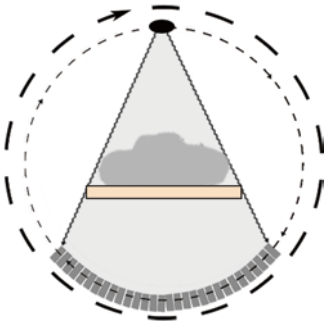

Fig. 5 This picture shows the general principles of a CT scan: the patient lies on the moving table, and an X-ray beam generated by the X-ray tube crosses the patient's body. Once they have crossed the patient, they interact with the detection system placed opposite to the X-ray source. The X-ray tube and the detection system rotate together around the patient

$$I = I_0 e^{-\int_0^L \mu(x)dx} \tag{5}$$

This formula indicates that the intensity of X-ray beam measured by the detector (**I**) is equal to the product of the intensity of X-ray beam originating from the source ($\mathbf{I_0}$) multiplied by the Euler number (**e**) elevated to the integral of every X-ray linear attenuation coefficient ($\boldsymbol{\mu}(\mathbf{x})$) from the origin (**0**) to (**L**), where **L** is the distance between the source and the detector covered by the beam.

X-ray beam generated from the rotating source when crossing human body and its deep structures interacts with tissues and yields them energy; **this interaction is different depending on tissue composition** (water, blood, lipids, bone and crystalline structures) **and the rotation degree of the source**.

Detection system is made of different detectors. Although early CT scanners used gas ionisation-detectors, in modern CT scanners detection system consists of solid-state detectors made of ceramic of rare-earth oxides, which have high capture efficiency (total amount of emerging X-rays absorbed by the detector) and conversion efficiency (capability to accurately convert X-rays into electric signal). Detectors are aligned side by side, divided by thin septa made of tungsten to minimise the "**noise**" of the image (i.e. artefacts from **scattered radiation** generated by X-rays interaction with body structures), and are able to capture the greatest amount of X-rays emerging from the patient. Once the X-ray beams emerging from human body reach the detection system with intensity value **I**, they are transformed into electric pulses by the **data-acquisition-system** (**DAS**). These electric pulses, converted into data series, will be then processed and analysed by the computer, and then converted into axial images series.

CT Generations [4, 5]

From an engineering point of view, we describe four generations of CT scanner (Fig. 6).

1. **First generation**

The first CT scanner (MARK 1) was made by EMI in 1972. It was only a head scanner, and required about 20 min to obtain a complete axial scan of the head, with a slice thickness of 13 mm. It consisted of a box-shaped gantry in which lay the head of the patient, an X-ray beam source generating a very narrow beam, and a detection system containing a couple of detectors placed against each other in two adjacent rows to scan two slices concurrently and reduce acquisition time. The complex X-ray source—detection system scanned the head moving in the gantry according to a **translation–rotation process**, in which were sampled 160 detection data by a translation movement of the system for every degree of rotation, and an overall 180° rotation.

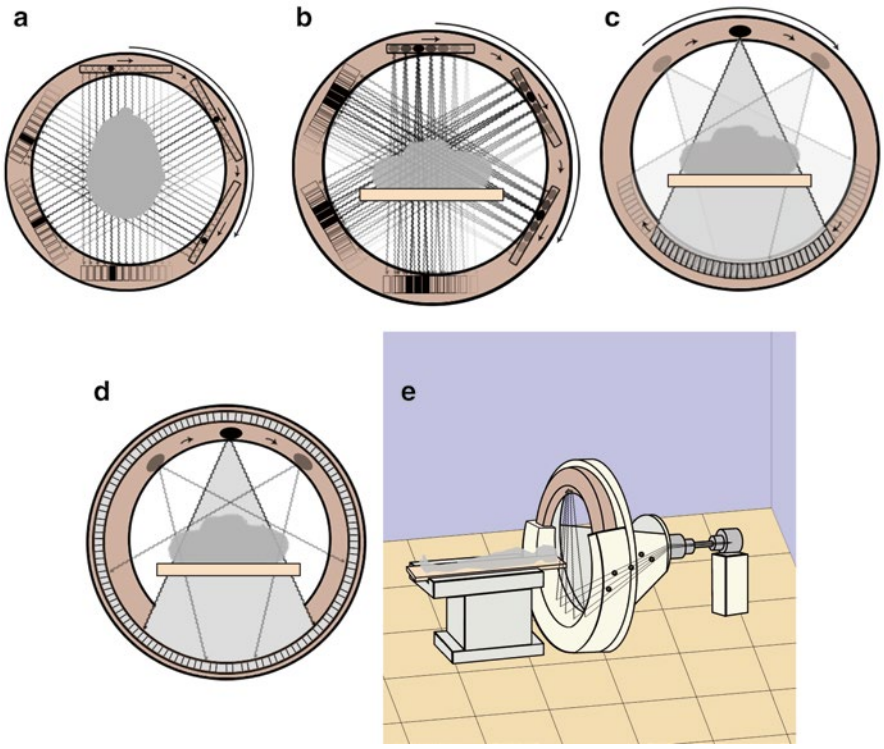

Fig. 6 This picture shows the five generations of CT scanners. The third generation scanners are the most diffuse in clinical practice nowadays

2. **Second generation**

This generation differs from the first because of the use of **an X-ray narrow cone beam** and of **a detection system with multiple detectors** (**from 3 for the first model up to 20 for the latest**); the detectors are not placed on multiple rows, but **on a single row**. The complex X-ray source–detection system moved according to a **translation–rotation** movement. The CT scanner was implemented with a moving table, a laser indicator and the capability to tilt the gantry, allowing not only the head scan, but also the body scan for the first time. Scanning time was lesser than first generation, allowing to scan one slice of the chest holding one breath; there were still severe movement artefacts, and to limit them it was necessary to avoid the translation movement, maintaining the rotation movement.

3. **Third generation**

In principle, the power supply of CT scanners was provided by electric cables which limited the movement of the system constituted by the complex X-ray source–detection system: in fact, after a 360° rotation, the system had to stop and then re-start moving in the opposite verse. This limitation allowed only sequential axial scans.

In the third generation of CT scanners has been introduced the "**slip rings**" technology. It has been a revolution. In fact, with the introduction of this technology,

electric cables have been abolished, allowing a continuous rotational movement of the system, over the 360°, and abolishing the need of a translation–rotation movement. A new era of **Helical CT** started (see below).

Another improvement in CT technology that led to further decrease of scan timing has been the use of a detection system which consists of multiple detectors placed not on a single slice but on multiple slices, so that the use of cone-beam X-rays covers a greater section of the body in little time; this is the **multislice-CT** technology (see below).

Nowadays, the principal manufacturers produce only multislice CT scanners with this kind of architecture, which allows to generate sequential or helical CT scans.

4. **Fourth generation**

The fourth generation has not had a great impact. In fact, high production costs were a limitation for its development. It differed from third generation in the architecture of the detection system: in fact detectors cover entirely the inner part of the gantry, and only the X-ray source (placed adjacent to the detectors and slightly inclined to them) rotates in the gantry.

5. **Fifth generation**

Electron beam computed tomography (**EBCT**) was developed to evaluate heart. It consisted of a cathode that generated an electron beam, diverted and rotated by an electromagnetic fold; the electrons hit four semicircular anodes placed around the patient, generating X-rays captured by detectors placed adjacent to the anodes. Despite the high temporal resolution (about 50 ms), EBCT did not have great success due to high costs and intrinsic technician limitations.

Spiral-Volume Scanning and Multislice-CT [2–7]

With the introduction of "slip rings" technology in 1987, a new era started in CT. In fact, the capability to have a continuous rotating movement allowed not only to achieve faster scans in lower time but also multiaxial images. Before this innovation, scanners allowed to obtain only axial images for the limited movement of the complex X-ray source–detection system because of electric cables; in fact CT scanners were able to execute only **axial sequential scans** (**slice-by-slice**).

Third generation CT scanners with "**slip rings**" technology work with a continuous rotating movement of the complex X-rays-source–detection system; while the complex rotates, the table moves consensually along the *z*-axis (the longitudinal axis of the patient; the other two axes, *x* and *y*, are perpendicular to *z*-axis and represent the coordinates of axial images). This innovation, together with improvements in computing calculation speed, took CT scanner to a higher level, and in the early 1990s, Kalender et al. [5] developed the algorithm of **spiral volume scanning** (**Spiral or Helical-CT**) (Fig. 7).

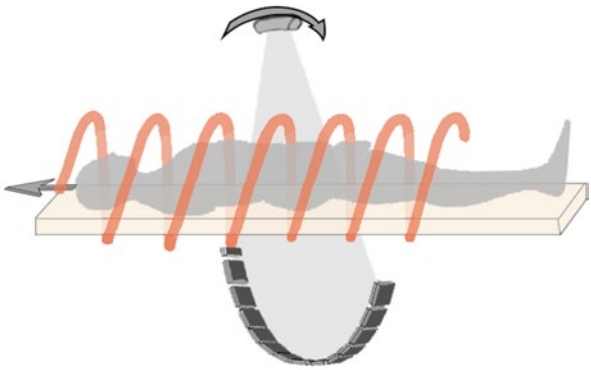

Fig. 7 This picture shows the principle of the helical-CT: the scan can be acquired with the patient placed on a moving table which moves during the continuous rotation of the complex X-ray tube. detection system around the patients. This continuous rotation with an angle >360° is possible thanks to the slip rings technology

Beside the introduction of "slip rings" technology, researchers developed a new system to improve Helical-CT scan faster than before. The idea was to create a new detection system, or better, to improve the old detection system in order to obtain more data in less acquisition time. The engineers created a detection system made of not only a single array of detectors (slice), but multiple rows of detectors, aligned in arrays, side by side. This detection system is able to capture X-rays-beam in a wider range along the *z*-axis. **These scanners are called multislice-CT** (**MSCT**) **scanners**. Nowadays there are CT-scanners capable to cover in a single rotation a field of view of 128 mm, using 256-rows detectors in a 0.5 s rotation time; this means that in 1 s it can cover a body section of about 26 cm, and a slice thickness of 0,675 mm, very impressive!

Currently, MSCT scanners are a fundamental instrument to evaluate patients, in particular for the great amount of clinical information they provide in very little time, especially, but not only, in emergency.

The recent manufacturing developments in CT-scanner technology, such as dual and multi-energy scanners, are exposed below.

Images Reconstruction [2, 4, 5, 7]

As we have seen before, in CT scanners images are created comparing data acquired from different acquisition obtained at different rotation degrees.

Computer represents every scan circle as a matrix with a 512×512 of 3D boxes called **voxels** (Fig. 8). Every voxel has three axes mutually perpendicular: *x* and *y* are the axes perpendicular to the longitudinal axis of the patient (called ***z*-axis**), and every voxel on a screen is represented by a 2D square, called **pixel**. To create 2D images, the computer has to obtain for every voxel, and hence pixel, the corresponding **attenuation coefficient value** ($\boldsymbol{\mu}_v$).

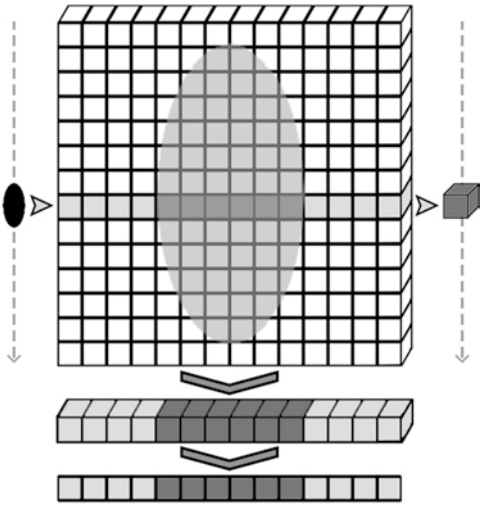

Fig. 8 This picture shows the principle of the image reconstruction. The volume acquired can be divided in matrix constituted of voxels, which can be imagined as many little cubes one beside the other. Once the computer has calculated the attenuation coefficient value of every voxel (μ_v), the voxel will be converted into pixel and the μ_v will be converted into HU

To obtain **attenuation coefficient** ($\boldsymbol{\mu}_v$) of the voxel, the computer must extract the linear coefficient attenuation value ($\boldsymbol{\mu}$) for every emerging X-ray beam (**I**) intercepted by the detectors during a 180° rotation, knowing the X-ray beam intensity at origin ($\mathbf{I_0}$) and the distance covered by the beam (**L**), according to the formula (6) derived from the formula (5):

$$\int_0^L \mu(x)\,dx = -\frac{1}{L}\ln\left(\frac{I}{I_0}\right) \tag{6}$$

The computer can calculate every voxel attenuation coefficient ($\boldsymbol{\mu}_v$) **knowing the linear attenuation coefficient** ($\boldsymbol{\mu}$) **of every projection obtained during a 180° rotation**, because in the gantry the intensity of X-ray beam emerging from human body, and thus linear attenuation coefficient ($\boldsymbol{\mu}$), measured on the same direction and opposite verse (0° and 180°, 1° and 181° and so on) are equal. **The algorithms used by the computer** could be the **filtered back-projection** (**FBR**) or, in most recent CT scanners, the **iterative algorithms**.

For convention, once the computer has achieved the correct attenuation coefficient value ($\boldsymbol{\mu}_v$) for every voxel of the matrix, this value has to be converted into an integer according to the formula (7):

$$\text{CT number}(\text{HU}) = \left[1000 \times (\mu_v - \mu_{\text{water}})\right] / \mu_{\text{water}} \tag{7}$$

where μ_{water} is the attenuation coefficient of water. We remember here that μ_v of air is 0 because X-ray beam is not attenuated along his route.

CT number indicates the density of the tissue included in the analysed voxel; the unit of measurement of CT number is called **Hounsfield Unit** (**HU**).

These values are included in a scale note as **Hounsfield Scale**, where the value of water is 0, the value of bone is +1,000 and air −1,000. This value, as we have said

before, changes according to the type of tissue; in particular fat has a negative value, whereas blood and abdominal organs have a positive Hounsfield value. This concept is very important to correctly interpret imaging findings (e.g. a steatotic liver has a middle HU lower than a non-pathologic liver because the steatotic liver contains more fat than normal).

Now the computer has all data to build an image on the monitor: 3D voxels included in the 512×512 matrix (spatial resolution) with a defined CT number are converted into 2D pixels with a defined CT number using a predefined **kernel**, that is, an algorithm of reconstruction that allows to obtain images "smoother" or "sharper" in order to better evaluate different districts, such as lung or abdominal organs. Sharp kernels such as the B46f allow to evaluate structures in which the tissues differs for very high density values, like lung and bone, whereas smooth kernels such as the B20f allow us to evaluate structures in which the tissues do not differ for high degrees of density, like the abdomen or the mediastinum (Fig. 9). For every pixel is assigned a different shade of gray of a grayscale according to CT number; in particular pixel with higher HU values, like bone, tend to appear white, while those with lower HU values, like air, tend to appear black.

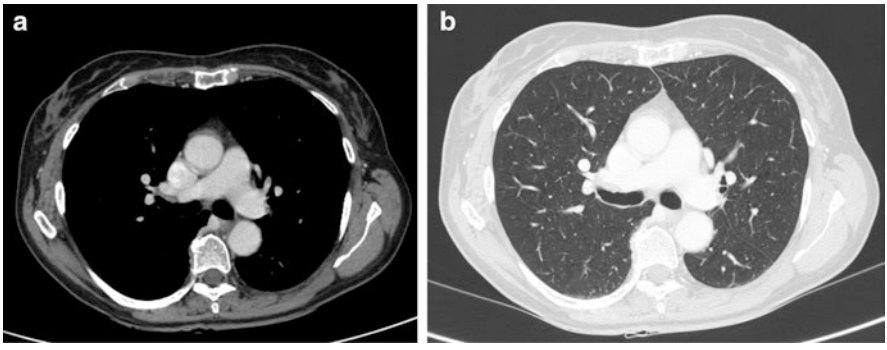

Fig. 9 These pictures show the same slice of the chest CT examination of a patient, reconstructed with two different kernels: in (**a**) it has been used a smooth kernel (B20) in order to evaluate the mediastinum; in (**b**) has been used a sharp Kernel (B46f) which allows to better analyse the lungs

Monitors can show about 250 shades of gray despite the 2,000 values of the Hounsfield scale; moreover, human eye can discern about 100 shades of gray, and so more HU values will be grouped in a single gray shade. Radiologists when analysing images have to select the **window of view**, namely, select the **window centre** (e.g. 0 HU for water) and **window width** (the range of CT number to display); this process, called **windowing**, allows to change the **contrast resolution** of the image, modifying the shades of gray of the image in which are grouped ranges of HU to better visualise anatomic details.

The analysis of tissues that differ for very low HU, like abdominal organs, requires greater resolution contrast and radiologists analyse the images easier choosing a narrow window width (400–500 HU) and with the window centre at 20–40 HU, whereas to analyse bones details radiologists choose a large window width (2,000 HU) and an higher window centre (550–600 HU) (Fig. 10).

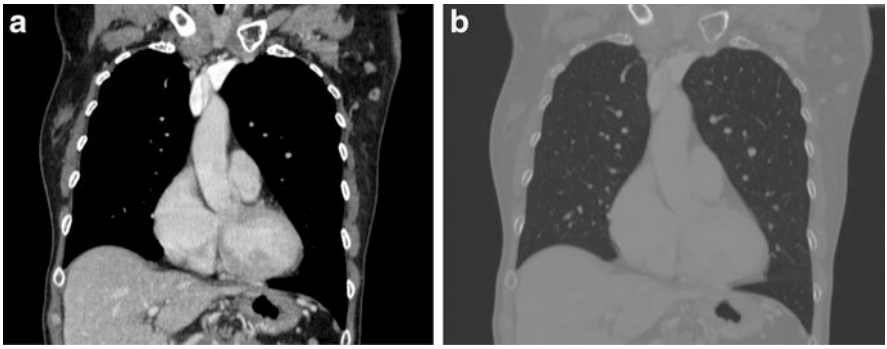

Fig. 10 These pictures show the same coronal slice of a CT examination of the chest of one patient: they are reconstructed with the same kernel (smooth, B20). In (**a**) has been set a narrow window width with the centre at 20–40 HU in order to better evaluate tissues which differs between them having very low HU values; in (**b**) has been chosen a large window width with a high window centre at 550 HU in order to better evaluate bone and lung structures

Post-processing

In modern systems, every radiological investigation (radiographs, US, CT, angiography and MRI) is collected in a digital file, which format is defined **DICOM** (Digital Imaging and Communication in Medicine). This kind of file can be read and analysed on a PC by various software.

Modern software, moreover, allow to reformat images in various ways, thanks to specific algorithms, developed by biomedical informatics engineering: this is the post-processing, and it is a fundamental phase of the interpretation of CT-findings.

Let us talk about the principal post-processing methods used in clinical practice:

1. **Multi Planar Reconstruction** (**MPR**) (Fig. 11): once CT scans were composed only by axial images; as we have seen before, with the introduction of slip rings and then Spiral and Multislice CT technology, it was possible to obtain very thin scans (nowadays up to 0.625 mm thin!); this method allows the radiologists to obtain sectional imaging of the body along any axis of the space (sagittal, coronal, oblique) starting from an axial acquisition. Thin layer longitudinal axial acquisition (indifferently if sequential or spiral) is the only care needed to obtain optimal and diagnostic cross-sectional imaging using MPR. This is the main post-processing method used and allows to clarify doubts derived from misunderstandings in the analysis of the longitudinal axis images only. A particular method very useful for the evaluation of the vessels is the so-called "**Stretching MPR**" (Fig. 12) in which, thanks to different software, the vascular structures are "stretched" along the long axis, allowing to evaluate the course and any narrowing or enlargement.

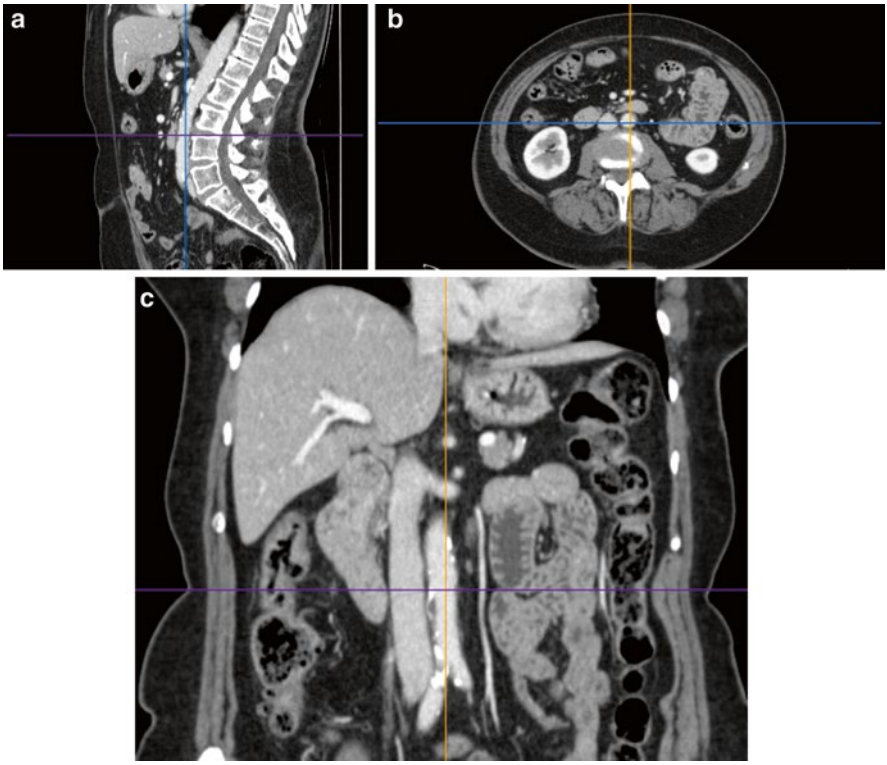

Fig. 11 These pictures show a Multi-Planar Reconstruction (MPR) elaborations of the same patient. (**a**) sagittal view. (**b**) axial view. (**c**) coronal view

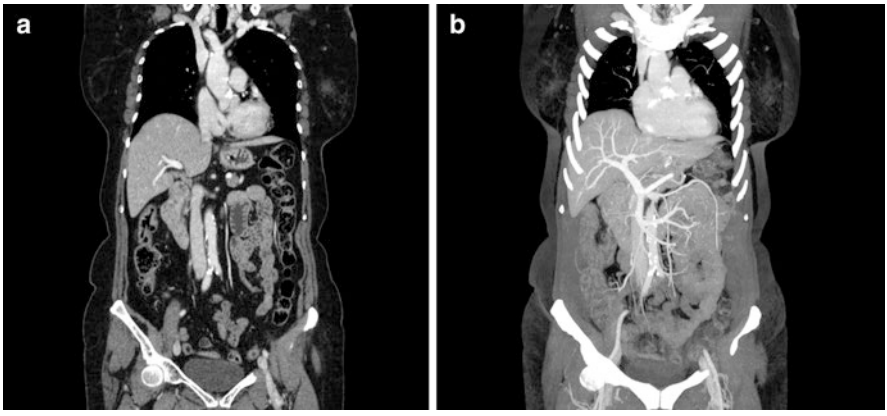

Fig. 12 The pictures show the "Stretched" Multi-Planar Reconstruction (MPR) elaborations of the right coronary artery. (**a**) VR of the heart and of right coronary artery. (**b**, **c**) A normal "stretched" right coronary artery

2. **Maximum Intensity Projection** (**MIP**) (Fig. 13): with this method, we can obtain an image constituted by a fusion of a packet of adjacent images (from 2 to all the images of the study). For every pixel of the matrix of this reconstructed image is assigned the highest HU value among all the images of the packet. The images obtained with this method, which in some way have a 3D aspect, allow to obtain a better definition of tissues with high linear attenuation coefficient (like the vessels in contrast medium CT, see below) and often help radiologist and clinicians to identify small findings otherwise difficult to detect only with MPR.

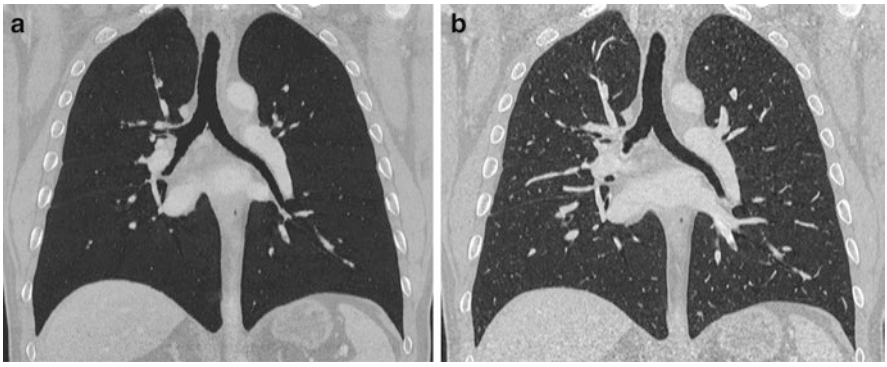

Fig. 13 These pictures show the Maximum Intensity Projection (MIP) elaborations of the body of the same patient. (**a**) normal non-MIP coronal view. (**b**) MIP coronal view, enhancing in particular the vascular structures

3. **Minimum Intensity Projection** (**MinIP**) (Fig. 14): it is analogous to the MIP, but in this case for every pixel of the matrix of the reconstructed image is assigned the lowest HU value of that same point of the matrix of all the images of the packet. This method is helpful to identify structures with low linear attenuation coefficient, such as pathologies of Wirsung duct, biliary tract or pulmonary emphysema.

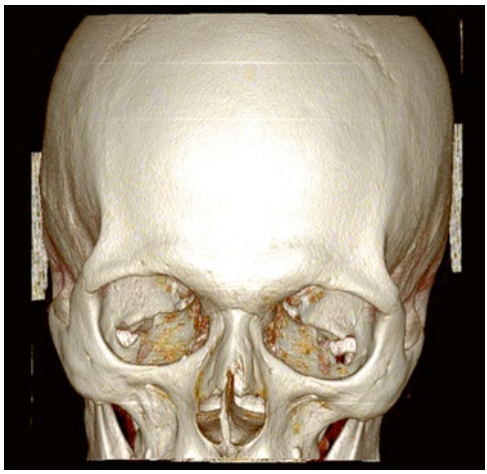

Fig. 14 The picture shows the Volume Rendering (VR) elaboration of the skull

4. **Volume rendering** (**VR**): thanks to this method, it is possible to obtain 3D model of the body from 2D images (thin layer axial acquisition is needed); this is possible converting the pixel of the images in voxel, and every voxel in small polyhedral. It is possible to choose the structures to represent modifying the window of view, and underlined them with different colours. This kind of post-processing allows to obtain very impressive images, useful in particular for clinics to approach in a more familiarly way the pathologic findings and for the surgeons in the preoperative planning.

Contrast Agents [2, 3]

A radiologic study can be made with or without contrast agent (or contrast medium). What are contrast mediums? **They are substances**, obviously compatible with human organism, **that because of their compositions enhance the structures in which they diffuse and improve the contrast resolution of the images** once they are administered in the body by various ways.

There are different contrast mediums. We can classify them as follows:

- **Natural contrast agents**, such as air, water and CO_2.
- **Artificial contrast agents**:

  Barium sulphate
  Diatrizoic acid
  Injective iodinated contrast agents
  Gadolinium based drugs (**used only in MRI**)
  Sulphur hexafluoride (**used only in US**)

These contrast agents can be administrated in the human body by various ways: for example they can be administered directly in the gastrointestinal tract by mouth or anus, or can be injected directly in the blood (intravenously or intra-arterially) and are indispensable in every radiological investigations (MRI, CT, traditional radiology, US, angiography and interventional radiology).

In CT are used natural contrast agents, diatrizoic acid and iodine based contrast agents:

1. **Natural contrast agents** (air, CO_2 and water) are used in such studies in which is needed the distension of GI tract, like CT-enteroclysis or virtual colonoscopy.
2. **Diatrizoic acid** is used when we have to study the G.I. tract, in particular coupled with air in CT-enteroclysis.
3. **Intravenous iodinated contrast agents** are used in many condition, and could be consider essential to obtain diagnostic scans, in particular in vascular CT. Now we analyse them in detail focusing on their composition, precautions for use, dose, fluxes and possible adverse reactions.

Intravenous Iodinate Contrast Agents and Contrast CT Acquisition [2, 3, 8, 9]

These water-soluble drugs are organic molecule covalent linked with iodine atoms. Iodine has a great atomic number ($Z=53$) and has a very high X-ray linear attenuation coefficient ($\boldsymbol{\mu}$); when an iodinate contrast agent is injected intravenously, it spread in the plasma linked to plasmatic proteins, and follows the haematic circle from veins to lungs and then to the arteries of the great circle.

It is then eliminated by the kidney and minimally by the liver, settling in the urinary tract by (pelvic, ureters and bladder) and in the biliary tract (gallbladder); in wealthy people, about 85 % of the total amount of contrast agent is eliminated after 12 h from administration, 95 % in a period between the 24 and 96 h.

They may be divided into two categories:

1. **Ionic iodinate contrast agents** (ioxaglate, metrizoate or diatrizoate): tend to have high osmolality (except ioxaglate). They are no more used nowadays because of their high osmolality and high risk of adverse reactions onset.
2. **Non-ionic iodinate contrast agents** (iomeprolo, iopromide, iopamidol, iohexol, iodixanol and iodixanol).

There are many non-ionic iodinate contrast agents, at various iodine concentrations (for example, iopromide can be found in formulas between 300 and 400 mg/dl). To obtain an optimal contrast CT-examination, the radiologist has to correctly set up some parameters concerning total amount and fluxes, according to the patient and the type of study to be made:

- **Contrast medium iodine concentration**: The total amount of contrast agent to be administer is lower for higher iodine contrast agent concentration.
- **Weight**: patient with higher weight need more contrast agent. In particular, for contrast medium with a 370 mg/dl iodine concentration, the radiologist can calculate approximately the total amount of contrast necessary for the CT-scan multiplying the weight of the patient by a conversion factor of 1,7. Anyway it is important administering the lowest contrast medium amount useful to obtain diagnostic images and in order to limit of a contrast induced nephropathy (CIN, see below).
- **Examination type**: based on the venous access and the type of CT-study the radiologist has to make, once he has to set up the total amount of contrast agent, he has to decide the injection flux: for example, if he has to make a scan which target is to enhance arterial structures, he need to inject a lesser total amount of contrast medium (despite those calculated based on the weight) at a very high flow rate (from 4,0 to 7,0 ml/s), in order to maximise the contrast resolution in arterial districts. On the other hand, for a contrast CT-scan of the head, are used lower flow rate (2.5 ml/s) to enhance in the best possible way the cerebral tissues.

It could be streamlined in this ways:

Arterial studies: high fluxes and lower total amount of contrast agent despite those calculated on the weight.
Parenchymal and venous studies: low fluxes.

- Furthermore, we must remember that for several studies it is necessary to use a **dual** or **multiphase** contrast agent administration: the contrast agent could be administered in two ore more times with different flow rates.

After the contrast medium injection, it is important to administer a saline bolus (a dose between 20 and 30 ml) in order to wash out the venous access and limit adverse reaction in the injection site and the creation of artefacts on the images.

The evaluation of the contrast medium spread in human vessels during its administration, and thus the correct time of acquisition of CT-scan, is possible relying on standard known physiological circulation times (for example, a parenchymal study 80–90 s after the beginning of contrast agent administration) or using two more precise methods:

- **Bolus tracking**: based on the scanogram (the preliminary 2D scan which allows to choose the limit of our CT-scan and the correct field of view (FOV)), the radiology technician chooses a single slice which will be scan sequentially to evaluate the changing in HU value of a determined region of interest (ROI). The ROI position depends on the type of scan to make and on the CT-scanner specifications. For example, the technician can decide to acquire a supradiaphragmatic slice, choosing the descending aorta as ROI; this ROI has a mean basal HU value that increase with the contrast medium infusion. Concurrently with the contrast medium infusion, the CT-scanner makes sequential scans of the single slice previously chosen; when the selected ROI reaches a mean HU value greater than a threshold value previously established by the technician, the CT-scanner starts scanning the selected body region.
- **Bolus test**: even in this case a ROI of a single slice of the scanogram made by the technician is chosen and monitored with sequential scans during the contrast medium infusion. This method is similar to bolus tracking, but in this case a little amount of contrast agent (between 10 and 15 ml) is used just to evaluate the arrival time of this bolus of contrast agent after the beginning of injection; no CT-scan is made after the bolus infusion. Based on the calculated bolus arrival time, the technician can set up the beginning time of the following CT-scan.

Based on scan and contrast medium administration time, the contrast agent will be spread in different body districts, and this fact allows to enhance them in the best way possible.

For example (taking no notice of the total amount of contrast) a patient with a suspected pulmonary embolism has to be examined with a so-called ANGIO-CT scan; this kind of examination is made scanning the chest very soon after i.v. contrast agent administration; in this way the greatest amount of contrast agent is in the pulmonary circle, enhancing it in the best way possible and allowing the radiologist to find minus images suspected of embolism.

If, in the same patient, a new CT-scan will be acquired soon later, in absence of a massive lung embolism, will be visualised the principal arterial structures (aorta, epiaortic vessels, abdominal vessels).

A CT-scan made after 80 s after the start of the infusion, will better enhance the parenchymal structures, such as mediastinum and abdominal organs, because the contrast medium has had the time to spread in this organs following blood circle through arteries and capillaries; the pulmonary circle and the arteries in this case will be not well enhanced as the prior CT-scans.

A CT-Scan made between 5 and 15 min after the start of i.v. infusion, will enhance well the excretory ways (calyceal system, the ureters and the bladder) because of the elimination of contrast medium by kidneys, whereas the other organs will be lesser evident because of the uniform spread of contrast agent through the venous circle in the whole body.

Contrast Induced Nephrotoxicity (CIN), Acute Adverse Contrast Reactions, and Other Risks Related to Non-ionic Iodinate Contrast Agent i.v. Infusion [10–14]

In CT, non-ionic iodinate contrast medium is injected intravenously; like any other drug, it has certain relative contraindications for its use and after its administration there could be some adverse reactions which are important to be recognised and managed: a correct pathologic and laboratoristic anamnesis and a close cooperation with the clinicians are fundamentals. There are two principal kinds of adverse reaction:

1. **Contrast induced nephrotoxicity (CIN)**
2. **Acute adverse reaction**

Contrast induced nephrotoxicity (**CIN**) is the first adverse reaction we must pay attention; it is defined as a sudden deterioration in renal function, in the absence of any other causes, following the injection of contrast medium. It is indicated by an increase of at least 0.5 mg/dl of the basal level of serum creatinine.

The CIN is a not unpredictable complication of contrast medium administration because can occur even in wealthy patient with no risk factors or chronic kidney disease (CKD); anyway it is known that there is an increased risk of CIN or of aggravation of nephropathy in patients with high serum creatinine level [8].

According to Herts et al. [12], a more accurate parameter than the only creatinine serum level could be used to evaluate kidney function, the estimated Glomerular Flow Rate (**eGFR**) [13]. This parameter can be obtained using the **MDRD** [14] or the **Cockcroft–Gault formula**, knowing age, sex, weight, race and height of the patient. There are five different stages of Kidney Failure (Table 1):

Before the execution of every CT-examination (even in emergency conditions if possible) it is recommended to calculate the eGFR of the patient using the serum creatinine value of a blood examination not older than 7 days.

Table 1 Stage of kidney disease according to the egfr rate

eGFR value	Stage of chronic kidney disease
>90 ml/min/1.73 m^2	1 (no disease)
60–89 ml/min/1.73 m^2	2
45–59 ml/min/1.73 m^2	3a
30–45 ml/min/1.73 m^2	3b
15-29 ml/min/1.73 m^2	4
<15 ml/min/1.73 m^2	5

According to the ESUR manual on contrast media guidelines 8.1, we can consider patients at risk for CIN:

1. Patients with **eGFR <60 ml/min/1.73 m^2** who have to undergone examinations with **intra-arterial** infusion of contrast medium (i.e. angiographic examinations)
2. Patients with **eGFR <45 ml/min/1.73 m^2** who have to undergone examinations with **intra-venous** infusion of contrast medium (all the CT examinations)

Other known risk factors are:

- History of renal disease
- Age >70
- Dehydration
- Cardiac failure (NYHA class 3 or 4) or recent myocardium infarcts (<24 h)
- Intra-aortic balloon pump
- Periprocedural hypotension
- Low haematocrit values
- History of diabetes mellitus or gout
- Metformin or metformin-containing drug combinations or nephrotoxic drugs assumption.

In CT (where all the examinations which requires contrast medium are executed with an intra-venous administration) for those patients with a eGFR value <45 ml/min/1,73 m^2 or with other known risk factors, it is necessary to think about alternative diagnostic examinations if possible, consult with the clinicians and the nephrologist, and, if it was really indispensable making a contrast medium examination, provide an adequate hydration with 0.9 % saline solution (1.0–1.5 ml/Kg) at 100 ml/h 6–12 h before and 4–6 h after the contrast medium injection; in this case it is moreover recommended the use of *N*-acetyl-cysteine, although there are not still secure scientific evidences in the CIN prevention. Anyway, in all of these cases it is required a new evaluation of eGFR 48–72 h after the examination.

Patients in chronic haemodialytic treatment can undergo contrast medium examination with no problems because the contrast medium can be eliminated from the blood thanks to the haemodialysis.

It is necessary to consult the nephrologist if it is required a contrast CT examination in patients with acute renal insufficiency and if a CIN occurred despite these precautions.

Acute adverse reactions could be the classified in:

1. **Mild reaction** (not medical care required): pain on injection, heat sensation during the injection, mild urticaria and mild angioedema.
2. **Moderate reactions** (medical care required, but not life threatening management): severe urticarial and angioedema, bronchospasm or transient hypotension with tachycardia.
3. **Severe reactions** (life threatening management required): altered mental status, glottis edema, anaphylactic shock, cardio-pulmonary arrest.

There are no secure data about the frequency of the acute adverse reactions after the intravascular administration of non-ionic iodinate contrast agent, but in several studies it is comprise between 5 and 15 % of all patent. Although a serious acute adverse reactions could be happen in subjects with no history of allergies, during the anamnesis it is important to investigate if the patient is atopic, if in the past he has had adverse reaction to iodinate contrast agents or any allergen, identifying the triggering substances and specifying which kind of reactions occurred after the contact.

Unfortunately, we must remember that preliminary intradermal skin testing is not predictable for an adverse reaction. Moreover, we don't know well the pathologic mechanisms of contrast-medium acute adverse reactions, although several studies indicate the degranulation of basophiles and Mast-cell by a mechanism IgE-independent and the consequent liberation of histamine, as the principal etiologic mechanism of anaphylactoid reactions. Based on this, we can identify patients "**at risk**" for an adverse reaction (i.e. the **atopic patients**): they are those with a known history of **moderate or severe adverse reaction** to iodinate contrast agent or other allergens, and those with a not well-identified history of adverse reactions. We have to administer them an anti-allergic premedication. Unfortunately, the premedication is useful to avoid mild and moderate adverse reactions, whereas it seems to have no effect on the severe reactions.

There are several premedication protocols (according to the ACR Committee on Drugs and Contrast Media—Manual on Contrast media Version 8 2013) [10]:

1. **Elective premedication**:
   - **Prednisone** (50 mg by mouth) 13, 7 and 1 h before the contrast agent administration, or **Methylprednisolone** (32 mg by mouth) 12 and 2 h before the injection.
   - **Diphenhydramine** (50 mg i.v., i.m or by mouth) 1 h before the contrast agent administration (obligatory with Prednisone, optional with Methylprednisolone).
2. **Emergency premedication**:
   - **Methylprednisolone sodium succinate** (40 mg. i.v.) or **Hydrocortisone sodium succinate** (200 mg i.v.) every 4 h until the contrast agent administration; if the patient is allergic to one of those drugs before mentioned, **Dexamethasone sodium sulphate** (7.5 mg i.v.) or **Betamethasone** (6.0 mg i.v.) every 4 h until the contrast agent administration.
   - **Diphenhydramine** (50 mg i.v.) 1 h before the contrast agent administration.

Contrast medium warming to human temperature before injection (around 37 °C) decreases the risk of acute adverse reactions.

In those cases in which an acute severe reaction occurred in a patient "not at risk" or "at risk" (even if it was taken every precaution) the medical and paramedical equipment has to be prepared to act quickly, in particular if a patient has a severe acute adverse reaction which endangers the patient life; the structure must ensure in every case the basic cardiac and advanced life support to the patient.

We must remember other possible adverse reactions, given below, which contra-indicate the use of iodinate contrast medium:

- **Lactic acidosis in patients who take Metformin**: Metformin is a drug used in the treatment of diabetes mellitus type 2. For those patients who regularly take it, after the administration of contrast medium a lactic acidosis may occur. The ESUR 8.1 contrast media guidelines suggest for patients who have to undergo intravenous contrast medium administration:

  1. In patients with eGFR > 45 ml/min/1.73 m^2 and without any known comorbidities it is not necessary to suspend the therapy with Metformin.
  2. In patients with renal dysfunction (eGFR between 45 and 30 ml/min/1.73 m^2) it is necessary suspending the administration of metformin 48 h before the contrast injection and reintroduce it with caution after 48 h if there have been no changes in renal function after the contrast agent administration.
  3. In patient with eGFR < 30 ml/min/1.73 m^2 contrast medium administration is contraindicated.

- **Possible arising of sickle cell crisis in patients affected by sickle cell anaemia**.
- **Possible arising of myasthenic crisis in subjects with myasthenia gravis or suspected thymoma**.
- **Possible arising of hypertensive crisis in subjects with phaeochromocytoma or thyrotoxicosis**.

In the end, if an **extravasation of contrast agent** occurs in the cutaneous or subcutaneous tissues, it could determine reactions that in the most of cases are not serious (such as local erythema and edema) but sometimes could be serious (from the appearance of ulcers to the compartment syndrome). To limit this occurrence, can be taken precautions such as testing the venous access injecting normal saline solution at high flow rate; if a complication occurs, it is important monitoring the patient, elevate the limb and, in the worst cases, ask for a surgical advice.

For other information, including the non-ionic iodinate contrast agent management in children and pregnant women, see the ESUR contrast media guidelines 8.1 (http://www.esur.org/guidelines) and the ACR Committee on Drugs and Contrast Media – Manual on Contrast Media (http://www.acr.org/Quality-Safety/Resources/Contrast-Manual).

Radiobiology [13, 15–21]

As we have seen before, CT-scanners use X-rays to obtain an image. X-rays are ionising electromagnetic waves that produce various effects on biologic structures, which can be divided in two groups:

1. **Stochastic effects**: these are **probabilistic effects**, i.e. they can manifest themselves more likely, but not necessarily, increasing the amount of radiation dose administered to the patient. There is not a dose threshold value for this kind of effects, and their development is deferred with respect to time of administration. **The stochastic effects of X-rays on biological structures are the mutagenic effects on DNA**:
   (a) In **somatic cells**, the mutagenic effects of X-rays could determine or cellular death (apoptosis) or neoplasms development. In pregnancy, embryos and foetuses could develop malformations of various type or miscarriages, depending not only on the doses but even on the gestational time.
   (b) In **germinal cells**, the X-rays mutagenic effects could determine or cellular death (apoptosis) or irreversible DNA mutations with variable effects on the product of conception (foetal malformations, miscarriages).

Tissues with great replication rate, such as hematopoietic tissues, are more sensible to stochastic effects despite those with low replication rate, such as bone or nervous tissues.

2. **Non-stochastic effects**: these effects are **not probabilistic**, i.e. there is a threshold value of X-rays radiation dose for which these effects appear. Of course, the dose threshold and the biologic reactions are different for every tissue. The knowledge of this kind of effect is very important in radiotherapy and nuclear medicine.

Every time we make a CT-scan, we have to know the dose administered to the patients, to minimise the X-ray exposure of the patients. In particular, we have to know these concepts:

1. When an X-ray beam interacts with a mass, it gives energy to the mass. **The "absorbed dose" (D) is the measurement of the average amount of energy $(\mathbf{d}\bar{\varepsilon})$ absorbed by an element with a certain mass (dm)**; this concept is expressed by the formula (8)

$$D = \frac{d\bar{\varepsilon}}{dm} \tag{8}$$

The SI unit of measurement is Gray (Gy): one Gy corresponds to one Joule absorbed by a mass of 1 Kg, according to the formula (9):

$$1\,Gy = \frac{1J}{1Kg} \tag{9}$$

In clinical practice the submultiples are often used, **mGy** and **cGy** (respectively 10^{-3} and 10^{-2} Gy).

2. The absorbed dose determines different biologic effects in relation to the type of the radiation and tissue involved. **The "equivalent dose" (H) is the measurement of biologic effects inducted by the absorbed dose (D) of a specific radiation (R) in a specific organ or tissue (T)**; this concept is expressed by the formula (10):

$$H_T = \sum_R w_R D_{T,R} \tag{10}$$

where $\mathbf{w_R}$ is the weighted factor of the specific radiation (**R**).

The SI unit of measurement is Sievert (Sv) according to the formula (11):

$$1\,Sv = \frac{1J}{1Kg} \tag{11}$$

Even here, in clinical practice, the submultiples are commonly used, **mSv** and **cSv**, (respectively 10^{-3} and 10^{-2} Sv).

3. A human body consists of different tissues and organs; for a certain dose, there will be different biological effects depending on the characteristics of every single tissue of the human body. **The "effective dose" (E) is the weighted sum of the equivalent dose (HT) multiplied by every single tissue weighted factors (wt) which constitutes human body**: it is expressed by the formula (12):

$$E = \sum_T w_t H_t = \sum_T w_t \sum_R w_R D_{T,R} \tag{12}$$

The tissue weighted factor ($\mathbf{w_T}$) is specific for every tissue of human body, and the sum of the values of $\mathbf{w_T}$ is 1.

The SI unit of measurement is the same of the equivalent dose, the Sievert (Sv).

These concepts are very difficult to evaluate, and in particular tissue weighted factor ($\mathbf{w_T}$) and the weighted factor of the specific radiation ($\mathbf{w_R}$) derived from experimental data.

In CT, in particular in volumetric CT-scans, we must remember that the same volume of tissue could be irradiated different times during the spiral acquisition. The absorbed dose is experimentally measured making CT-scans of CT acrylic phantoms (with different sizes for adult and paediatric patients) that contain holes in which are placed cylindrical dosimeters. This method allows us to obtain the so-called computed tomography dose index (CTDI), expressed in Gy; these values are reviewed continuously by the scientific community and are converted into effective doses using the above formulas.

Every year we are exposed to natural radiation, and the world average equivalent dose is 2,4–3 mSv. According to Metter et al. the CT average effective doses range from 2 mSv of a head CT-scan to 16 mSv for a coronary angiography (Table 2). It is important remembering that these values are very important, because

Table 2 Summary of radiation dose delivered to the patients according to the type of ct exam performed

Examination	Adult effective dose (Metter et al.) (mSv)	Values reported in literature (mSv)
Head	2	0.9–4.0
Neck	3	–
Chest	7	4.0–18.0
Chest for pulmonary embolism	15	13–40
Abdomen	8	3.5–25
Pelvis	6	3.3–10
Three-phase liver study	15	–
Spine	6	1.5–10
Coronary angiography	16	5.0–32
Calcium scoring	3	1.0–12
Colonoscopy	10	4.0–13.2

Levey AS, Coresh J, Balk E, et al. National Kidney Foundation practice guidelines for chronic kidney disease: evaluation, classification, and stratification. Ann Intern Med. 2003;139:137–47
Mettler FA Jr, Huda W, Yoshizumi TT, Mahesh M. Effective doses in radiology and diagnostic nuclear medicine: a catalog. Radiology 2008;248(1):254–63

in only one scan (few seconds or minutes) we are administering great effective doses to the patient, increasingly the probability to induce stochastic effects to the patients.

It is fundamental limiting as much as possible the total radiation exposition of the patient and in particular the CT-examinations have to be justified and made to confirm a specific clinical question or to search a pathologic condition after an accurate anamnesis, clinical examination, appropriates laboratory exams and non-invasive procedures, such as US.

References

1. Borsa F, Scannicchio D. FISICA con applicazioni in biologia e in medicina Edizioni Unicopli. 2004.
2. Brant William E, Helms CA. Fundamentals of diagnostic radiology. 3rd ed. Philadelphia, PA: Lippincott Williams & Wilkins; 2006. Italian edition – Verduci Editore.
3. Prokop M, Galanski M. Spiral and multislice tomography of the body. 1st ed. Stuttgart, Germany: Thieme; 2002.
4. Cunningham IA, Judy PF. Computed tomography. The biomedical engineering handbook. 2nd ed. West Palm Beach, FL: CRC; 2000. Editor: Joseph D. Bronzino.
5. Kalender WA. X-ray computed tomography. Phys Med Biol. 2006;51:R29–43.
6. Goldman LW. Principles of CT and CT technology. J Nucl Med Technol. 2007;35(3):115–28.
7. Goldman LW. Principles of CT: multislice CT. J Nucl Med Technol. 2008;36(2):57–68.
8. Kumamaru Kanako K, Hoppel Bernice E, Mather Richard T, Rybicki FJ. CT angiogrphy: current technology and clinical use. Radiol Clin North Am. 2010;48(2):213–35. doi:10.1016/j.rcl.2010.02.006.

9. Bae KT. Intravenous contrast medium administration and scan timing at CT: considerations and approaches. Radiology. 2010;256(1):32–61.
10. ACR Committee on Drugs and Contrast Media. Manual on contrast media version 8. 2012. http://www.acr.org/Quality-Safety/Resources/Contrast-Manual.
11. ESUR guidelines on contrast media 8.1. http://www.esur.org/guidelines/.
12. Herts BR, Schneider E, Poggio ED, Obuchowski NA, Baker ME. Identifying outpatients with renal insufficiency before contrast-enhanced CT by using estimated glomerular filtration rates versus serum creatinine levels. Radiology. 2008;248:106–13.
13. Levey AS, Coresh J, Balk E. National Kidney Foundation practice guidelines for chronic kidney disease: evaluation, classification, and stratification. Ann Intern Med. 2003;139:137–47.
14. Levey AS, Bosch JP, Lewis JB, Greene T, Rogers N, Roth D. A more accurate method to estimate glomerular filtration rate from serum creatinine: a new prediction equation. Modification of Diet in Renal Disease Study Group. Ann Intern Med. 1999;130:461–70.
15. Stephen AE et al. American College of Radiology white paper on radiation dose in medicine. J Am Coll Radiol. 2007;4:272–84.
16. Bauhs JA et al. CT dosimetry: comparison of measurement techniques and devices. RadioGraphics. 2008;28:245–53.
17. Goldman LW. Principles of CT: radiation dose and image quality. J Nucl Med Technol. 2007; 35(4):213–25.
18. ICRP. The 2007 recommendations of the International Commission on Radiological Protection. ICRP; 2007 publication 103. http://www.icrp.org/publication.asp?id=ICRP%20Publication% 20103).
19. Mettler Jr FA, Huda W, Yoshizumi TT, Mahesh M. Effective doses in radiology and diagnostic nuclear medicine: a catalog. Radiology. 2008;248(1):254–63.
20. Tamm PD et al. CT radiation dose reduction: how to implement change without sacrificing diagnostic quality. RadioGraphics. 2011;31:1821–32.
21. UNSCEAR. Report of United Nations Scientific Committee on the Effects of Atomic Radiation to general assembly. http://www.unscear.org/docs/reports/gareport.pdf.

CT Imaging of Coronary Arteries

Michele Porcu, Marco Francone, Giovanni Maria Argiolas, Giuseppe Cannavale, Mario Piga, Jasjit S. Suri, Iacopo Carbone, Carlo Catalano, and Luca Saba

Introduction to Cardiac Imaging

Cardiovascular diseases (CVD), and in particular coronary artery disease (CAD), are among the principle causes of mortality and morbidity in Europe and in the USA, representing high sanitary costs for insurance and national health systems.

In the USA, 83.6 million American adults suffer from CVD (42.2 million with an age ≥60), and among these, 15.4 millions suffer from a CAD [1]. The average incidence of first cardiovascular event varies from 3/1,000 among men between 35 and 40 y.o. up to 74/1,000 among men between 85 and 94 y.o., whereas among women similar values have been founded 10 years later in life [1]. The direct and indirect costs of CVD for 2009 have been about 300 billion dollars [1]. These numbers show the importance of a proper management of this kind of patients.

Coronary angiography (**CA**) is still the gold standard for the real-time visualisation and assessment of coronary circle, and a fundamental interventional tool for intravascular thrombolysis and stenting placement procedures.

M. Porcu, M.D. • L. Saba, M.D. (✉)
University of Cagliari, Cagliari, Italy
e-mail: lucasaba@tiscali.it

M. Francone, M.D. • G. Cannavale, M.D. • I. Carbone, M.D. • C. Catalano, M.D.
Department of Radiology, Oncology and Pathology, La Sapienza University, Rome, Italy

G.M. Argiolas, M.D.
Department of Radiology, Azienda Ospedaliero Brotzu (A.O.B.),
di Cagliari, Cagliari 09100, Italy

M. Piga, M.D.
Department of Radiology, Azienda Ospedaliero Universitaria (A.O.U.),
di Cagliari – Polo di Monserrato, s.s. 554 Monserrato, Cagliari 09045, Italy

J.S. Suri, Ph.D., M.B.A., Fellow AIMBE.
AtheroPoint LLC, Roseville, CA, USA

R. Trivedi et al. (eds.), *3D Imaging Technologies in Atherosclerosis*,
DOI 10.1007/978-1-4899-7618-5_2

Intracoronary ultrasonography (**ICU**) is a complementary examination that allows the evaluation of plaque morphology and the assessment of the coronary walls. These fundamental tools have the disadvantages of being invasive (in fact they are based on the selective catheterisation of the coronary arteries through an arterial access, which generally is the brachial or the femoral artery) and not without intraoperative and postoperative complications, such as plaque rupture followed by thrombosis in situ and ischemia, death and infections.

Coronary CT angiography (CTA), despite CA and ICU, is a non-invasive examination that offers a global evaluation of the coronaries, including vessel lumen, conditions of the coronary walls, plaque type and morphology and relationships of the vessels with the heart. CTA is also considered a better examination than cardiac MRI for the assessment of the coronary arteries [2].

For these reasons, CTA has become a very important instrument to evaluate CAD; in particular it is a preliminary examination for such symptomatic patients with a low-intermediate risk for CAD [3], which could need a more invasive examination such as CA and ICU. Of course, in CTA the execution of interventional procedures, such as stenting placement and intravascular thrombolysis, is not yet possible.

It is moreover important to remember that cardiac CT is an examination which can be made not only for the assessment of coronary arteries, but even for many other conditions, including valve disease, cardiac tumours and pericardium diseases [4].

In this chapter we focalise on:

- Normal coronary anatomy
- American Heart Association (AHA) left ventricle segmentation model and coronary distribution territories
- Coronary Artery Calcium Score (CACS)
- CTA examination, including technique of execution
- CTA indications
- Principal CADs and imaging findings

Normal Coronary Artery Anatomy

The two main coronary arteries, right and left, originate from the sinuses of Valsalva, at the origin of the aortic root, between the aortic valve and the sino-tubular junction. They course along the epicardial surface, wrapped by fat [5].

Normally there are three sinuses of Valsalva: the right (or anterior) sinus, the left (or posterior) sinus and the non-coronary sinus. The **right coronary artery** (**RCA**) origins from the right coronary sinus, whereas the **left coronary artery** (**LCA**) origins from the left coronary sinus [5].

1. **RCA**: After its origin it courses anteriorly and laterally along the right atrioventricular groove and then goes to the acute margin of the right ventricle; it supplies the free wall of the right ventricle and can be divided into three main portions:
   (a) **Proximal portion**: from origin in the right sinus of Valsalva to the acute marginal origin.
   (b) **Mid portion**: from the acute marginal origin to the horizontal tract of the posterior right atrioventricular groove.
   (c) **Distal portion**: the last tract that bifurcates into two important vessels:
      - **Posterior descending artery (PDA)**: It courses along the posterior interventricular groove, supplying the posterior third of the interventricular septum.
      - **Posterolateral left ventricular branches (PLV)**: They course along the posterior portion of the left atrioventricular groove, and supply the posterior surface of the left ventricle.

   Moreover, from the RCA originate branches for the **conus** (although in 50 % of the cases this branch origins from the aortic root), the **sinoatrial node** (about 60 % of the cases, in 40 % it origins from left circumflex artery (LCX)), **acute marginal branches** and **atrioventricular nodal branch** [5].
2. **LCA**: It originates from left sinus of Valsalva; it originates as **left main artery (LMA)**, and then divides into (Fig. 1) [5]:
   (a) **Left anterior descending artery (LAD)**: It courses anteriorly along the interventricular groove to the apex. From this artery originate:
      - The **septal perforator arteries** which supply the anterior two-thirds of the interventricular septum.

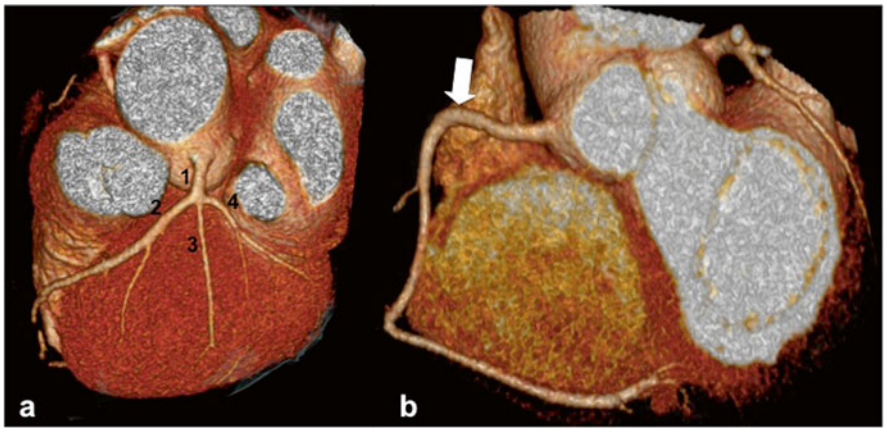

Fig. 1 (**a**) *1*: Common trunk; *2*: left anterior descending artery; *3*: intermediate branch. (**b**) *Arrow*: Circumflex artery

- The **diagonals**, which supply the anterolateral portion of the left ventricle; they are up to six, and they are numbered sequentially as they arise (D1, D2 …).

Moreover, LAD can be divided into three main portions:

- **Proximal portion**: from the origin to the first septal perforator or diagonal artery.
- **Mid portion**: from the origin of the first septal perforator or diagonal artery to the second diagonal.
- **Distal portion**: from the origin of the second diagonal up to the apex.
- Occasionally, the LMA does not divide but trifurcates into LAD, LCX and a middle branch between them, known as **ramus intermedius.**

(b) **Left circumflex artery (LCX)**: It courses along the left atrioventricular groove up to the obtuse margin of the heart (in 80–85 % of patients, see below); it supplies the lateral portion of left ventricle. From this artery originates the **obtuse marginal arteries** (**OM**) numbered sequentially as they arise (OM1, OM2 …). It can be divided into two portions:

- **Proximal portion**: from origin to the origin of the greatest OM
- **Distal portion**: from the origin of the greatest OM.

There is another one important concept to explain: **the dominance** (Fig. 2). The dominance of the coronary circulation is determined by the origin of the atrioventricular nodal artery, PDA and PLV. In fact, the dominance can be [5]:

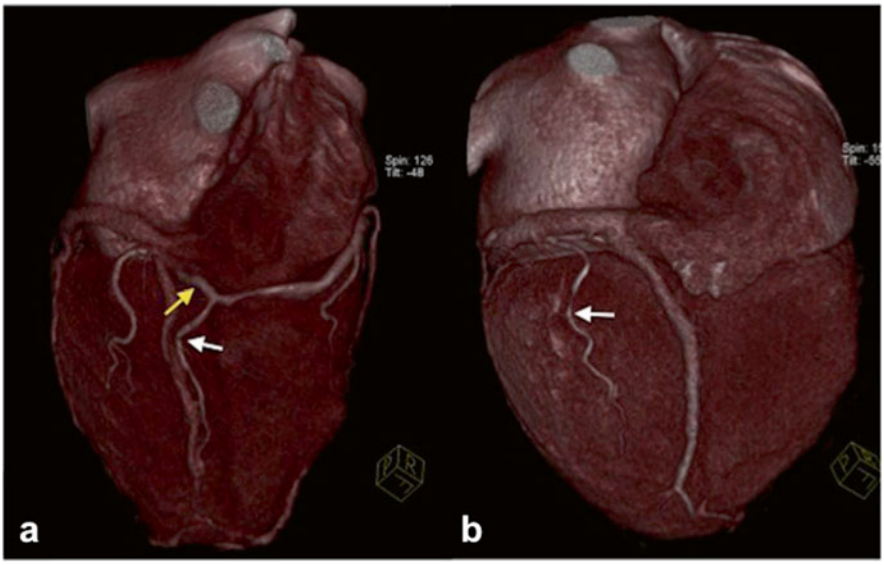

Fig. 2 (**a**) Right dominance: The posterolateral branch (*yellow arrow*) and the posterior interventricular branch (*white arrow*) originate from the right coronary artery. (**b**) Left dominance: The posterior interventricular branch (*arrow*) originates from the circumflex artery

1. **Right dominance** (**80–85 %**): the atrioventricular nodal artery, PDA and PLV originate from RCA.
2. **Left dominance** (**8–10 %**): the atrioventricular nodal artery, PDA and PLV originate from LCX.
3. **Codominance** (**7–8 %**): the PDA originates from the RCA and the PLV originates from the LCX.

American Heart Association Left Ventricle Segmentation Model and Coronary Distribution Territories

According to the AHA left ventricle segmentation model [5, 6] we can divide the left ventricle cavity into three regions on the long axis, and the walls in 17 segments (**seen on a short-axis plane and numbered in anticlockwise**) **as you can see in the table** (Table 1) **and in the figure** (Fig. 3).

Regarding the **blood supply**, the LAD provides for the supply of blood of the segments 1, 2, 7, 8, 13 and 14; LCX provides for the supply of blood of the

Table 1 AHA left ventricle segmentation model

Basal region	Mid-cavity	Apical region
Anterior (1)	Anterior (7)	Anterior (13)
Anteroseptal (2)	Anteroseptal (8)	Septal (14)
Inferoseptal (3)	Inferoseptal (9)	Inferior (15)
Inferior (4)	Inferior (10)	Lateral (16)
Inferolateral (5)	Inferolateral (11)	Apex (17)
Anterolateral (6)	Anterolateral (12)	

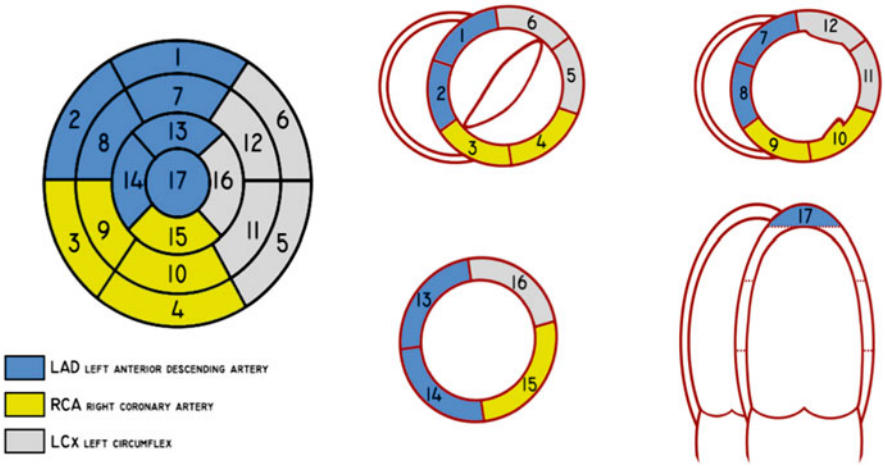

Fig. 3 AHA left ventricle segmentation model and blood supply

segments 5, 6, 11 and 12, meanwhile RCA (when it is dominant) supplies segments 3, 4, 9, 10 and 15 [6]. The segment 17 can be supplied by any of the three arteries, but generally is assigned to the LAD [6].

The Coronary Artery Calcium Score

The CACS is a method of evaluation of the amount of calcium localised in the coronary arteries, which is indicative of the risk of cardiac major events [7], but its use in clinical practice is controversial [8]. It has been introduced in the clinical practice with the invention of the electron beam scanners, and many authors have proposed different methods of measurement of this score.

The most important and tested in clinical practice is the so-called Agatston-Janowitz score [8, 9] introduced by Agatston and colleagues in 1990: it is a semi-quantitative method calculated on the basis of basal ECG-gated scans at 130 kV and 630 mA, with a slice thickness of 3 mm, on a matrix of 512 × 512 [8]. In order to be included in the calculation of the score, all the calcifications of the coronary arteries must cover a surface of more than 1 mm^2 and have to have a value of at least 130 HU [8]. The area of every single calcification is then multiplied for an attenuation-weighting factor (with a value between 1 and 4) according to the highest HU value of the plaque [8]. In this way it is possible to calculate the calcium score of the single vessels, or the total calcium score given by the sum of the calcium vessels calcium score [8]. Nowadays various software which automatically calculate the CASC are available, in particular using the Agatston-Janowitz method.

The indications for the execution of the CT scan for the CASC are the evaluation of asymptomatic patients with an intermediate risk for CAD (values higher than 400 according to the Agatston-Janowitz score suggest modifications in the lifestyle and medical therapy in order to reduce the risk of major cardiac events), and of symptomatic patients as screening before invasive procedures or CTA (CTA could be useless in patients with high calcium score because of the increased incidence of artifacts), or if it is impossible to execute other examinations [8].

The CASC is directly related with the risk of major cardiac events, and it has been seen a gradual decrease of the overall survival related with the increase of the Agatston score, in particular for value above 1,000 [10].

Anyway, it is important to underline that the CASC does not allow the evaluation of the patency of the coronary arteries and the number, the morphology and the characteristics of the non-calcified plaques [8].

CTA Examination

Thanks to the introduction of single-source 64-slice CT scanner, CTA has become a very useful and feasible exam for the assessment of coronary arteries. In fact this kind of CT scanners, because of their high temporal (up to 150 ms) and spatial

resolution, have higher sensitivity and specificities in CAD detection (sensitivity 85–99 % and specificity 86–96 %) despite 4-slice (sensitivity and specificity between 76 and 93 %) and 16-slice CT scanner (sensitivity and specificity between 82 and 95 %) [11]. In addiction, the introduction of 128-slice, 256-slice and 320-slice CT scanner in clinical practice and the dual source CT (DSCT) has further improved spatial and temporal resolution (up to 75 ms in DSCT), and allows to **reduce radiation dose in combination with some dose-saving strategies** (see below).

The great challenge of CTA is freezing a continuous moving structure, and the collaboration of the team radiologist-technician with the patient has to be as best as possible in order to make a diagnostic exam.

The anamnesis is a fundamental part of radiology (**and of course in medicine**), **and in particular in CTA**: The radiologist has to know every useful data of the patient for the correct interpretation of the examination. In particular the radiologist has to investigate on familiarity for CAD, previous and/or coexisting pathologies (diabetes, hypercholesterolemia, hypertension …), smoke, symptomatology (angina, dyspnea …) and possibly the results of previous tests executed (basal and stress electrocardiography, basal and stress echocardiography …); moreover, since CTA is an examination which involves the use of **iodinate contrast medium**, the radiologist must investigate about any risk factors concerning that (see Chap. "Principles of Computed Tomography").

After the anamnesis, the radiologist has to explain to the patient the phases and the risks related to the procedure, obtaining the informed consent.

Once assured about this, another important step is the measurement of the **heart beat rate** (**HBR**): in patients with **HBR >65 bpm** the use of **β-blockers** could be necessary (in particular β1-selective blockers, such as metoprolol, atenolol) so as to lower HBR and to make the rhythm more regular [12]. We obtain better scans if the heart beat rate is <65 bpm, and **this value is indispensable if a prospective ECG-triggering acquisition mode is chosen** (**for the use of β-blockers in transplanted heart see below**). Contraindications to their use are seen in the table (Table 2) [12].

As these conditions are excluded, the radiologist could administer a premedication of β-blockers orally. For **metoprolol**, one 50 mg dose at least 1 h before the examination monitoring the HBR every 15 min: if it does not lower <65 bpm (or <60 bpm if the HBR is irregular) and after a 15-s breath hold there is not any lowering of the frequency, metoprolol I.V. can be administered when the patient lies on the moving table, one 2.5 mg dose in 1 min, and if necessary another 2.5 mg dose after 5 min; if the HBR still remains elevated after 5 min the last bolus could be

Table 2 Contraindications to β-blockers

Heart rate <60 bpm
Systolic blood pressure <100 mmHg
Uncompensated cardiac failure
Aortic stenosis
Allergy to β-blockers
Asthma or COPD on β2-agonist inhaler
Active bronchospasm
Second- or third-degree atrioventricular block

given up to two additional single doses of 5 mg every 5 min (maximum I.V. dose: 15 mg) [12]. If metoprolol I.V. is given, the patient has to be observed at least 30 min after the last administration; if the HBR is <45 bpm, the radiologist has to consider the use of atropine, whereas if bronchospasm occurs it is necessary administering a β-agonist (for example albuterol) [12].

Patients with severe arrhythmias (such as atrial fibrillation) are very difficult to evaluate because of the irregular heart rhythm; further technologic improvements have still to be made [13].

Anxious patients have to be ensured, because anxiety is related with high HBR; if it would be necessary, it is moreover advised administering oral benzodiazepine such as **diazepam** 5 mg (5–15 drops 15 min before the examination).

After these preliminary moments, the patient can be placed supine on the moving table, with ECG electrodes positioned on his/her chest, and a cannula (minimum dimension 18G) inserted in the right antecubital vein. ECG is registered and analysed by the CT scanner in real time. **Every CTA is achieved through ECG-gated scans**.

The technician makes the scanogram, and then places a ROI on the aortic root: the scan delay time from the beginning of contrast medium I.V. infusion is chosen according to a **bolus test** (20 ml contrast medium bolus at the same flow of the examination) or an **automatic bolus-triggering** technique [5], knowing the technical specifics of the own CT scanner. The scan has to cover the chest from the diaphragm up to the aortic arch, in order to cover the heart and the great thoracic vessels. In certain cases, the scan has to cover also the epiarotic vessels (in particular in patients with arterial coronary artery bypass graft (CABG), see below). Few seconds before the beginning of the scan, it is recommended to administer **nitroglycerine 0.4 mg sublingual** (spray or tablet) to dilate the coronary arteries [14].

The next step is the contrast medium infusion: Generally **a 50–60 ml contrast medium bolus** is administered, with a **biphasic** (contrast medium bolus followed by a 50 ml saline solution bolus to wash the right chambers and better evaluate RCA) or **triphasic technique** (contrast medium bolus followed by a mixture of contrast medium and saline solution to evaluate right chamber, and followed then by a bolus of saline solution) [5], with a flow of 5–6 ml/s.

The acquisition mode depends on the type of scanner used; for a **single-source CT scanner** (64-slice CT scanner or more) two different techniques can be used (it is necessary that the patient holds the breath during the examination):

- **"Retrospective ECG gating"** (Fig. 4): It is a spiral scan, with a very low pitch (0.2–0.4) [11], acquired continuously and simultaneously to the ECG [15]. Once scan is obtained, CT scanner elaborates the projection data acquired during the helical scan with the ECG, and **reconstructs the exam "retrospectively"**, obtaining images of the entire cardiac cycle. The images can be reconstructed in two different ways, with the partial scan reconstruction or the multiple-segment reconstruction (see below).

  The advantages of this technique are **a good temporal resolution** (**80–250 ms**) [15] better than prospective ECG-triggering acquisition, whereas **the**

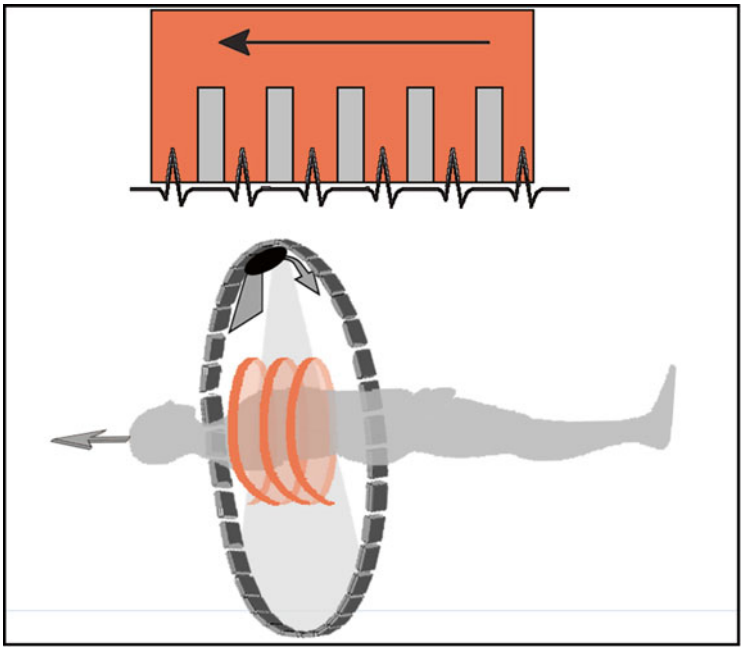

Fig. 4 Retrospective ECG gating: The scan is obtained with a spiral CT during the entire cardiac cycle and it is then retrospectively reconstructed according to the registered ECG

absorbed dose is very high (**between 7.6 and 31.8 mSv**) [16] because of continuous radiation emission during the scan (very low pitch and great overlap in the same section of the thorax) [15].

- **"Prospective ECG triggering"** (Fig. 5): Even in this case, the scan is made synchronised with the ECG. **It is a sequential scan: data acquisition takes place only in a predefined temporal window of the R-R cycle** (i.e., in the diastolic phase, when the heart is more stable, between 20 and 80 % of the R-R cycle; or between 50 and 80 % if the rhythm is lower, in order to reduce the amount of radiation dose), **and the X-ray tube turns only when triggered by the ECG signal registered by the CT scanner** [11].

The most important advantage of this technique is **a lower radiation exposure** (**absorbed dose values between 2.1 and 9.2 mSv**) [16] compared with the retrospective ECG gating, but it has even **a lower temporal resolution** (**200–250 ms**) [15], requiring an HBR necessarily lower than 65 bpm, and it is also more subject to artifacts. Recent studies [17, 18] have shown that prospective ECG-triggering CTA are similar in quality to those obtained with retrospective ECG gating with a lesser dose of radiations (about 76.5 %) [17].

The step-and-shoot technology with dual-source CT in patients with less than 70 bpm allows to obtain diagnostic images in more than 97 % of the cases reducing the amount of dose given to the patient compared to retrospective ECG gating analysis [19].

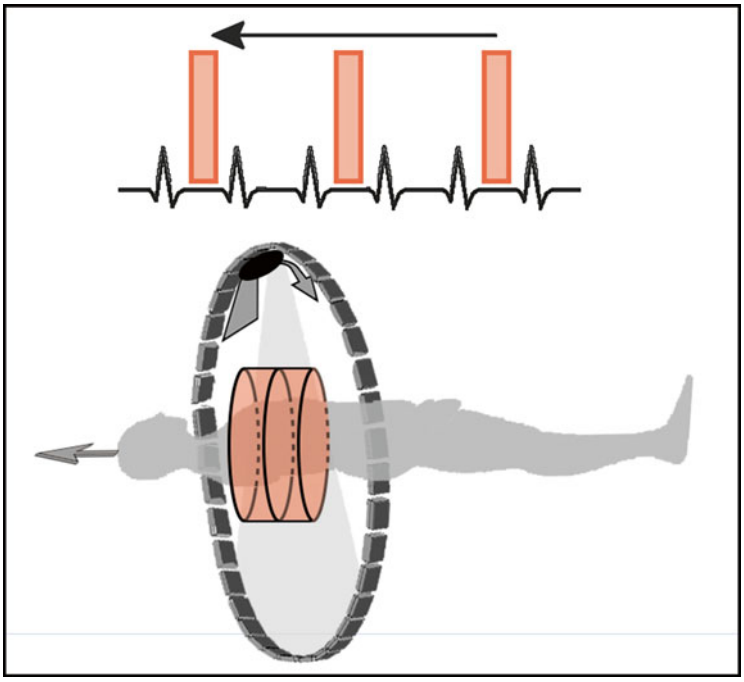

Fig. 5 Prospective ECG triggering: The scan is obtained with a sequential CT during a predetermined phase of the cardiac cycle, according to the ECG

With the introduction in clinical practice of the **dual-source CT scanner**, temporal resolution has been further improved, up to 75 ms, allowing a new acquisition mode, known as **"flash mode"**: this method, thanks to a high pitch (>3.4) and large detector coverage, consents to acquire a heart scan during a single heart beat in a quarter of second with very low radiation doses (<1 mSv) [11].

The examinations can be **reconstructed in two methods**:

- **Partial scan reconstruction**: With this modality, used either for retrospective ECG gating and prospective ECG triggering acquisition modes, the data used for the reconstruction derived from a predefined R-R interval of a single heart cycle [15].
- **Multiple-segment reconstruction**: In this reconstruction modality scan projection data used to obtain the images are selected from various sequential heart cycles [15]. This modality can be used only with retrospective ECG gating acquisition mode [15].

If the CT scanner uses filtered backprojection reconstruction algorithms, the B46f kernel is the most used in clinical practice; the latest CT scanners use iterative image reconstruction algorithms with a substantial reduction in radiation doses (see below).

Once the exam has been correctly executed, the radiologist using different post-processing techniques analyses it, such as **MIP, or volume rendering**, which is useful in particular for clinicians to have a simple and anatomic view of the

Table 3 Elements of a correct report

Report data
Clinical question for the examination
Use of drugs before the examination (β-blockers, nitroglycerin, benzodiazepine)
Acquisition mode (retrospective ECG gating, prospective ECG triggering …)
IV contrast medium bolus information (type, quantity, administration modality)
Imaging findings, indicating: • Dominance of the coronary circle (right, left or codominance) • Coronary findings (including malignant and non-malignant anomalies), describing type, location and extension of lesions • Other cardiac findings • Non-cardiac findings

coronaries [20]. **Curved multiplanar reformation** is widely used because it allows to "stretch" the coronaries, in order to follow the entire course of the vessels and to depict lumen and wall abnormalities [20].

A correct report includes [5] **all the information seen above** (Table 3).

Before talking about the principal CTA indication and principal image findings in CADs, it is important remembering that nowadays there are many **dose reduction strategies** which allow to obtain very good examinations with lower radiation doses than in the past; in fact, with the prospective-ECG-triggering and flash acquisition mode seen before we can obtain examination at low doses using lower peak kilovoltage values (100 kV are sufficient if the patient has a BMI <25 kg/m^2, and 80 if the BMI is <20 kg/m^2) [11]; another way to reduce radiation dose is **the use of the iterative image reconstruction algorithms**, which allows to obtain CTA with lower radiation doses, lower noise and better quality despite the traditional backprojection algorithms [11, 21–23].

In the pediatric population in order to obtain a diagnostic examination sedation could be required if the little patients are not collaborative with different approaches (midazolam 0.1 mg/kg/dose with the anesthesiologic assistance) [24]. Sedation and breath hold would not be required in newborn and quiet babies, especially if modern faster scanners are used. It is of course important giving the lowest radiation of dose "as low as reasonably achieved" ("ALARA") to the patient, adopting several strategies, like increasing the pitch value, reducing the volume coverage and tube kV (80 kV with a weight less than 25 kg) and adjusting the value of mAs to the weight of the patient [24]. It is moreover preferable to use the ECG-gated acquisition to limit the motion artifacts, and if available, prospective ECG triggering or the flash acquisition mode than retrospective ECG gating mode.

CTA Indications

Like other radiologic examinations that involve X-rays, CTA can be executed if there is a favourable risk-benefit ratio for the patient, and this risk has to be evaluated individually for every single patient [3]. CTA is indicated for **symptomatic**

patients that on the bases of age, sex, symptoms and previous non-radiologic examinations have a **low to intermediate probability of significant CAD**, in particular symptomatic young patients with no ECG changes and serial enzymes negative, with an ECG uninterpretable, unable to exercise or stress test, with uninterpretable or equivocal stress test, or with suspected non-aterosclerotic coronary anomalies (such as anatomic anomalies or aneurisms) [3, 25].

A detailed meta-analysis of different studies have confirmed the correlation between CAD severity detected on CTA examinations and increased risk of related heart adverse events: the absence of CAD is related with a low risk of adverse cardiac events, whereas a non-obstructive or obstructive CAD is associated with an increase of the likelihood of adverse cardiac events [26]. Another study [27] confirms these data and extends the outcome over the 5 years.

Other indications are **the evaluation of stents and CABG before the execution of a CA**.

Thanks to technical improvements and introduction of modern CT scanners (single-source 64-slice or more and dual source) in clinical practice and in Emergency Departments (ED), another emerging indication for CTA is the evaluation of acute chest pain in ED (not as a replacement examination, but done besides clinical evaluation, ECG and serum cardiac enzyme) [11, 14]. In fact, the so-called **triple rule out** allows to evaluate at the same time, and eventually exclude (or confirm), three important clinical conditions [14]:

- **Coronary thrombosis**
- **Pulmonary embolism**
- **Thoracic aortic dissection**

Currently there is still no indication as screening examination for asymptomatic patients because of the high radiation exposure [3]; thanks to the technological improvements for dose reduction such as flash acquisition mode (see above [11]) we can even imagine that in few years CTA will become a screening examination for CAD.

Dual-source CTA is a useful examination in the pediatric population, in particular in those with a high likelihood of coronary artery anomalies [28], and when associated with ECG-triggered prospective spiral acquisition with high pitch, low tube current tube and iterative reconstruction method [29].

Principal CADs and Imaging Findings

Atherosclerosis is the principal coronary disease, but it is not the only one; in fact, as we have seen before, other pathologic conditions that have been evaluated are the anatomic malignant and non-malignant variants, aneurisms and fistulas and the evaluation of stents and bypass grafts.

Coronary Anatomic Anomalies

Coronary anatomic anomalies are inborn anomalies that occur in 1 % of the general population [30], even if necropsies show lower incidence (0.3 %) [30]. Moreover, it is known that sometimes patients with congenital heart diseases have one or more associated coronary artery anomalies [31]. There are many anatomic variants and could manifest in young patients with symptoms like atypical chest pain shortness of breath or acute myocardial infarction [32], but most of that have no clinical outcome [5]; thereby, some of them are malignant and have to be recognised and described.

Some of these anomalies could be not recognized with the traditional CA [33]. CTA is the best examination available in the study of these clinical conditions [32] because of its intrinsic ability in the global morphologic study of the heart and vessels.

Malignant coronary anomalies (Fig. 6) manifest clinically with chest pain, dyspnoea, syncope, myocardial infarction, ventricular fibrillation or sudden death, rarely with reproducible effort angina [30]. There are many different malignant variants, and **Bland-White-Garland syndrome** [34] is one of them: even known as ALCAPA syndrome (anomalous origin of the left coronary artery from the pulmonary artery), and consists of the anomalous origin of the left coronary artery (or, sometimes, of the right coronary artery, ARCAPA, which is a more favourable

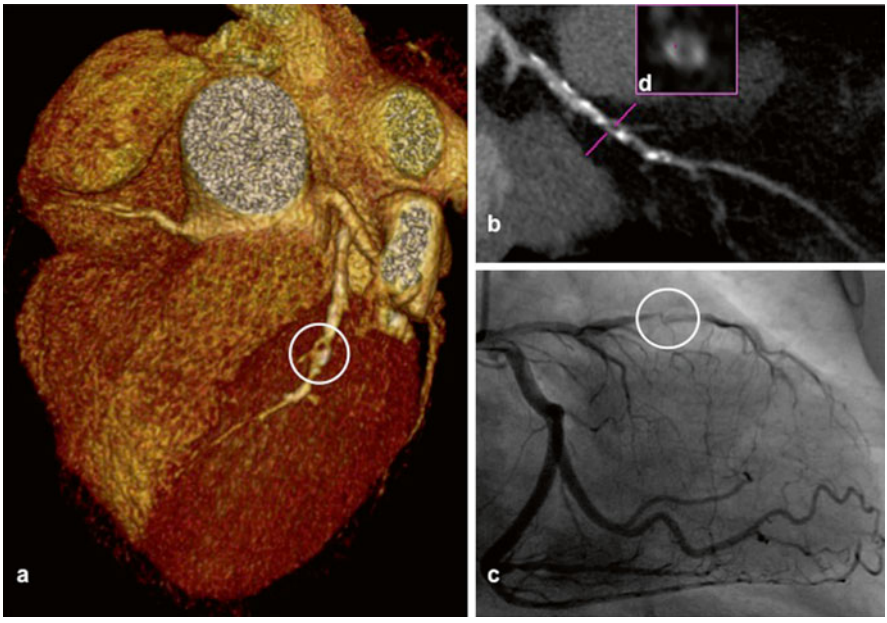

Fig. 6 Volume-rendering reconstruction demonstrates a malignant coronary anomaly with interarterial course of the right coronary artery (*arrow*) that origins from the left sinus of Valsalva

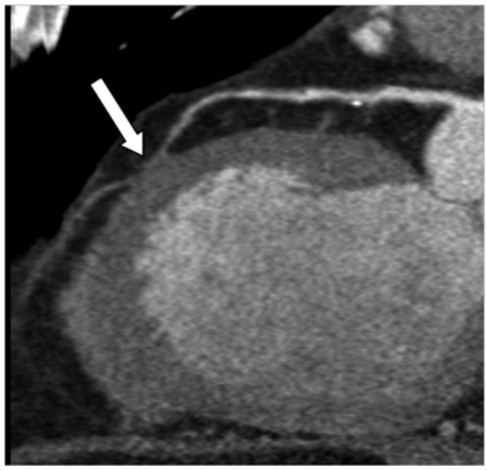

Fig. 7 Long-axis left ventricular multiplanar reconstruction illustrates a myocardial bridging (*arrow*) of the middle tract of the left anterior descending artery

condition [32]) from the pulmonary artery. The incidence is of 1/300,000 live birth, and without therapy the rate of death is 90 % during the first year of life [32]. If this condition is not corrected, and a compensatory and ectasic circle develops between RCA and left coronary circle as compensatory mechanisms, the patient survives and can develop early signs of pulmonary hypertension and of heart failure [32].

Coronary artery originating from the opposite sinus of Valsalva is another malignant anomaly: in this case, the acute angle formed at the origin of the vessel could be responsible of transitory ischemia during the systole [5].

Coronary artery with origin from the opposite or non-coronary sinus (ACAOS) associated with an interarterial course between the aortic root and common trunk of pulmonary artery is often found in young athletes and militaries, and requires surgical treatment for the high risk of sudden death [5]. The pathophysiological mechanisms of sudden death are still unclear, but it could be explained by a reduced blood flow due to the acute angle which often characterised the emergency of the coronary artery associated with the intramural course and the compression of the artery every systolic phase [32]. ACAOS associated with prepulmonic, intraseptal and retroaortic course are considered benign [32].

Coronary artery fistulas are discussed below in this chapter.

Another important condition is the **"myocardial bridging"** (Fig. 7), an **anomalous course of a coronary tract through myocardium**, preceded and succeeded by a normal epicardial course [5]. Myocardial bridging is visualised on CA as a systolic narrowing of an epicardial coronary [35], whereas in CTA it is visualised as a tract of coronary surrounded by myocardial fibres using multiplanar reformation [36]. The significance of this condition is still debated, but it has been seen that atherosclerosis is present with higher frequency in the segment proximal to the tunnelled tract and at this level an endothelial dysfunction is moreover present which could predispose to vasospasm and thrombosis [35]. When radiologists encounter a myocardial bridging they have to report it; the treatment, medical or surgical, will be evaluated by the clinical team.

In the end, it is important to remember that in certain cases we could be unable to find a coronary artery because of an **atresia or agenesis,** in particular in those cases of **single coronary artery**. This finding has a prevalence of 0.024/0.066 % in the general population, and could be associated with other congenital heart disorders [37]. It could be totally asymptomatic and find as an incidental finding in the execution of a CTA. The anomaly is classified into three different groups according to the Lipton classification [37]; the prognosis of patients with this pathological condition is not clear: it of course depends on the presence of other heart anomalies associated, but it has even seen that a major cardiac event occurs in 15 % of patient under 40 years [37]. At the moment there are no guidelines on the management of the patient with this condition [37].

Coronary Stenosis: Atherosclerosis and Atherosclerotic Plaques

Pathophysiology and Clinical Manifestation

Coronary atherosclerosis is the most important disease of the coronary arteries. Atherosclerosis is a well-known and described clinical condition related to various factors, including familiarity, tobacco smoke, obesity, hypertension, diabetes, high cholesterol serum levels and reduced physical activity. In particular, it consists of the development of plaque on arterial walls that reduce the vessel lumen, diminishing the blood supply to heart walls.

Atherosclerosis begins at birth and progresses in a non-linear and unpredictable manner [8], but statistically this development will be faster and greater if the patient has one or more of the risk factors mentioned before [38].

Coronary plaques originate in intimal tunica as focal accumulation of foam cells rich in lipids, and become bigger accumulating lipids and involving intima and media tunica [38]; with time they change their composition and occupy the vessel lumen, restricting it.

Atherosclerotic plaque may lead to various pathologic conditions [38] such as the **development of aneurism and dissection or the rupture of the arterial wall** (we will talk about the coronary aneurism in the following paragraphs).

Another pathologic condition which could happen is **the progressive growth of the plaque, determining critic stenosis**: as the vessel lumen becomes smaller even the blood supply becomes smaller, and when the blood supply is not sufficient to satisfy the request of myocardium (the fixed obstructive stenosis of the vessel lumen generally has to be >75 % under stress and >90 % at rest [38]) clinical manifestations appear: angina pectoris (stable, unstable; under pressure or at rest), dyspnoea, arrhythmias, myocardium ischemia or infarct and death. Sometimes, such as in transplanted hearts [39] and patients with long story of diabetes, myocardium infarction can occur with no symptoms.

In the end, **plaque rupture and wall thrombosis with infarction of the tissue supplied by the vessel involved** can occur, determining the typical unstable angina with infarction of the myocardium.

Some plaques can calcify, in part or totally, becoming more stable; others remain soft, and their rupture can determine wall thrombosis, ischaemia and infarction of the myocardium supplied by the vessel. Presently the virtual intravascular endoscopy in CTA is useful for the evaluation of coronary artery patency, in particular to evaluate the presence and compositions of the plaques [40].

Nowadays CTA allows to evaluate the characteristics of the atherosclerotic plaques, but it is important to underline that it has still a much lower spatial resolution compared to IVU. The introduction in clinical practice of dual- or multi-energy CT still does not provide a morphologic evaluation of coronary atherosclerotic plaques comparable with IVU due to the insufficient spatial resolution of this technique; nowadays further improvements of this technology will make possible a detailed morphologic characterisation of the plaques even with this technique [41–43].

CTA Findings

In CTA we can distinguish three types of coronary plaques [11]:

- **Non-calcified plaques** (Fig. 8): They can be recognised on CTA because they have a greater radiodensity than neighbouring soft tissue, but lesser than contrast medium of the vessel lumen. This kind of lesion is the most difficult to visualise on CTA [38] and more prone to rupture and vessel thrombosis.
- **Calcified plaques** (Fig. 9): Plaques completely calcified, with radiodensity greater than neighbouring soft tissues and contrast medium of the vessel lumen.
- **Mixed plaques** (Fig. 10): Plaques with calcium content between 20 and 80 %, within a single lesion or a segment of the coronary artery.

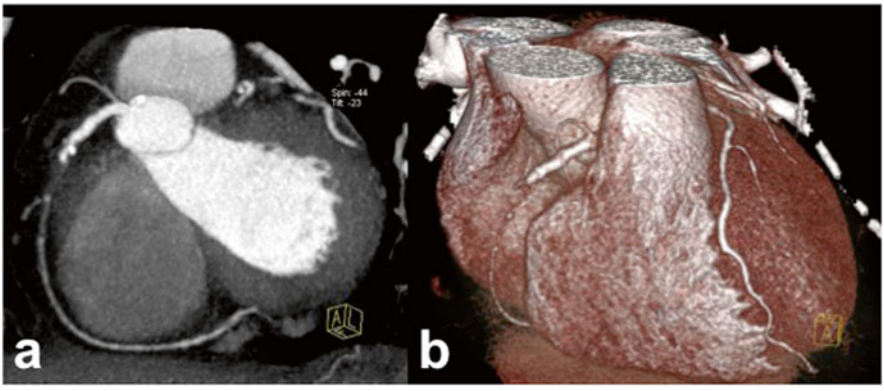

Fig. 8 Occlusion at the third proximal of the right coronary artery, with rehabilitation of the vessel by anastomotic hetero-coronary circulation; multiplanar reconstruction (**a**) demonstrates that a soft plaque is present at the proximal tract of the right coronary artery, completely occluding the lumen. This finding is confirmed in volume rendering three-dimensional reconstruction (**b**)

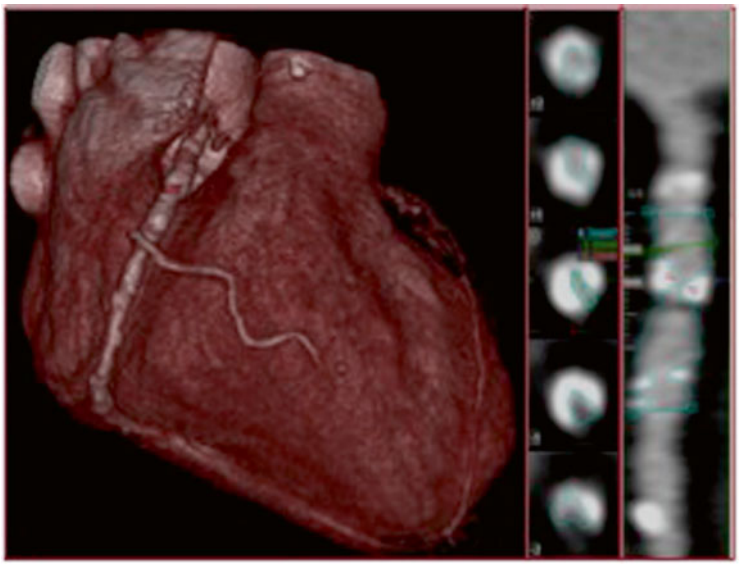

Fig. 9 Multiple calcified plaques on proximal tract of the right coronary artery: multiplanar reconstructions show calcified lesions that fill the vessel lumen >70 %

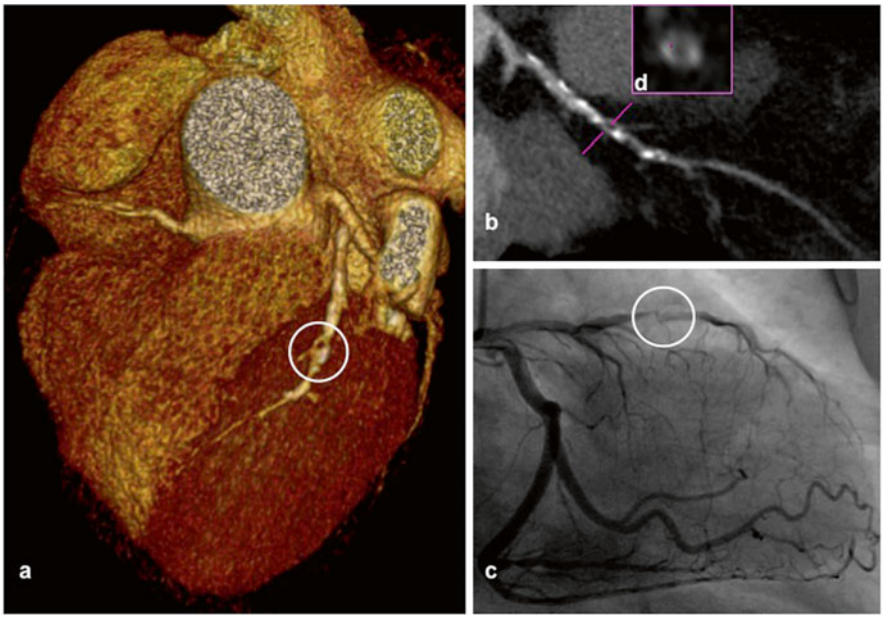

Fig. 10 Volume rendering (**a**) and multiplanar reconstruction (**b**) show multiple plaques on the anterior descending artery with severe stenosis of the lumen due to a fibro-calcified lesion on the middle tract, illustrated also by a cross section of the vessel (**d**). Coronary angiography (**c**) confirms the severe degree of stenosis at that level

Proximal and mid portions of the coronaries are the locations in which atherosclerotic plaques are more often localised and the ostium is rarely involved [8]. A study has revealed that there is even a correlation between the angle of bifurcation of the left coronary and the development and dimension of the plaques in this artery [44]. In native coronary arteries, plaque rupture occurs in the proximal tract of the LAD, in the proximal or distal tract of the RCA, and anywhere in the LCX [8].

The severity of stenosis is calculated as diameter stenosis, rather than area stenosis [8]; this is possible according to the formula (1) [8]

$$N = 1 - (A / B) \tag{1}$$

where **N** is the **critical narrowing** of the vessel converted and expressed in percentage (%), **A** is the **actual lumen** of the vessel at the critical narrowing level, expressed in millimetres (mm), and **B** is the **expected lumen** diameter at the same level of *A*, measured from intima to intima, and expressed in millimetres (mm).

Because of the progressive tapering of the coronary arteries, the **expected lumen** (**B**) is obtained as an average of the normal arterial segment lumen **proximal** (**P**) to and **distal** (**D**) to *A* according to the formula (2)

$$B = (P + D) / 2 \tag{2}$$

These two points (*P* and *D*) are equidistant one to each other and expressed in mm.

In practice there are many software able to calculate *N*% using the so-called stretching MPR, choosing the critical narrowing of the vessel and *P* or *D*.

There are six degrees of coronary artery stenosis, according to the N value [8] from normal to the total occlusion (Table 4).

CTA Report

To write a correct CTA report, it is fundamental to analyse the entire coronary circle (in particular with curved multiplanar reformation), indicating the dominance of the circle (right, left or codominance), and describing every coronary artery (Table 5 [8]):

Table 4 Coronary artery stenosis degree

Normal—no diameter reduction (*N*=0 %)
Minimal—*N* with a value between 1 and 25 %
Mild—*N* with a value between 26 and 50 %
Moderate—*N* with a value between 51 and 70 %
Severe—*N* with a value between 71 and 99 %
Occlusion—*N*=100 %

Table 5 Report data for coronary stenosis

Description of plaque: • Number • Location • Morphology (eccentric, concentric) • Extension • Types (non-calcified, calcified-mixed) • Presence-absence of ulceration
Degree of stenosis
Characteristics of the distal circulation
Presence-absence of collateral circles (although this can be better visualised in CA) [17]

Coronary Artery Dilatation: Ectasia, Aneurisms

Definitions, Aetiology, Pathophysiology, Classification and Clinical Manifestations

Arterial abnormal dilatations are rare clinical findings that can affect coronary circle.

The aetiology varies depending on the geographic location and age; in Western countries atherosclerosis is the most common, followed by congenital and infectious causes, whereas in Japan the principal cause is the Kawasaki's disease [39]. Other causes are vasculitis such as Takayasu's disease [45], or medical and surgical procedures such as angiography, stent placement or CABG (see below) [34].

Arterial wall damage is the common pathophysiologic mechanism (except for congenital dilatation, which is often born as compensatory mechanism as a consequence of congenital fistula or other coronary anomalies) [34]; in particular in atherosclerosis, it is a consequence of wall weakening due to the atherosclerotic plaques, in vasculitis for different inflammatory mechanisms acting on the arteries walls and in infective dilatation because of direct invasion of the wall by microbes or septic micro embolisation of the vasa vasorum [34]. There are two types of dilatation:

1. **Ectasia**: **It is a diffuse dilatation of coronary artery** [34, 46]. More properly, it is a diffuse dilatation of the vessel (at least 1.5 times the normal vessel diameter) that extends along it for 50 % or more of its length [34]. There are four types of ectasia (Table 6 [34]), and types I and II are those with the worst prognosis [34].
2. **Aneurysm**: **It is a focal dilatation of a coronary artery** [34]. We have to distinguish between "true" and "false" aneurysms (called pseudoaneurysms), according to the numbers of layers involved: in fact in the "**true" aneurysms** the wall of the lesion involves all the layers which constitute the vessel, i.e. the tunica intima, media and adventitia [34], while in the **pseudoaneurysms** are involved only one or two layers because there is a damage of the integrity of the vessel wall (this kind of lesions are more frequently seen after chest trauma or catheter-based procedures [34]).

Table 6 Ectasia types

Type I: ectasia in 2 or 3 vessels
Type II: ectasia in one vessel and aneurism in another
Type III: ectasia in one vessel
Type IV: coronary aneurism in one vessel

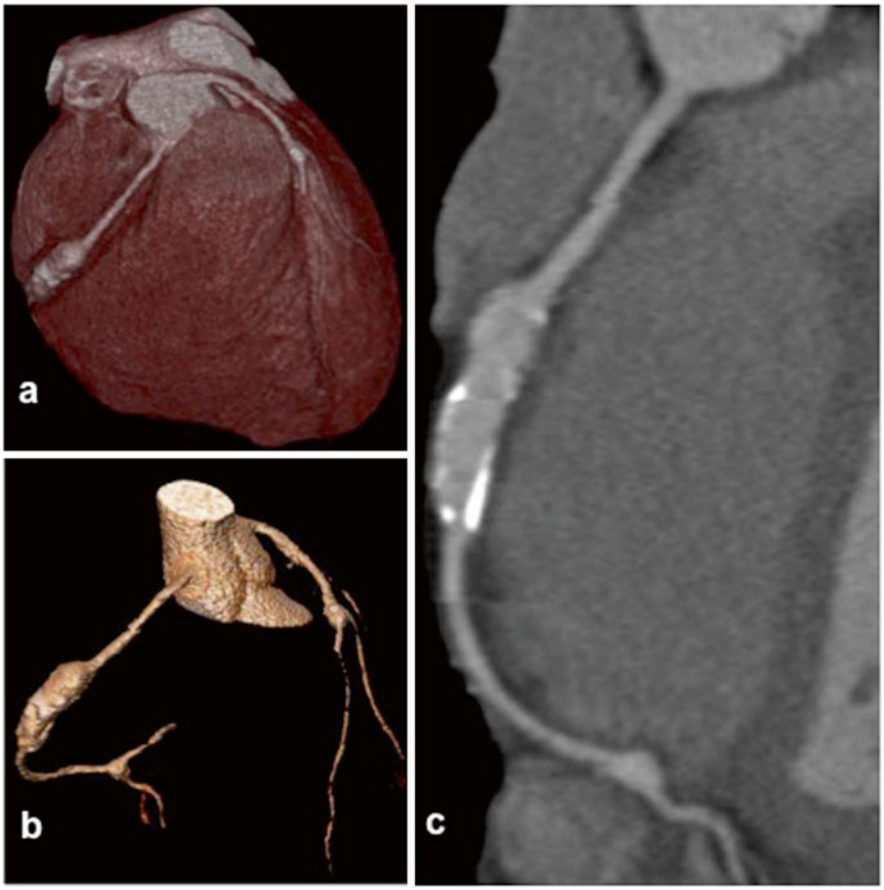

Fig. 11 Coronary CTA in a patient with Kawasaki's disease: volume-rendering reconstructions (**a** and **b**) show a fusiform aneurism on middle tract of the right coronary artery. Curved multiplanar reconstruction (**c**) demonstrates the partially calcified walls of the aneurism

Moreover, according to their morphology, they can be divided into **"saccular" aneurysm,** characterised by **a transverse diameter greater than the longitudinal** [34], usually located distal to a stenosis, adjacent to it, and more prone to thrombosis and rupture [34], and **"fusiform" aneurysm**, characterised by **a transverse diameter smaller than the longitudinal** [34] (Fig. 11).

Coronary dilatation clinically can be silent or manifest with symptoms according to the underlying causes [34]. Atherosclerotic dilatation could manifest with symptoms similar to those of atherosclerotic stenosis [34]; for dilatation derived from

other conditions, the symptoms could be the same, but associated with others related to the underlying disease, such as septic fever for infective dilatations, or cutaneous and other systemic symptoms (asthenia, weight loss, fever) for vasculitis [34].

Coronary dilatations can evolve determining complications such as distal embolisation, rupture, fistulas, hemopericardium, thrombosis, dissection and vessel compression [34].

CTA Findings

A coronary dilatation is characterised by an anomalous enlargement of the arterial wall, with the characteristics mentioned before. The walls could be normal, thinner or thicker than those of the other tracts, and lumen patent (hyperdense) or stenotic because of the deposition of low-attenuation materials inside. Of course there could be not only one but multiple dilatation along the same coronary or in different arteries.

CTA Report

In a correct CTA report, coronary dilatations have to be described indicating every characteristic of them, in particular including the type, size and extension (Table 7).

Coronary Artery Dissection

Definition, Aetiology, Pathologic Findings and Clinical Features

Coronary artery dissection can be defined as a delamination of the layers that constitute the walls of the coronary arteries with the evidence of an intimal flap. When this event occurs, the blood can flow through the "true lumen", which inner walls are constituted by the normal intima of the vase, or through the so-called false lumen, generated by the delamination of the layers and separated by the true lumen by the intimal flap [47]. If the dissection is characterised by the presence of a wide connection between true and false lumen thanks to the presence of at least two

Table 7 Report data for coronary artery dilatation

Type (ectasia or aneurysm)
Number
Location
Dimensions of the aneurism/maximum diameter of the ectasia
Dimension of the residual lumen
Walls characteristics (thin, normal, thick)
Any associated anomalies
Characteristics of the distal circulation

lumens (one proximal and one distal), the vessel assumes a larger calibre, and there is a high risk of rupture of the outer walls (more fragile) with the possibility of rupture of the outer fragile layer with hemopericardium and cardiac tamponade. If there is only an orifice without a wide connection between the true and the false lumen, the continuing blood flows in the false lumen could contribute to the delamination process, restricting the true lumen and leading to the closure of it with ischaemia and infarction of the territory distal to the occlusion, and even to the rupture in pericardiac space with hemopericardium and cardiac tamponade.

According to the aetiology, coronary artery dissection could be **post-traumatic** (for example iatrogenic after a stent placement during angioplasty) or **spontaneous**.

Spontaneous coronary artery dissection is a rare event with a not clear aetiology and pathogenesis, related in particular with intense physical exercise, pregnancy or use of oral contraceptives [48].

Clinically both types of dissections can manifest with sudden typical or atypical chest pain, dyspnea, palpitations, syncope or sudden death. This condition can be identified on CA or CTA.

CTA Findings and Reports

On CTA a coronary dissection can be suspected if on CTA an anomalous enlargement of the vessel in one or more points and a linear hypodensity corresponding to the intimal flap in the vessel lumen are observed, which anyway must not be confused with any artifacts.

In analogy with the aortic dissection [47], sometimes it can be possible distinguishing the false lumen from the true according to the "beak sign": the false lumen forms two wedges outer the true lumen, and generally appears hypodense than the true lumen because of the delayed enhancement of the contrast medium. The true lumen could progressively narrow up to the complete occlusion (Fig. 12).

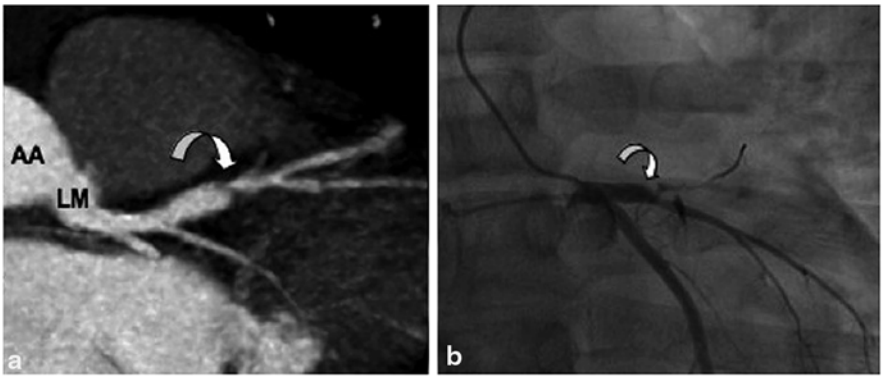

Fig. 12 (**a**) Curved planar reconstruction shows a focal dissection of the middle tract of the left anterior descending artery (*curved arrow*; *AA* aortic sinus, *LM* left main artery). (**b**) Angiographic exam confirms this finding (*curved arrow*)

Table 8 Report data for coronary artery dissection

Location
Vessel involved, with origin and termination
Length
Features of false and true lumen
Other associated conditions: vessel rupture, vessel patency, active bleeding, hemopericardium, aortic dissection

A correct report should include in particular information about the location, the vessel involved, the feature of the vessel walls and other pathologic conditions related, such as hemopericardium, anomalous sparing of contrast medium for active bleeding or involvement of the aortic root (Table 8).

Coronary Artery Fistulas

Definition, Aetiology, Pathologic Findings and Clinical Features

A coronary artery fistula is an anomalous termination of the coronary circle [49]. It is a direct connection of a coronary artery (RCA in 50 % of patients, LCA in 42 % and both in 5 % [49]) with one of this structure, bypassing the capillary bed [49]:

- A cardiac chamber (the most common, in particular right ventricle and atrium)
- A pulmonary artery or a pulmonary vein
- Superior vena cava or coronary sinus

This pathologic condition determines a left-to-right shunt, with a reduction of blood supply to the myocardium, followed by a series of adaptive changes like the development of collateral circles, right ventricular enlargement and hypertrophy of the residual myocardium.

It is a not frequent CA finding (0.3–1.3 % of patients who are undergoing CA) [49]. In most cases fistulas are congenital, derived from embryogenic disorders; in other cases they are complications of other clinical conditions, such as chest blunt trauma, evolution of aneurisms or microtrauma after CABG.

The most common pathologic findings of fistulas are dilatation of the vessel involved with mural thinning, concomitant atherosclerosis and thrombosis, accompanied by myocardial hypertrophy with focal fibrosis [49]. In most cases they are singular, and rarely multiple [49].

From a clinical point of view, the clinical presentation depends on the severity of the left-to-right shunt [49]; patients could be asymptomatic if the entity of the shunt is modest. In symptomatic patients the most important clinical manifestation is the right ventricular enlargement with pulmonary hypertension [49]; others can be arrhythmias, myocardial ischemia or infarction and heart failure. Most of adult patients are asymptomatic [49], whereas an important left-to-right shunt will manifest clinically easier in young patients.

Table 9 Report data for coronary artery fistulas

Number
Location
Origin (LCA; RCA) and termination (cardiac chamber, pulmonary vein or artery, cardiac sinus or superior cava vein)
Dimensions
General conditions of the rest of the circle, including ectasia, aneurisms or thrombosis
Evaluation of the heart: dimensions of the cardiac chambers, thickness of myocardium, pulmonary hypertension signs

CTA Findings and Report

CTA can reveal the presence of enlarged fistulas, evaluating the possible presence of ectasia or focal aneurysms of the coronary circle, with or without thrombosis [49]. Small fistulas can be visualised only on CA. A correct description of a fistula should contain in particular information about location, dimensions, origin and termination (Table 9).

Coronary Stent

Stents, Complications and Clinical Manifestation

Stenting is a well-known revascularisation procedure; it consists of the placement of a stent (an expandable metallic device) in the coronary artery via specific catheters in angioplasty procedures; stent contributes to maintain coronary artery patent after the angioplasty [50]. During the same procedure, one or more stents can be applied, including tandem stents (one beside the other); in particular **bifurcation lesions** can be treated placing "T", "Y" or "V" stents according to the degree of the angle between the two branches [50]. Most of the modern stents are coated with antiproliferative drugs such as sirolimus or paclitaxel to help prevent in-stent restenosis [50].

There could be many complications after a stent placement, such as **thrombosis**: the rate of this complication is low, between 1 and 2 % [50], and the risk is higher using longer stents [50]. Clinically, it manifests as acute myocardial ischaemia [50]. Patients that assume antiplatelet therapy discontinuously or with additional risk factors such as diabetes mellitus or low ejection fraction have an increased risk of thrombosis [50]. Timing of thrombosis is different using coated or non-coated stents: in fact in the case of **non-coated stents**, this complication can occur more often acutely (within 48 h after the stent procedure) or subacutely (between 2 and 30 days after intervention) [50], whereas when **coated stents are used**, the complication typically occurs 30 days after stenting.

Restenosis is another complication after CABG: this long-term condition is defined as **a vessel lumen narrowing of more than 50 % that occurs after a stent**

placement [50], because of several factors, such as excessive arterial healing after angioplasty, vascular remodelling and neointimal hyperplasia [50]. Clinically it manifests as recurrence angina [50]. The risk is higher using non-coated stents (up to 40 %) despite the coated stents (up to 10 %) [50]. Care should be taken in the evaluation of neointimal hyperplasia in the edges of the stents [8]. The bifurcation lesions are more prone to restenosis [50].

Dissections, ectasia and aneurisms are infrequent but important complications that can develop in the coronary artery segments adjacent to stent [8]; the pathophysiologic mechanisms is not fully understood, but probably derived from microtraumatisms during the procedure and inadequate healing after the stent placement due to antiproliferative drugs, FANS and cortisone [34].

CTA Findings

In CTA, stents are visualised as metallic cylindrical devices applied in coronary along the coronary walls. Because of their metallic structure, streak artefacts can be visualised; useful tips to minimise artefacts could be the use of a correct filtered backprojection kernel (B46f) [50] or iterative reconstruction algorithms.

Normally, radiologist can observe the coronary artery lumen patent: **low-attenuation areas inside the stent are indicative of in-stent thrombosis or restenosis, with variable degrees of stenosis** [8]. An abnormal accumulation of contrast medium inside the arterial wall, accompanied by intimal flap, should suggest a coronary dissection, whereas an anomalous enlargement of the lumen should suggest the presence of aneurisms or ectasia (see above).

Not only the evaluation of stent is important, but even of the segment adjacent to the stent and the edges of the stent [8] (Fig. 13).

CTA Report

A correct coronary stent description should include in particular information about the number, the location and moreover the patency or stenosis of it (Table 10).

Coronary Artery Bypass Graft

Definition, Types of CABG and Complications

CABG is a surgical revascularisation procedure that allows restoring an adequate blood flow in the coronary circle in patients with advanced CAD, bypassing a severe stenosis or occlusion. The surgical procedure consists of the creation of a vascular connection between the aorta and the tract of the coronary circle distal to the critic

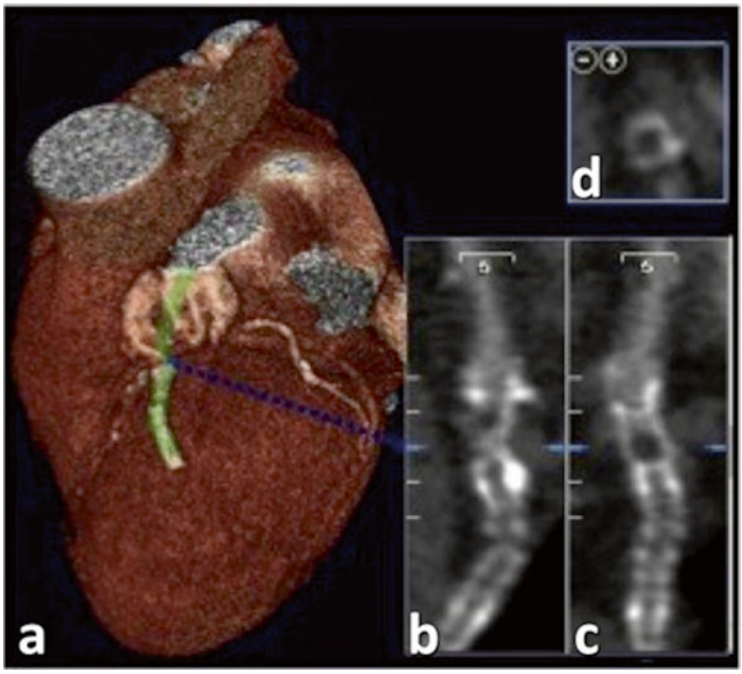

Fig. 13 (**a**) CTA volume-rendering reconstruction illustrates a stent placed on the anterior descending artery, with interruption of the vessel on its middle tract. (**b**), (**c**) and (**d**) curved multiplanar reconstructions reveal multiple low-attenuation areas inside the stent due to in-stent restenosis

Table 10 Report data for coronary stent

Number
Location
Length
Patency/stenosis: in case of stenosis, radiologist has to indicate the degree of stenosis (see "coronary stenosis") and contrast runoff in the coronary segments distal to the stenosis [8]
Any lateral branches excluded, in particular in bifurcating lesions [8]
Other complications such as dissection, ectasia or aneurisms

obstruction or occlusion using a vascular arterial or venous graft. Vascular graft could be:

- With the anatomic origin left in place, and the distal end attached to the target vessel.
- **Free**: proximal and distal ends of the vessel are disconnected from their original anatomic attachment and reassembled.
- **Composite**: two or more vessels linked to each other, when a double- or triple-bypass graft is required.

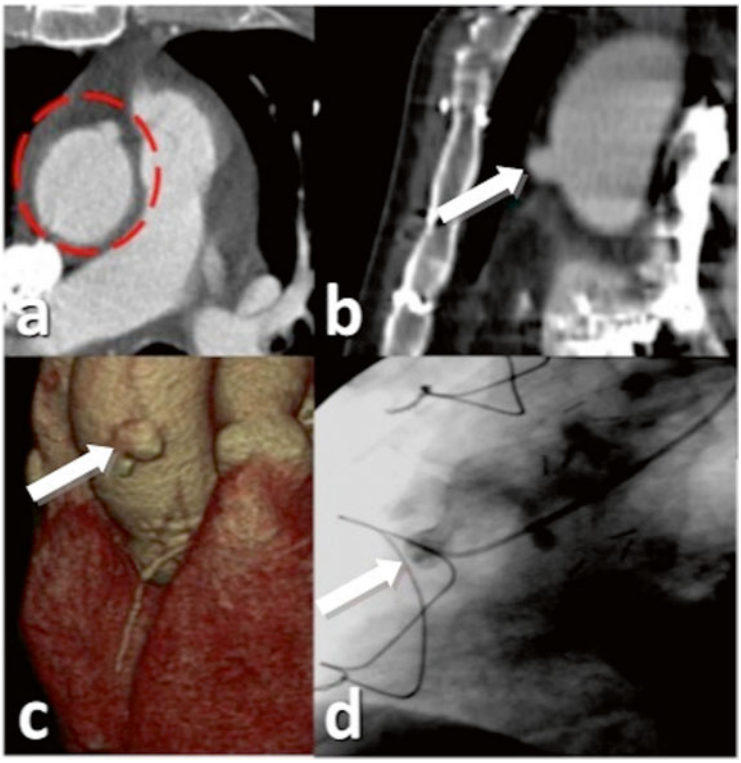

Fig. 14 Occluded venous bypass graft on right coronary artery (*arrows*). CTA images illustrate the occlusion at the origin of the graft on axial plane (**a**), coronal plane (**b**) and volume rendering (**c**). This finding is confirmed by the angiographic exam (**d**)

In addition, vascular grafts could be venous or arterial: in the case of **venous graft** (Fig. 14) the saphenous vein (SV) is chosen. Obviously, it is used as a free or composite graft, harvested from the leg and linked at the ascending aorta and at the coronary circle, beyond the obstructive lesion [51]. Sometimes, during the CABG procedure, a mechanical aortovenous connector is used which makes quicker the suture of the venous graft to the ascending aorta [51] and alters the normal appearance of the graft [51].

In the case of **arterial graft** (Fig. 15) there is the great advantage that they are **more resistant to thrombosis than the venous graft** [51], having a better long-term patency than venous grafts [8] with a lower rate of postoperative mortality and a long-term patency rate of above 90 % at 10 years [51].

Internal mammary artery (**IMA**) is the most used. Both the IMA can be used, but **left IMA** is used in particular to revascularise LAD, maintaining intact its origin from subclavian artery [51], whereas the **right IMA** could be exploited maintaining its origin at the subclavian artery, as a free graft with the proximal end linked to the ascending aorta, or as a composite graft linked with a left IMA graft [51].

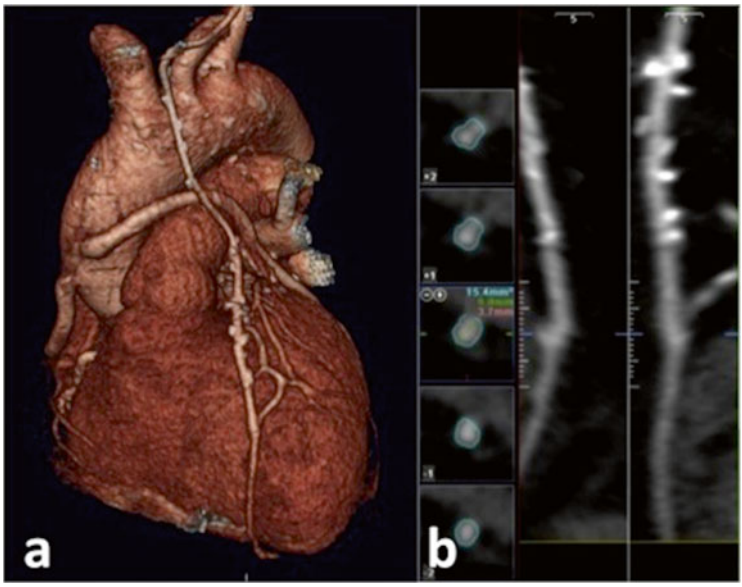

Fig. 15 (**a**) Volume-rendering reconstruction shows a LIMA bypass on left anterior descending artery. (**b**) Curved multiplanar reconstruction demonstrates the patency of the arterial graft

Table 11 Early complications of CABG

Thrombosis: 10–15 % of patients [23], more frequent in venous than arterial grafts
Graft spasm: difficult to be seen in CTA
Graft malposition or kinking: more frequent in longer grafts
Pericardial effusion: rarely become hemodynamically significant despite its prevalence (22–85 %) [51]
Pleural effusion
Iatrogenic complication
Sternal infection: with a prevalence of 2–20 % [23]; mediastinitis occurs in 1–4 % of patients, and has a mortality rate of about 25 % [51]
Pulmonary embolism

Even other arteries can be used as valid alternatives to IMA, such as **radial,** or less the **gastroepiploic artery** [51].

A CABG procedure can be vitiated by different complications, which can be divided in [51]:

1. **Early complications** (within the first 30 days after the procedure) (Table 11)
2. **Late complications** (over 30 days after the procedure) (Table 12)

Table 12 Late complications of CABG

Late stenosis and occlusion
Graft aneurysms: it requires a surgical correction if exceeding 2 cm of diameter. The main pathophysiologic mechanism is the accelerated atherosclerosis, especially in venous graft, with the development of pseudoaneurysms [51]. These aneurysms may complicate with dissection, thrombosis, rupture or fistulisation with adjacent structures [8]

Table 13 Report data for CABG

Type of CABG
Patency/stenosis/occlusion of the CABG
General conditions of the rest of the circle
Presence of early or late cardiac or extracardiac complications

CTA Findings and Report

CTA is a fundamental examination for the CABG evaluation [52], and the results are very similar to those obtained in CA in the assessment of the patency of the CABG in the follow-up [53]; in particular, it is important in the evaluation of the early (1 month, in particular if associated with symptoms like pain and dyspnoea) and late (more than 1 month) complications and to make sure of the patency of the graft. Beam-hardening artefacts because of metallic clips are frequent findings.

A complete evaluation of the CABG must include the terminal ends, with particular regards on anastomoses.

The knowledge of the procedure and of the type of graft is fundamental not only to write a correct report, but even to do a correct CTA, that will have to include the epiaortic vessels in the case of left IMA CABG with the anatomic origin left in place.

A correct report should indicate in particular the type of CABG and the early or late complications exposed in the previous paragraph (Table 13).

The Transplanted Heart: The Coronary Allograft Vasculopathy

The coronary allograft vasculopathy is a diffuse process of the coronary circle of the transplanted heart, due in particular to **concentric narrowing of the vessel lumen** [39]. It is a particular form of atherosclerosis due to immunomediated injury and other non-immunologic factors, which first appear in the small distal branches of the coronary circle and then extending proximally. The consequences are myocardial ischaemia and heart failure [39]. It is clinically silent, because the transplanted heart is denervated, and it is the leading cause of death in these patients after the first year post-transplant [39].

CTA findings can provide information on the vessel wall conditions and of the degree of lumen stenosis, in order to plan an eventual revascularisation procedure.

Table 14 Coronary allograft vasculopathy scale [24, 25]

Grade A: discrete proximal tubular stenosis
Grade B: diffuse concentric lumen narrowing
Grade C: irregular diffuse concentric lumen narrowing

There are still no universally staging scale for the evaluation of coronary allograft vasculopathy [39]; Gao and colleagues proposed a three-grade classification scale, based on CA findings, but available even for CTA [39, 54] (Table 14).

When radiologist has to execute a CTA in transplanted patients, he or she has to remember that the transplanted heart is denervated with HBR between 80 and 100 bpm; as we have seen before, a correct CTA has to be executed with an HBR lower than 65 bpm. Transplanted heart is not responsible to β-blockers as a normal heart, and thus sometimes it is necessary to use β-blockers at higher doses [39]. (Naama R. Bogot et al. [39] described a procedure with the administration of repeated 50 mg doses of metoprolol up to a cumulative dose of 200 mg, or a single I.V. dose of 50–100 mg of esmolol just before CT.)

References

1. Go AS, et al. Heart disease and stroke statics—2013 update: a report from the American Heart Association. Circulation. 2013;127:e6–245.
2. Hamdan A, et al. A prospective study for comparison of MR and CT imaging for detection of coronary artery stenosis. JACC Cardiovasc Imaging. 2011;4(9):50–61.
3. Bastarrika G, et al. CT of coronary artery disease. Radiology. 2009;253(2):317–38.
4. Kakouros N, et al. The utility of cardiac CT beyond the assessment of suspected coronary artery disease. Clin Radiol. 2012;67:695e708.
5. Sundaram B, et al. Anatomy and terminology for the interpretation and reporting of cardiac MDCT: Part 1, Structured report, coronary calcium screening, and coronary artery anatomy. AJR Am J Roentgenol. 2009;192:574–83.
6. Cerqueira MD, et al. Standardized myocardial segmentation and nomenclature for tomographic imaging of the heart: a statement for healthcare professionals from the cardiac imaging committee of the council on clinical cardiology of the American Heart Association. Circulation. 2002;105:539–42.
7. Lee J. Coronary artery calcium scoring and its impact on the clinical practice in the era of multidetector CT. Int J Cardiovasc Imaging. 2011;27:9–25.
8. Sundaram B, et al. Anatomy and terminology for the interpretation and reporting of cardiac MDCT: Part 2, CT angiography, cardiac function assessment, and noncoronary and extracardiac findings. AJR Am J Roentgenol. 2009;192:584–98.
9. Agatston AS, et al. Quantification of coronary artery calcium using ultrafast computed tomography. J Am Coll Cardiol. 1990;15(4):827–32.
10. Patel J, et al. All-cause mortality in asymptomatic persons with extensive Agatston scores above 1000. J Cardiovasc Comput Tomogr. 2014;8:26–32.
11. Sun Z, et al. Coronary CT angiography: current status and continuing challenges. Br J Radiol. 2012;85:495–510.
12. Pannu HK, et al. β-blockers for cardiac CT: a primer for the radiologist. AJR Am J Roentgenol. 2006;186:S341–5.
13. Hassan A, et al. Technical challenges of coronary CT angiography: today and tomorrow. Eur J Radiol. 2011;79:161–71.

14. Bastarrika G, et al. Cardiac CT in the assessment of acute chest pain in the emergency department. AJR Am J Roentgenol. 2009;193:397–409.
15. Cody DD, et al. AAPM/RSNA physics tutorial for residents technologic advances in multidetector CT with a focus on cardiac imaging. RadioGraphics. 2007;27:1829–37.
16. Sun Z. Multislice CT angiography in cardiac imaging: prospective ECG-gating or retrospective ECG-Gating? Biomed Imaging Interv J. 2010;6(1), e4.
17. Qin J, et al. Prospective versus retrospective ECG gating for 320-detector CT of the coronary arteries: comparison of image quality and patient radiation dose. Clin Imaging. 2011;35:193–7.
18. Carrascosa P, et al. Accuracy of low-dose prospectively gated axial coronary CT angiography for the assessment of coronary artery stenosis in patients with stable heart rate. J Cardiovasc Comput Tomogr. 2010;4:197–205.
19. Stolzmann P, et al. Dual-source CT in step-and-shoot mode: noninvasive coronary angiography with low radiation dose. Radiology. 2008;249(1):71–80.
20. Schoepf UJ, et al. CT of coronary artery disease. Radiology. 2004;232:18–37.
21. Silva AC, et al. Innovations in CT dose reduction strategy: application if the adaptive statistical iterative reconstruction algorithm. AJR Am J Roentgenol. 2010;194:191–9.
22. Leipsic J, et al. Adaptive statistical iterative reconstruction: assessment of image noise and image quality in coronary CT angiography. AJR Am J Roentgenol. 2010;195:649–54.
23. Scheffel H, et al. Coronary artery plaques: cardiac CT with model-based and adaptive-statistical iterative reconstruction technique. Eur J Radiol. 2012;81:e363–9.
24. Siripornpitak S, et al. Cardiac CT angiography in children with congenital heart disease. Eur J Radiol. 2013;82:1067–82.
25. Sun Z, et al. Coronary CT angiography: how should physicians use it wisely and when do physicians request it appropriately? Eur J Radiol. 2012;81:e684–7.
26. Habib PJ, et al. Association of cardiac events with coronary artery disease detected by 64-slice or greater coronary CT angiography: a systematic review and meta-analysis. Int J Cardiol. 2013;169:112–20.
27. Dougoud S, et al. Prognostic value of coronary CT angiography on long-term follow-up of 6.9 years. Int J Cardiovasc Imaging. 2014;30(5):969–76. doi:10.1007/s10554-014-0420-1.
28. Han BK, et al. Safety and accuracy of dual-source coronary computed tomography angiography in the pediatric population. J Cardiovasc Comput Tomogr. 2012;6:252–9.
29. Zheng M, et al. Image quality of ultra-low-dose dual-source CT angiography using high-pitch spiral acquisition and iterative reconstruction in young children with congenital heart disease. J Cardiovasc Comput Tomogr. 2013;7:376–82.
30. Angelini P, et al. Coronary anomalies: incidence, pathophysiology, and clinical relevance. Circulation. 2002;105:2449–54.
31. Yu F-F, et al. Congenital anomalies of coronary arteries in complex congenital heart disease: diagnosis and analysis with dual-source CT. J Cardiovasc Comput Tomogr. 2013;7:383–90.
32. Pleva L, et al. Congenital coronary anomalies. Cor Vasa. 2014;56:e27–36.
33. Torres FS. Role of MDCT coronary angiography in the evaluation of septal vs interarterial course of anomalous left coronary arteries. J Cardiovasc Comput Tomogr. 2010;4:246–54.
34. Diaz-Zamudio M, et al. Coronary artery aneurysms and ectasia: role of coronary CT angiography. RadioGraphics. 2009;29:1939–54.
35. Alegria JR, et al. Myocardial bridging. Eur Heart J. 2005;26:1159–68.
36. Choi HS, et al. Pitfalls, artifacts, and remedies in multi-detector row CT coronary angiography. RadioGraphics. 2004;24:787–800.
37. Aldana-Sepulveda N, et al. Single coronary artery: spectrum of imaging findings with multidetector CT. J Cardiovasc Comput Tomogr. 2013;7:391e399.
38. Kumar V, Abbas AK, Fausto N. Robbins and Contran pathologic bases of disease—Italian Version—Capitolo 11: Frederick J. Schoen: Vasi sanguigni. Philadelphia, PA: Elsevier; 2006. p. 511–554.
39. Bogot NR, et al. Cardiac CT of the transplanted heart: indications, technique, appearance, and complications. RadioGraphics. 2007;27:1297–309.

40. Sun Z, et al. CT virtual intravascular endoscopy assessment of coronary artery plaques: a preliminary study. Eur J Radiol. 2010;75:e112–9.
41. Brodoefel H, et al. Accuracy of dual-source CT in the characterisation of non-calcified plaque: use of a colour-coded analysis compared with virtual histology intravascular ultrasound. Br J Radiol. 2009;82:805–12.
42. Vliegenthart R, et al. Dual-energy CT of the heart. AJR Am J Roentgenol. 2012;199:S54–63.
43. Kang DK, et al. Dual-energy computed tomography for integrative imaging of coronary artery disease: principles and clinical applications. Semin Ultrasound CT MR. 2010;31(4):276–91.
44. Sun Z, et al. Multislice CT angiography assessment of left coronary artery: correlation between bifurcation angle and dimensions and development of coronary artery disease. Eur J Radiol. 2011;79:e90–5.
45. Soto ME, et al. Coronary CT angiography in Takayasu arteritis. JACC Cardiovasc Imaging. 2011;4(9):958–66.
46. Ozcan OU, et al. Coronary artery ectasia. Cor Vasa. 2013;55:e242–7.
47. McMahon MA, et al. Multidetector CT of aortic dissection: a pictorial review. RadioGraphics. 2010;30:445–60.
48. Sharma N, et al. Spontaneous left main coronary artery dissection in pregnancy. Int J Cardiol. 2012;159:e11–3.
49. Zenooz NA, et al. Coronary artery fistulas: CT findings. RadioGraphics. 2009;29:781–9.
50. Pugliese F, et al. Multidetector CT for visualization of coronary stents. RadioGraphics. 2006;26:887–904.
51. Frazier AA, et al. Coronary artery bypass grafts: assessment with multidetector CT in the early and late postoperative settings. RadioGraphics. 2005;25:881–96.
52. Khedr SA, et al. Diagnostic value of MDCT angiography in assessment of coronary artery bypass graft. Egypt J Radiol Nucl Med. 2013;44:183–91.
53. Romagnoli A, et al. Diagnostic accuracy of 64-slice CT in evaluating coronary artery bypass grafts and of the native coronary arteries. Radiol Med. 2010;115:1167–78.
54. Gao SZ, et al. Accelerated coronary vascular disease in the heart transplant patient: coronary arteriographic findings. J Am Coll Cardiol. 1988;12:334–40.

CT of Carotid Arteries

Kimberly Kallianos, Ana M. Franceschi, John R. Carr, William A. Mehan, and Jason M. Johnson

Carotid Computed Tomography Angiography (CTA) Overview

Stroke is the fourth leading cause of death and the leading cause of long-term serious disability in the United States [1]. Treatment and management advancements for ischemic injury have increased the demand for accurate and reliable imaging techniques to rapidly identify both intra- and extracranial carotid artery pathology [2, 3].

Computer tomography angiography (CTA) of the carotid arteries provides detailed assessment of the vessels with direct luminal visualization. Carotid CTA imaging is a valuable assessment tool for risk stratification in patients presenting with acute cerebrovascular disease. Large vessel occlusion, such as carotid arterial occlusion, occurs in more than 10 % of patients presenting with transient ischemic attack (TIA) and is a predictor for future decline in functional status [4]. In the acute stroke setting, direct visualization of luminal occlusion and evaluation of the surrounding collateral vessels provides confirmation of clinically suspected stroke and allows for subsequent targeted treatment, such as intravenous thrombolysis and pharmacomechanical endovascular therapies. Carotid CTA can be combined with concurrent CT perfusion for evaluation of brain parenchymal perfusion as well as CTA of the intracranial arteries to assess for intracranial vascular thrombosis and to demonstrate intracranial aneurysms or arteriovenous malformations, both of which may be contraindications to thrombolytic therapy.

Carotid CTA is highly accurate for evaluating long-standing carotid stenosis in symptomatic and asymptomatic patients. The ability to distinguish complete

K. Kallianos • A.M. Franceschi • J.R. Carr • W.A. Mehan • J.M. Johnson (✉)
Department of Radiology, University of California, San Francisco, USA
e-mail: Jason.Johnson@ucsf.edu

R. Trivedi et al. (eds.), *3D Imaging Technologies in Atherosclerosis*,
DOI 10.1007/978-1-4899-7618-5_3

occlusion versus hairline residual lumen is particularly useful as it may affect the decision to therapeutically intervene. This differentiation is limited with other flow-sensitive imaging techniques such as ultrasound or magnetic resonance angiography (MRA). Detailed anatomical assessment of the carotid vessels can detect other differential pathological processes such as dissection and vasculopathy, which are of utmost importance for patients with neurological symptoms.

Advantages

Carotid computed tomography angiography (CTA) is widely available, minimally invasive, and allows for high-resolution rapid assessment of the carotid arteries. Rapid interrogation of the intra- and extra-cranial vasculature within minutes offers major benefits in the evaluation of acute stroke in the emergency department. The short scan time also enables evaluation of patients who may be unable to tolerate the longer scan times involved with other modalities, such as critically ill patients or patients with altered mental status. Furthermore, carotid CTA is less prone to motion-related artifacts in patients compared to flow-related imaging such as MRA [5]. Modern multidetector CT provides rapid scanning time, increased resolution, and decreased radiation dose [6]. Unlike MRA, metallic foreign bodies, implanted metallic hardware, such as pacemakers, aneurysm clips, and various orthopedic devices are not a contraindication to CTA. Therefore, a greater percentage of patients are able to undergo carotid imaging with computer tomography compared to magnetic resonance imaging.

Carotid duplex ultrasound is a noninvasive modality for screening patients at high-risk for carotid artery disease, including those with history of stroke, TIA, cervical carotid bruits, and as a preoperative evaluation to coronary artery bypass graft surgery (CABG) or aortic valve replacement (AVR) procedures [7]. However, ultrasound may be suboptimal for assessment in certain populations, particularly patients with heavily calcified carotid arteries or those with atherosclerotic disease at the skull base or in the proximal common carotid artery [5]. The availability of specially trained vascular sonographers and the length of examination in the urgent evaluation of carotid disease such as during an acute stroke may be suboptimal in potential candidates for revascularization or thrombolytic therapy.

Limitations

Carotid CTA provides limited evaluation of small vessels and distal branch occlusions relative to conventional angiography [8]. In carotid CTA, the rapid speed of image acquisition may create a challenge to obtaining optimal contrast bolus timing and vessel opacification, as the rapid CT acquisition can outpace the flow of contrast-opacified blood. Patients with cardiac dysfunction such as heart failure or arrhythmias may particularly prove challenging to contrast bolus timing. The inability of CTA to sequentially image during contrast injection to detect delayed contrast

opacification and real-time collateral flow is a limitation relative to traditional angiography [9]. The primary risks of carotid CTA include exposure to ionizing radiation and iodinated contrast which has a 0.2–0.7 % adverse reaction rate [10]. These factors will be further discussed below.

Technique

General Protocol

While the specific technique may vary between institutions, carotid CTA images are generally acquired following a single bolus injection of 35–100 ml of nonionic contrast material into an antecubital vein at 3.5–6 ml/s. The timing of the CT angiography study is typically programmed in one of three ways. (1) A set scan time delay can be used (i.e., 18–25 s after the start of the contrast injection). This option has the benefit of being the least technically complicated which is useful for CT technologists that do not often perform CT angiography and when using older equipment that may lack a bolus-tracking feature (2). A contrast bolus-tracking technique is performed using a low-dose scan at a set level after the initiation of the contrast injection with automatic scan triggering once the Hounsfield units (HU) of the vessel of interest (i.e., aorta or carotid artery) exceed a set threshold—typically of 50–100 HU. (3) Using a scan time set using data from a time-density curve (TDC) (Fig. 1). This technique begins with a localizer scan at the level of the aorta, common carotid artery, or internal carotid artery. After identification of the level of the vessel of interest, a small bolus of contrast and saline chaser is injected at the same intended rate of the actual CTA examination (i.e., 3.5–6 ml/s). A continuous low-dose (i.e., 80 kV, 100 mAs) single-section scan is performed 5 s after the start of the contrast medium injection at a rate of one scan per second. Scanning is continued until washout of the contrast medium from the artery of interest is observed. The time-to-peak enhancement is calculated from the TDC; 2–4 s is added to the peak enhancement time to arrive at the optimal scan time. If a CT perfusion of the brain is performed as part of as a comprehensive neurovascular examination, the CT perfusion dataset can be used to generate a TDC for a subsequent CTA. The TDC method is the most technically challenging, requires added work for the technologist and also utilizes additional contrast medium, but has the advantage of assessing the optimal contrast timing for an individual patient. This is typically most important in older patients, patients with poor cardiac output and those with atrial fibrillation.

Contrast Issues

The bolus rate and iodine concentration affect the quality of three-dimensional (3D) CTA reconstructions. Injections of high-concentration contrast with an increased iodine-delivery rate produce improved arteriovenous contrast differentiation at the

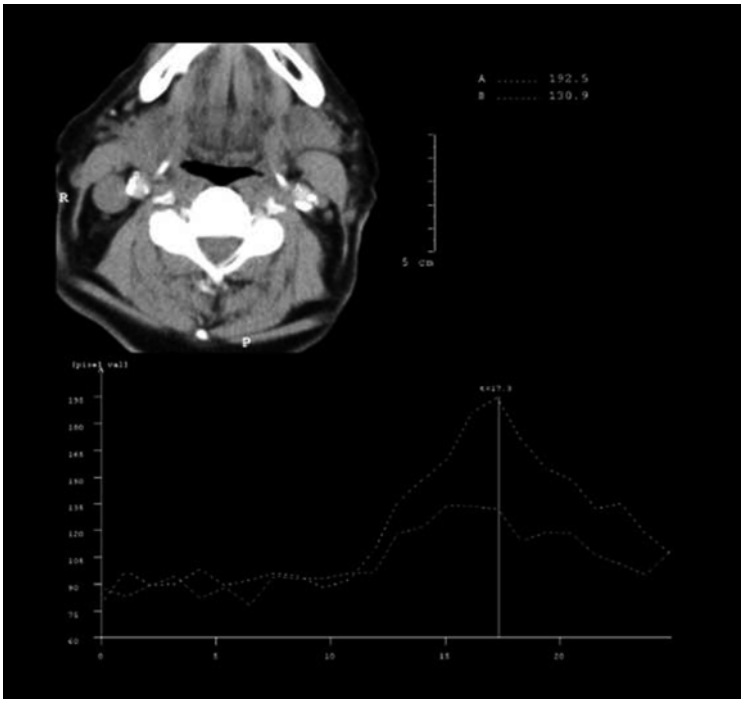

Fig. 1 Low-dose axial CT image performed during test bolus of contrast injection with ROI placed over the region of the carotid bifurcations and revealing peak contrast enhancement 17 s after injection initiation

level of the cavernous internal carotid artery (ICA). With the same rate of iodine delivery, injections of intermediate-concentration contrast agents increase the HU of both the cavernous ICAs and also the cavernous sinuses, with poorer resultant arteriovenous differentiation [11].

The optimal phase of arterial enhancement has been a topic of discussion in multiple studies, with the optimal arterial attenuation on CTA typically deemed to be ≥150 HU [12]. An attenuation difference of at least 50 HU between arterial and venous structures on CTA has proved to be the threshold for 3D rendering purposes with intensity-based software [13]. Studies have demonstrated that early arterial phase examinations may overestimate severe/critical carotid artery stenosis [14]. Early arterial phase acquisitions also have an affect on the evaluation of CTA source images (CTA-SI) and intracranial collateral flow [15, 16].

Several variations of the general carotid CTA protocol have been suggested, including rapid injection of smaller contrast volumes and also those using slower injection methods. One method of rapid injection is characterized by injecting a small contrast bolus (35–50 ml) at 6 ml/s after timing assessment with generation of a TDC. This technique allows for a tight contrast bolus, which is beneficial to obtain the maximal vessel opacification. Alternately, injection of iodinated contrast at a

slower rate of 3.5–4.0 ml/s followed by imaging after a 25 s delay is less prone to timing errors that could result in unacceptable vessel opacification [17].

For patients requiring both cervical vessel evaluation and parenchymal evaluation, such as in the setting of radiation-induced cervical atherosclerotic disease in patients with head and neck cancer, a split-bolus technique may be employed. Approximately half of the standard contrast bolus is initially given. After a delay of approximately 45 s, the second half of the bolus is then given either followed by a bolus-tracking scan or a set time delay after which the scan is then performed. This method provides good parenchymal enhancement and robust arterial opacification with the benefit of only a single radiation exposure to the patient. The limitations of this protocol however include slightly more complex timing required for the technologist and suboptimal arteriovenous contrast for a dedicated arterial evaluation.

Dual Energy

The photon array from a source at a single peak kilovoltage (kVp) consists of a continuum of energies including the characteristic energies of the anode material. The average energy of a photon array (i.e., X-ray beam) is approximately one-third of the energy of the kVp. Conventional "single"-energy CT depicts various anatomic regions on the basis of differences in photon attenuation between adjacent structures. This difference in attenuation is primarily a function of the photoelectric effect and Compton scattering and is largely dependent on the atomic number of the materials involved. "Dual"-energy CT (DECT) extends the capabilities of single-energy CT so that structures with similar densities but different elemental compositions are distinguished according to their electron density differences in addition to their atomic number [18]. Furthermore, DECT may be desirable because of the superior imaging capabilities that can be achieved without a substantial increase in radiation dose. The basic principle of the DECT is to obtain two datasets with different X-ray energy levels from the same anatomic region and material decomposition on the basis of attenuation differences at different energy levels [19, 20].

DECT acquisition is manufacturer dependent and can be achieved by different physical implementations, including dual-spin CT, dual-source CT (DSCT), fast kilovoltage switching in a single source CT, or a sandwich detector–based CT which produces projections with two different energy levels for each exposure [21].

Dual energy imaging exploits the energy dependence of the CT attenuation of calcium and iodine, thus the Hounsfield units will differ at varying energy levels due to a difference in electron density. With a dual-source CT scanner, one tube can be set to 80 kV and the other to 140 kV, enabling two different energy data sets to be acquired simultaneously with one acquisition. DECT then enables digital subtraction of bone and calcified structures from CTA images, thus allowing for evaluation of carotid stenosis in the presence of large calcified plaques. However, dual-energy subtraction CT may overestimate the degree of carotid stenosis compared to other methodologies, such as multiplanar CTA reformats (MPR) and conventional angiography [22].

Optimization for 3D

Multiple techniques for carotid CTA image reformation can be performed using dedicated post-processing software, including multiplanar reformats (MPR), maximum intensity projection (MIP), and three-dimensional (3D) volume-rendering (VR) reformatting techniques [23]. A high-resolution dataset of approximately 1 mm slice thickness and no interslice gap allows for excellent quality 3D reconstructions. Finer datasets such at 0.9 mm slice thickness with a 0.45 mm interval between slices (50 % slice overlap) allows for preservation of maximal data from the helical scan acquisition at the cost of significantly greater slice number. Datasets of a more coarse nature, such as 1.5–2.0 mm slice thickness, result in mild degradation of reconstructed images, but are much less processor intensive for computer workstations.

Post-Processing

The practitioner of CTA should be knowledgeable about workstation-based post-processing techniques. Post-processing should include evaluation of the CTA source images as well as the reformatted images such as MPR, MIP, or volume-rendering images.

Once the data sets have been generated, post-processing must be applied to segment the helical volume and harness the information contained therein. The large volume of data typically obtained with CTA requires accurate, time-efficient, and reproducible image post-processing to enable disease interpretation. The axial image plane, formerly the plane with the highest image quality in a single detector CT scanner acquisition, is no longer the only plane available for image interpretation. Axial image viewing is time-consuming, inefficient, and possibly less accurate than viewing reformatted images. With modern CTA acquisition, near isotropic data sets can be obtained, which allow manipulation in all imaging planes and projections without significant loss of image quality. Therefore, a dedicated 3D workstation to enable a real-time interactive approach to image manipulation and interpretation has now become a necessity. Furthermore, many authors advocate the use of 3D image display for both diagnosis and procedure planning. Available post-processing techniques on the clinical 3D workstations include multiplanar reconstruction (MPR), maximum intensity projection (MIP), volume rendering (VR), and shaded surface display (SSD).

High efficiency in detecting and evaluating stenoses has made cross-sectional evaluation of MPR aligned to the vessel course the gold standard in analyzing CTA images. On the other hand, freely rotatable maximum intensity projection images (3D-MIP) can be created for a quick assessment of vessel status. Using conventional single energy CT, the ability to quantify highly calcified stenoses is often limited, as the vascular lumen within the calcified area is often obscured after 3D-MIP reconstruction [23].

Multiplanar Reconstruction (MPR)

The MPR algorithm enables a reordering of specific acquired image voxels along a predefined vascular centerline to provide a 2D image of the vessel of interest. As all arteries are curved at some point in their distribution, curved MPR (cMPR) is an extension of the MPR process that enables display of a curved plane prescribed along an individual vessel contour or centerline, thus displaying the entire vessel midline on a single 2D image. Curved MPRs provide a comprehensive cross-sectional display of arterial luminal sizes over long segments and can be especially useful in reviewing large vascular territories such as the brachiocephalic trunk through to the middle cerebral artery (Fig. 2). CMPRs are the most equipped post-processing method to reduce artifact from vessel calcification and arterial stents. However, cMPR can be user-dependent and requires manual or semi-automated tracing of each vessel centerline (Fig. 3). Also, it is imperative that at least two orthogonal planes for each arterial segment are created to ensure accurate quantification of eccentric atherosclerotic plaque. The orthogonal planes are essential for determining the true cross-sectional diameter of a vessel (Fig. 4). Other limitations of cMPR are that only one arterial segment can be displayed at a time and the limited spatial perception due to the absence of anatomical landmarks such as vessel bifurcations. A new potential solution for these limitations has been described: multipath curved planar reformations (MPCPRs). The MPCPR method allows multiple longitudinal vessel cross-sections to be displayed simultaneously and therefore allows branching patterns to be seen without obscuring vessel wall calcifications and stents, thus restoring spatial perception.

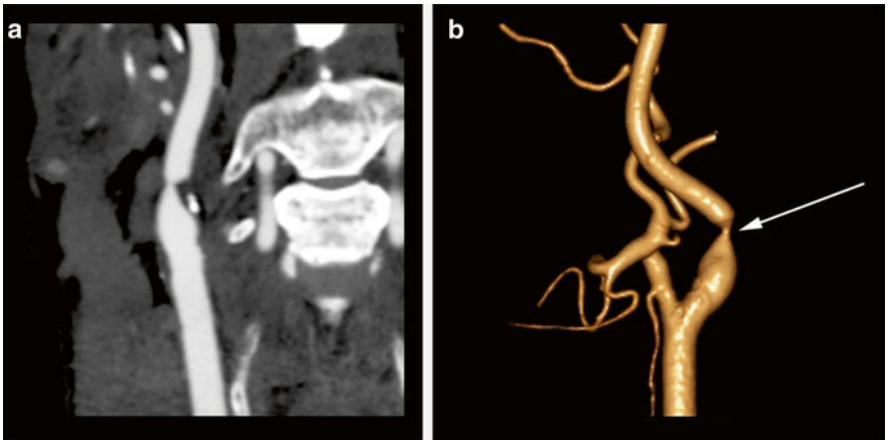

Fig. 2 63-year-old male with abnormal carotid Doppler ultrasound. (**a**) A curved MPR CTA reveals severe stenosis of the proximal right internal carotid artery leading to a "string" sign. (**b**) A surface-shaded display image shows the degree of focal high-grade stenosis (*arrow*) without the "straightening" of the curved MPR function. This display can be useful for the interventionalist in pre-procedure planning. Images courtesy of Daniel Ginat, M.D.

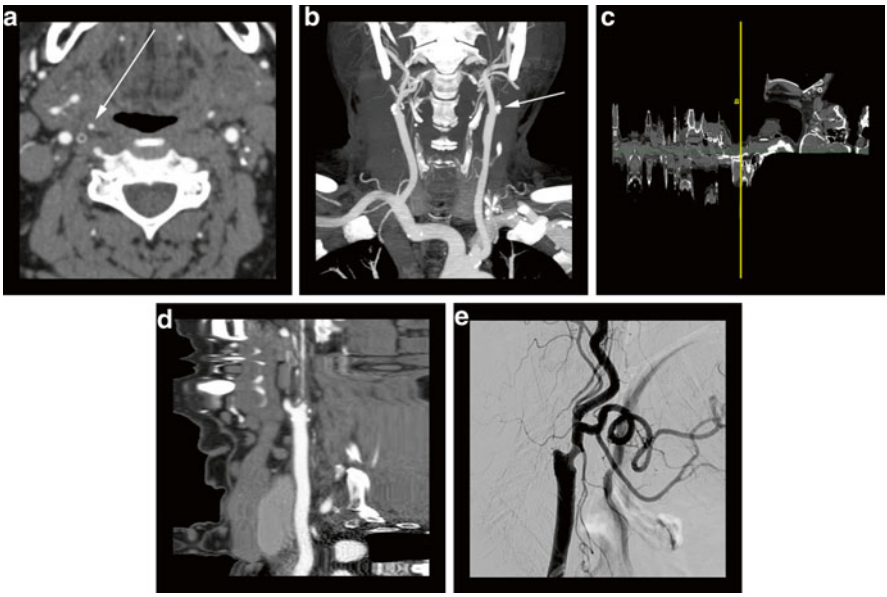

Fig. 3 75-year-old male presenting for cerebrovascular evaluation. (**a**) Axial CTA image reveals a completely occluded left internal carotid artery at the origin and a critical stenosis of the right internal carotid artery origin with a residual "hairline" lumen (*arrow*). (**b**) Coronal CTA MIP image reveals prominent bilateral external carotid arteries with poor visualization of the residual right internal carotid artery. The left internal carotid artery "stump" (*arrow*) is visualized. (**c**) Computer generated "straightened" curved MPR reveals failure of the computer algorithm to accurately assign the centerline to the residual internal carotid artery vessel—a common pitfall seen with critical stenoses. (**d**) "Straightened" curved MPR of the same vessel with manual assignment of the centerline depicts the long segment of critical stenosis. (**e**) Lateral projection digital subtraction angiography of the right carotid artery with injection of the common carotid artery reveals long segment critical stenosis of the proximal right internal carotid artery as seen best in (**d**)

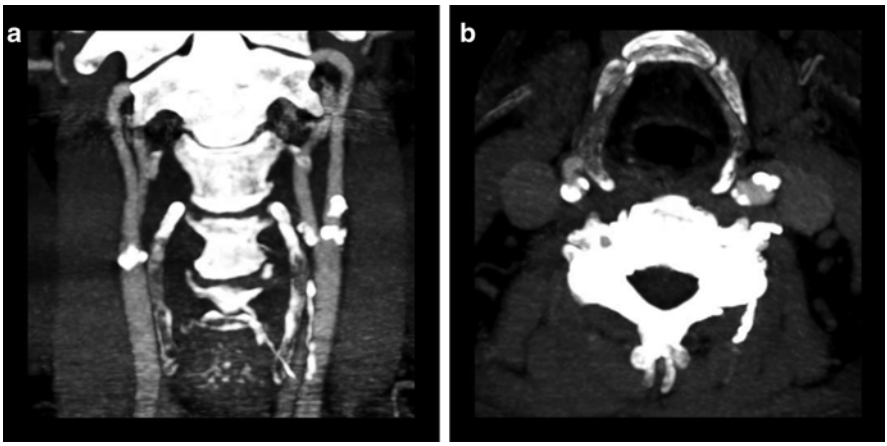

Fig. 4 88-year-old male presenting with transient ischemic attack. (**a**) A coronal CTA MIP image displays moderate predominantly calcified atherosclerotic disease of the bilateral carotid bifurcations. The MIP technique allows the higher density calcified atherosclerotic plaques to obscure the vessel lumen. (**b**) An axial CTA MIP image through the level of the carotid bifurcations more accurately displays the mild left and moderate right stenosis at the level of the internal carotid artery origins

MIP

The technique of MIP provides images that most closely resemble those obtained with conventional DSA and therefore are often desired by interventionalists to enable a quick overall review of the vasculature for significant lesion determination prior to endovascular or surgical treatment. To obtain a MIP image, a specific algorithm is applied to the source data within the 3D workstation. This algorithm involves applying a threshold attenuation value and selecting out the highest attenuation voxels along lines projected through the given volume data set. These selected high-attenuation voxels are then incorporated into a 2D angiogram-like image, useful for demonstrating vessel opacification and residual vessel lumen. The limitations of MIP include vessel obscuration by other high-attenuation voxels, such as calcification, stents or bone, and the inability to display 3D relationships of vessels and adjacent anatomical structures. These limitations become a major problem with heavy arterial wall calcification or arterial stents, as the vessel lumen can become obscured. Also, when vessel relationships need to be determined prior to surgical intervention, this 2D MIP method is limited. However, MIP weaknesses can be partially mitigated by selectively cropping adjacent high-density structures (bones, vessel wall calcification, and stents), using alternate planes of projection and setting variable attenuation threshold values (Fig. 5).

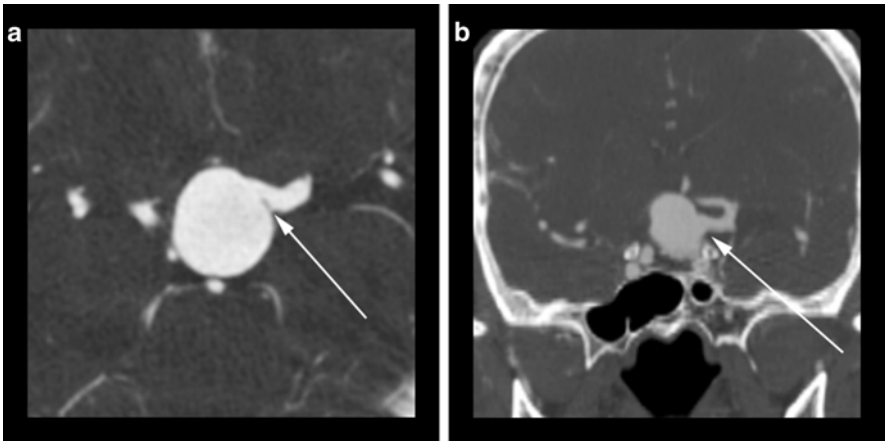

Fig. 5 (**a**) An axial CTA image reveals a giant basilar tip aneurysm with apparent incorporation of the left posterior cerebral artery (*arrow*). (B) A coronal CTA MIP image reveals that the left vertebral artery origin arises (*arrow*) from the middle aspect of the body of the aneurysm which would preclude a traditional coil embolization without protective measures

Shaded Surface Display (SSD)

SSD is a process in which apparent surfaces are determined within the volume of data and an image representing the derived surfaces is displayed. SSD provides an anatomical overview but like MIP and VR, has difficulty discriminating calcification, fails to display lumen detail and can over-estimate stenosis; therefore, SSD is generally not recommended for vessel caliber measurements (Fig. 2b).

Volume-Rendering (VR)

Dedicated computer software on 3D workstations allows for a VR algorithm to be applied to the source data. Volume rendering (VR) represents the most advanced form of 3D post-processing. The principle of VR involves taking the entire volume of source data, adding the contributions of each voxel along a line from the viewer's eye through the data set, and displaying the resulting composite for each pixel of the display. It is of high fidelity to the acquired data set, preserving all the density values within the voxels. Histogram trapezoids with various user-defined settings of opacity, brightness, and color may be applied to create attractive carotid artery images (Fig. 6). However, one must interpret volume rendering with caution, as many of the user-adjusted variables may dramatically alter the apparent size of the vessel lumen.

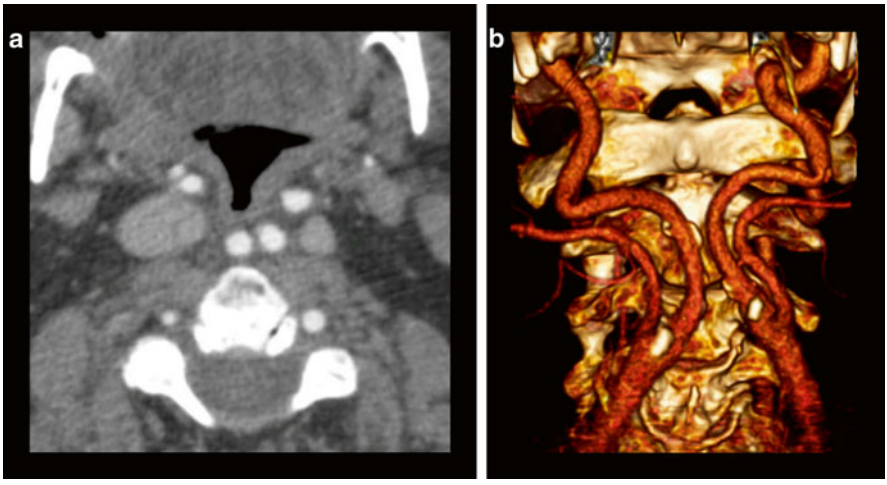

Fig. 6 88-year-old male presenting with stroke-like symptoms. (**a**) Axial CTA image reveals "kissing" internal carotid arteries (*arrow*) which lie in a retropharyngeal location. (**b**) 3D volume rendering better displays the abnormal medial orientation of the carotids

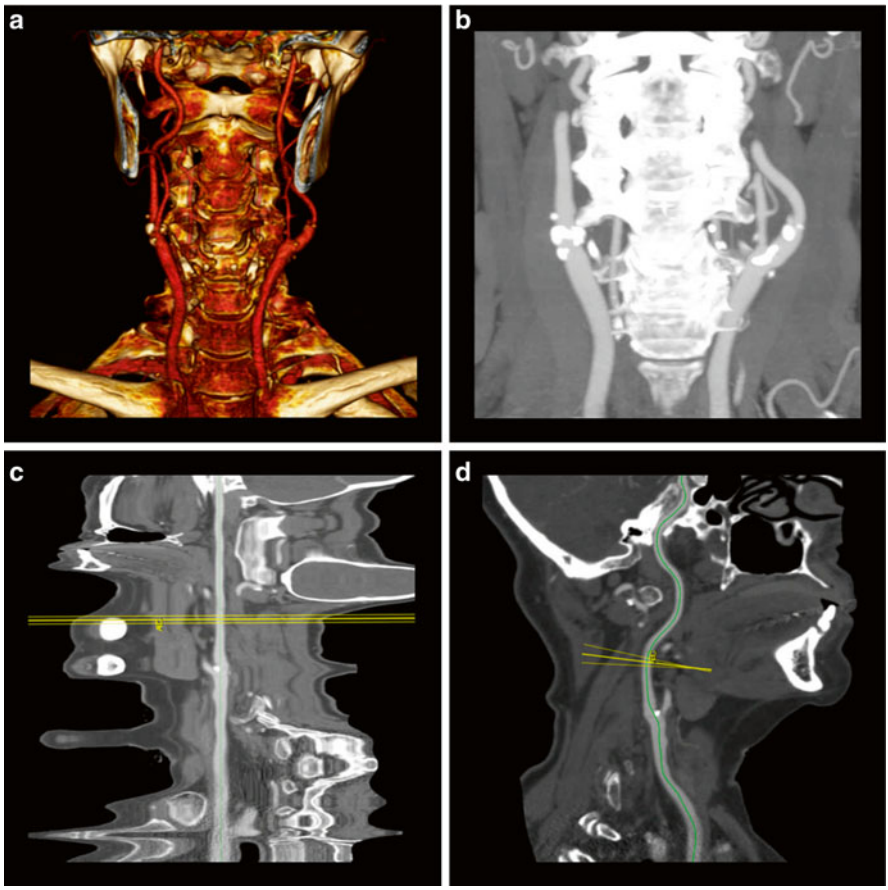

Fig. 7 73-year-old female presenting with stroke-like symptoms. (**a**) A coronal orientation 3D volume rendering reveals bilateral calcified plaque at the carotid bifurcations, but does not allow for accurate assessment of the degree of stenosis. (**b**) A coronal orientation CTA MIP also displays the presence of calcified plaque but offers little information on the effects on the underlying artery lumen. (**c**) A "straightened" curved MPR CTA image of the left carotid artery shows that the atherosclerotic plaque has negligible effects on the vessel lumen. (**d**) A "stretched" curved MPR CTA image from the same dataset provides another view of the left common carotid artery with display of the centerline from the aortic arch through to the ipsilateral middle cerebral artery

Although VR can be used to illustrate vessel opacification, stenoses, and course, MIP is the better choice to quantify lumen change. VR preserves 3D anatomical relationships, unlike MIP; however, VR, like MIP, still has limitations with vessel calcification and arterial stents. Therefore, this fundamental limitation precludes the exclusive use of VR and MIP techniques in a large proportion (approximately 60 %) of patients undergoing cerebrovascular evaluation (Figs. 7 and 8).

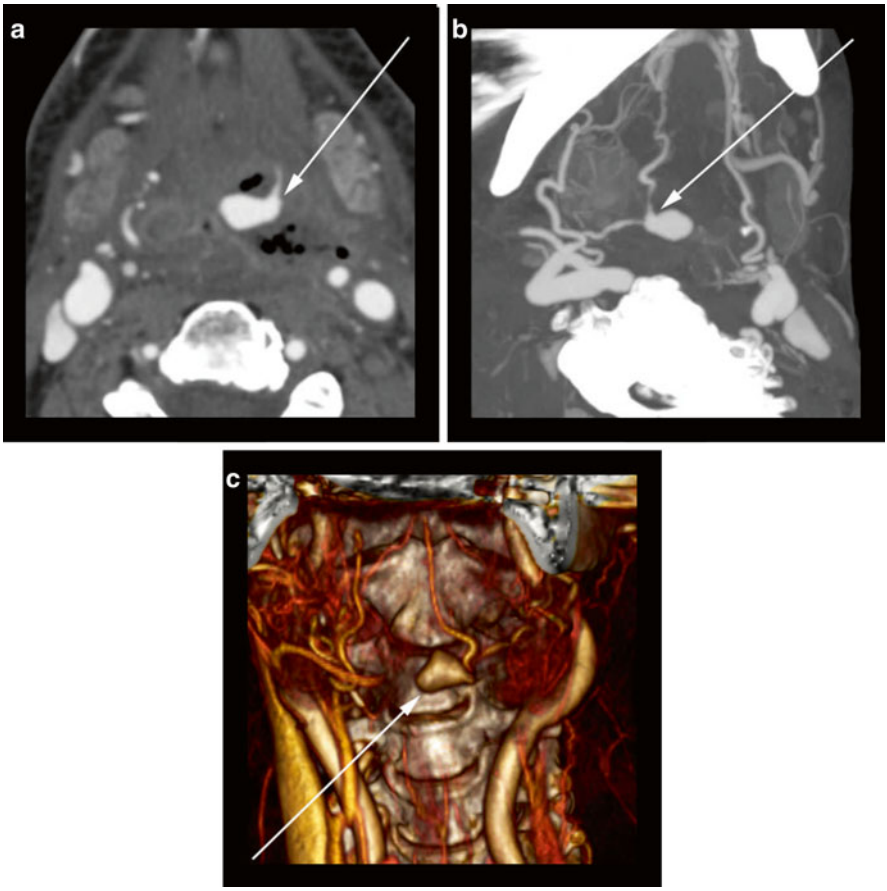

Fig. 8 52-year-old woman with head and neck cancer status post-surgical resection, flap reconstruction, and radiation therapy. (**a**) Axial CTA image reveals a large pseudoaneurysm (*arrow*) involving a branch of the external carotid artery surrounded by necrotic oropharyngeal tissue. (**b**) Oblique MIP CTA image displays the course of the parent branch artery from the external carotid artery origin (*arrow*). (**c**) Coronal orientation 3D volume rendering reveals the irregular shape of the aneurysm (*arrow*) along with information on the relationship to surrounding anatomic structures

Combined 3D Methods

In clinical practice, a combination of the available 3D reformatting methods is employed to accurately diagnose cerebrovascular disease. In the event that complete evaluation of all arterial segments is felt to be limited, then review of the original source images should be performed. Anatomical overview and quick significant disease localization can be achieved with the MIPs or the VR images. If arterial calcification or a stent obscure the arterial lumen, then a combination of

MPR/CMPR is used. Dual-energy CT acquisition is a potential option for severe arterial calcification, as this tool enables subtraction of the wall calcification to unmask the adjacent arterial lumen. A dual-energy post-processing software program is available to enable calcified structures (atherosclerotic plaque and bone) to be identified separately from iodinated contrast, and subsequently calcification can be subtracted.

Billing and Documentation

According to the American College of Radiology (ACR), post-processing to provide multiplanar reformations through 3D renderings is mandatory for the exam to be considered CT angiography. Thus, two-dimensional (2D) post-processing no longer constitutes a CTA study. When CT scanning is performed using contrast enhanced dynamic-timed imaging and 2D reformatted axial images are obtained or multiplanar reconstructions (MPR) (e.g., coronal, sagittal, or even an off-axis view) are obtained, this should be reported with a standard CT with contrast code that identifies the anatomic area studied. None of these 2D planar reconstructions qualify as "angiographic" reconstruction. A full documentation and interpretation of a CTA includes not only vessel pathology, but also an assessment of the end organs of the vessels examined for secondary findings and potential alternative causes for the patient's symptoms. Organs adjacent to the examined vessels should also be viewed for potential pathology.

Acceptable post-processing techniques that constitute a CTA study include the following, and physicians must state in their dictation that one of these 3D techniques was utilized: maximum intensity pixel (MIP), volume-rendered images, surface-shaded rendering, and/or 3D reconstructed images. Archival of these 3D renderings is also clearly defined by the ACR. It is necessary to have a permanent archive of 3D images acquired on a CTA study. When reformatted images are acquired and interpreted in addition to the CT axial images, the reformatted images are a part of the study and should be permanently archived.

Reports should also document the degree of any hemodynamically significant stenosis (typically regarded as greater than 50 %). The North American Symptomatic Carotid Endarterectomy Trial (NASCET) described a method of quantifying internal carotid artery stenosis. The diameter of the stenotic segment is divided by the diameter of a normal, distal segment of internal carotid artery (where walls are parallel) and subtracted from 1 ($1-(A/B)$) [24].

Image Processing Limitations

Technical limitations to post-processing may exist, with the main ones being secondary to heavy arterial wall calcification or the presence of an arterial stent, as discussed above. Reviewing the axial source data can be a simple measure to overcome these

problems. Post-processing artifacts can also occur, secondary to inadvertent vessel subtraction, particularly with MIP images. Other limitations of MIPs include anatomic overlap of adjacent structures and loss of structural detail with increasing slab thickness. MIP images can be degraded by high-density structures within the imaged field of view, including bone, calcium, stents, and coils. There can also be limited grading of stent lumens on MIP images and thus difficulty with evaluating in-stent restenosis.

With MPRs (especially curved MPRs), artifacts, such as production of pseudostenoses and/or occlusions as a result of inaccurate centerline definition, can occur (Fig. 3c). There can also be limited spatial perception with MPR data sets. Operator dependence is another potential limitation of CMPRs. Eccentric atherosclerotic plaque may be underestimated with the CMPR technique as a result of tracing only the centerline of the artery. Volume-rendered images may not demonstrate aneurysmal dilation of a vessel due to partial luminal thrombosis. Again, review of the axial source data can help solve these problems. Also, anatomic overlap of adjacent structures and loss of structural detail with increased slab thickness may occur with VR post-processing techniques similar to MIP.

To date, there are no fully automated algorithms to detect vessel centerlines, to segment out bony structures, or to detect/subtract vessel wall calcification. However, with constant software updates, these tools are likely to become available in the near future. A new investigational tool is dual-energy MDCTA that allows automatic subtraction of bone and potentially calcified atherosclerotic plaque, based on differential attenuation of bone, calcium, and iodine on a dual-energy scan as discussed above.

Safety

Carotid CTA is noninvasive and is associated with fewer risks than traditional carotid angiography. However, the exposure to ionizing radiation and the intravenous administration of iodinated contrast material should be considered when prior to carotid CTA.

Radiation

American exposure to medically related ionizing radiation doses has increased nearly sevenfold since the 1980s and accounts for approximately 50 % of the total radiation dose to the population [25]. As the population ages, the increasing utilization of medical imaging will necessitate the discussion of dose-reduction techniques amongst radiologists and clinicians. Appropriate patient selection is an important

factor that can be achieved by identifying patients who will most benefit from CTA. Nonionizing radiation imaging modalities, such as ultrasound and MRI, should be considered for patients when feasible and in the absence of factors favoring the use of CT imaging.

Optimization of CT imaging parameters can allow for image acquisition with a lower radiation dose. For example, a dose reduction from 120 to 100 kVp and a reduction from 235 to 140 mA have been shown to lead to a dose reduction of 62 % while still producing source images and 3D reconstructions of diagnostic quality [26]. In a related study, improved signal to noise ratio of the intracranial vessels was demonstrated at 80 kVp compared to 120 kVp despite an increased image noise [27].

Contrast Media

Nonionic, low-osmolar contrast media is associated with a variety of allergic reactions, which rarely (approximately 4 in 10,000 [28]) can be life-threatening. Proper training is essential for both the supervising physician and support staff in the recognition of and appropriate treatment for a range of contrast reactions. Identifying patients at increased risk of severe contrast reactions prior to injection of iodinated contrast is important to ensure patient safety. Premedication regimens including corticosteroids and anti-histamines should be considered in patients with prior allergic reactions to contrast media or a history of other serious allergies, as these patients are at increased risk for future reactions.

Contrast-induced nephropathy (CIN) is another risk of the administration of iodinated contrast, which tends of occur more frequently in patients with acute kidney injury and/or chronic renal insufficiency. While there is no absolute renal function cutoff, risks and benefits of carotid CT imaging must be weighed with the patient's underlying renal function when deciding whether to proceed with carotid CTA.

The rapid intravenous injection of iodinated contrast material may rarely be associated with the development of contrast extravasation in 0.1–0.9 % of cases [29]. While most episodes of contrast extravasation resolve without major complication, compartment syndrome may develop if a large volume of contrast material is introduced into a small body compartment. In the setting of large volume contrast extravasation, patients should be evaluated by a physician for evidence of increased compartment pressures including findings of neuromuscular compromise such as pain or paresthesias [30]. Reduction of the volume of contrast media as well as multiphase injections methods have been investigated to reduce the risk of contrast associated complications following carotid CTA [31].

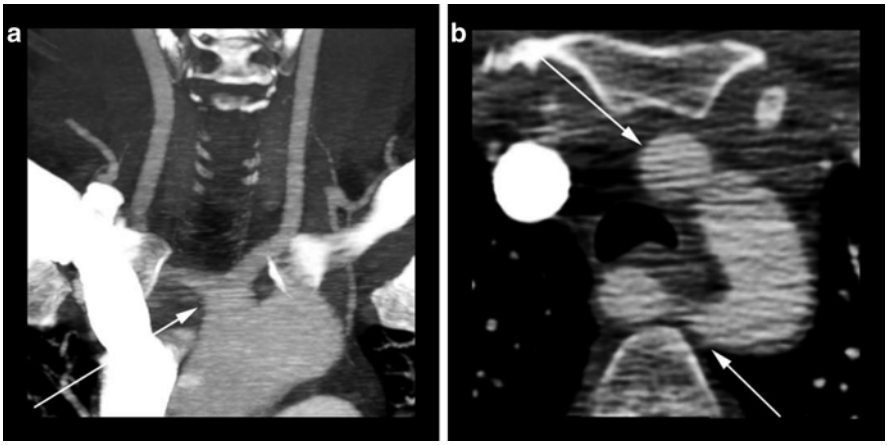

Fig. 9 64-year-old female presenting for acute stroke evaluation. (**a**) A coronal CTA MIP image displays a common origin (*arrow*) of the bilateral common carotid arteries in the setting of an aberrant right subclavian artery. (**b**) A standard axial CTA image reveals the common origin of the carotid arteries (*top arrow*) as well as the aberrant right subclavian artery (*bottom arrow*) coursing behind the esophagus and trachea

Anatomy of the Carotid Arteries

Although many anatomic variants exist, the classical anatomy of the aortic arch includes an independent origin of the left common carotid artery from the aortic arch. The right common carotid artery classically originates from the bifurcation of the brachiocephalic (innominate) artery into the right subclavian and right common carotid arteries (Fig. 9).

The bifurcation of the common carotid arteries typically occurs at the level of the C3-C4 vertebral bodies. After the carotid bifurcation, the external carotid artery (ECA) typically courses anteromedially through the neck, and the ICA courses posterolaterally (Fig. 6). The ICA provides the arterial supply to the brain and eyes, while multiple branches of the ECA supply the remainder of the head and neck. The ICA is generally larger in caliber, but does not demonstrate any branch vessels in the neck [32].

The intracranial portion of the ICA is divided into multiple segments. The petrous segment traverses the petrous portion of the temporal bone and extends to the level of foramen lacerum. The cavernous sinus surrounds the cavernous portion of the intracranial ICA. The ophthalmic segment of the ICA is the first intradural portion contained within the subarachnoid space. The intracranial ICA gives off multiple branches, including the vidian and ophthalmic arteries, with the terminal portion branching into the posterior communicating and anterior choroidal arteries, as well as the anterior and middle cerebral arteries (Fig. 10).

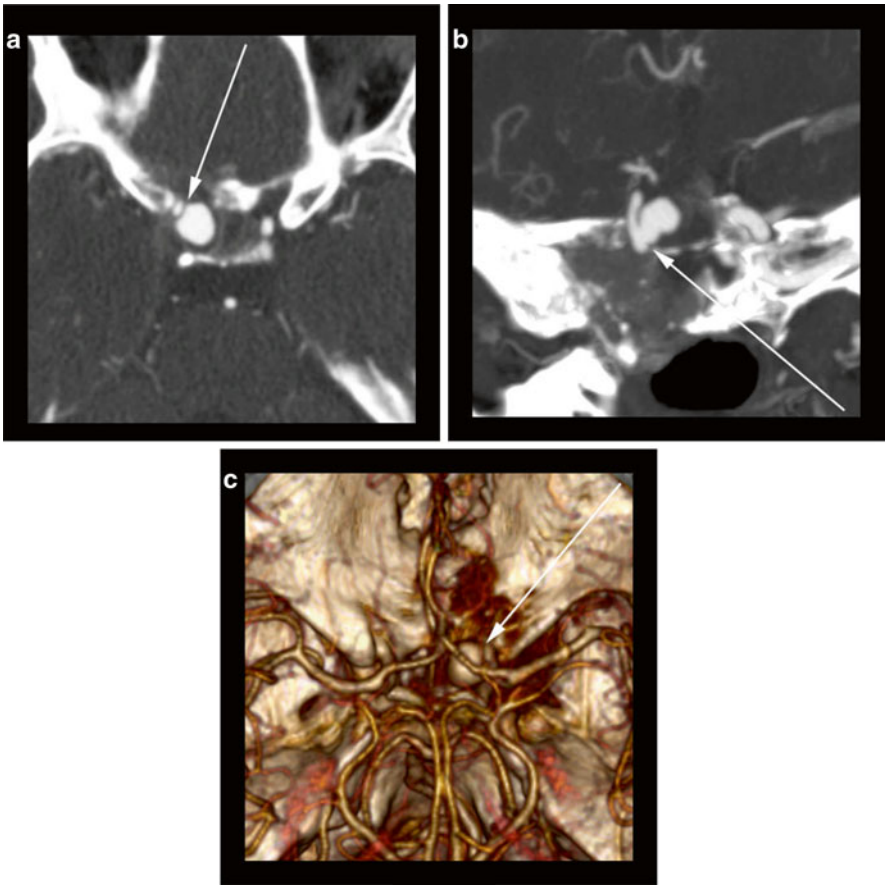

Fig. 10 55-year-old with history of recurrent invasive nasopharyngeal carcinoma. (**a**) Axial CTA image reveals a saccular aneurysm arising (*arrow*) from the communicating segment of the right internal carotid artery just distal to the ophthalmic segment. The "raw" axial image at the level which best shows the aneurysm does not reveal the aneurysm neck or display the origin. (**b**) An oblique coronal CTA MIP reveals the irregular shape of the aneurysm neck (*arrow*) along with the relationship of the aneurysm to the parent vessel. (**c**) A craniocaudal view of a 3D volume rendering allows for visualization of the aneurysm (*arrow*) along with providing anatomic information about the surrounding structures. These types of views can be extremely helpful for pre-procedure planning

Pathology

Atherosclerosis

The most common pathology of the carotid arteries is atherosclerotic disease. Frequently developing at the carotid bifurcation, studies suggest that the flow dynamics, such as turbulent flow, may lead to the development of atherosclerotic

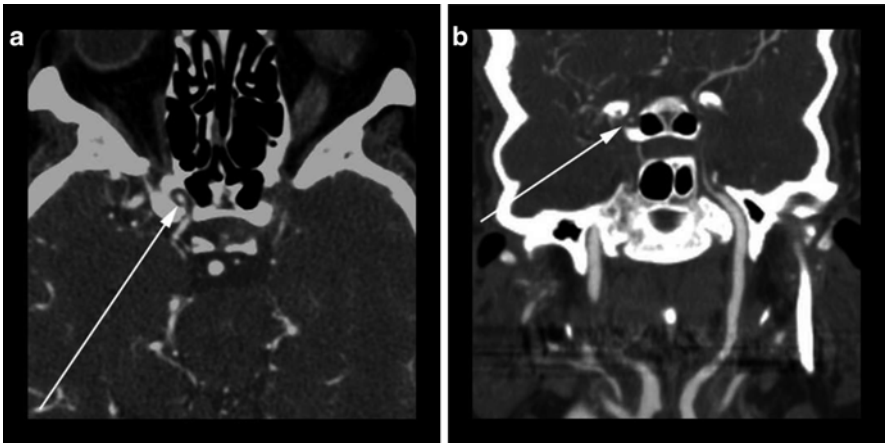

Fig. 11 75-year-old female with chronic headaches and transient ischemic attack. (**a**) Axial CTA image shows moderate stenosis of the anterior genu of the right cavernous segment (*arrow*) of the internal carotid artery and critical stenosis of the left internal carotid artery at the same level. (**b**) Coronal oriented curved MPR CTA image depicts the long segment abnormality (*arrow*) involving the distal left internal carotid artery

plaque [33]. CTA can detect plaque in the carotid arteries of multiple consistencies, including calcified, noncalcified (soft), as well as mixed. In addition, CTA can evaluate plaque morphology, which has been identified as a risk factor for stroke, independent of the degree luminal narrowing [34] (Fig. 11).

The volume and configuration of plaque may lead to various degrees of carotid stenosis. The most common method for calculating the degree of stenosis involves comparison of the narrowest luminal diameter with the luminal diameter of the normal distal vessel, with both measurements made in a CT plane perpendicular to the lumen. The North American Symptomatic Carotid Endarterectomy Trial (NASCET) criteria to calculate the degree of luminal diameter are frequently utilized, as discussed above [35]. Other methods for calculating the degree of carotid luminal stenosis have also been proposed [36].

The degree of carotid stenosis has been associated with the risk of symptomatic cerebrovascular disease. Surgical options for carotid revascularization procedures include carotid endarterectomy (CEA) and carotid stent placement [35, 37]. Patients with symptomatic stenosis evidenced by transient ischemic attack (TIA), stroke, or amaurosis fugax in the presence of carotid arterial luminal narrowing greater than 70 % have been shown to benefit from carotid endarterectomy or stenting [38]. Even before the North American Symptomatic Carotid Endarterectomy Trial (NASCET) demonstrated a reduced risk for ischemic stroke with surgical intervention in symptomatic patients with greater than 70 % stenosis, imaging played a pivotal role in defining who may benefit from carotid artery revascularization [35] (Fig. 12).

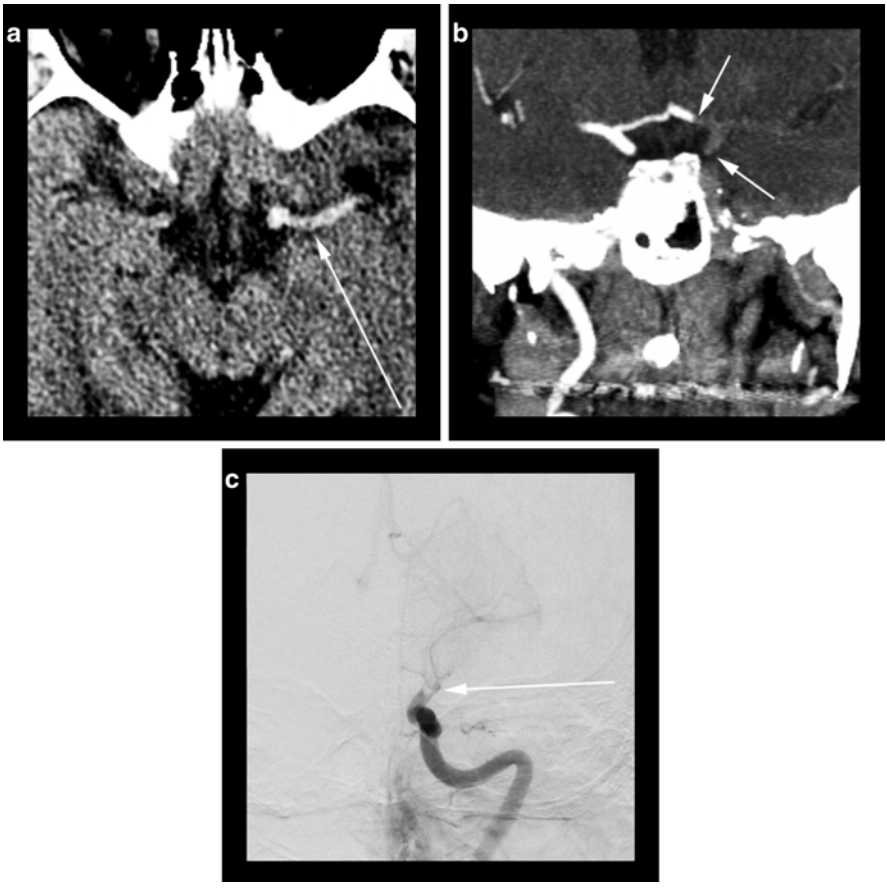

Fig. 12 (**a**) An axial noncontrast CT image of the head reveals an asymmetric hyperdense left internal carotid artery terminus and left proximal middle cerebral artery (*arrow*). (**b**) A coronal CTA MIP image reveals nonopacification of the left internal carotid artery terminus (*right arrow*), proximal left anterior cerebral artery (*left arrow*) and the left proximal middle cerebral artery. (**c**) A frontal projection digital subtraction angiogram with injection of the left internal carotid artery corroborates findings from the CTA (*arrow*)

Three-dimensional tools to evaluate the carotid anatomy are beneficial beyond assessment of degree of stenosis (Figs. 13 and 14). The technical aspects of carotid endarterectomy are influenced almost exclusively by the level of the carotid bifurcation and the quality of the proximal and distal endpoints of the endarterectomy site, which are easily assessed by carotid CTA. Additionally, the three-dimensional vascular anatomy at the level of the aortic arch, common carotid, and distal internal carotid artery are factors influencing the technical success of carotid artery stenting [38].

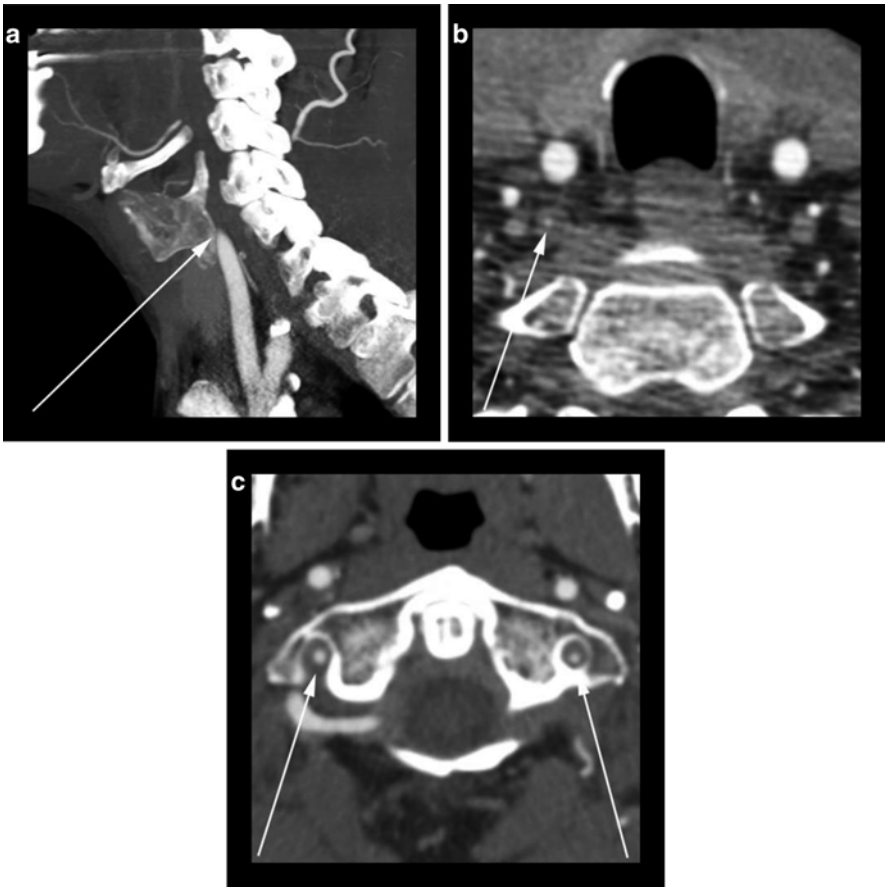

Fig. 13 50-year-old male presenting with dizziness and vertigo. (**a**) Sagittal CTA MIP suggests complete proximal occlusion (arrow) of the right vertebral artery related to mixed density atherosclerotic plaque. (**b**) An axial CTA image shows a string of contrast opacification (*arrow*) within the vertebral artery lumen suggesting the MIP reconstruction overestimated the degree of stenosis. (**c**) An axial CTA image at the level of the C1 vertebral body shows bilateral V2 and V3 segment vertebral artery opacification (*arrows*); although, it cannot be ascertained on this single phase CTA examination whether flow within the vertebral arteries is antegrade or retrograde

Recent studies have demonstrated that enhancement of the vasa vasorum in patients with 50–70 % luminal narrowing is strongly associated with acute neurological symptoms. Therefore, vasa vasorum enhancement may serve as an additional factor to evaluate risk of stroke in patients with similar degrees of carotid stenosis, which is readily evaluated by carotid CTA [39] (Fig. 15).

Conventional carotid angiography is the gold standard for detection of carotid artery stenosis and occlusion. When compared to conventional angiography, carotid CTA demonstrates excellent performance with a sensitivity and specificity of 98.4

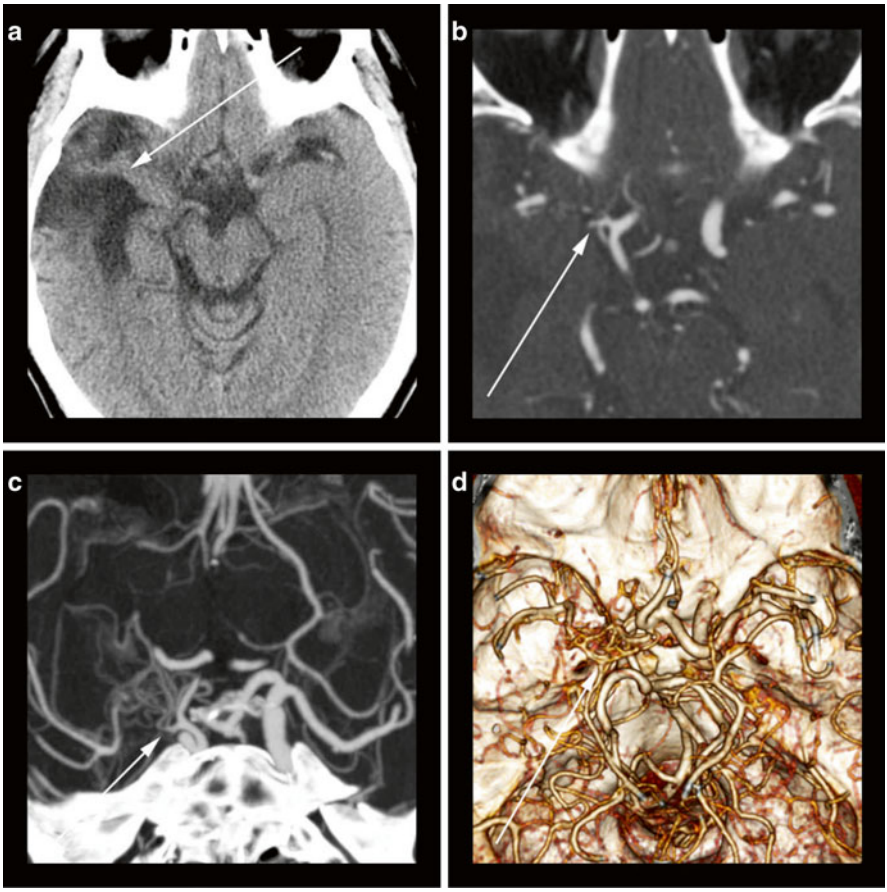

Fig. 14 50-year-old male with history of chronic right middle cerebral artery infarction. (**a**) Noncontrast CT of the head reveals chronic encephalomalacia involving the right anterior temporal lobe (*arrow*) as well as *ex vacuo* dilatation of the right lateral ventricle. (**b**) Axial CTA image reveals findings of a critical and likely chronic stenosis of the right proximal M1 segment (*arrow*) of the middle cerebral artery. There is asymmetric increased size and opacification of the ipsilateral lenticulostriate vessels. (**c**) An oblique coronal orientation CTA MIP better displays the relationship of the middle cerebral artery stenosis (*arrow*) and the surrounding asymmetric dilated lenticulostriate vessels. (**d**) A 3D volume rendering from craniocaudal orientation reveals the "tangle" of dilated lenticulostriate vessels but obscures the underlying middle cerebral artery stenosis (*arrow*). An arteriovenous malformation could have a similar appearance from this reconstruction

and 98.1 % for vessel occlusion [40]. The diagnostic accuracy of carotid CTA compared to angiography has been evaluated in multiple studies, with a recent meta-analysis evaluating 28 studies showing a overall sensitivity of carotid CTA for evaluating the degree of carotid occlusion of 97 % with a specificity of 99 % [41]. Specific assessment of the accuracy of carotid CTA in the evaluation of ICA occlusion versus severe stenosis has been performed, revealing a sensitivity of 97 % and specificity of 99 % [41]. Carotid CTA also demonstrated a sensitivity of 85 % and

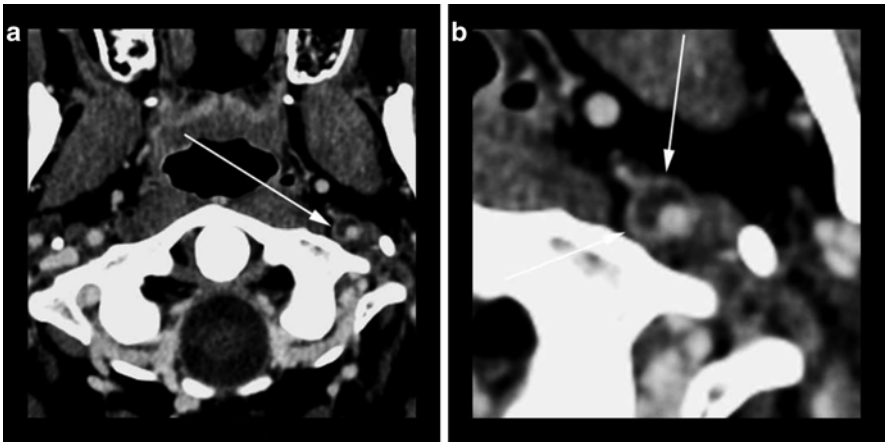

Fig. 15 49-year-old male presenting with stroke-like symptoms. (**a**) Axial CTA image reveals peripheral low density cresentric atherosclerotic plaque and vasa vasorum enhancement (*arrow*). (**b**) A magnified version of the same image better displays the enhancement of the vasa vasorum (*arrows*)

specificity of 93 % in the diagnosis of severe stenosis, as defined by 70–99 % luminal narrowing (Fig. 3).

In comparison with other noninvasive techniques, such as MRA and Doppler, carotid CTA possesses excellent sensitivity and specificity in the diagnosis of vessel occlusion. Assessment of the degree of stenosis and residual luminal diameter by carotid CTA has been shown to compare favorably to traditional catheter angiography, magnetic resonance angiography, and carotid ultrasound [42–44].

In combination with ultrasound, carotid CTA has a role in the evaluation of recurrent stenosis and vessel patency following carotid artery stenting. Carotid CTA is particularly useful to confirm abnormal ultrasound findings and to evaluate anatomically difficult locations such as the upper cervical and intracranial carotid arteries. Metallic artifact can limit evaluation depending of the size and length of the involved segment; however, CTA has been shown to have less artificial luminal narrowing when interrogating cobalt and stainless steel stents when compared to contrast-enhanced MRA [45]. Recent developments of novel post-processing algorithms, including dual-energy techniques, have also improved the accuracy of carotid CTA in the evaluation of stent patency.

Aneurysms

Ruptured aneurysms involving the intradural intracranial vasculature are among the most frequent causes of subarachnoid hemorrhage (SAH). While digital subtraction angiography (DSA) has been considered the gold standard, CTA has become the initial screening tool in the evaluation of SAH, followed by DSA in equivocal cases and for endovascular therapy planning. DSA is an operator-dependent invasive

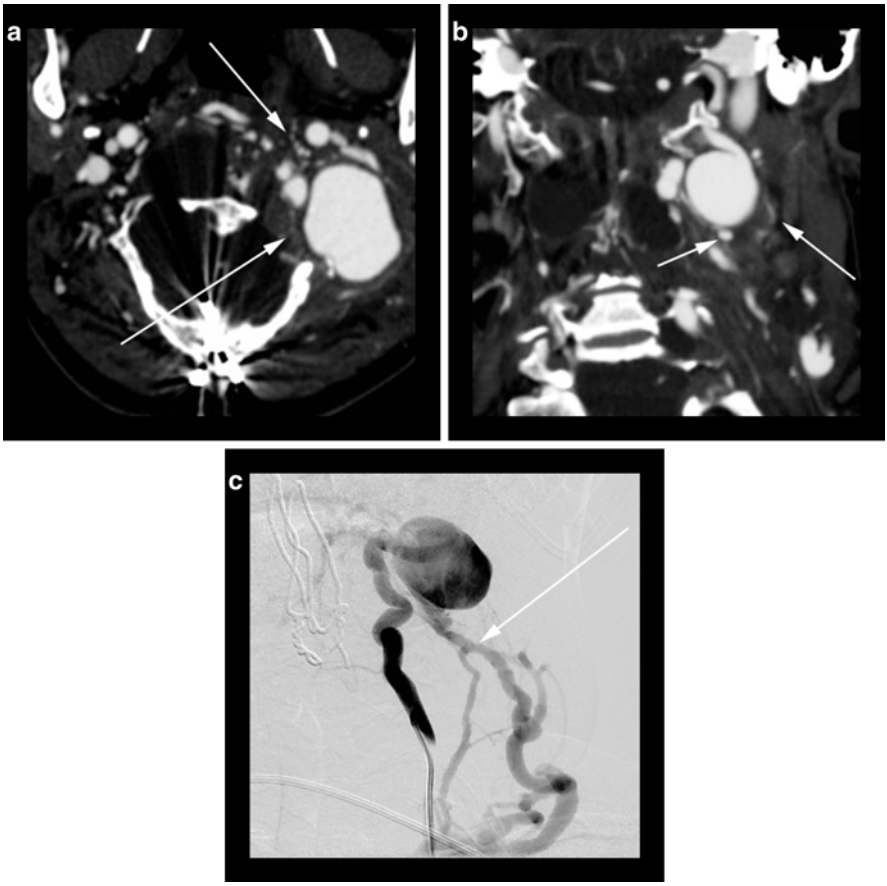

Fig. 16 Adult patient with neurofibromatosis type I presented with rapid onset of neck paid. (**a**) Axial CTA image shows a giant aneurysm (*bottom arrow*) arising from the left vertebral artery with arterialization of surrounding small venous structures (*top arrow*). Surgical changes related to prior craniocervical junction decompression are also noted. (**b**) Coronal CTA image displays the relationship of the aneurysm (*right arrow*) to surrounding structures (*left arrow*). (**c**) Oblique projection DSA image with injection of the left vertebral artery shows opacification of the venous structures (arrow) surrounding the giant aneurysm

procedure carrying up to a 1–2 % risk of neurologic deficits; however, CTA is easily performed in the emergency setting following an initial noncontrast head CT [46, 47]. Furthermore, CTA has been shown to appropriately describe key characteristics such as lobularity, the size of dome and neck, and the relationship with adjacent arterial branches, therefore assisting in selection of treatment (surgical clipping versus endovascular therapy) [46, 48] (Figs. 16 and 17).

Areas of concern in performing carotid CTA for aneurysm assessment include technical factors, such as venous contamination and improper bolus tracing, which may impede the evaluation of small aneurysms thereby decreasing the sensitivity

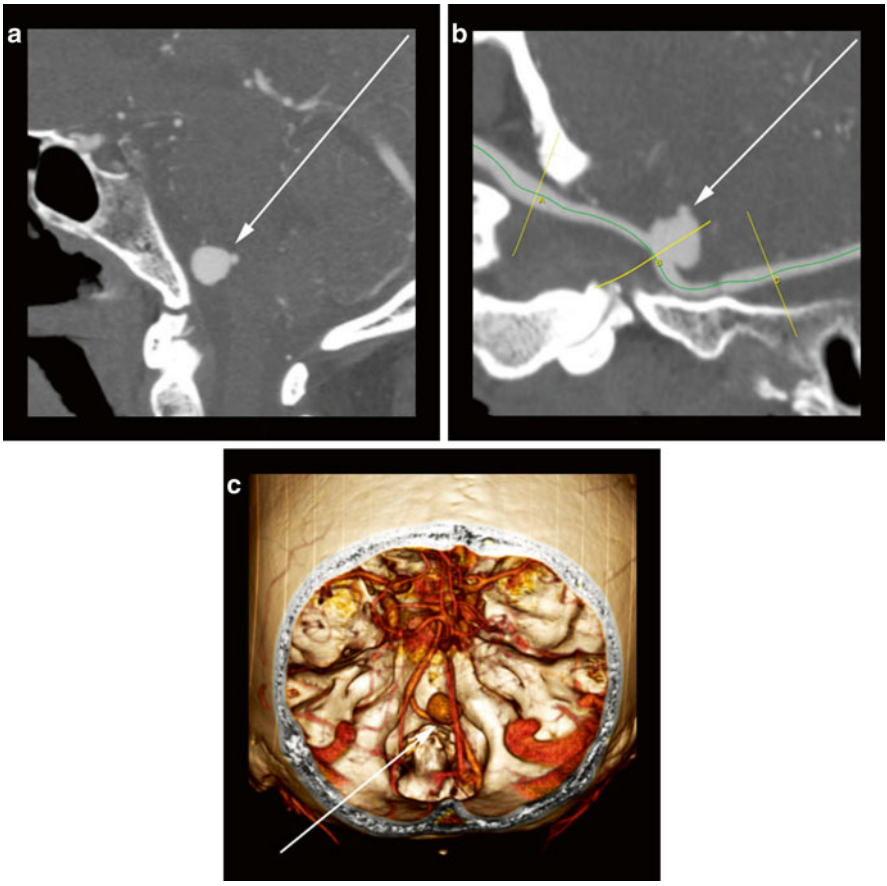

Fig. 17 91-year-old male with V4 segment vertebral artery aneurysm. (**a**) Sagittal CTA image reveals an irregularly shaped aneurysm in the region of the right vertebral artery with focal outpouching "nipple" (*arrow*) off of the posterior aspect. (**b**) A stretched curved MPR CTA reformat better depicts the orientation of the aneurysm (*arrow*) to the parent vessel. (**c**) Posterior oblique 3D volume rendering of the CTA data provides another assessment of the aneurysm orientation (arrow) to the parent vessel and surrounding bones

of CTA. However, modern post-processing software including volume-rendering techniques, maximum intensity projections and multiplanar reconstruction has further enhanced interpretation of CT angiographic data, even in aneurysms <3 mm in size [49, 50].

Due to its lower spatial resolution, CTA may have limited utility in the evaluation of small (less than 2 mm) supraclinoid ICA blood-blister aneurysms. Blister aneurysms are wide-neck shallow aneurysms which lack the outer layer of intima media, while still retaining the adventitial layer covered by thin fibrous tissue, differentiating

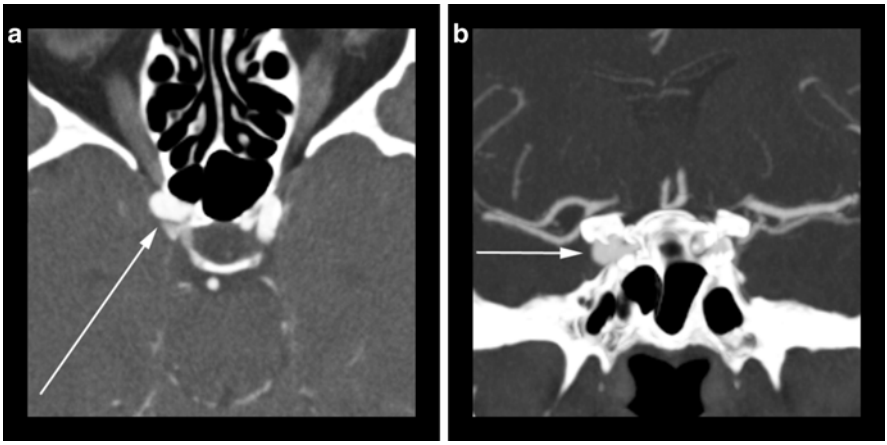

Fig. 18 55-year-old male presenting with stroke-like symptoms. (**a**) Axial CTA image reveals abnormal dilatation (*arrow*) of the cavernous segment of the right internal carotid artery. (**b**) A coronal CTA MIP image better displays the aneurysm (*arrow*) of the cavernous segment of the right internal carotid artery

them from "classic" saccular aneurysms. They occur at nonbranching sites of the supraclinoid ICA, most commonly at the superior/dorsal aspect of the greater curvature, with a distinctive broad-based triangular shape on imaging studies. Furthermore, while rare—constituting only 0.5–2 % of all ruptured intracranial aneurysms—blister aneurysms have a propensity for re-bleeding and rapid enlargement with progression to a saccular shape; and if left untreated, they frequently portend a dismal clinical outcome. Therefore, in the setting of acute SAH with negative CTA findings, DSA may be performed to exclude a blister aneurysm [46, 51, 52].

Other interesting entities include large and giant aneurysms of the cavernous, ophthalmic, and hypophyseal segments of the ICA, which frequently present with signs and symptoms of mass effect on surrounding structures. Ophthalmic and hypophyseal ICA aneurysms tend to cause compression of the optic nerve, resulting in visual field deficits and decreased visual acuity. Due to their intradural location, prompt treatment with therapeutic ipsilateral ICA occlusion, stent-assisted coil embolization or flow-diverting stent placement is indicated to prevent rupture and ensuing SAH [53] (Fig. 10). Cavernous carotid aneurysms represent 3–5 % of all intracranial aneurysms and frequently present as opthalmoplegia or facial numbness due to cranial nerve palsy (CN III, IV, V, and VI). Being extradural, cavernous carotid aneurysms are a rare cause of SAH, with spontaneous intramural thrombosis eventually developing in 13–20 % (Fig. 18). Rarely, this may lead to thrombosis of the ipsilateral proximal ICA, therefore eliminating the feeding vessel and enabling conservative treatment [54, 55]. A potential complication of a ruptured cavernous ICA aneurysm is the formation of a direct, high-flow cavernous-carotid fistula.

Aneurysms of the extracranial portion of the ICA are rare, representing only 0.5–1.9 % of all carotid surgical interventions and have been associated with Neurofibromatosis type 1 vasculopathy. Prior to diagnosis, extracranial ICA aneurysms tend to enlarge to giant sizes and present with palpable neck mass, pain, dysphagia, hoarseness, and Horner's syndrome. Prompt surgical intervention, with therapeutic occlusion of the feeding artery is standard of care [56]

Dissection

Carotid artery dissection may lead to stroke, pseudoaneurysm formation, and potentially Horner's syndrome by disrupting the cervical sympathetic chain. Other signs and symptoms of dissection are variable depending of the location of vessel injury, but may include headache or neck pain. Etiologies of carotid dissection include trauma and spontaneous dissection. Spontaneous dissection is more commonly seen in patients with underlying arteriopathy such as fibromuscular dysplasia (FMD) [57]. Dissection has been shown to be the etiology of 10–25 % of strokes in young and middle-aged patients, and should be considered in such patients who present with stroke in the absence of traditional risk factors [58].

Dissection of the carotid arteries can be evaluated with carotid CTA. In patients with dissection, blood traveling between the vessel intima and media allows for the creation of a false lumen, which can be visualized as a flap within an opacified vessel. However, thrombosis of the false lumen may prevent passage of contrast, precluding visualization of the intimal flap. A clue to the presence of carotid artery dissection in the presence of a thrombosed false lumen may be focal smooth luminal narrowing with expansion of the cross-sectional area of the artery (Fig. 19).

Pseudoaneurysm

A potential complication of blunt craniocervical trauma is the development of carotid artery pseudoaneurysm, or accumulation of blood within the subadventitial layer of the vessel. The most common locations of blunt carotid arterial injuries include the cervical ICA immediately proximal to the base of the skull, as well as the petrous and cavernous segments (Fig. 19). The accepted mechanism of injury to the carotid artery is hyperextension or rotation over the transverse processes of C1 and C2, leading to overstretching of the vascular wall and subsequent traumatic injury [59]. Even though the incidence of blunt carotid and vertebral arterial injury in multiple trauma victims is very low, with carotid dissections occurring in only up to 1.6 % of patients, they are associated with a high morbidity and mortality rate, with an overall stroke rate of 21–64 % [60, 61]. These injuries are usually asymptomatic on presentation, with a delayed onset of neurological symptoms/stroke

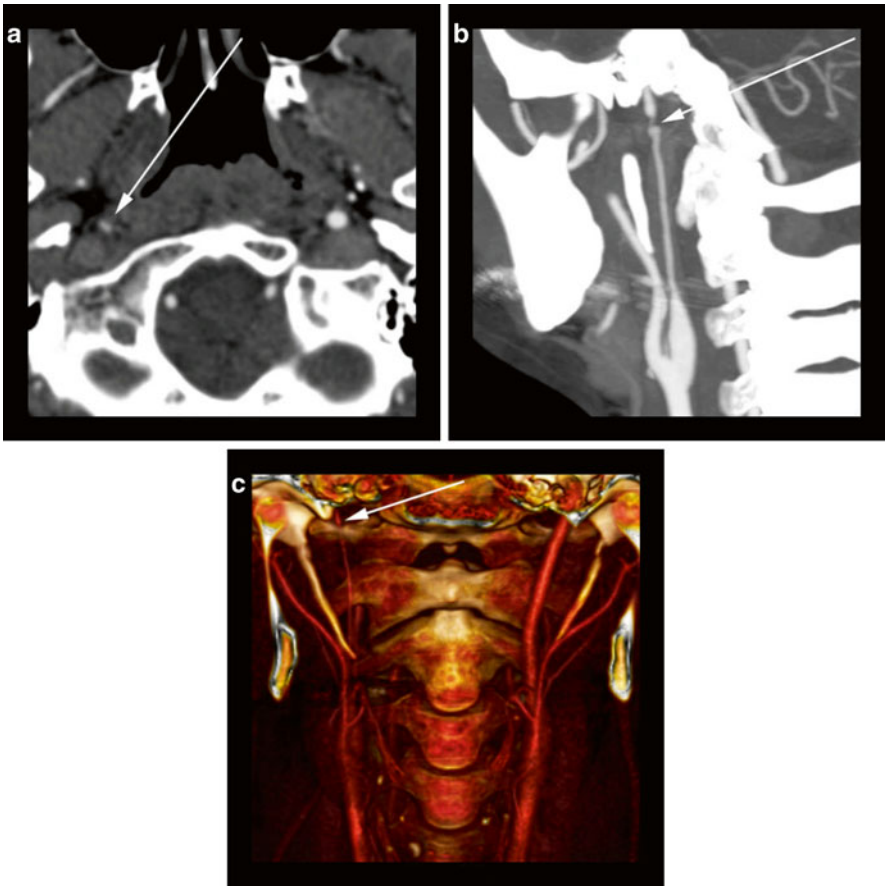

Fig. 19 34-year-old female presenting with acute onset of neck pain after motor vehicle accident. (**a**) Axial CTA image reveals abnormal diminutive caliber (*arrow*) of the right distal cervical internal carotid artery as well as a small focal irregularity suggestive of dissection with small pseudoaneurysm formation. (**b**) An oblique coronal CTA MIP image better depicts the long segment attenuation of the cervical internal carotid artery as well as the focal luminal abnormality (*arrow*) associated with a severe focal stenosis. (**c**) A 3D volume rendering of the CTA data also displays the dissection flap (*arrow*) but fine vessel detail is lost due similar density structures along the path of the vessel which is a potential pitfall of VR reconstructions

usually 10–72 h following injury. Since immediate administration of systemic anticoagulation therapy followed by endovascular and/or surgical repair can dramatically reduce the rate of ischemic neurological events, prompt evaluation and early diagnosis is crucial [62–64].

Blunt injuries of the carotid arteries are identified as vessel wall abnormalities on CTA, including intimal injury manifested by intimal irregularity, dissection with raised intimal flap or intramural hematoma, pseudoaneurysm, vessel occlusion/

thrombosis, and transection with active hemorrhage [63]. Pseudoanurysms are classified as Grade 3 carotid injuries according to the Denver Criteria, with a 26 % risk of embolic stroke in untreated cases. On CTA, they are classically seen as contrast-filled outpouchings/ballooning contained within the arterial wall.

Craniocervical CTA has emerged as the standard screening technique in evaluating patients with blunt trauma to the carotid arteries allowing for quick and noninvasive 3D visualization of suspected injuries. Volumetric data acquisition and modern post-processing techniques allow for creation of 2D and 3D images in various planes using MIPs, which has been shown to increase the accuracy of CTA for detecting vascular injuries in trauma victims [63]. Various factors can lead to suboptimal or nondiagnostic CTAs in the setting of trauma, including technical factors: beam hardening artifact due to dense intravenous contrast in the veins, poor contrast opacification of the arteries and motion artifact, as well as patient-related limitations such as streak artifact from metallic foreign bodies/bullet fragments, dental amalgam, and spinal hardware.

Since the majority of blunt trauma victims undergo whole body CT as part of their work-up, craniocervical CTA can easily be integrated into the initial imaging protocol. The high accuracy of CTA in detecting clinically relevant craniocervial vascular injuries approaches that of intra-arterial digital subtraction angiography (DSA) with sensitivity and specificity for detection of blunt neck vascular injury reported at 100 % [62]. Furthermore, CTA has the clear advantages of being readily available in most emergency departments, ease of performance (noninvasive, and non-operator dependent), the ability to detect other associated injuries, and a minimal complication rate. DSA should be performed as a follow-up imaging examination in patients with equivocal or nondiagnostic CTA results, normal CTA in symptomatic patients with signs of vascular injury, as well as for endovascular treatment of blunt carotid injury [65].

Vasculopathy

Vasculitis involving the carotid arteries including Takayasu and giant cell arteritis can lead to vessel wall thickening, luminal stenosis, occlusion, and aneurysm formation which can be assessed by carotid CTA [66]. Other inflammatory processes can also affect the carotid arteries including carotidynia, which is an idiopathic inflammatory process of the carotid bifurcation with characteristic radiographic findings [67].

Noninflammatory vasculopathies, including fibromuscular dysplasia (FMD), are well evaluated by carotid CTA. FMD affects medium-sized vessels and shows a female-bias affecting mostly patients 20–60 years of age. The carotid arteries are the second most commonly involved vessels in FMD, following the renal arteries [68]. Representing 85 % of all FMD cases, type II involves the vessel media and is characterized by a “string of beads” appearance. Type II FMD is also associated with aneurysm formation (Fig. 20).

Fig. 20 An oblique sagittal CTA MIP image reveals irregularity (*arrow*) of the left cervical internal carotid artery in a pattern consistent with fibromuscular dysplasia

Conclusion

Noninvasive carotid artery assessment has drastically improved in recent years. The combined use of carotid CTA with either MRA or ultrasound has almost completely replaced DSA in the evaluation of both extracranial and intracranial carotid artery disease as well as for evaluation of the posterior circulation. With careful multimodality evaluation and avoidance of the above-described imaging pitfalls, appropriate patient triage, and treatment recommendations can be performed in a cost-efficient and noninvasive manner. Future advances in neurovascular imaging will bring improved resolution for evaluation of smaller and distal intracranial vessels, improved speed, motion correction, and reduced contrast for CTA techniques. These improvements will aid in the noninvasive triage of patients towards appropriate treatment paradigms for cerebrovascular disease in the outpatient and in the emergency setting.

References

1. Mathews TJ et al. Annual summary of vital statistics: 2008. Pediatrics. 2011;127(1):146–57.
2. Schellinger PD, Fiebach JB, Hacke W. Imaging-based decision making in thrombolytic therapy for ischemic stroke: present status. Stroke. 2003;34(2):575–83.
3. Truwit CL. CT angiography versus MR angiography in the evaluation of acute neurovascular disease. Radiology. 2007;245(2):362–6. discussion 366.
4. Poisson SN et al. Intracranial large vessel occlusion as a predictor of decline in functional status after transient ischemic attack. Stroke. 2011;42(1):44–7.
5. Johnson JM, MeaderA, Hunt DT. Pearls and pitfalls of noninvasive carotid imaging. In: Abbara S, Kalva S editors. Vascular imaging pearls and pitfalls. Springer USA (NY) 2012.

6. Mahesh M. Search for isotropic resolution in CT from conventional through multiple-row detector. Radiographics. 2002;22(4):949–62.
7. Irace C et al. Arterial remodeling of the common carotid artery after aortic valve replacement in patients with aortic stenosis. Stroke. 2002;33(10):2446–50.
8. Shrier DA et al. CT angiography in the evaluation of acute stroke. AJNR Am J Neuroradiol. 1997;18(6):1011–20.
9. Fox AJ et al. Identification, prognosis, and management of patients with carotid artery near occlusion. AJNR Am J Neuroradiol. 2005;26(8):2086–94.
10. Cochran ST, Bomyea K, Sayre JW. Trends in adverse events after IV administration of contrast media. AJR Am J Roentgenol. 2001;176(6):1385–8.
11. Nagahata M et al. Bolus injection of contrast agents with various iodine concentrations and delivery rates for intracranial three-dimensional CT angiography: evaluation of intracranial arteriovenous contrast using a multidetector-row CT scanner. Radiat Med. 2008;26(8):494–8.
12. Claves JL et al. Evaluation of contrast densities in the diagnosis of carotid stenosis by CT angiography. AJR Am J Roentgenol. 1997;169(2):569–73.
13. Rubin GD et al. Multi-detector row CT angiography of lower extremity arterial inflow and runoff: initial experience. Radiology. 2001;221(1):146–58.
14. Bartlett ES et al. Diagnosing carotid stenosis near-occlusion by using CT angiography. AJNR Am J Neuroradiol. 2006;27(3):632–7.
15. Schramm P et al. Comparison of CT and CT angiography source images with diffusion-weighted imaging in patients with acute stroke within 6 hours after onset. Stroke. 2002;33(10): 2426–32.
16. Lima FO et al. The pattern of leptomeningeal collaterals on CT angiography is a strong predictor of long-term functional outcome in stroke patients with large vessel intracranial occlusion. Stroke. 2010;41(10):2316–22.
17. Johnson JM et al. Quality of extracranial carotid evaluation with 256-section CT. AJNR Am J Neuroradiol. 2013;34(8):1626–31.
18. Johnson TR et al. Material differentiation by dual energy CT: initial experience. Eur Radiol. 2007;17(6):1510–7.
19. Alvarez RE, Macovski A. Energy-selective reconstructions in X-ray computerized tomography. Phys Med Biol. 1976;21(5):733–44.
20. Liu X et al. Quantitative imaging of element composition and mass fraction using dual-energy CT: three-material decomposition. Med Phys. 2009;36(5):1602–9.
21. Kang MJ et al. Dual-energy CT: clinical applications in various pulmonary diseases. Radiographics. 2010;30(3):685–98.
22. Korn A et al. Dual energy CTA of the carotid bifurcation: advantage of plaque subtraction for assessment of grade of the stenosis and morphology. Eur J Radiol. 2011;80(2):e120–5.
23. Sparacia G et al. Imaging processing for CT angiography of the cervicocranial arteries: evaluation of reformatting technique. Radiol Med. 2007;112(2):224–38.
24. Ota H et al. Quantitative vascular measurements in arterial occlusive disease. Radiographics. 2005;25(5):1141–58.
25. Schauer DA, Linton OW. NCRP Report No. 160, ionizing radiation exposure of the population of the United States, medical exposure–are we doing less with more, and is there a role for health physicists? Health Phys. 2009;97(1):1–5.
26. Singh S et al. Radiation dose optimization and thoracic computed tomography. Radiol Clin North Am. 2014;52(1):1–15.
27. Bahner ML et al. Improved vascular opacification in cerebral computed tomography angiography with 80 kVp. Invest Radiol. 2005;40(4):229–34.
28. Morcos SK. Review article: acute serious and fatal reactions to contrast media: our current understanding. Br J Radiol. 2005;78(932):686–93.
29. Singh J, Daftary A. Iodinated contrast media and their adverse reactions. J Nucl Med Technol. 2008;36(2):69–74. quiz 76-7.
30. American College of Radiology. ACR manual on contrast media. Reston, VA: ACR; 2013.

31. Bae KT, Tran HQ, Heiken JP. Multiphasic injection method for uniform prolonged vascular enhancement at CT angiography: pharmacokinetic analysis and experimental porcine model. Radiology. 2000;216(3):872–80.
32. Osborn AG, Jacobs JM, Osborn AG. Diagnostic cerebral angiography. 2nd ed. Philadelphia, PA: Lippincott-Raven; 1999. p. 462.
33. Motomiya M, Karino T. Flow patterns in the human carotid artery bifurcation. Stroke. 1984;15(1):50–6.
34. Rothwell PM, Gibson R, Warlow CP. Interrelation between plaque surface morphology and degree of stenosis on carotid angiograms and the risk of ischemic stroke in patients with symptomatic carotid stenosis. On behalf of the European Carotid Surgery Trialists' Collaborative Group. Stroke. 2000;31(3):615–21.
35. North American Symptomatic Carotid Endarterectomy Trial Collaborators. Beneficial effect of carotid endarterectomy in symptomatic patients with high-grade carotid stenosis. N Engl J Med. 1991;325(7):445–53.
36. Bartlett ES et al. Quantification of carotid stenosis on CT angiography. AJNR Am J Neuroradiol. 2006;27(1):13–9.
37. Hobson 2nd RW. Update on the Carotid Revascularization Endarterectomy versus Stent Trial (CREST) protocol. J Am Coll Surg. 2002;194(1 Suppl):S9–14.
38. Wyers MC et al. The value of 3D-CT angiographic assessment prior to carotid stenting. J Vasc Surg. 2009;49(3):614–22.
39. Romero JM et al. Vasa vasorum enhancement on computerized tomographic angiography correlates with symptomatic patients with 50 % to 70 % carotid artery stenosis. Stroke. 2013;44(12):3344–9.
40. Lev MH et al. CT angiography in the rapid triage of patients with hyperacute stroke to intraarterial thrombolysis: accuracy in the detection of large vessel thrombus. J Comput Assist Tomogr. 2001;25(4):520–8.
41. Koelemay MJ et al. Systematic review of computed tomographic angiography for assessment of carotid artery disease. Stroke. 2004;35(10):2306–12.
42. Jaff MR et al. Imaging of the carotid arteries: the role of duplex ultrasonography, magnetic resonance arteriography, and computerized tomographic arteriography. Vasc Med. 2008; 13(4):281–92.
43. Link J et al. Spiral CT angiography and selective digital subtraction angiography of internal carotid artery stenosis. AJNR Am J Neuroradiol. 1996;17(1):89–94.
44. Berg M et al. Multi-detector row CT angiography in the assessment of carotid artery disease in symptomatic patients: comparison with rotational angiography and digital subtraction angiography. AJNR Am J Neuroradiol. 2005;26(5):1022–34.
45. Lettau M et al. Carotid artery stents: in vitro comparison of different stent designs and sizes using CT angiography and contrast-enhanced MR angiography at 1.5 T and 3 T. AJNR Am J Neuroradiol. 2009;30(10):1993–7.
46. Yoon DY et al. Detection and characterization of intracranial aneurysms with 16-channel multidetector row CT angiography: a prospective comparison of volume-rendered images and digital subtraction angiography. AJNR Am J Neuroradiol. 2007;28(1):60–7.
47. McKinney AM et al. Detection of aneurysms by 64-section multidetector CT angiography in patients acutely suspected of having an intracranial aneurysm and comparison with digital subtraction and 3D rotational angiography. AJNR Am J Neuroradiol. 2008;29(3):594–602.
48. Franklin B et al. Diagnostic accuracy and inter-rater reliability of 64-multislice 3D-CTA compared to intra-arterial DSA for intracranial aneurysms. J Clin Neurosci. 2010;17(5):579–83.
49. Lubicz B et al. Sixty-four-row multisection CT angiography for detection and evaluation of ruptured intracranial aneurysms: interobserver and intertechnique reproducibility. AJNR Am J Neuroradiol. 2007;28(10):1949–55.
50. Jehle D et al. Case series of 64 slice computed tomography-computed tomographic angiography with 3D reconstruction to diagnose symptomatic cerebral aneurysms: new standard of care? Neurol Int. 2012;4(1), e2.

51. Uysal E et al. Detection and evaluation of intracranial aneurysms with 16-row multislice CT angiography: comparison with conventional angiography. Emerg Radiol. 2008;15(5):311–6.
52. Gaughen Jr JR et al. Utility of CT angiography in the identification and characterization of supraclinoid internal carotid artery blister aneurysms. AJNR Am J Neuroradiol. 2010;31(4):640–4.
53. Gonzalez AM et al. Blood blister-like aneurysms: single center experience and systematic literature review. Eur J Radiol. 2014;83(1):197–205.
54. Sastri SB, Sadasiva N, Pandey P. Giant cavernous carotid aneurysm with spontaneous ipsilateral ICA occlusion: report of 2 cases and review of literature. J Neurosci Rural Pract. 2013;4 Suppl 1:S113–6.
55. van Rooij WJ, Sluzewski M. Unruptured large and giant carotid artery aneurysms presenting with cranial nerve palsy: comparison of clinical recovery after selective aneurysm coiling and therapeutic carotid artery occlusion. AJNR Am J Neuroradiol. 2008;29(5):997–1002.
56. Moratti C, Andersson T. Giant extracranial aneurysm of the internal carotid artery in neurofibromatosis type 1. A case report and review of the literature. Interv Neuroradiol. 2012;18(3):341–7.
57. Slovut DP, Olin JW. Fibromuscular dysplasia. N Engl J Med. 2004;350(18):1862–71.
58. Vertinsky AT et al. Comparison of multidetector CT angiography and MR imaging of cervical artery dissection. AJNR Am J Neuroradiol. 2008;29(9):1753–60.
59. Liang T et al. Review of multidetector computed tomography angiography as a screening modality in the assessment of blunt vascular neck injuries. Can Assoc Radiol J. 2013; 64(2):130–9.
60. Biffl WL et al. Blunt carotid arterial injuries: implications of a new grading scale. J Trauma. 1999;47(5):845–53.
61. Burlew CC, Biffl WL. Imaging for blunt carotid and vertebral artery injuries. Surg Clin North Am. 2011;91(1):217–31.
62. Langner S et al. Whole-body CT trauma imaging with adapted and optimized CT angiography of the craniocervical vessels: do we need an extra screening examination? AJNR Am J Neuroradiol. 2008;29(10):1902–7.
63. Liang T et al. Imaging of blunt vascular neck injuries: a clinical perspective. AJR Am J Roentgenol. 2013;201(4):893–901.
64. Liang T et al. Imaging of blunt vascular neck injuries: a review of screening and imaging modalities. AJR Am J Roentgenol. 2013;201(4):884–92.
65. Roberts DJ et al. Diagnostic accuracy of computed tomographic angiography for blunt cerebrovascular injury detection in trauma patients: a systematic review and meta-analysis. Ann Surg. 2013;257(4):621–32.
66. Maksimowicz-McKinnon K, Clark TM, Hoffman GS. Takayasu arteritis and giant cell arteritis: a spectrum within the same disease? Medicine (Baltimore). 2009;88(4):221–6.
67. Comacchio F et al. Carotidynia: new aspects of a controversial entity. Acta Otorhinolaryngol Ital. 2012;32(4):266–9.
68. Plouin PF et al. Fibromuscular dysplasia. Orphanet J Rare Dis. 2007;2:28.

CT Imaging of Intracranial Vessels

Sandra A. Cornelissen, Marco Das, and Alida A. Postma

Abbreviations

4D-CTA	Dynamic time-resolved CTA
ACA	Anterior cerebral artery
Acom	Anterior communicating artery
BA	Basilar artery
CECT	Contrast-enhanced CT
CTA	CT angiography
CTV	CT venography
DSA	Digital subtraction angiography
DWI	Diffusion-weighted imaging
ICA	Internal carotid artery
MCA	Middle cerebral artery
MDCT	Multidetector CT
MIP	Maximum intensity projection
MPR	Multiplanar reformations
MRA	MR angiography
NECT	Non-contrast-enhanced CT
PCA	Posterior cerebral artery
Pcom	Posterior communicating artery
RCVS	Reversible cerebral vasoconstriction syndrome
TCD	Transcranial Doppler
VA	Vertebral artery
VPCT	Volume perfusion CT
VR	Volume rendering

S.A. Cornelissen, M.D., Ph.D. • M. Das, M.D., Ph.D. • A.A. Postma, M.D., Ph.D. (✉)
Department of Radiology, MUMC+, Maastricht, The Netherlands
e-mail: l.jacobi@mumc.nl

R. Trivedi et al. (eds.), *3D Imaging Technologies in Atherosclerosis*,
DOI 10.1007/978-1-4899-7618-5_4

Table 1 Indications for CT of the intracranial vessels with recommended protocol

	NECT	CTA	CTV	4D-CTA	VPCT
Stroke	x	x		(x)	x
Hemorrhagic stroke	x	x	(x)	(x)	(x)
AVM		x		x	
Fistula		x		x	
Aneurysms		x			
Venous thrombosis	x		x		
Moyamoya	x	x		(x)	(x)
Vasculitis	x	x			
RCVS	x	x			
Brain death	x	x[a]	x[a]		

[a]Adjusted timing to local guidelines and rules

In the last 20 years, CT evolved from single-slice scanning towards multidetector-row CT (MDCT). Technical advances in MDCT have increasingly improved spatial and temporal resolution. Fast volume coverage within a few seconds has nowadays become possible, e.g., allowing vessel imaging of the whole body. CT angiography (CTA) has become a valuable noninvasive alternative to cerebral digital subtraction angiography (DSA) for diagnosing pathology of intracranial vessels [1] (Table 1).

Because acquired MDCT data are nowadays nearly isotropic, various image post-processing techniques can be applied. CTA data can be viewed in arbitrary directions without loss of image quality, maximum intensity projections (MIP) can be interactively calculated, and 3D visualizations of the vascular tree can be constructed. For detection of intracranial aneurysms, CTA has largely replaced DSA as the first-line imaging modality [1]. MRA techniques are also used for screening on vessel pathology; however, CTA with its higher spatial resolution and better availability is often used for detailed imaging and treatment planning. New applications like dynamic CTA and dual-energy CT (DECT) are emerging and are more and more used in daily practice.

This chapter aims to give an update on state-of-the-art CT imaging of intracranial vessels.

The anatomy of the intracranial vessels and some anatomical variations are described first. This is followed by technical aspects of CT imaging of the intracranial vessels. Finally, indications and protocols for imaging the intracranial vasculature are described.

Anatomy of the Intracranial Vessels

Brain tissue has a high oxygen demand and has hardly any capabilities of anaerobic metabolism, which makes it totally dependent on oxygen and nutrients supplied via the circulating blood [2]. Total disruption of blood flow to the brain causes unconsciousness within 5–10 s. The brain is supplied by both the carotid

Fig. 1 Anatomy of the internal carotid artery. Lateral projection of angiographic image during selective contrast injection in the right internal carotid artery. The C2–C4 segments are pointed out

arteries and the vertebral arteries. The carotid arteries arise from the aortic arch and the brachiocephalic trunk and the vertebral arteries originate from the subclavian arteries. The carotid and vertebrobasilar system are connected to each other via the circle of Willis.

Carotid Arteries

The internal carotid artery (ICA) enters the mastoid bone through the carotid canal. The vessel ascends in vertical direction, followed by a horizontal course (vertical and horizontal petrous (C2) segment) and then runs anterior to the tympanic cavity. The ICA is separated from the tympanic cavity by a 0.5 mm thick bony plate. It traverses the foramen lacerum of the sphenoid bone to enter the middle cranial fossa (C3 segment). Then the ICA traverses the cavernous sinus (C4 segment), after which it perforates the dura near the clinoid process (Fig. 1).

Some variations of the ICA should be recognized because they can influence surgical or interventional procedures [3]. An aberrant course of the ICA through the middle ear [4] should be recognized to prevent complications in middle ear surgery. Another aberrant course of the ICA is the lateral pharyngeal ICA (Fig. 2) in which the internal carotid arteries are elongated and course partially in the midline just posterior to the pharyngeal wall.

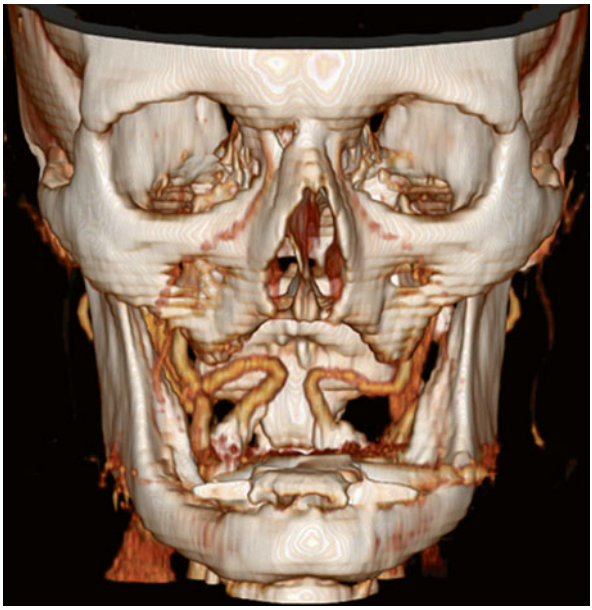

Fig. 2 Seventy-eight y/o old male, presenting with TIAs in the left hemisphere. CTA shows bilateral high-grade carotid stenosis with calcification and medialization of the internal carotid arteries: kissing carotids

Circle of Willis and Its Variations

The circle of Willis provides a potential source of collateral blood flow between the carotid and the vertebrobasilar circulation in case of occlusive vascular disease. The anatomy of the circle of Willis is illustrated in Fig. 3. The ICA bifurcates into the middle cerebral artery (MCA) and the first segment of the anterior cerebral artery (ACA), also called the A1 segment. The bilateral A1 segments are connected to each other by the anterior communicating artery (Acom), after which they give rise to the A2 segments which course anteriorly. Some millimeters caudal from the top of the ICA the posterior communicating artery (Pcom) originates from the ICA and courses posteriorly to join the P1 segment of the posterior cerebral artery (PCA), which originates from the basilar artery. The circle of Willis is highly variable [5, 6] and is complete in only 20–25 % of people [7]. When incomplete, there is a potential risk of insufficient collateral blood flow in case of large vessel occlusion.

Figure 4 illustrates a well-known variant, a hypoplastic left A1 segment with filling of the left A2 via the Acom.

Most variations in the circle of Willis occur at the location of the Pcom; a complete posterior part of the circle is only present in 31 % of people [6]. Absence or hypoplasia of the Pcom is often seen. Another variant is the fetal PCA or fetal configuration of the PCA, in which the Pcom has the same caliber as the PCA and is combined with a hypoplastic P1 segment (Fig. 5) [8]. In these patients collateral blood flow to the PCA territory from the vertebrobasilar system in case of carotid occlusion is diminished or absent. This variant is even more important when combined with an ipsilateral absent A1 segment.

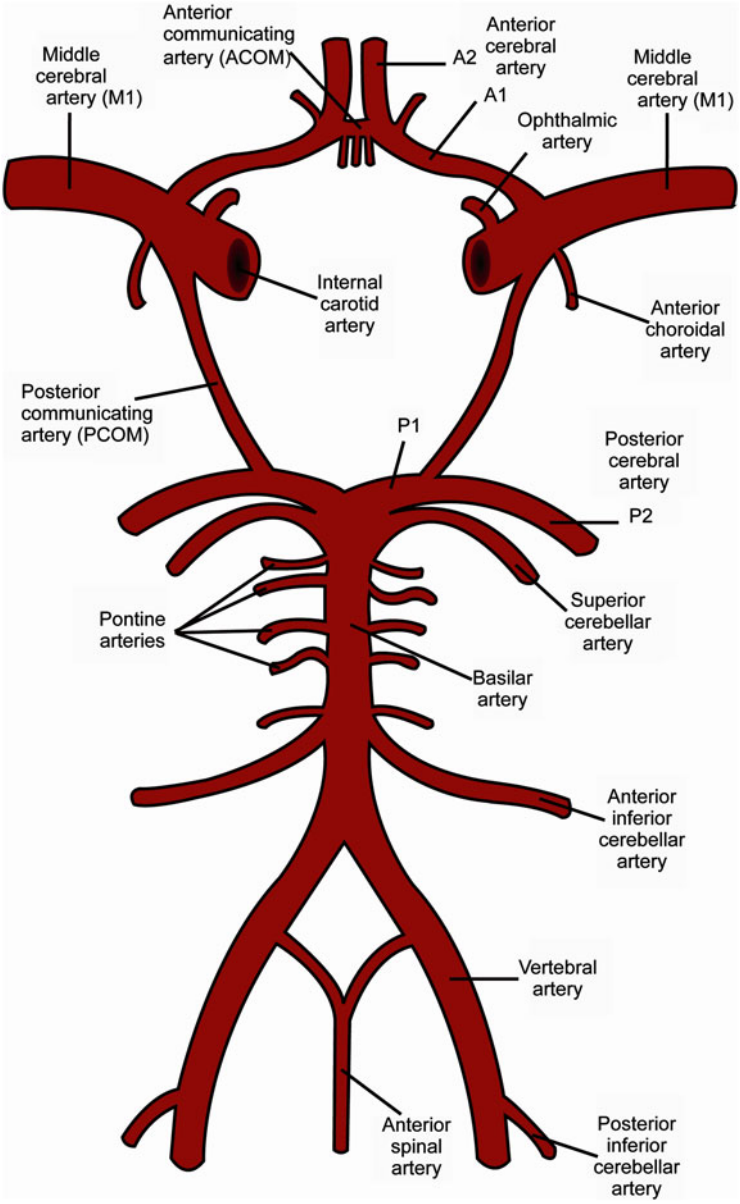

Fig. 3 Anatomy of the circle of Willis

Another frequently encountered variation is the presence of an infundibulum of the Pcom. An infundibulum is a widening of the ICA located exactly at the origin of the Pcom. It is symmetric and should be smaller than 2 mm, and the Pcom originates from its apex. This variant should be distinguished from an aneurysm.

Normally two anterior cerebral arteries are present, one for each hemisphere. In case of an azygos anterior cerebral artery the ACA territories of both hemispheres

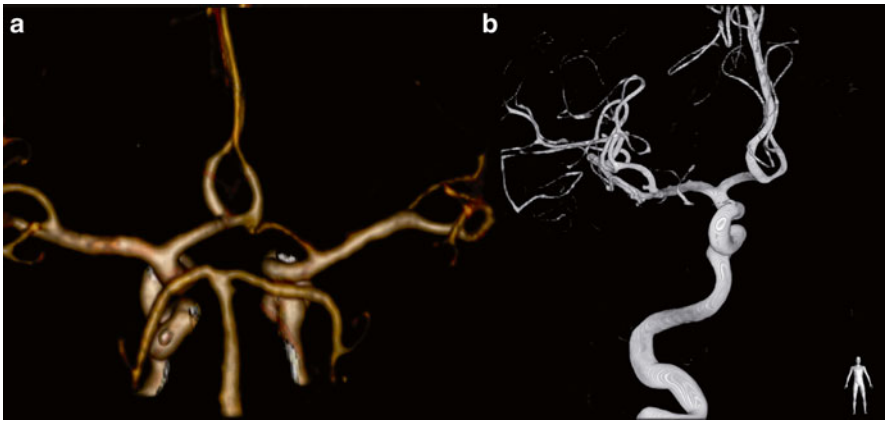

Fig. 4 Fifty-six y/o female presented with subarachnoid hemorrhage. No aneurysms were found at CTA and DSA. CTA (**a**) demonstrates a hypoplastic left A1 segment, the Acom is demonstrated, suggesting that the left A2 is (partially) supplied via the Acom. DSA (**b**) demonstrates filling of the left A2 segment after contrast administration of the right carotid artery

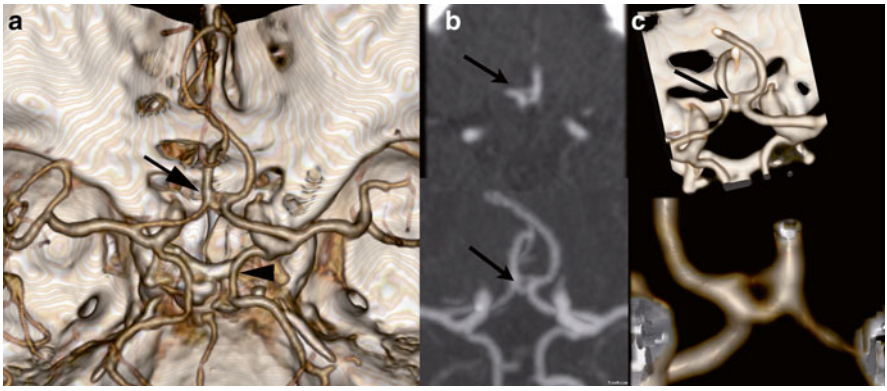

Fig. 5 An 80 y/o male presented with ischemic stroke in the left hemisphere. No occlusions were found at CTA. Two normal variants were present. The fenestration of the Acom (*arrows*) is demonstrated at CTA of the circle of Willis (**a**), at the CTA source images (**b**), MIP reconstructions (**c**), and detailed volume rendering without (**d**) and with bone removal (**e**). The *arrowhead* points out bilateral fetal configuration of posterior cerebral artery (**a**)

are supplied by a single midline A2 segment (Fig. 6), which is rare and has a prevalence of 0.2–4.0 %. It is associated with aneurysms.

In case of a trifurcated ACA, the Acom gives rise to three anterior cerebral arteries, one of which probably is a persisting median callosal artery (Fig. 7). A bihemispheric ACA represents hypoplasia of one A2 segment, which only supplies the callosomarginal arteries. The contralateral A2 segment then provides the major arterial supply of the ACA territories bilaterally. A more rare persisting prim-

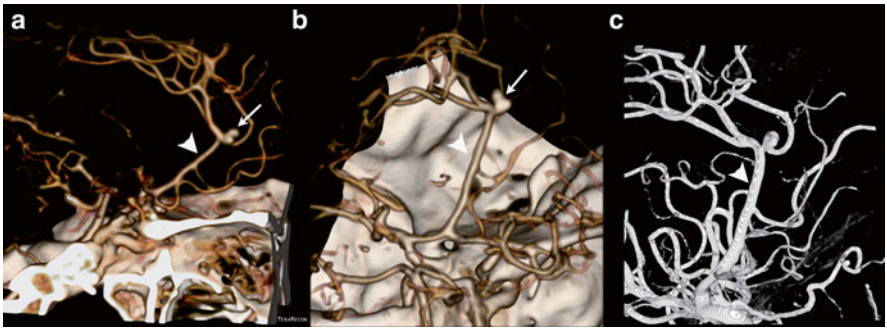

Fig. 6 A 50 y/o male presented with a subarachnoid hemorrhage, due to a pericallosal aneurysm (*arrow*). As coincidental normal variant an azygos configuration of the anterior cerebral artery was present. The pericallosal aneurysm was treated by surgical clipping. Lateral (**a**) and superior oblique (**b**) view of volume-rendered CTA demonstrates the azygos configuration (*arrowheads*). The *arrow* points to the bilobar pericallosal aneurysm. These findings were confirmed at DSA (**c**)

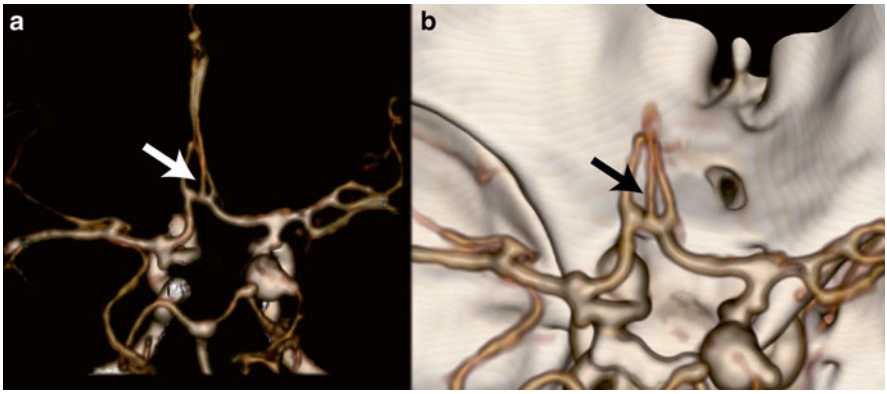

Fig. 7 A 32 y/o female presented with a subarachnoid hemorrhage, based on a posterior communicating aneurysm. A persistent median artery as coincidental finding is shown at VR CTA (*arrows*)

itive olfactory artery [8] is illustrated in Fig. 8. Most ACA anomalies have a higher prevalence of aneurysms [9, 10].

The anterior part of the circle of Willis can also be incomplete. The Acom can be hypoplastic or absent. A hypoplastic A1 segment has a prevalence of 14 %, whereas the absence of an A1 segment has a prevalence of 2 % [6]. In a fenestration the arterial lumen divides into separate lumens that converge. In case of the basilar artery this represents a persisting non-fusion of two longitudinal neural arteries [9]. Fenestrations increase the incidence of aneurysms, probably because turbulent flow is created in the proximal and distal end of the fenestration [10]. However, in practice aneurysms are seldom found at the fenestration [11]. Intracranial arterial fenestration is more common in the vertebrobasilar arteries than in the arteries of the anterior circulation (Fig. 5) [11].

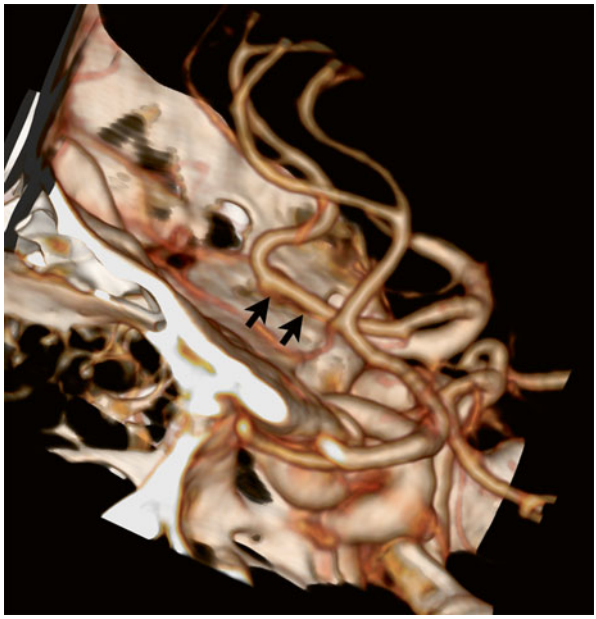

Fig. 8 Sixty-seven y/o male presented with head trauma and (traumatic) subarachnoid hemorrhage. No aneurysm or vascular malformation was found. A rare variant, an olfactory extension of anterior cerebral artery, was noted (*arrows*) and shown at the lateral oblique VR CTA of circle of Willis

In the middle cerebral artery, duplications and fenestrations can occur, as well as an accessory MCA [8, 12]. These variants are infrequent and mostly clinically insignificant.

Venous Anatomy

The venous drainage of the brain courses via the deep and the superficial venous system. The internal cerebral veins drain in the vein of Galen, which merges with the inferior sagittal sinus to form the straight sinus, which drains in the superficial venous system. The superficial venous sinuses are formed by the superior sagittal sinus, transverse sinuses, and sigmoid sinuses which drain bilaterally in the internal jugular vein. Fenestrations can also occur in the venous sinuses.

Persistent Carotid-Basilar Artery Anastomoses

In the embryologic development of the intracranial circulation primitive carotid-basilar artery connections are present which usually regress completely [13]. Rarely, such connections remain patent through adult life and should be recognized before surgery or interventions. The trigeminal artery is the most common persisting

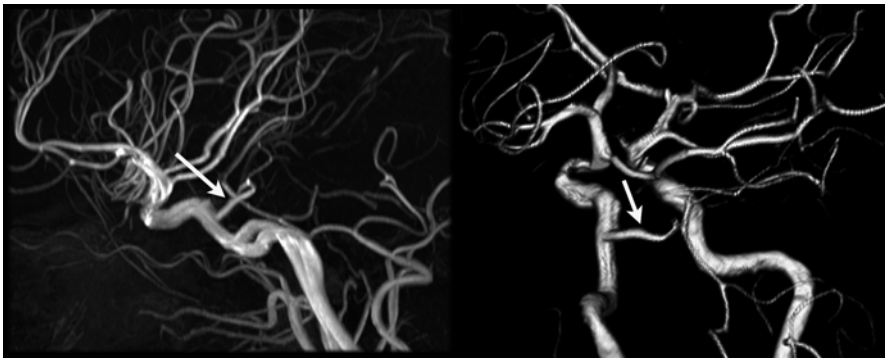

Fig. 9 Thirty-five y/o old woman, MR angiographic exam performed for surveillance of ophthalmic aneurysm after coiling. *Arrow* points to persisting trigeminal artery. In this patient, the persistent trigeminal artery only supplies the posterior fossa because of a bilateral fetal configuration of the posterior cerebral artery

carotid-basilar anastomosis [14]. This most cranially situated persistent carotid-basilar anastomosis has a prevalence of 0.1–0.6 % [15]. Two patterns are most commonly encountered. In the first pattern the persistent trigeminal artery connects with the upper basilar artery and supplies the posterior cerebral artery and superior cerebellar artery territories. Alternatively, one or two fetal type posterior cerebral arteries are present and the trigeminal artery supplies the posterior fossa (Fig. 9). In a variant persisting trigeminal artery a cerebellar artery originates from the ICA. A persistent trigeminal artery should be recognized before performing a Wada test to avoid infusion of barbiturates into the posterior fossa [16].

Another, more rare, persisting anastomosis is a primitive hypoglossal artery with a prevalence of 0.02–0.1 % [17]. A primitive hypoglossal artery represents a connection between the proximal cervical ICA and the basilar artery that traverses the hypoglossal canal. A persisting proatlantal intersegmental artery originates at a similar location but traverses the foramen magnum. This connection can also arise from the external carotid artery [8].

Vertebrobasilar Arteries

The most common variation of the vertebrobasilar system is the vertebral artery continuation as posterior inferior cerebellar artery (PICA), illustrated in Fig. 10 [19]. The reported prevalence is about 4.4 % [18]. Recognizing this variation is important before performing cerebral angiography. Duplications and fenestrations of the vertebrobasilar system can occur. In a duplication the two vessels have a different course (Fig. 11); in case of a fenestration the two lumina correspond to the same path [19].

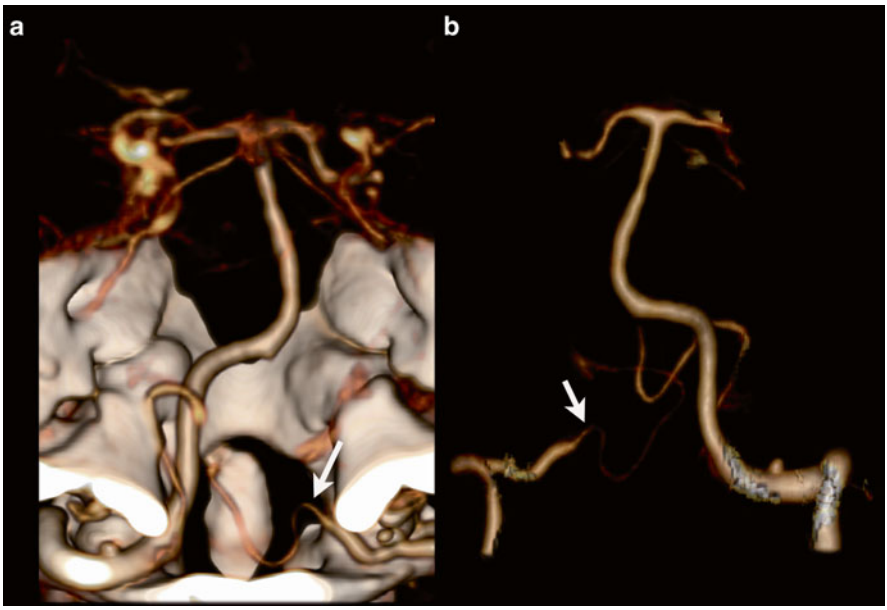

Fig. 10 Seventy-four y/o female, CTA performed for evaluation of subarachnoid hemorrhage. Right vertebral artery ends in posterior inferior cerebellar artery. VR-CTA posterior view (**a**) and VR-CTA after bone-removal anterior view (**b**) demonstrate a pica ending of the left vertebral artery (*arrows*)

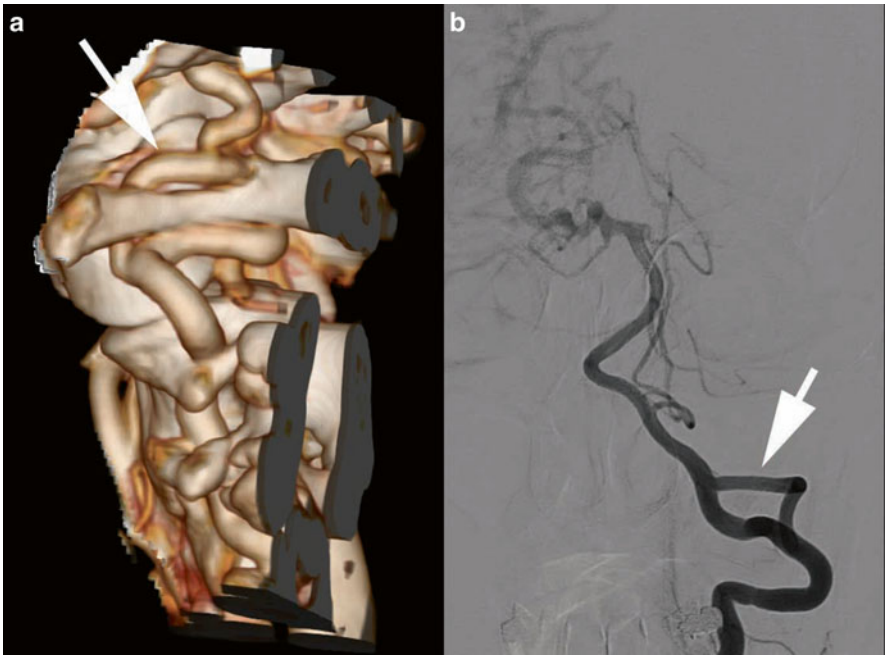

Fig. 11 Fifty-six y/o female presented with a large arteriovenous malformation (AVM) of the brain. A CTA was followed by DSA for evaluation of the AVM. VR-CTA (**a**) depicts the duplication of the left vertebral artery (*white arrows*) at the craniocervical region, which is easier depicted at DSA (**b**) because of bone subtraction

Technical Considerations

This paragraph gives an introduction on basic CT scanning parameters, contrast media (CM) characteristics, and settings, which are important for high-quality CT angiography (CTA) of the intracranial vessels.

Scanning Parameters

For detailed imaging of intracranial vessels a high spatial resolution is mandatory. Therefore, the thinnest possible collimation is recommended. Imaging should be fast to minimize motion artifacts and to potentially reduce the length of the contrast bolus. Therefore fastest gantry rotation in combination with a slightly overlapping pitch should be chosen. Image quality in terms of signal-to-noise ratio is best if an overlapping helix of data is acquired. The degree of overlap of acquired image data can be set by the pitch, which is the table speed divided by the collimation. A tube voltage of 120 kV is commonly used, but kV settings of 100 kV have been proven to improve contrast-to-noise ratio (CNR). Images should be reconstructed with thin slices (e.g., 1 mm or less) with an overlap of 30 % (e.g., slice increment of 0.7). This allows the use of isotropic data for optimal post-processing (e.g., multiplanar reformation (MPR) in arbitrary directions).

Contrast Media

To achieve optimal enhancement in CTA, the amount of iodine injected per second (iodine delivery rate (IDR) or iodine flux in gI/s) is the most important factor [20, 21].

Different concentrations of iodine can be used; typically the concentration ranges between 300 mg iodine/ml and 400 mg iodine/ml. For optimal vessel enhancement, an iodine delivery rate (IDR) of 1.6–2.0 g/s is recommended (e.g., 80–100 ml of iopromide 300 mg/ml at 6 ml/s). Contrast agent injection should be followed by a saline chaser with the same flow rate for better bolus shaping and for flushing the dead space from the site of injection to the region of interest.

Contrast media (CM) have a high viscosity dependent on temperature and osmolality. Increasing the CM temperature to body temperature prior to injection significantly decreases its viscosity [22]. Thus pre-warming CM prior to injection to body temperature is recommended at all times.

Timing

The preferred method for timing of the acquisition with respect to CM injection is bolus triggering. A region of interest (ROI) is placed in the internal carotid artery (ICA) just below the skull base. After CM injection this slice is continuously imaged

and the Hounsfield units (HU) of the ROI are automatically measured. The scanner automatically starts scanning when the Hounsfield units exceed a certain threshold (mostly 120 HU). This method results in the best timing and optimal arterial enhancement. Adequate training of technicians is important, as manual scan start might be required if patient movement has occurred or the ROI was difficult to place due to anatomical variations.

Alternatively, a test bolus can be used. A small amount of CM (e.g., 20 ml) is injected at the same rate as the original bolus, and then a slice through the carotid arteries is scanned continuously. The time between injection and contrast arrival in the carotid arteries is measured. This delay is then used for the actual scan. The advantage of this method is its robustness; it is tailored to the individual patient and his or her cardiac output. However, additional CM is used, which does not contribute to the imaging.

CT Venography of the Brain

CT imaging is also suitable to image the venous structures of the brain. Venous sinus thrombosis can be detected with CT as well as with MRI with equal sensitivity [23, 24]. For the detection of venous sinus thrombosis CT imaging is performed 40 s after the start of contrast injection. For venous imaging the injection speed can be lower than for arterial imaging, e.g., injection speed 3 ml/s, IDR 0.9 g/s followed by a saline chaser of 40 ml with 3 ml/s. The whole vertex should be included in the scanning volume to depict the whole superior sagittal sinus. Bone subtraction can be used to calculate maximum intensity projections (MIPs) of venous structures [25]; however source images should also be viewed to prevent misdiagnosis caused by bone subtraction artifacts due to the close relation of the dural sinuses with surrounding bone.

Dual-Energy CT of the Intracranial Vessels

Dual-energy CT (DECT) is nowadays available on selected scanners. Scanning with two different energies simultaneously makes it possible to decompose materials with high and low atomic number by their attenuation differences for different X-ray energies [26]. In atoms with a low atomic number, Compton scatter is the main interaction with diagnostic X-ray photons. For atoms with a high atomic number, the photoelectric effect plays the main role. If an X-ray photon has slightly more energy than the k-shell electron-binding energy of an atom, photoelectric absorption can take place, which leads to a sudden increase in X-ray attenuation at this energy (k-edge) [27]. The k-shell electron is then ejected and its vacancy is filled up by adjacent electrons and characteristic X-rays are emitted [28]. The k-edges of iodine (33.2 keV) and calcium (4 keV) are sufficiently different from the

k-edges of the constituents of soft tissue (0.01–0.53 keV) to be detected by dual-energy imaging. One of the energies is chosen at a low value, mostly 80 kV. The other energy is chosen higher, e.g., 140 kV. The spectrum of energies emitted by the X-ray source always forms a Gaussian bell curve, so also photons around 33 keV are present in an 80 kVp (kilo Volt peak) bundle. These are strongly attenuated because they approximate the k-edge of iodine. Based on the DECT-data iodine, calcium and hemorrhage can be discriminated. The characterization of iodine and calcium can be used for bone removal [27]. The characterization of iodine and hemorrhage can be used to calculate iodine only and virtual non-contrast images and can be used to differentiate CM from hemorrhage, e.g., after interventional procedures and for the analysis of intracranial hemorrhage [29–33]. Alternatively, DECT data can be used to calculate mono-energetic reconstructions, which can be applied for reduction of beam-hardening artifacts, for instance around dental restorations [34] and metallic implants [35]. The first potential applications of such reconstructions for angiographic applications have been reported for pulmonary CTA [36] and CTA of abdomen and extremities [37]. CNR for angiographic images can be increased for low kV reconstructions, potentially allowing for the use of less contrast agent [38, 39], which can also be applied in cranial CTA [29].

Bone Removal

Bone subtraction can be performed to simplify vessel analysis. Bone subtraction can be performed in various ways. First, two scans can be performed (non-contrast enhanced–contrast enhanced) which are subtracted from each other [40, 41]. Secondly, various vendors developed software for threshold-based bone subtraction. A third alternative is DECT based bone subtraction [42–44].

Caution should be taken, as the degree of stenosis can be overestimated due to blooming artifacts or because of the suboptimal distinction of calcification and iodine due to poor enhancement of the artery [44]. Furthermore, segmentation errors may occur, especially at the skull base. Thus bone removal techniques can only be an add on—viewing of the source images, including post-processing, is always recommended.

Dynamic Evaluation of the Vessels

Dynamic evaluation of the vessels is possible with time-resolved CTA, a relatively new application, also called time-invariant CTA, dynamic CTA, or 4D-CTA [45, 46, 47]. It has the potential benefit to demonstrate collateral vessels and drainage flow, next to the depiction of the cranial vessels [47, 48].

With the newest MDCT scanners, allowing for a large coverage in the z-direction or a back-and-forth sliding table (shuttle mode), dynamic CTA with high temporal

resolution has become possible [49, 50]. The first applications of dynamic CTA (4D-CTA) for imaging of arteriovenous malformations have been described recently [46, 51–53]. Dynamic evaluation of the vessels is also described in the evaluation of ischemic stroke patients [50, 54, 55] and in venous occlusions [48].

Post-processing Techniques

Scanning with thin collimation and reconstructing thin overlapping slices allow for possibilities of reconstruction in arbitrary angles without sacrificing spatial resolution. Scan thin, review thick is the basic rule [56]. Several post-processing techniques are available.

Multiplanar Reformat

High near-isotropic resolution of CT allows interactive slice reconstruction in arbitrary angles. In multiplanar reformat (MPR) the mean attenuation from the pixels is used. The slab can be reconstructed in arbitrary thickness. To ensure good quality of MPR images in the *z*-direction, an overlap of 30 % of the slice width is recommended [56]. Care should be taken for partial volume of vessels with adjacent bone. An occlusive thrombus is not obscured by MPR reconstructions, in contrary to volume and surface rendering.

Maximum Intensity Projection

The maximum HU value of a selected stack of slices is displayed in a maximum intensity projection (MIP). The thickness of the MIP and its direction can be changed interactively. This is especially suited for evaluating the patency of vessels which do not course exactly in a thin slice. MIP projections facilitate the diagnosis of vessel occlusions [57]. However, MIP projections have limitations. Structures with high density like bones or calcifications in the selected stack of slices hamper the analysis of nearby vascular structures. Secondly, MIP projections are actually 2D representations of 3D data, making 3D relations between different structures difficult to evaluate [58].

Volume Rendering and Surface Rendering

Nowadays many different choices regarding 3D rendering of vascular structures are available. In the past, surface rendering was the mostly used technique. With the increased availability of computational power, currently volume-rendering

techniques (VRT) are most often used. In VRT, each voxel is represented by the percentages of the different tissues it contains. Each tissue type is given a color and transparency. Three-dimensional representations are then computed by ray casting, simulating rays of light traversing the dataset [58]. 3D representations of CT data vary per company. The window and level settings of such renderings can often be changed interactively.

Caution should be taken, as 3D rendering techniques allow image manipulation which might also conceal pathologies—thus source images should be interpreted at all times.

Indications

Indications for CT of the circle of Willis and intracranial arteries are expanding over the years, thanks to the increase in quality and availability of CTA. Even though DSA is still considered the gold standard, CTA and MRA are the first-choice noninvasive imaging modalities, thanks to good availability—especially CTA—and high quality of diagnostic imaging.

The detection of anatomical variations of the circle of Willis is highly accurate with CTA compared with DSA, with an overall agreement of 92.4 %. However, the detection of hypoplastic segments with CTA is more difficult and CTA has a low sensitivity [59]. CTA has a high sensitivity and specificity compared to DSA for the detection of the fetal origin of the posterior cerebral artery, a relatively frequent and relevant anatomical variation [60].

In this section concerning the indications of CTA we discuss stroke and intracranial atherosclerosis imaging, imaging of aneurysms, vasculitis, vascular malformations like AV-fistulae and arteriovenous malformations, and less frequent diseases like reversible cerebral vasoconstriction syndrome and Moyamoya. CTA in brain death procedure is discussed.

Ischemic Stroke

Stroke, "a cerebrovascular accident (CVA)," is an acute neurological deficit.

Most strokes (80 %) are due to an ischemic event. Twenty percent of strokes are hemorrhagic.

The etiology of stroke varies with the stroke subtype [61] as well as its outcome and recurrence risks.

Etiological mechanisms are atherosclerotic strokes, small vessel disease, cardioembolic disease, or undetermined/other [62].

- Atherosclerotic (ASVD) strokes are the most common type of acute arterial ischemia.

- 40–50 % of stroke is due to atherosclerosis. Most occlusions in larger vessels are due to emboli. Common locations for symptomatic atherosclerosis are
  - Origin of ICA (bifurcation)—Caucasians
  - Intracavernous portion of the ICA
  - First/M1 segment of the MCA—African and Asian heritage, diabetes [63]
  - Origin and distal portion of VA
  - Midportion of BA

The locations of atherosclerotic lesions are ethnically different. In Europe extracranial atherosclerosis is the most common cause of ischemic stroke, whereas in Americans of African origin, Asians, and Hispanics intracranial atherosclerosis is more important [64, 65]. Recent publications suggest a larger role for intracranial atherosclerosis in symptomatic patients [66, 67].

- Small vessel disease accounts for 15–30 % of ischemic stroke. Lacunar infarcts (<15 mm) are due to small artery occlusions of penetrating arteries. These can be embolic, atheromatous, or thrombotic. Lacunar infarcts are found in the basal ganglia, thalami, internal capsule, pons, and deep white matter. Most lacunar infarcts are silent/asymptomatic, although strategically placed infarctions can cause neurological deficit.
- Cardioembolic disease accounts for 15–25 % of stroke. The most important cardiac abnormalities which can lead to stroke are atrial fibrillation, myocardial infarction, valvular heart disease, and a patent oval foramen.
- In about 25 % the cause of stroke is due to other causes or remains unknown.

The literature is based mainly on extracranial atherosclerotic disease, located at the carotid bifurcation; less literature focuses on intracranial atherosclerotic disease. In proximal/extracranial atherosclerosis the vulnerable plaque with hemorrhage, ulceration, and calcification of plaques is frequently found, whereas in intracranial luminal stenosis of the middle cerebral artery the percentage of lipid area and the presence of intraplaque neovascularity probably plays a key role leading to ischemic stroke [68]. In a Chinese population the presence of intracranial calcifications was an independent risk factor of ischemic stroke [69].

The mechanisms of stroke in intracranial atherosclerosis can be divided into local thrombotic occlusion, artery-to-artery embolism, branch occlusive disease of the orifice of deep perforating arteries, hemodynamic (hypoperfusion), or a combination of these [70]. This can explain the different patterns of infarcts.

In situ thrombotic occlusion leads to the largest infarctions. Intracranial atherosclerosis usually is a slowly developing process, so collateral circulation can develop in chronic atherosclerotic disease. The size of the infarction is dependent on the presence of collateral circulation, the speed of the occlusion, and hemodynamics. Whole territory infarcts are therefore less frequent.

In artery-to-artery embolism emboli from the more proximal occlusion can be entrained with the bloodstream to distal branches and result in an occlusion with large strokes. Examples are thrombi from carotid bifurcation plaques and cardiac emboli (Fig. 12). The latter account for larger strokes due to larger emboli and less

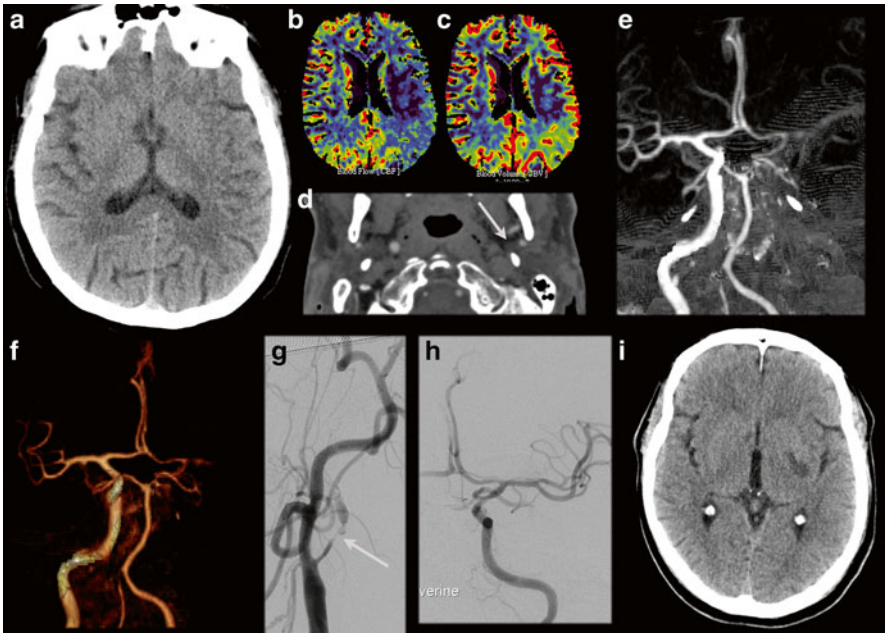

Fig. 12 A 62 y/o male patient presented with a right-sided hemiparesis. NECT shows a slight hypodensity and faint loss of gray-white matter differentiation at the posterior border of the left lentiform nucleus (**a**) and i.v. rTPA was given with initially good clinical recovery. However, the hemiparesis recurred and at that time a VPCT (**b**: CBF, **c**: CBV) and CTA were performed. The VPCT shows CBF/CBV perfusion mismatch with increased MTT (not shown). Coronal MIP (**e**) and VR (**f**) of the CTA show occlusion of the left internal carotid artery (**d**, source image) from the bifurcation with an occlusion of the left MCA. The patient went on for DSA and intra-arterial recanalization of the left carotid bifurcation stenosis (**g**) and subsequent thrombectomy of the left MCA thrombus. A good recanalization was obtained (**h**). Follow-up CT 1 day later shows a lacunar infarction in the left lentiform nucleus (**i**), but no other signs of ischemia in the left MCA territory. Initially there was some residual motor deficit, but at discharge there was no neurological deficit

collateral circulation. Intracranial MCA stenosis can give artery-to-artery emboli to distal M2 segments.

Occlusions of the origin of a perforating artery can be due to an intracranial atherosclerotic plaque. The pathophysiology of these occlusions differs from the small vessel disease, but can lead to the same small infarctions (Fig. 12).

Imaging in acute stroke can be divided into differentiating hemorrhagic stroke and ischemic stroke, imaging of vessel occlusion (Figs. 12, 13, 15, and 17), and determining the core and penumbra of the infarction (Figs. 14 and 16).

In the acute setting a non-contrast-enhanced CT (NECT) of the brain can reveal hemorrhage. The ASPECTS score [71, 72] can be used to try to determine the extent of the infarction in the initial phase. Early signs of ischemic stroke are effacement of sulci, hypodensity of the brain parenchyma, loss of gray-white matter differentiation,

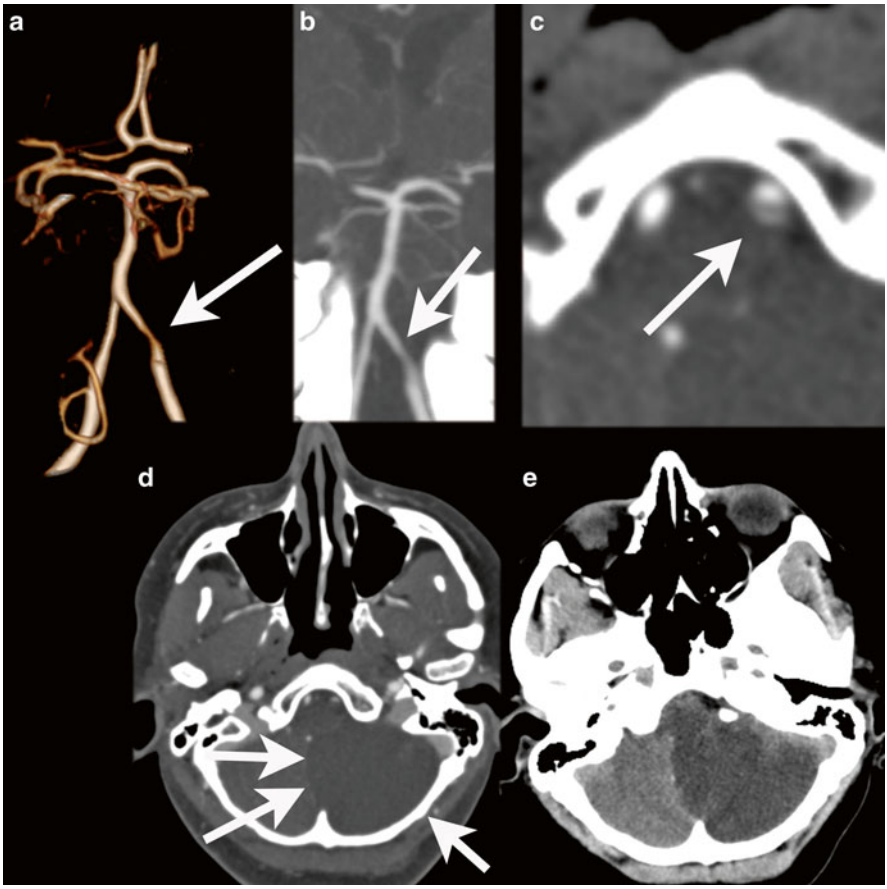

Fig. 13 Vertebral artery dissection with PICA infarction. A 49 y/o female presented with dizziness, neck pain, nystagmus, and ataxia of the left arm. Initial NECT was normal. CTA demonstrates a tapering of the distal segment of the left vertebral artery, with a double-lumen sign on the CTA source images. A large infarction of the PICA territory in the left cerebellar hemisphere with mass effect was noted 2 days after the onset of symptoms. DE-CTA was performed at day 2. Bone-removed VR shows tapering of the distal segment of the left vertebral artery (**a**), also visible on the MIP reconstructions (**b**). Detailed images of the vertebral artery (**c**) Images at at 80 kVp demonstrates clearly the true and false lumen of the dissected left vertebral artery. At 120 kVp images this is also seen to a lesser extent, the mass effect of the cerebellar infarction is already noted at the CTA (**d**), but better seen at NECT at follow-up at day 3 (**e**)

and in the insular region called the "insular ribbon sign" and a hyperdense vessel sign [73] (Fig. 18).

Defining irreversibly damaged parts of the brain can be done by MRI with diffusion-weighted imaging (DWI) or with CT perfusion (Fig. 14). Vascular imaging can be performed with CTA [74], MRA [75], or DSA; the latter is the gold standard, but is preferably used in selected cases [74]. CTA can also be calculated from the VPCT dataset, thereby lowering the radiation dose [50, 76]. In case of an inconclusive CTA or MRA an adjunct MRA or CTA can lower the need for DSA [77].

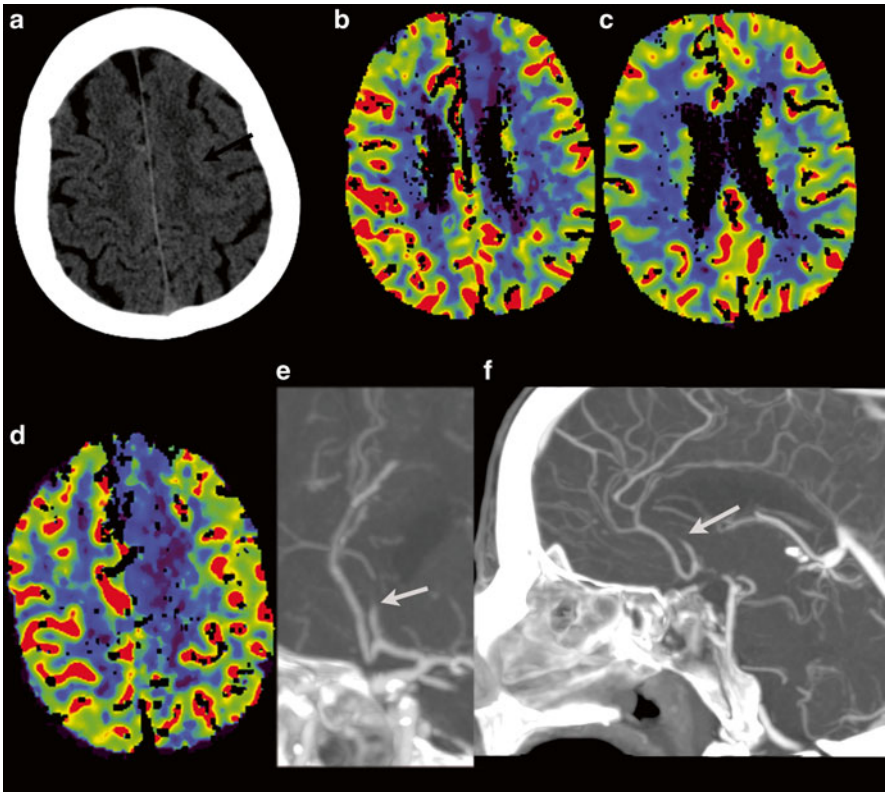

Fig. 14 Seventy-two y/o female. Presented with speech disturbances and left-sided motor deficit. NECT shows subtle effacement of the sulci of the left hemisphere (**a**, *black arrow*). VPCT shows CBF/CBV mismatch (**b** and **c**), with reduced flow in the territory of the left anterior cerebral artery (**d**). CTA shows occlusion of the left A2 segment, *white arrow* (**e**: oblique MIP, **f**: lateral MIP), without abnormalities of the other intra- and extracranial vessels. She received i.v. rTPA. Clinical follow-up demonstrated recovery of the paresis with MRC grade 4 of right arm and leg

The accuracy of CTA for evaluation of intracranial atherosclerotic disease is good, especially in stenosis larger than 50 % [74, 78], and is increasing with newer and more sophisticated scanners [79]. CTA can show the site and severity of the stenosis, the length of the thrombus, and the presence of collateral circulation [80] (Fig. 15). Time-resolved CTA or 4D-CTA (Fig. 19) can give additional information about the leptomeningeal collateral filling [45, 47] or the clot burden [54] (Fig. 16).

Recently more attention is drawn to the presence of intracranial calcifications [81–84] (Fig. 20), and their association with stenosis and white matter abnormalities [85–87].

The therapy of acute stroke is aimed at recanalization in reperfusion therapies like intravenous rTPA and in selected patients intra-arterial recanalization [88]. Recurrent stroke is prevented by antithrombotic medication, antiplatelet agents, and treatment of risk factors [89].

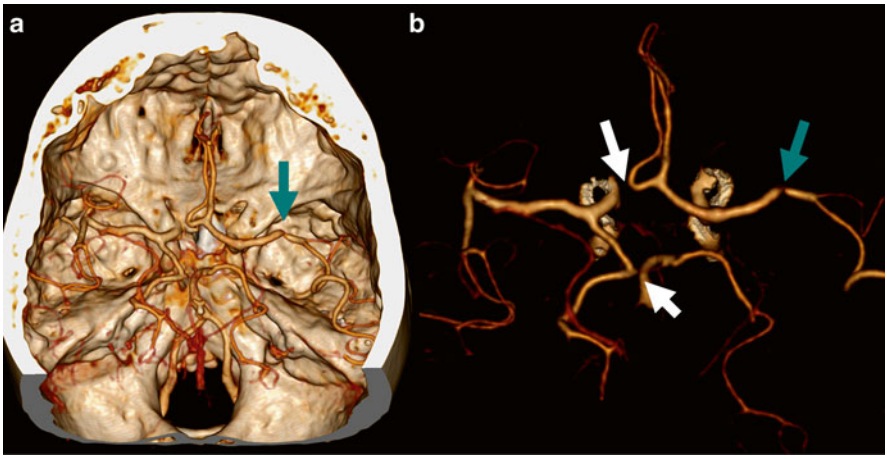

Fig. 15 A 84 y/o female presented with right-sided hemiparesis and aphasia due to a left MCA territory stroke. CTA demonstrated a left MCA stenosis (*blue arrow*). As normal variant, hypoplasia of the right A1 segment is present, as well as hypoplasia of the P1 segment (*white arrows*). Volume rendering (VR) (**a**) and VR after bone removal (**b**) from DECTA are shown

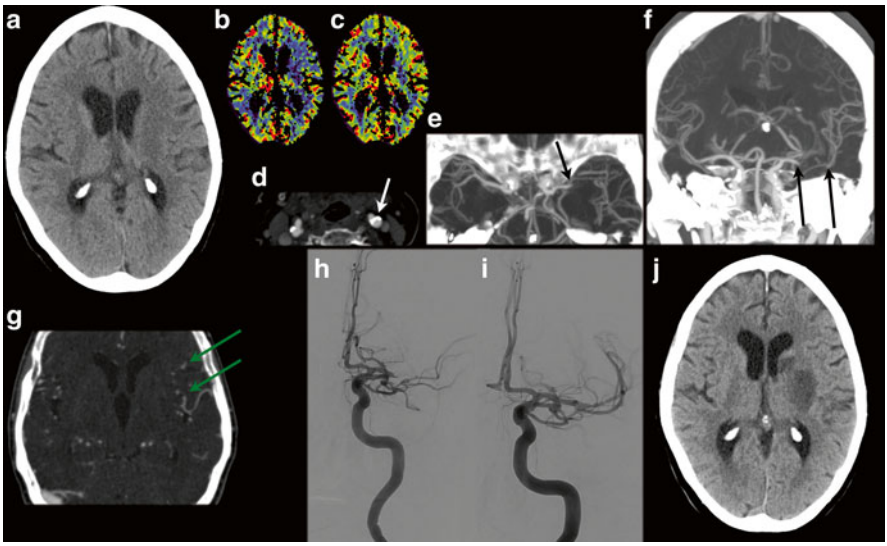

Fig. 16 A 72 y/o female presented with sudden right-sided paresis of the arm and leg. A facial asymmetry was noted and dysarthria was present. NECT scan shows diminished differentiation of the gray and white matter at the upper part of the left lentiform nucleus (**a**). CT perfusion images show a CBF/CBV mismatch (**b** and **c**), with a suspected core at the left lentiform nucleus and penumbra at the left frontal cortex. CTA demonstrates calcifications at the carotid bifurcation (**d**) and a left middle cerebral artery occlusion (**e**, transverse MIP reconstruction; **f** coronal MIP reconstruction). The length of the thrombus can be appreciated on the coronal MIP (**f**, between the *black arrows*) and collateral filling is present (**g**, *green arrow*). The patient went on for intra-arterial thrombectomy. (**h**) DSA before successful recanalization of the left MCA (**i**). Follow-up NECT at 1 day shows infarction in the left lentiform nucleus (**j**). At discharge only mild aphasia and no motor or sensory symptoms were present

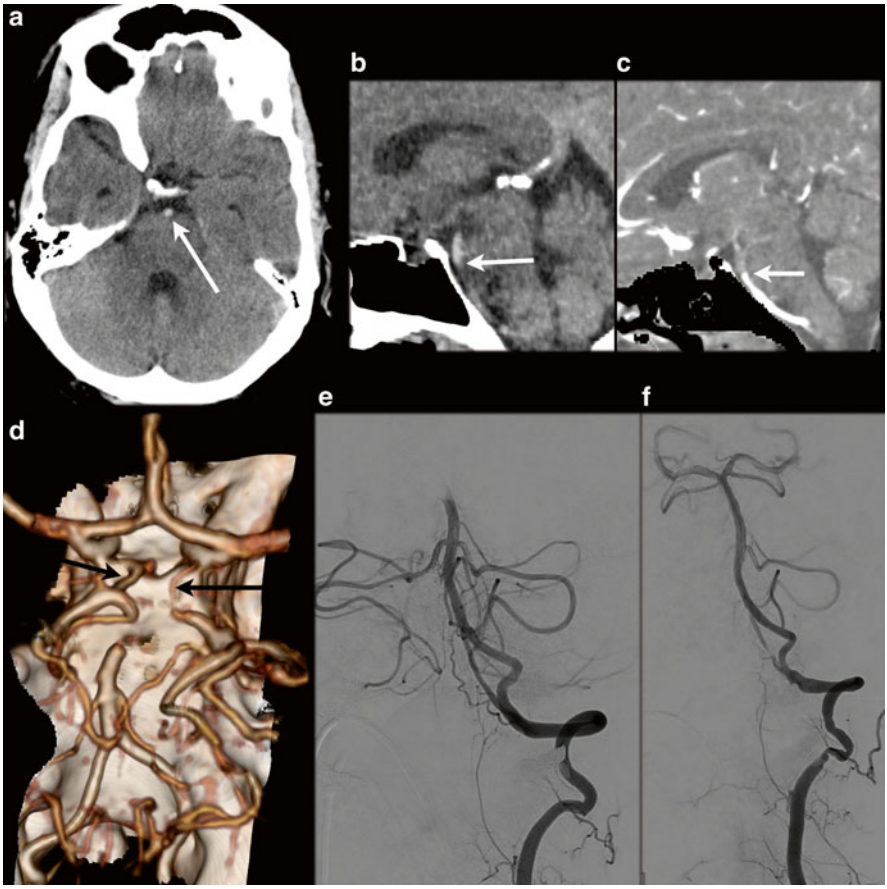

Fig. 17 A 46 y/o male presented with left-sided hemiparesis and dysarthria after ablation procedure for atrial flutter. NECT shows normal density and normal gray-white matter differentiation. A dense artery sign is present in the distal basilar artery (**a**, *white arrow*), suggestive of basilar artery occlusion. Subsequent CTA conforms an occlusion of the distal basilar artery (**b**: sagittal NECT, **c**: CTA sagittal MPR), matched images. 3D VR (**d**) shows the occluded distal basilar artery; there is collateral blood flow to the P2 segments via de bilateral Pcoms (*black arrows*). DSA confirms the occlusion (**e**) and intra-arterial thrombectomy was performed with successful recanalization (**f**). After 3 months only mild balance disturbances were present

Hemorrhagic Stroke

In the work-up for hemorrhagic stroke, non-enhanced CT can be followed by imaging for detection of underlying vascular malformations, aneurysm, or tumors [29, 33].

NECT demonstrates the presence, exact location, and extension of the hemorrhage. Secondary signs of an underlying abnormality can be the age of the patient, presence of large vessels, mass effect, and lobar location.

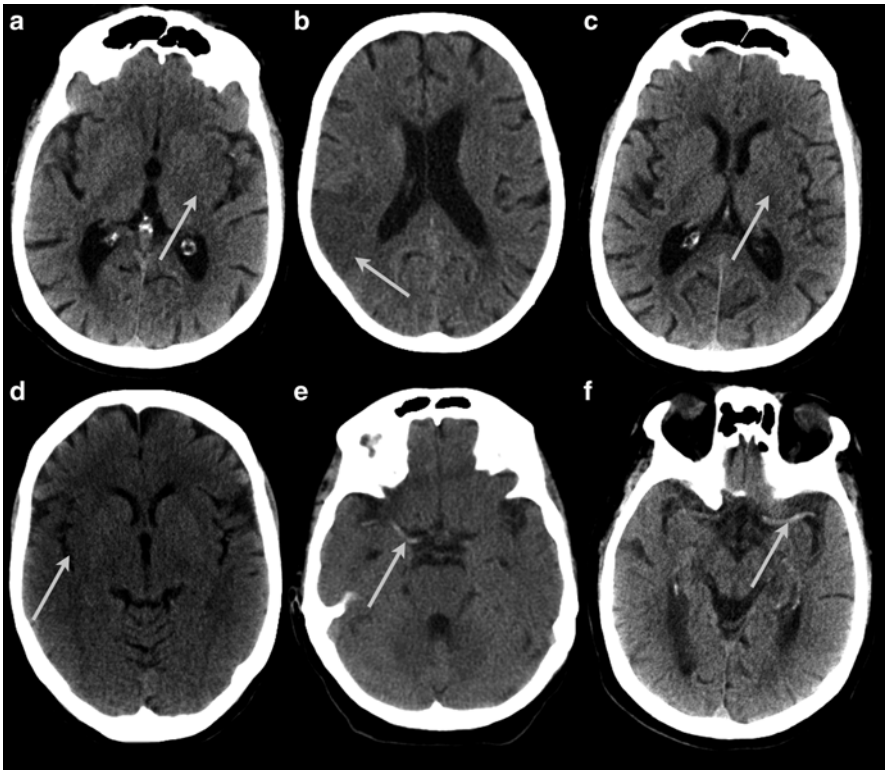

Fig. 18 Signs of infarctions on NECT. (**a**) A partial insular ribbon sign and diminished differentiation of the left lentiform nucleus. (**b**) Hypodensity of the parenchyma, loss of gray-white matter differentiation, and effacement of sulci of the right parietal lobe. (**c**) Disappearance of left lentiform nucleus. (**d**) Right insular ribbon sign. (**e** and **f**) Dense artery sign of the MCA right (**e**) and left (**f**)

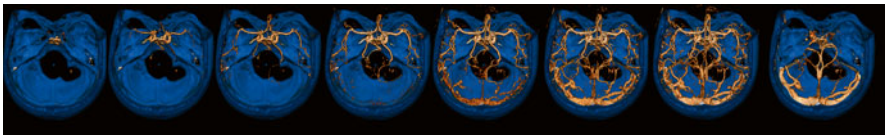

Fig. 19 Fifty-four y/o female, presenting with right-sided motor and sensory deficit and aphasia for which she received i.v. rTPA. NECT, VPCT, and CTA were without abnormalities. Shown are the VR images from the 4D-CTA with bone suppression (*blue*) derived from the dynamic phases of the VPCT. Normal arterial and venous phases are demonstrated by this 4D-CTA

In patients who present with an acute intracerebral hematoma, CTA of the intracranial vessels should be performed and is a fast noninvasive method for identifying its etiology [90].

A focal contrast deposition in the hematoma, next to the vessel, is called a spot sign.

The identification of the "spot sign" on CTA can predict whether the hematoma is likely to expand [91, 92], but the impact on clinical outcome is subject to discussion.

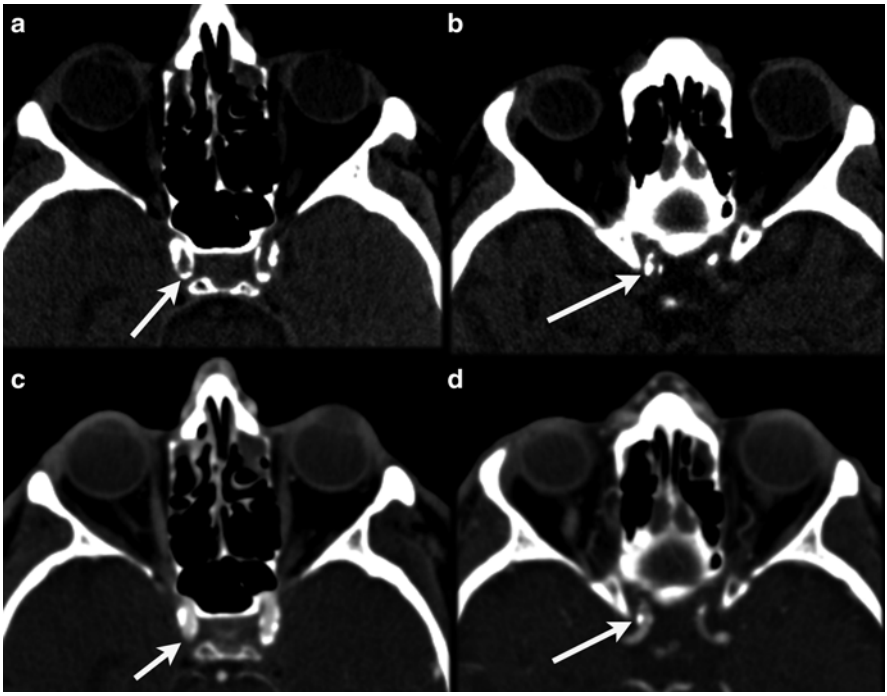

Fig. 20 Intracranial calcifications are better depicted on thin slice NECT images (**a** and **b**), compared to CTA source images (**c** and **d**) due to identical HU of iodine and calcifications

Contrast extravasation, contrast pooling in the hematoma rather than just a spot, is even more predictive than the spot sign for hematoma growth [93] (Figs. 21 and 22).

Vascular malformations like arteriovascular malformations, fistula, and cavernous malformations can present with intracranial hemorrhage. Capillary telangiectasia and developmental venous anomalies are less likely to present with hemorrhage.

CTA can detect arteriovenous malformations (AVM) in about 90 % of cases, depending on their size. The detection rate is lower in small AVM lesions, whereas the detection rate is up to 100 % in lesions larger than 3 cm [94]. Detection of fistula with CTA can be more challenging.

AVM

AVMs consist of arterial feeders, a nidus, and draining veins. Around 50 % of AVMs present with hemorrhage. Seizures or focal neurological deficits can also be presenting symptoms [95].

AVMs can be classified according to the Spetzler and Martin classification, depending on the size, location in eloquent areas, and the absence or presence of deep venous drainage [96].

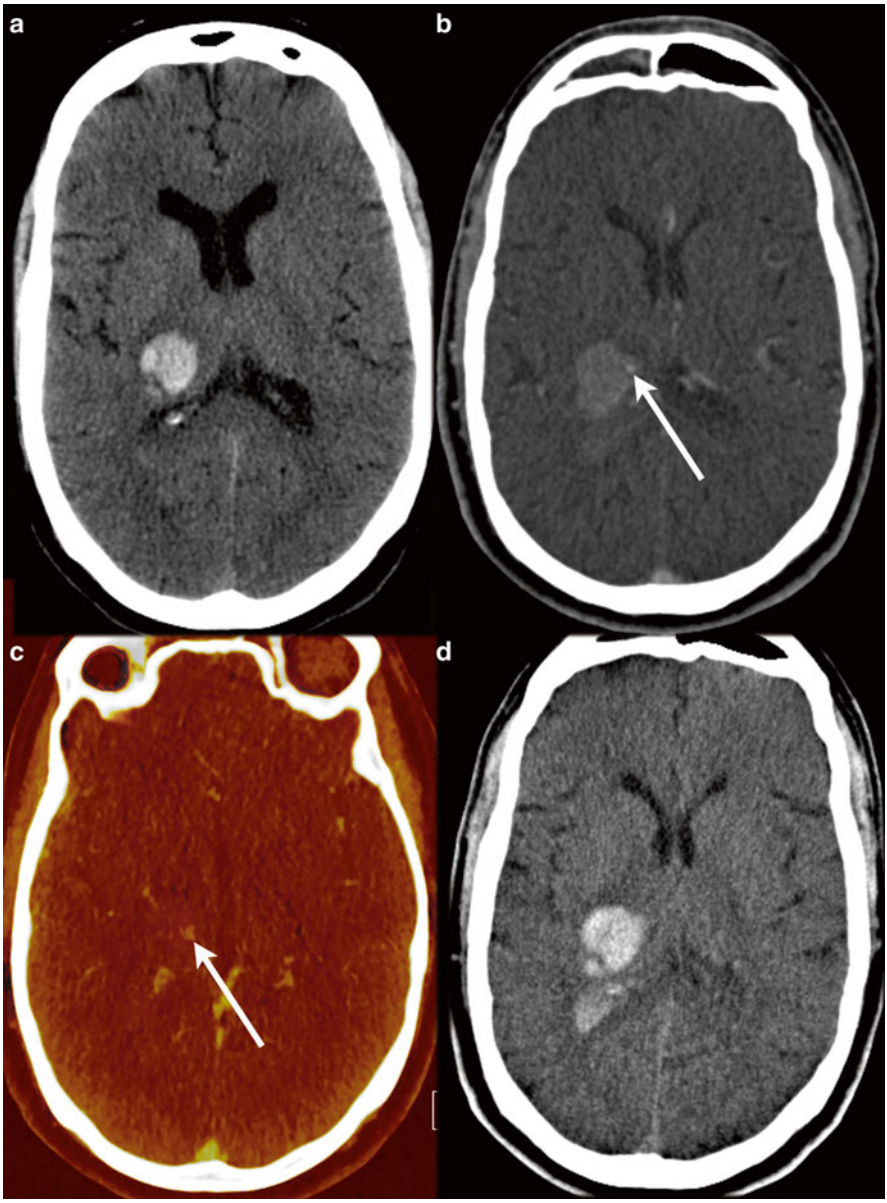

Fig. 21 A 58 y/o male presented with left-sided hemiparesis and headache. NECT shows hemorrhage in the right thalamic region (**a**). Due to progression of symptoms CT with DE-CTA was repeated within 2 h. NECT demonstrates progression of the hemorrhage (**d**), extending into the lateral ventricle. A contrast spot is seen at the source images of the CTA at the level of the hemorrhage, consistent with the spot sign (**b**). This is even better depicted on the fused image, post-processed from the DE-CTA, where iodine is highlighted in *yellow* (**c**)

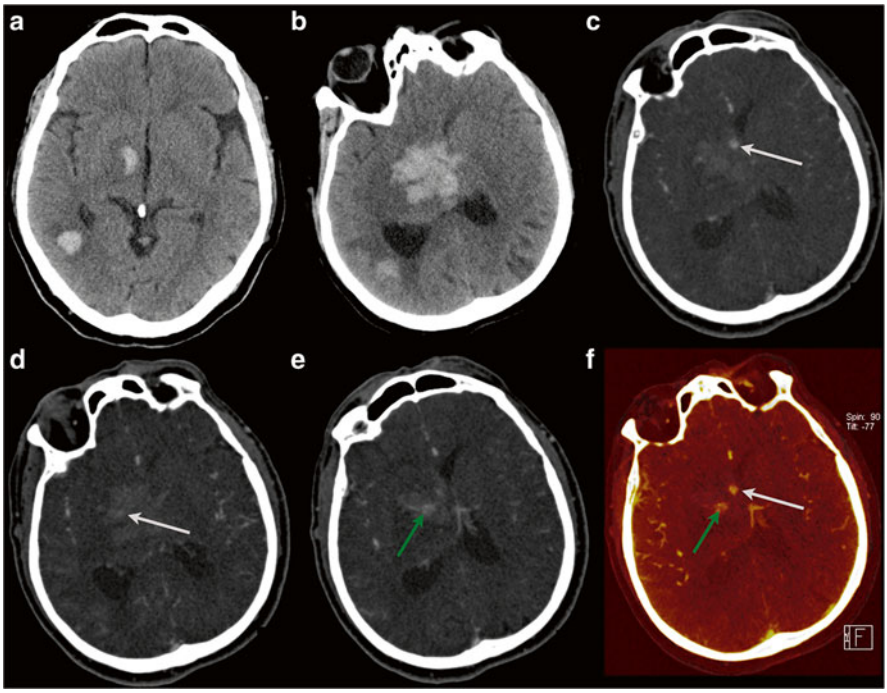

Fig. 22 Sixty-five y/o male with a history of idiopathic thrombocytic purpura (ITP) and low platelet count presented with left-sided motor deficit, sensory disturbances, hemianopsia, and facial nerve paralysis. NECT shows two hemorrhagic foci in the right thalamus and the right temporo-occipital white matter (**a**). Because of clinical deterioration follow-up NECT with additional DE-CTA was performed. NECT shows enlargement of both hematomas with signs of brain stem herniation (**b**). DE-CTA demonstrates a spot sign at the anterior and lateral parts of the thalamic hemorrhage on the source images (**c** and **d**, *white arrows*) and contrast extravasation more centrally in the hemorrhage (**e** and **f**, *green arrows*). Fusion images of iodine overlay on virtual non-contrast CT demonstrate the extravasation in *yellow* (**f**, *green arrow*) (adapted from Postma AA et al. © Curr Radiol Rep 2015:3:16, with permission)

Diagnoses can be made with CTA, MRI, and MRA and/or DSA. CTA can demonstrate the feeding vessels, the nidus, and the venous drainage [95]; also associated aneurysms can be detected. A study of Mikami CTA detected all AVMs and demonstrated critical feeders and their geometric associations with the nidus [97]. They emphasize the use of post-processing techniques and advocate the use of 3D volume rendering with transparency imaging (Figs. 23, 24, and 25). CTA can depict all vessels, without being influenced by flow. However DSA still is considered the gold standard and can selectively image the feeding vessels and can assess flow velocities within the AVM and its venous drainage.

Therapy varies from conservative, operative, endovascular, and radiation therapy or a combination of these, depending on the size, location, feeders, and the drainage pattern [98].

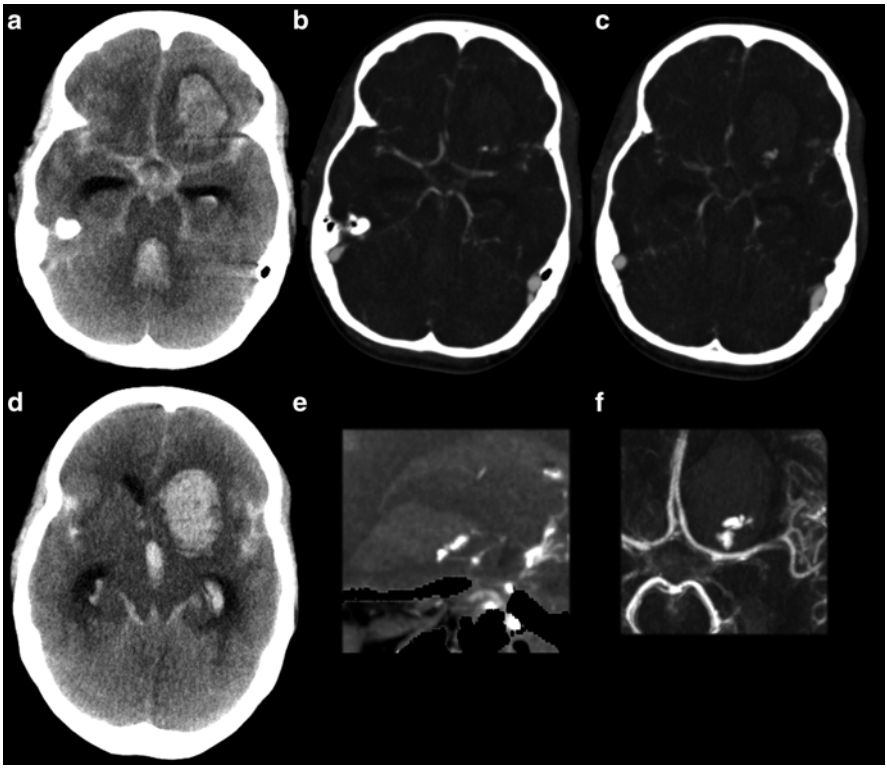

Fig. 23 Thirty-five y/o female presented postpartum with hypertension, headache, and seizures. NECT showed a large left frontal hematoma and severe subarachnoid hemorrhage, including intraventricular hemorrhage and hydrocephalus. CTA showed a vascular malformation at the left frontal lobe, suggestive of an AVM. NECT at presentation (**a** and **d**). Source images of the CTA (**b** and **c**). Lateral and transverse MIP reconstruction (**e** and **f**)

Fistula

Dural AV fistulas (DAVF) comprise about 15 % of all vascular malformations in the brain. DAVF is an abnormal connection of the arterial and venous system, with involvement of one or more dural sinus [99]. The size and drainage pattern of DAVFs can vary, resulting in variation in symptoms and presentations, the most important being pulsatile tinnitus, hemorrhage, headache, and to a smaller extent seizures [100]. Several classification types exist; classifying the fistulas can be based on the site of venous drainage and the presence or absence of cortical vein drainage (Borden classification) or classification can be based on the direction of the dural sinus drainage, the venous flow architecture, and the presence or absence of cortical vein drainage (Cognard classification).

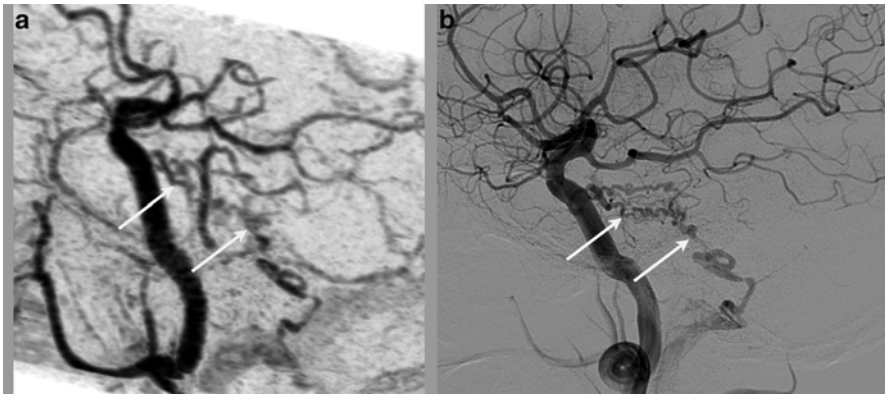

Fig. 24 A 47 y/o male presented with right-sided pulsatile tinnitus. 4D-CTA (**a**) of the posterior circulation demonstrates a tentorial dural AV fistula (*white arrows*), confirmed at DSA (**b**). Courtesy of F.J.A. Meijer, Radboud UMC, Nijmegen, The Netherlands

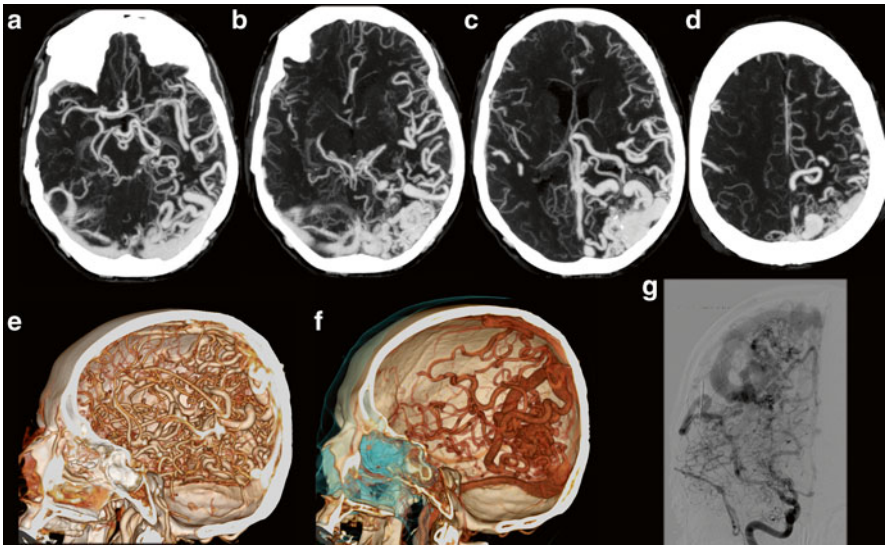

Fig. 25 A 56 y/o female presented initially with a seizure due to a large dural AV fistula. Consequently she was admitted to the emergency room with a large intracranial hemorrhage. Shown here are the VR images of the CTA (**e** and **f**), the MIP (**a**–**d**) images, and DSA images (**g**). The MIP images are helpful to determine the full extent of the vascular malformation, which is more complicated in VR CTA. However, dynamic information from i.a. DSA is needed. Shown is a large vascular malformation with multiple small arterial feeders and dilated (cortical) veins. DSA shows the main feeder from the external meningeal artery

The diagnostic work-up of DAVF consists of radiological imaging. High-resolution CTA and MRA have been studied as an alternative to the gold standard DSA, with moderate sensitivity [100, 101]. More recently 4D-CTA is described as alternative to conventional CTA which allows for identification of early venous filling, patterns of venous drainage, and type of feeding artery [46, 51] (Fig. 24).

Aneurysms

Subarachnoid hemorrhage (SAH), blood in the subarachnoid space, can be detected on a non-enhanced CT scan with high reported accuracy up to a sensitivity of 97 % [102, 103]. Nontraumatic SAH is due to rupture of a cerebral aneurysm in up to 80 % of cases [104]. Aneurysmal SAH is a serious condition, with high percentages of short-term complications (hydrocephalus, edema, and vasospasm), long-term sequelae (neurological deficits and cognitive disturbances), and death. After diagnosing a nontraumatic SAH, a search for underlying aneurysmal pathology has to be started.

Most aneurysms are saccular aneurysms, whereas other forms like dissecting, fusiform, blister type, and giant aneurysms are less frequently encountered (Figs. 26, 27, and 28).

The gold standard for detection of cerebral aneurysms is still considered cerebral digital subtraction angiography (DSA), but in clinical practice CTA is frequently used as first-line imaging for noninvasive evaluation of aneurysms [105]. Multiple studies compared the sensitivity of CTA with DSA. Villablanca et al. showed a high sensitivity for the detection of aneurysms smaller than 5 mm, with an accuracy of 99 % [106]. Pechlivanis stated that in 92 % of the aneurysms CTA can provide the information about the aneurysm needed for surgical planning [107]. An equal sensitivity of CTA in detection of aneurysms larger than 3 mm was found by Karamessini et al. They found that all Acom and MCA bifurcation aneurysms were detected, but some locations, e.g., Pcom, remained problematic. The delineation features of the aneurysm were best depicted in 3D visualization [108]. Recent technical advantages like iterative reconstruction techniques can possibly improve the delineation of arteries in the posterior fossa [109]. Ramasundara et al. studied the accuracy of CTA with and without bone subtraction as well as with MPR and 3D VR post-processing. Both showed high sensitivities and specificities compared to DSA for the detection of aneurysms and for assessing the suitability of endovascular versus surgical treatment [110]. This in contrary to Chen et al., who demonstrated a lower accuracy for nonsubtracted CTA compared to subtracted volumetric CTA in a 320-detector row CT [105].

Attention should be paid to the presence of multiple aneurysms in up to 15 % of cases (Fig. 26). In cases of negative CTA or equivocal cases DSA should be performed.

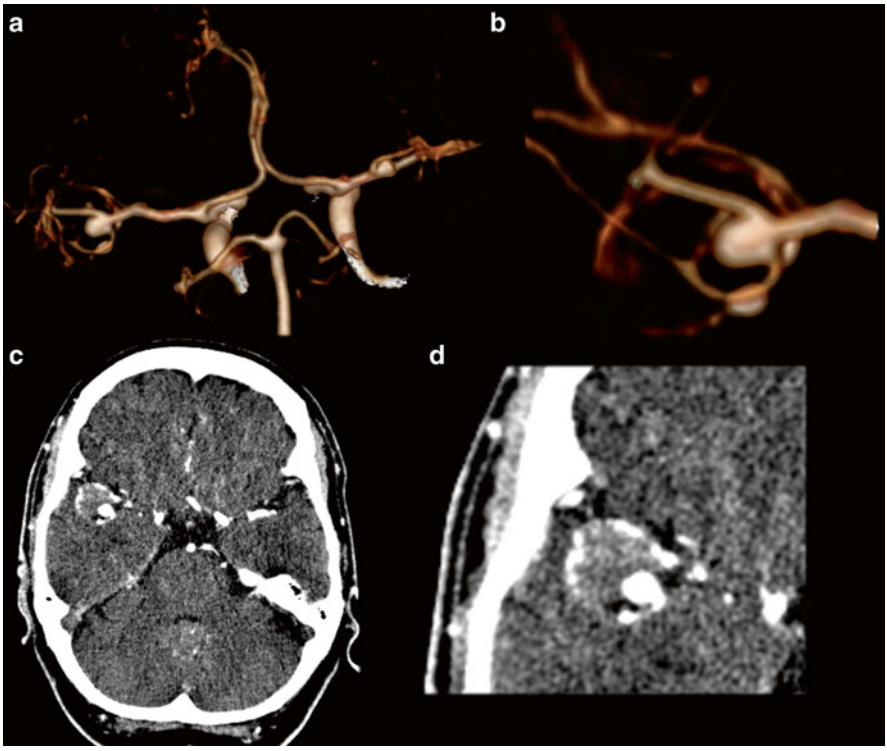

Fig. 26 A 62 y/o female was evaluated for an incidental finding of a partially thrombosed aneurysm of the right MCA. VR reconstructions (**a** and **b**) show the flow in the non-thrombosed part of the right MCA aneurysm, but the thrombus with calcified wall itself is better depicted on the source images (**c** and **d**). A mirror aneurysm is present at the left MCA bifurcation

Imaging in the postoperative period after surgical treatment with titanium clips can be performed with CTA for evaluation of residual aneurysms [111, 112] (Figs. 29 and 30).

Venous Sinus Thrombosis

Venous thrombosis is a relatively uncommon cause of stroke, which accounts for 1–2 % of stroke. Accurate and prompt diagnosis is important because therapy can reverse the disease process. The superficial venous system, the superior sagittal sinus, and the transverse sinus are more often involved than the deep venous system, that is, the internal cerebral veins, the vein of Galen, and the straight sinus.

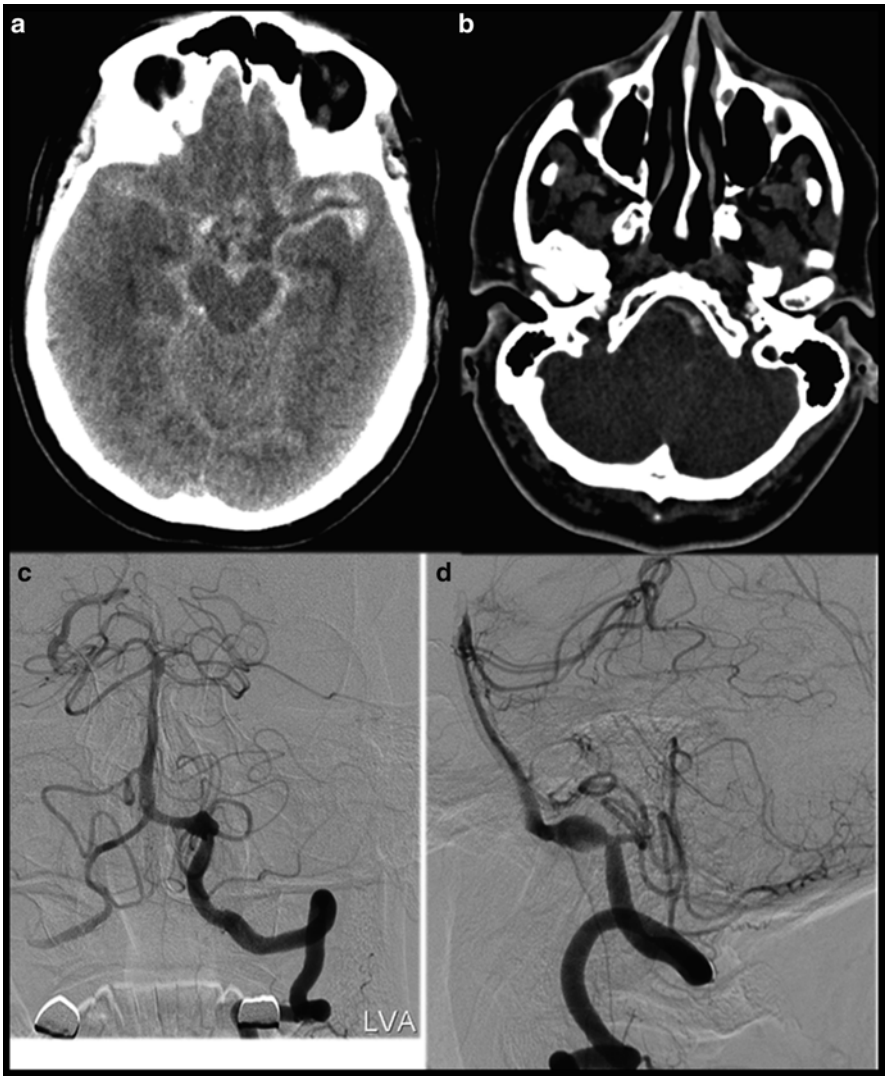

Fig. 27 A 69 y/o old male presented with progressive headache for 4 days. NECT (**a**) shows massive subarachnoid hemorrhage. CTA demonstrates a dissecting aneurysm of the intracranial segment of the left vertebral artery, shown here on the source images (**b**). DSA confirms the presence of the dissecting aneurysm of the left vertebral artery (**c** and **d**)

The symptoms of venous thrombosis are dependent of the location and the extent of the venous thrombosis, the duration of the occlusion, and the status of the collateral pathways. Headache, reduced consciousness, seizures, and neurological deficits may occur [113, 114]. Focal neurological deficits are related to parenchymal changes, which can be due to hemorrhage, vasogenic and cytotoxic edema, or infarction.

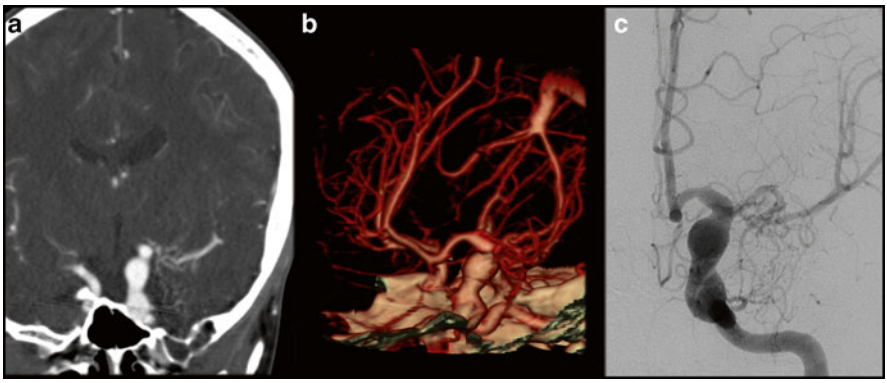

Fig. 28 A 14-year-old boy presented with non-related symptoms. As an incidental finding ectasia of the carotid artery was found and CTA was ordered. MIP images from the CTA (**a**), volume rendering (**b**), and DSA (**c**) show fusiform dilatation of the intradural segment of the carotid artery and proximal A1 segment

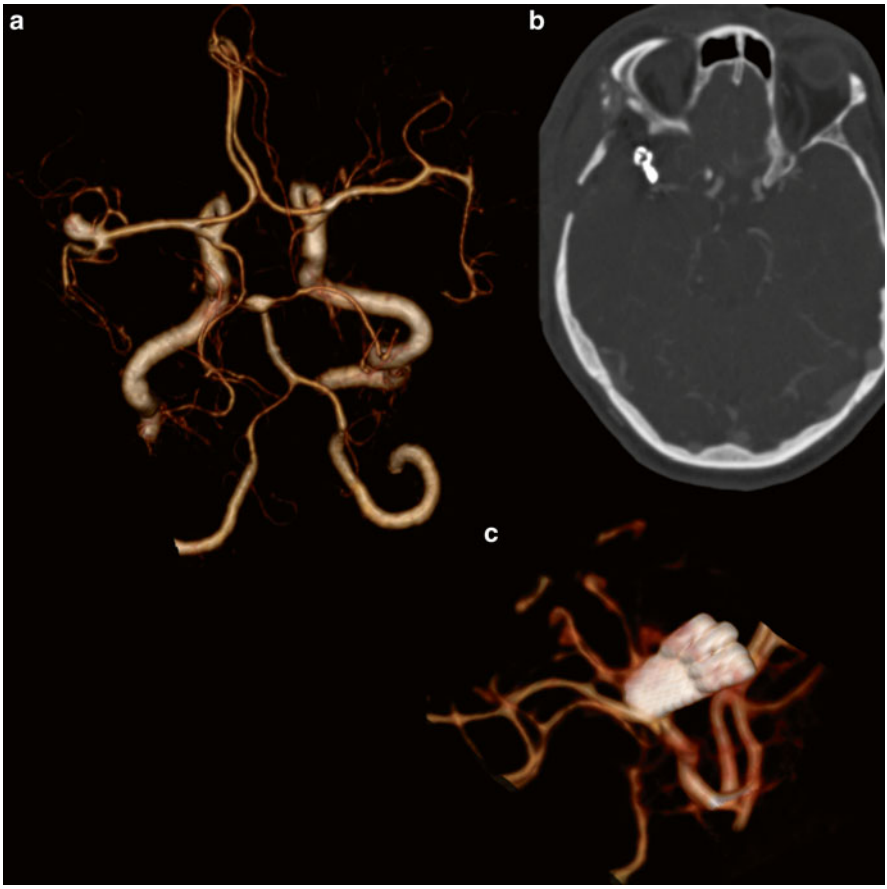

Fig. 29 Sixty-seven y/o female underwent a CTA for evaluation of an incidentally found large middle cerebral artery aneurysm (**a**, bone-removed DE-CTA). She underwent surgical clipping. Source images of the CTA (**b**) demonstrate the presence of several clips, and 3D visualization of the data reveals four surgical clips at the aneurysm (**c**), with no signs of residual aneurysm

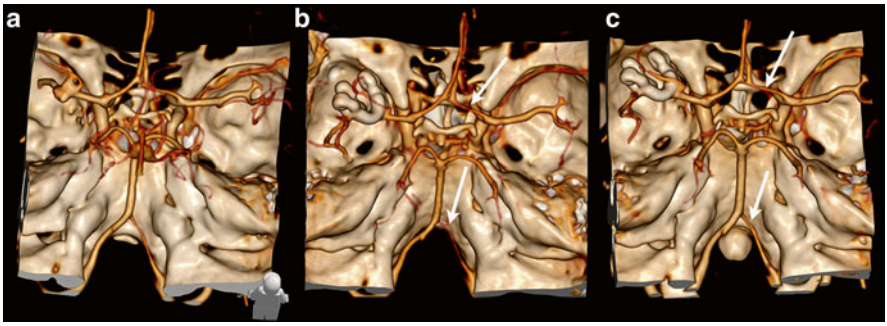

Fig. 30 A 54 y/o female underwent surgical clipping of an incidentally found asymptomatic MCA bifurcation aneurysm (**a**). Initial postoperative CTA shows no signs of residual aneurysm, but the calibre of the vessels is smaller than preoperatively with tapering of especially the distal vertebral artery and A1 segment (**b**, *white arrows*), consistent with vasospasm. At follow-up CTA there is normalization of the vessel calibres (**c**)

Causes of cerebral venous thrombosis [115] are diverse and often multifactorial ranging from prothrombotic disorders, hypercoagulability states, oral contraceptives, pregnancy, and puerperium as well as from direct invasion by infection or malignancy [115].

NECT can be very helpful in detection of attenuated vessel sign and cord sign (Figs. 31 and 32), and has high reported sensitivity and specificity (attenuated vein sign sensitivity of 100 % and specificity of 99.4 % and cord sign of 64.6 % and 97.4 %, respectively) [116]; however a normal NECT is never sufficient to rule out venous thrombosis. Brain swelling, local hypodense areas, or hemorrhagic foci can be appreciated on non-enhanced scans (Figs. 31 and 32). NECT is normal in about 30 % of patients [117].

On contrast-enhanced CT (CECT) there can be a sinus filling defect, surrounded by a dense rim of enhancement of dura and vasa vasorum: the empty triangle or empty delta sign (Fig. 32). Also enhancement of sinus wall and abnormal collateral venous drainage can be appreciated.

CTV is a rapid and accurate technique to demonstrate cerebral venous thrombosis, showing a filling defect of the veins and/or venous sinus (Fig. 32). Knowledge of the anatomy and its variants is crucial in identifying a thrombosis and differentiating it from normal variation.

The presence of arachnoid granulations in the sinus is a normal finding; they are usually small, but can obliterate the sinus and mimic venous thrombosis [118, 119] (Fig. 33).

An absent or hypoplastic transverse sinus with dominant flow on one side is a well-known variant and should not be confused with true thrombosis. A dominant right transverse sinus is more often present than left-sided prominence. Other important variations are an occipital sinus, which is more prevalent in younger chil-

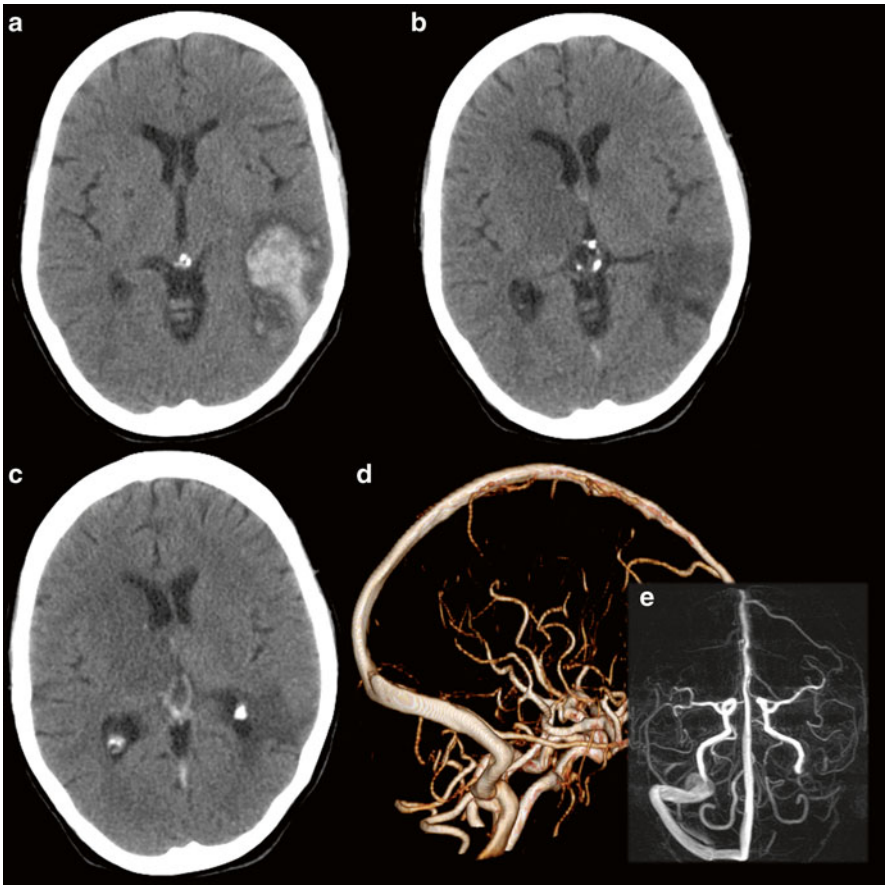

Fig. 31 A 57 y/o female patient presented with headache and mild right-sided deficit due to a large temporal lobe hematoma (**a**, NECT). Two weeks later she was readmitted because of subtle left-sided neurological deficit. NECT shows resorption of the hematoma (**b**), but swelling and hyperdensity of the right thalamus and basal ganglia are present (**c**). Hyperdensity of the internal cerebral veins and straight sinus is seen. Subsequent venous imaging (MRV) demonstrates thrombosis of the deep venous system and the left transverse sinus (**d** and **e**)

dren than adults, and is often associated with an absent or hypoplastic transverse sinus [120, 121] (Fig. 33). Sinus duplication or fenestration can mimic a thrombus (Fig. 34).

CTV is a reliable method to investigate the venous structures of the brain with high reported sensitivity [122]. Hereby source images, MIP, MPR, and VR post-processing can be used. MIP reconstructions should be handled with caution when no bone removal is used. Dense thrombi can give false-negative ratings at enhanced scans or CTV. There is a good inter-observer variability in the detection of venous thrombosis using CTV with bone removal technique [123]. DECT can also be used for automated bone removal (Figs. 31 and 34).

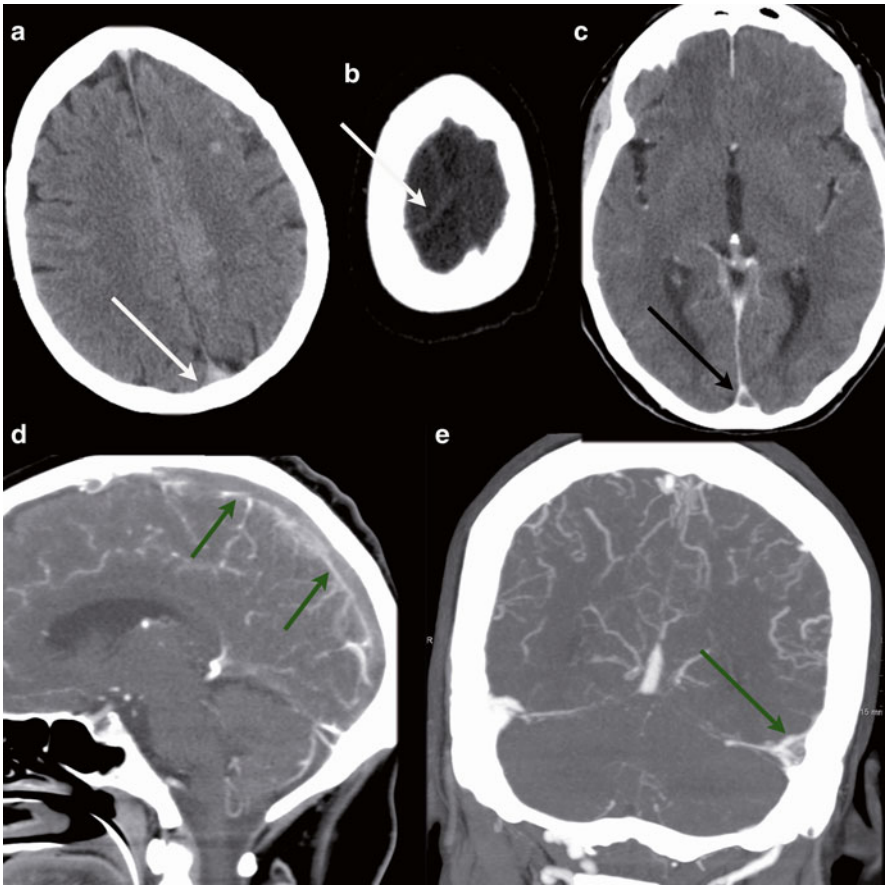

Fig. 32 A 60 y/o female with a history of gynecological malignancy presented with seizures and left-sided hemiparesis. Initial NECT shows motion artifacts and a left frontal hyperdensity, consistent with hemorrhage (**a**). There is a hyperdense aspect of the sagittal sinus and the cortical veins (*white arrows*) (**b**). Follow-up with CECT to rule out metastasis (**c**) shows an empty delta sign (*black arrow*). A CTV was performed showing a filling defect of the sagittal sinus (**d**, *green arrows*) and transverse sinus (**e**)

Demonstration of isolated cortical vein thrombosis can be difficult with CT, compared to MR, but unenhanced CT can probably aid in demonstrating the dense cord sign (Fig. 32).

4D CTA and CT perfusion can be obtained for evaluation of compensatory collateral pathways, and can be helpful in determination of the extent of thrombosis and can probably act as a prognostic indicator in sinus thrombosis [48, 124].

Therapy of cerebral sinus thrombosis is antithrombotic treatment with heparin or low-molecular-weight heparin to recanalize the sinus and to prevent propagation of the thrombus or thrombosis at remote sites of the body [125].

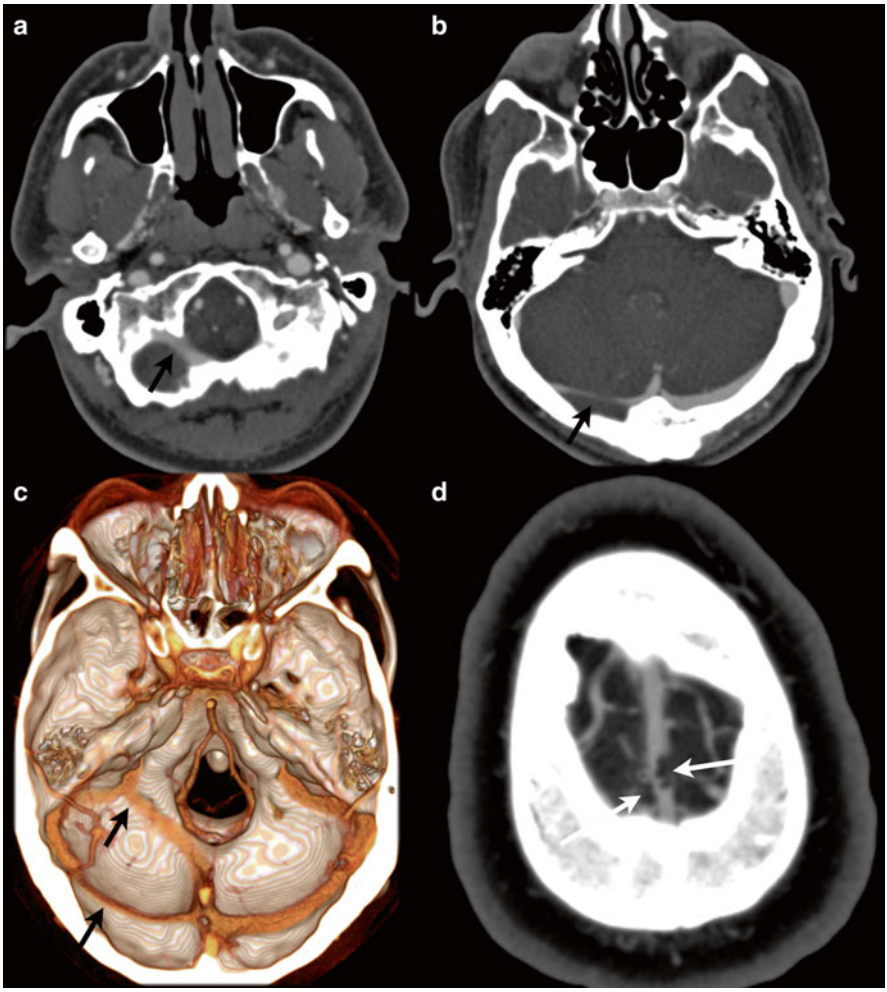

Fig. 33 Normal variants that can simulate sinus thrombosis. At the right an occipital sinus is present, draining via the marginal sinus (**a**, *black arrow*), while the right-sided transverse sinus is hypoplastic (**b, c**, *black arrow*). Arachnoid granulations are visible in the sagittal sinus (**d**, *white arrows*)

Reversible Cerebral Vasoconstriction Syndrome

Reversible cerebral vasoconstriction syndrome (RCVS) is characterized by severe acute headaches, often referred to as thunderclap headaches. These can be accompanied by acute neurological symptoms or seizures.

At imaging, diffuse segmental narrowing of the cranial arteries can be found [126–129], which resolves spontaneously within 1–3 months.

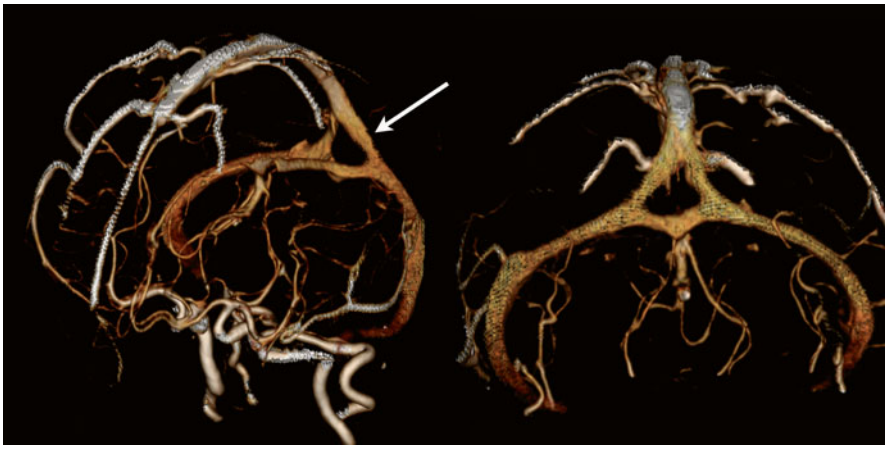

Fig. 34 Normal variants that can simulate sinus thrombosis. 3D VR from DE-CTA with bone removal of a 60 y/o patient showing duplication of the sagittal sinus at the level of the torcular (*white arrow*)

In about 60 % of the cases RCVS is secondary to a known etiology [129]. Precipitating conditions and factors associated with RCVS are postpartum period, preeclampsia and eclampsia, exposure to medications and alcohol, catecholamine-secreting tumors, trauma, as well as pathology of the large arteries like dissection, aneurysm, and dysplasia [127].

The complications of RCVS are ischemic or hemorrhagic stroke. Non-aneurysmatic subarachnoidal hemorrhage at the cortical surface can be present, but is less frequent.

Imaging characteristics are string of beads appearance of large- and middle-sized cerebral arteries. These can be depicted with angiography, but also noninvasive vascular imaging such as CTA and MRA can demonstrate these segmental narrowing of the vessels. Follow-up imaging will demonstrate the normalization of the diameters of the vessels.

Vasculitis

Cerebral vasculitis represents a heterogeneous group, characterized by inflammation and necrosis to the vessel wall [130].

Causes can be systemic autoimmune diseases such as SLE, dermatomyositis, and rheumatoid arthritis; systemic vasculitic disorders as Takayasu arteritis, Wegener's granulomatosis, and Behçet syndrome; viral and bacterial infections; or without a systemic disorder [131].

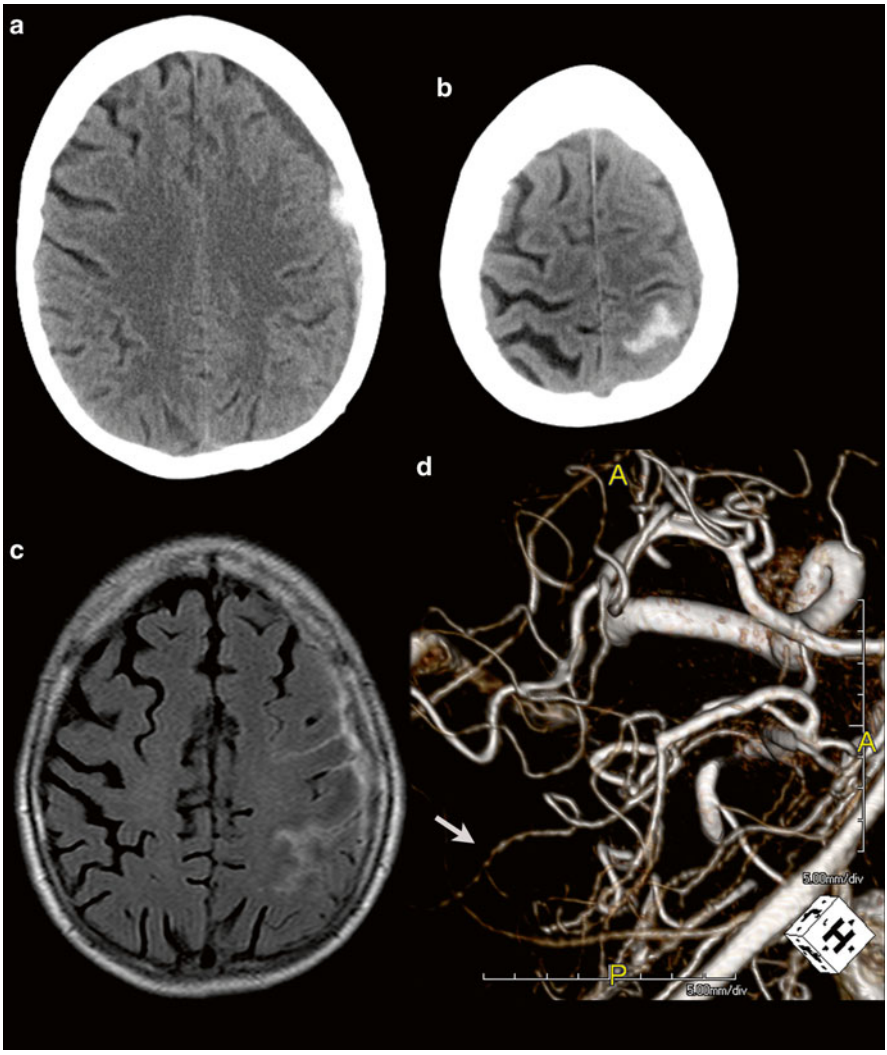

Fig. 35 A 40 y/o female with a history of systemic lupus erythematosus (SLE) presented with headache after mild trauma. NECT shows hemorrhage in the subarachnoid and subdural space at the left side (**a** and **b**). MRI FLAIR confirms the presence of hemorrhage (**c**) and subsequent MRA shows vascular calibre changes (**d**), consistent with (SLE) vasculitis

The primary angiitis of the CNS (PACNS) is a vasculitis of the brain and spinal cord, without any associated systemic disorder [132, 133].

Depending on the cause, large-, medium-, and small-sized vessels may be affected. Patients can present with stroke, headache, neurological deficits, stroke, and encephalopathy [130, 131].

Imaging can show ischemic and hemorrhagic lesions. Narrowing and dilatation of vessels can be shown on vascular imaging (Fig. 35). Therapy is dependent on the cause of the cerebral vasculitis.

Moyamoya

Moyamoya is a progressive intracranial arteriopathy, in which bilateral stenosis of the distal portion of the internal carotid arteries and their proximal branches result in transient ischemic attacks (TIA) or strokes [134]. The disease Moyamoya is named after the DSA appearance of the collateral blood vessels resembling a "puff of smoke," Moyamoya in Japanese. Patients with vasculopathy in association with other syndromes are diagnosed as Moyamoya syndrome (MMS), whereas the idiopathic variant in patients without risk factors is named Moyamoya disease (MMD).

There are two peak age groups, children of approximately 5 years old and adults between 40 and 50 years, females being affected more often than men.

The symptoms of Moyamoya are either due to the stenosis or a consequence of complications such as hemorrhage [135].

The vessel occlusion in Moyamoya is due to a combination of hyperplasia of smooth muscle cells and luminal thrombosis, contrary to atherosclerotic or inflammatory changes in other conditions.

Diagnostic imaging shows signs of ischemia or hemorrhage. CT angiography or MR angiography can show the intracranial stenoses in Moyamoya (Fig. 36). Whole-brain CT perfusion can be used to evaluate cerebral hemodynamic changes in Moyamoya before and after surgery [136].

The finding most suggestive of Moyamoya on MRI is reduced flow voids in the proximal arteries with numerous small flow voids at the level of the basal ganglia due to neovascularization (Fig. 37). The final diagnosis is based on the stenosis of the distal intracranial carotid artery, extending in the proximal anterior and middle cerebral arteries. The "classic puff of smoke" appearance is seen when collaterals start to develop (Figs. 36 and 37).

The goal of therapy in patients with Moyamoya is to prevent strokes, either by revascularization techniques or by medical therapy.

Brain Death

The diagnosis of brain death is based on clinical findings and neurological evaluation confirming deep coma and absence of brain stem reflexes. In some countries confirmative tests are required. In other countries instrumental confirmatory tests are necessary under special circumstances, as in intoxications or in patients where central nervous system depressants are given.

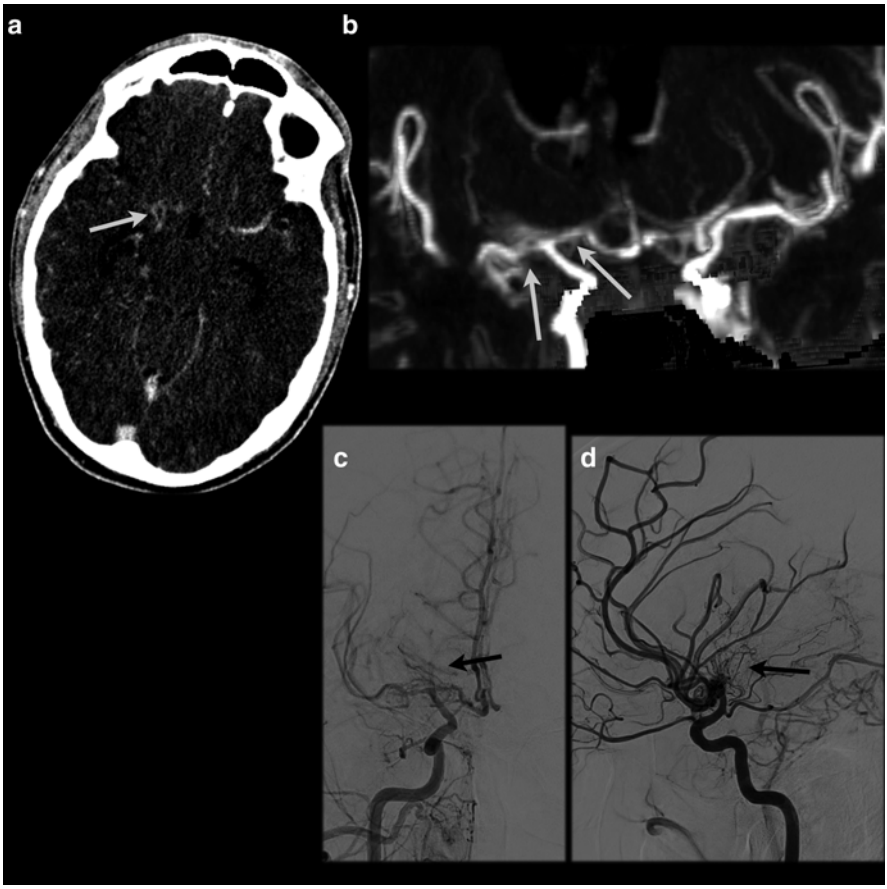

Fig. 36 A 38 y/o male with a history of cocaine abuse presented with headache, MRI (not shown) demonstrated multiple old and recent cerebral infarcts bilaterally, mainly supratentorial. Steno-occlusive disease was suspected and subsequently a CTA was performed to depict the vascular status. Source images demonstrate the collaterals filling with contrast (**a**), MIP shows occlusion of the right M1 and A1 segments with only faint visibility of collateral vessels (**b**). DSA confirms the occlusions of the M1 and A1 segments including the lenticostriatal collaterals, resembling a "puff of smoke," suggestive of Moyamoya syndrome (**c**, **d**)

The clinical diagnosis of brain death can be confirmed by demonstration of lack of brain cerebral function (EEG) or circulation (TCD, CTA, digital subtraction angiography (DSA), scintigraphy), depending on various national guidelines and rules.

CTA is emerging as an alternative to conventional cerebral DSA. In 1998 Dupas published a study on the accuracy of CTA in brain death diagnosis. Lack of opacification of the pericallosal arteries, cortical segments of the cerebral arteries, the

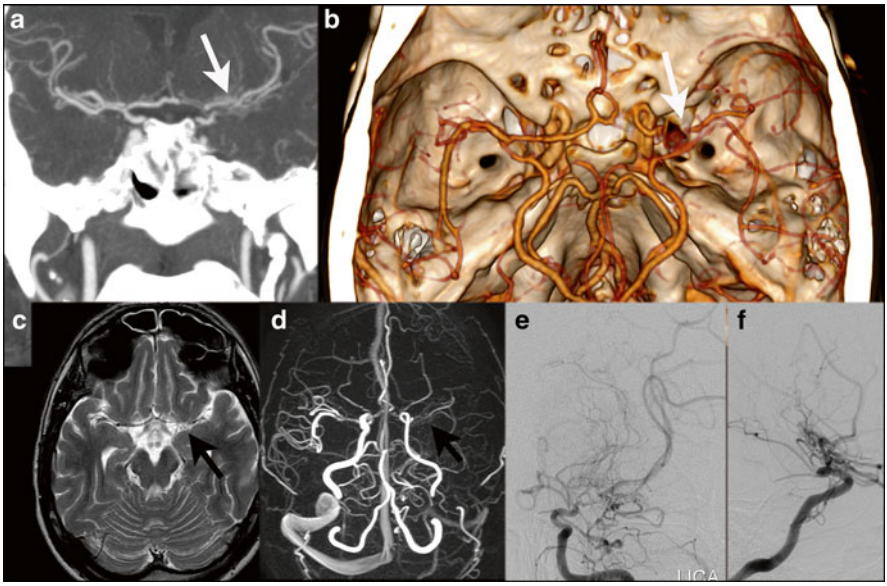

Fig. 37 A 37 y/o male initially presented with bilateral anterior thalamic infarcts as well as multiple infarctions in both hemispheres. CTA shows occlusions of the left A1 and M1 segments with collateral vessels (**a**, MIP; **b**, VR; *white arrows*). MR T2-weighted imaging demonstrates flow voids (**c**, *black arrow*) in these collaterals. MRA suggests occlusion of the left MCA (**d**). DSA confirms occlusions of the M1 and A1 segments with collaterals via the lenticostriatal arteries (**e**, **f**). These findings are consistent with Moyamoya disease

internal cerebral veins, the great cerebral vein, and the straight sinus, while opacification of the superficial temporal arteries was present, resulted in a 100 % sensitivity [137] (Fig. 38).

This led to the implementation of a 7-point CTA score for the evaluation of brain death (evaluation of both pericallosal arteries, cortical segments of the cerebral arteries, the internal cerebral veins, and one great cerebral vein), scanned in two phases after contrast administration (20 and 60 s).

Since then studies with various accuracies have been published regarding this 7-point score and other grading systems have been proposed; Frampas published a simplified 4-point grading system, with evaluation of only the cortical segments of the MCA and the internal cerebral veins and reported high sensitivity [138]. More recent absence of brain stem perfusion in CT perfusion studies in addition to CTA was studied for confirmation of brain death [139, 140], but is not yet implemented in national guidelines.

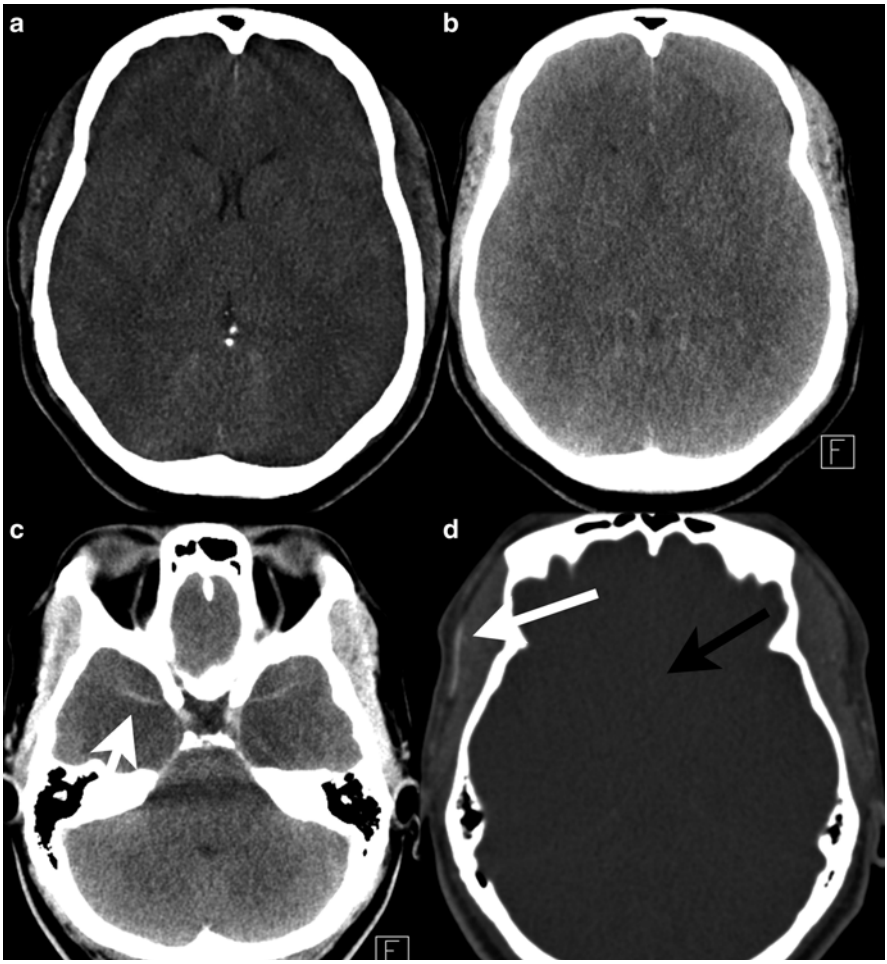

Fig. 38 Patient presented comatose with severe hyponatremia. Initial CT on day 1 (**a**) shows mass effect on the ventricles with spared gray-white matter differentiation. On day 2 (**b**) there is loss of differentiation, with severe hypodensity of the brain parenchyma, with visible left and right middle cerebral artery. The vessels appear relatively dense (**c**, *white arrow*), resembling enhancement of vessels, but this is due to the surrounding hypodensity of the brain parenchyma. This phenomenon is called a pseudo-subarachnoid hemorrhage sign. The next day 2-phase CTA was performed and demonstrates enhancement of the extracranial vessels (*white arrow*), while the intracranial arteries are not enhancing (**d**, *black arrow*). Cerebral circulation arrest was concluded

Acknowledgements Special thanks to Annika Stadler, Paul Hofman, and Christianne Hoeberigs for their valuable comments on the manuscript.

References

1. Lu L, Zhang LJ, Poon CS, et al. Digital subtraction CT angiography for detection of intracranial aneurysms: comparison with three-dimensional digital subtraction angiography. Radiology. 2012;262:605–12.
2. Guyton AC, Hall JE. Textbook of medical physiology. Philadelphia: W.B. Saunders Company; 1996.
3. Uchino A, Sawada A, Takase Y, Kudo S. MR angiography of anomalous branches of the internal carotid artery. AJR Am J Roentgenol. 2003;181:1409–14.
4. Chapman PR, Gaddamanugu S, Bag AK, Roth NT, Vattoth S. Vascular lesions of the central skull base region. Semin Ultrasound CT MR. 2013;34:459–75.
5. Iqbal S. A comprehensive study of the anatomical variations of the circle of Willis in adult human brains. J Clin Diagn Res. 2013;7:2423–7.
6. Li Q, Li J, Lv F, Li K, Luo T, Xie P. A multidetector CT angiography study of variations in the circle of Willis in a Chinese population. J Clin Neurosci. 2011;18:379–83.
7. Grossman R, Youssem D. Neuroradiology: the requisites. 2nd ed. St. Louis, MO: Mosby; 2003.
8. Dimmick SJ, Faulder KC. Normal variants of the cerebral circulation at multidetector CT angiography. Radiographics. 2009;29:1027–43.
9. Okahara M, Kiyosue H, Mori H, Tanoue S, Sainou M, Nagatomi H. Anatomic variations of the cerebral arteries and their embryology: a pictorial review. Eur Radiol. 2002;12:2548–61.
10. Sanders WP, Sorek PA, Mehta BA. Fenestration of intracranial arteries with special attention to associated aneurysms and other anomalies. AJNR Am J Neuroradiol. 1993;14:675–80.
11. Uchino A, Saito N, Okada Y, et al. Fenestrations of the intracranial vertebrobasilar system diagnosed by MR angiography. Neuroradiology. 2012;54:445–50.
12. Komiyama M, Nakajima H, Nishikawa M, Yasui T. Middle cerebral artery variations: duplicated and accessory arteries. AJNR Am J Neuroradiol. 1998;19:45–9.
13. Osborn AG. Diagnostic cerebral angiography. 2nd ed. Philadelphia: Lippincott Williams and Wilkins; 1998.
14. Uchino A, Saito N, Okada Y, et al. Persistent trigeminal artery and its variants on MR angiography. Surg Radiol Anat. 2012;34:271–6.
15. Saltzman GF. Patent primitive trigeminal artery studied by cerebral angiography. Acta Radiol. 1959;51:329–36.
16. Morris P. Practical neuroangiography. 2nd ed. Philadelphia: Lippincott Williams and Wilkins; 2007.
17. Oelerich M, Schuierer G. Primitive hypoglossal artery: demonstration with digital subtraction-, MR- and CT angiography. Eur Radiol. 1997;7:1492–4.
18. Pekcevik Y, Pekcevik R. Variations of the cerebellar arteries at CT angiography. Surg Radiol Anat. 2013;36(5):455–61.
19. Chng SM, Alvarez H, Marsot-Dupuch K, Mercier P, Lasjaunias P. "Duplicated" or "multiple" cervical internal carotid and vertebral arteries from fenestration, duplication and vasa vasorum to segmental rete. Interv Neuroradiol. 2004;10:301–7.
20. Fleischmann D. How to design injection protocols for multiple detector-row CT angiography (MDCTA). Eur Radiol. 2005;15 Suppl 5:E60–5.
21. Mihl C, Wildberger JE, Jurencak T, et al. Intravascular enhancement with identical iodine delivery rate using different iodine contrast media in a circulation phantom. Invest Radiol. 2013;48:813–8.
22. Kok M, Mihl C, Mingels AA, et al. Influence of contrast media viscosity and temperature on injection pressure in computed tomographic angiography: a phantom study. Invest Radiol. 2014;49(4):217–23.
23. Khandelwal N, Agarwal A, Kochhar R, et al. Comparison of CT venography with MR venography in cerebral sinovenous thrombosis. AJR Am J Roentgenol. 2006;187:1637–43.

24. Ozsvath RR, Casey SO, Lustrin ES, Alberico RA, Hassankhani A, Patel M. Cerebral venography: comparison of CT and MR projection venography. AJR Am J Roentgenol. 1997;169:1699–707.
25. Majoie CB, van Straten M, Venema HW, den Heeten GJ. Multisection CT venography of the dural sinuses and cerebral veins by using matched mask bone elimination. AJNR Am J Neuroradiol. 2004;25:787–91.
26. Hounsfield GN. Computerized transverse axial scanning (tomography). 1. Description of system. Br J Radiol. 1973;46:1016–22.
27. Coursey CA, Nelson RC, Boll DT, et al. Dual-energy multidetector CT: how does it work, what can it tell us, and when can we use it in abdominopelvic imaging? Radiographics. 2010;30:1037–55.
28. Bushberg JT, Seibert JA, Leidholdt EM, Boone JM. The essential physics of medical imaging. Philadelphia: Lippincott Williams and Wilkins; 2002.
29. Postma AA, Hofman PA, Stadler AA, van Oostenbrugge RJ, Tijssen MP, Wildberger JE. Dual-energy CT of the brain and intracranial vessels. AJR Am J Roentgenol. 2012;199:S26–33.
30. Tijssen MP, Hofman PA, Stadler AA, et al. The role of dual energy CT in differentiating between brain haemorrhage and contrast medium after mechanical revascularisation in acute ischaemic stroke. Eur Radiol. 2013;24(4):834–40.
31. Morhard D, Ertl L, Gerdsmeier-Petz W, Ertl-Wagner B, Schulte-Altedorneburg G. Dual-energy CT immediately after endovascular stroke intervention: prognostic implications. Cardiovasc Intervent Radiol. 2013;37(5):1171–8.
32. Phan CM, Yoo AJ, Hirsch JA, Nogueira RG, Gupta R. Differentiation of hemorrhage from iodinated contrast in different intracranial compartments using dual-energy head CT. AJNR Am J Neuroradiol. 2012;33:1088–94.
33. Kim SJ, Lim HK, Lee HY, et al. Dual-energy CT in the evaluation of intracerebral hemorrhage of unknown origin: differentiation between tumor bleeding and pure hemorrhage. AJNR Am J Neuroradiol. 2012;33:865–72.
34. Stolzmann P, Winklhofer S, Schwendener N, Alkadhi H, Thali MJ, Ruder TD. Monoenergetic computed tomography reconstructions reduce beam hardening artifacts from dental restorations. Forensic Sci Med Pathol. 2013;9:327–32.
35. Nicolaou S, Liang T, Murphy DT, Korzan JR, Ouellette H, Munk P. Dual-energy CT: a promising new technique for assessment of the musculoskeletal system. AJR Am J Roentgenol. 2012;199:S78–86.
36. Apfaltrer P, Sudarski S, Schneider D, et al. Value of monoenergetic low-kV dual energy CT datasets for improved image quality of CT pulmonary angiography. Eur J Radiol. 2014;83:322–8.
37. Sudarski S, Apfaltrer P, Nance W, et al. Optimization of keV-settings in abdominal and lower extremity dual-source dual-energy CT angiography determined with virtual monoenergetic imaging. Eur J Radiol. 2013;82:e574–81.
38. Bahner ML, Bengel A, Brix G, Zuna I, Kauczor HU, Delorme S. Improved vascular opacification in cerebral computed tomography angiography with 80 kVp. Invest Radiol. 2005;40:229–34.
39. Cho ES, Chung TS, Oh DK, et al. Cerebral computed tomography angiography using a low tube voltage (80 kVp) and a moderate concentration of iodine contrast material: a quantitative and qualitative comparison with conventional computed tomography angiography. Invest Radiol. 2012;47:142–7.
40. Lell MM, Ruehm SG, Kramer M, et al. Cranial computed tomography angiography with automated bone subtraction: a feasibility study. Invest Radiol. 2009;44:38–43.
41. Gratama van Andel HA, Venema HW, Streekstra GJ, et al. Removal of bone in CT angiography by multiscale matched mask bone elimination. Med Phys. 2007;34:3711–23.
42. Morhard D, Fink C, Graser A, Reiser MF, Becker C, Johnson TR. Cervical and cranial computed tomographic angiography with automated bone removal: dual energy computed tomography versus standard computed tomography. Invest Radiol. 2009;44:293–7.

43. Zhang LJ, Wu SY, Poon CS, et al. Automatic bone removal dual-energy CT angiography for the evaluation of intracranial aneurysms. J Comput Assist Tomogr. 2010;34:816–24.
44. Watanabe Y, Uotani K, Nakazawa T, et al. Dual-energy direct bone removal CT angiography for evaluation of intracranial aneurysm or stenosis: comparison with conventional digital subtraction angiography. Eur Radiol. 2009;19:1019–24.
45. Menon BK, Smith EE, Coutts SB, et al. Leptomeningeal collaterals are associated with modifiable metabolic risk factors. Ann Neurol. 2013;74:241–8.
46. Willems PW, Taeshineetanakul P, Schenk B, Brouwer PA, Terbrugge KG, Krings T. The use of 4D-CTA in the diagnostic work-up of brain arteriovenous malformations. Neuroradiology. 2012;54:123–31.
47. Frolich AM, Wolff SL, Psychogios MN, et al. Time-resolved assessment of collateral flow using 4D CT angiography in large-vessel occlusion stroke. Eur Radiol. 2014;24(2):390–6.
48. Ono Y, Abe K, Suzuki K, et al. Usefulness of 4D-CTA in the detection of cerebral dural sinus occlusion or stenosis with collateral pathways. Neuroradiol J. 2013;26:428–38.
49. Wang H, Ye X, Gao X, Zhou S, Lin Z. The diagnosis of arteriovenous malformations by 4D-CTA: a clinical study. J Neuroradiol. 2013;41:117–23.
50. Frolich AM, Psychogios MN, Klotz E, Schramm R, Knauth M, Schramm P. Angiographic reconstructions from whole-brain perfusion CT for the detection of large vessel occlusion in acute stroke. Stroke. 2012;43:97–102.
51. Beijer TR, van Dijk EJ, de Vries J, Vermeer SE, Prokop M, Meijer FJ. 4D-CT angiography differentiating arteriovenous fistula subtypes. Clin Neurol Neurosurg. 2013;115:1313–6.
52. Fujiwara H, Momoshima S, Akiyama T, Kuribayashi S. Whole-brain CT digital subtraction angiography of cerebral dural arteriovenous fistula using 320-detector row CT. Neuroradiology. 2013;55:837–43.
53. Willems PW, Brouwer PA, Barfett JJ, terBrugge KG, Krings T. Detection and classification of cranial dural arteriovenous fistulas using 4D-CT angiography: initial experience. AJNR Am J Neuroradiol. 2011;32:49–53.
54. Frolich AM, Schrader D, Klotz E, et al. 4D CT angiography more closely defines intracranial thrombus burden than single-phase CT angiography. AJNR Am J Neuroradiol. 2013;34:1908–13.
55. Smit EJ, Vonken EJ, van Seeters T, et al. Timing-invariant imaging of collateral vessels in acute ischemic stroke. Stroke. 2013;44:2194–9.
56. Prokop M, Galanski M. Spiral and multislice computed tomography of the body. Stuttgart: Thieme; 2003.
57. Gonzalez R, Hirsch J, Lev M, Schaefer P, Schwamm L. Acute ischemic stroke. 2nd ed. Heidelberg: Springer; 2011.
58. Fishman EK, Ney DR, Heath DG, Corl FM, Horton KM, Johnson PT. Volume rendering versus maximum intensity projection in CT angiography: what works best, when, and why. Radiographics. 2006;26:905–22.
59. Han A, Yoon DY, Chang SK, et al. Accuracy of CT angiography in the assessment of the circle of Willis: comparison of volume-rendered images and digital subtraction angiography. Acta Radiol. 2011;52:889–93.
60. van der Lugt A, Buter TC, Govaere F, Siepman DA, Tanghe HL, Dippel DW. Accuracy of CT angiography in the assessment of a fetal origin of the posterior cerebral artery. Eur Radiol. 2004;14:1627–33.
61. Marnane M, Duggan CA, Sheehan OC, et al. Stroke subtype classification to mechanism-specific and undetermined categories by TOAST, A-S-C-O, and causative classification system: direct comparison in the North Dublin population stroke study. Stroke. 2010;41:1579–86.
62. Chen PH, Gao S, Wang YJ, Xu AD, Li YS, Wang D. Classifying ischemic stroke, from TOAST to CISS. CNS Neurosci Ther. 2012;18:452–6.
63. Thomas GN, Chen XY, Lin JW, et al. Middle cerebral artery stenosis increased the risk of vascular disease mortality among type 2 diabetic patients. Cerebrovasc Dis. 2008;25:261–7.
64. Gorelick P, Han J, Huang Y, Wong KSL. Epidemiology. In: Kim JS, Caplan LR, Wong KSL, editors. Intracranial atherosclerosis. West Sussex: Blackwell Publishing Ltd.; 2008. p. 33–44.

65. Qureshi AI, Feldmann E, Gomez CR, et al. Intracranial atherosclerotic disease: an update. Ann Neurol. 2009;66:730–8.
66. Mattioni A, Cenciarelli S, Biessels GJ, van Seeters T, Algra A, Ricci S. Prevalence of intracranial large artery stenosis and occlusion in patients with acute ischaemic stroke or TIA. Neurol Sci. 2013;35(3):349–55.
67. Marquering HA, Nederkoorn PJ, Bleeker L, van den Berg R, Majoie CB. Intracranial carotid artery disease in patients with recent neurological symptoms: high prevalence on CTA. Neuroradiology. 2012;55:179–85.
68. Chen XY, Wong KS, Lam WW, Zhao HL, Ng HK. Middle cerebral artery atherosclerosis: histological comparison between plaques associated with and not associated with infarct in a postmortem study. Cerebrovasc Dis. 2008;25:74–80.
69. Chen XY, Lam WW, Ng HK, Fan YH, Wong KS. Intracranial artery calcification: a newly identified risk factor of ischemic stroke. J Neuroimaging. 2007;17:300–3.
70. Wong KSL, Caplan LR, Kim JS. Stroke mechanisms. In: Kim JS, Caplan LR, Wong KSL, editors. Intracranial atherosclerosis. West Sussex: Blackwell Publishing Ltd.; 2008. p. 33–44.
71. Bhatia R, Bal SS, Shobha N, et al. CT angiographic source images predict outcome and final infarct volume better than noncontrast CT in proximal vascular occlusions. Stroke. 2011;42:1575–80.
72. Puetz V, Dzialowski I, Hill MD, Demchuk AM. The Alberta stroke program early CT score in clinical practice: what have we learned? Int J Stroke. 2009;4:354–64.
73. Kucinski T. Unenhanced CT and acute stroke physiology. Neuroimaging Clin N Am. 2005;15:397–407. xi–xii.
74. Duffis EJ, Jethwa P, Gupta G, Bonello K, Gandhi CD, Prestigiacomo CJ. Accuracy of computed tomographic angiography compared to digital subtraction angiography in the diagnosis of intracranial stenosis and its impact on clinical decision-making. J Stroke Cerebrovasc Dis. 2013;22:1013–7.
75. Liu Q, Huang J, Degnan AJ, et al. Comparison of high-resolution MRI with CT angiography and digital subtraction angiography for the evaluation of middle cerebral artery atherosclerotic steno-occlusive disease. Int J Cardiovasc Imaging. 2013;29:1491–8.
76. Saake M, Goelitz P, Struffert T, et al. Comparison of conventional CTA and volume perfusion CTA in evaluation of cerebral arterial vasculature in acute stroke. AJNR Am J Neuroradiol. 2012;33:2068–73.
77. Hassan AE, Rostambeigi N, Chaudhry SA, et al. Combination of noninvasive neurovascular imaging modalities in stroke patients: patterns of use and impact on need for digital subtraction angiography. J Stroke Cerebrovasc Dis. 2013;22:e53–8.
78. Nguyen-Huynh MN, Wintermark M, English J, et al. How accurate is CT angiography in evaluating intracranial atherosclerotic disease? Stroke. 2008;39:1184–8.
79. Feldmann E, Wilterdink JL, Kosinski A, et al. The stroke outcomes and neuroimaging of intracranial atherosclerosis (SONIA) trial. Neurology. 2007;68:2099–106.
80. Nambiar V, Sohn SI, Almekhlafi MA, et al. CTA collateral status and response to recanalization in patients with acute ischemic stroke. AJNR Am J Neuroradiol. 2013;35(5):884–90.
81. Suzuki M, Ozaki Y, Komura S, Nakanishi A. Intracranial carotid calcification on CT images as an indicator of atheromatous plaque: analysis of high-resolution CTA images using a 64-multidetector scanner. Radiat Med. 2007;25:378–85.
82. Sohn YH, Cheon HY, Jeon P, Kang SY. Clinical implication of cerebral artery calcification on brain CT. Cerebrovasc Dis. 2004;18:332–7.
83. Kassab MY, Gupta R, Majid A, et al. Extent of intra-arterial calcification on head CT is predictive of the degree of intracranial atherosclerosis on digital subtraction angiography. Cerebrovasc Dis. 2009;28:45–8.
84. Park KY, Kim YB, Moon HS, Suh BC, Chung PW. Association between cerebral arterial calcification and brachial-ankle pulse wave velocity in patients with acute ischemic stroke. Eur Neurol. 2009;61:364–70.
85. Bleeker L, Marquering HA, van den Berg R, Nederkoorn PJ, Majoie CB. Semi-automatic quantitative measurements of intracranial internal carotid artery stenosis and calcification using CT angiography. Neuroradiology. 2011;54:919–27.

86. Pico F, Dufouil C, Levy C, et al. Longitudinal study of carotid atherosclerosis and white matter hyperintensities: the EVA-MRI cohort. Cerebrovasc Dis. 2002;14:109–15.
87. Chutinet A, Biffi A, Kanakis A, Fitzpatrick KM, Furie KL, Rost NS. Severity of leukoaraiosis in large vessel atherosclerotic disease. AJNR Am J Neuroradiol. 2012;33:1591–5.
88. Prince EA, Ahn SH, Soares GM. Intra-arterial stroke management. Semin Intervent Radiol. 2013;30:282–7.
89. Flemming KD, Brown Jr RD. Secondary prevention strategies in ischemic stroke: identification and optimal management of modifiable risk factors. Mayo Clin Proc. 2004;79:1330–40.
90. Romero JM, Artunduaga M, Forero NP, et al. Accuracy of CT angiography for the diagnosis of vascular abnormalities causing intraparenchymal hemorrhage in young patients. Emerg Radiol. 2009;16:195–201.
91. Wada R, Aviv RI, Fox AJ, et al. CT angiography "spot sign" predicts hematoma expansion in acute intracerebral hemorrhage. Stroke. 2007;38:1257–62.
92. Rizos T, Dorner N, Jenetzky E, et al. Spot signs in intracerebral hemorrhage: useful for identifying patients at risk for hematoma enlargement? Cerebrovasc Dis. 2013;35:582–9.
93. Hallevi H, Abraham AT, Barreto AD, Grotta JC, Savitz SI. The spot sign in intracerebral hemorrhage: the importance of looking for contrast extravasation. Cerebrovasc Dis. 2013;29:217–20.
94. Gross BA, Frerichs KU, Du R. Sensitivity of CT angiography, T2-weighted MRI, and magnetic resonance angiography in detecting cerebral arteriovenous malformations and associated aneurysms. J Clin Neurosci. 2012;19:1093–5.
95. Gross BA, Du R. Diagnosis and treatment of vascular malformations of the brain. Curr Treat Options Neurol. 2014;16:279.
96. Spetzler RF, Martin NA. A proposed grading system for arteriovenous malformations. J Neurosurg. 1986;65:476–83.
97. Mikami T, Hirano T, Sugino T, et al. Presurgical planning for arteriovenous malformations using multidetector row CT. Neurosurg Rev. 2012;35:393–9. discussion 399–400.
98. Bradac O, Charvat F, Benes V. Treatment for brain arteriovenous malformation in the 1998–2011 period and review of the literature. Acta Neurochir (Wien). 2013;155:199–209.
99. Gandhi D, Chen J, Pearl M, Huang J, Gemmete JJ, Kathuria S. Intracranial dural arteriovenous fistulas: classification, imaging findings, and treatment. AJNR Am J Neuroradiol. 2012;33:1007–13.
100. Cohen SD, Goins JL, Butler SG, Morris PP, Browne JD. Dural arteriovenous fistula: diagnosis, treatment, and outcomes. Laryngoscope. 2009;119:293–7.
101. Lee CW, Huang A, Wang YH, Yang CY, Chen YF, Liu HM. Intracranial dural arteriovenous fistulas: diagnosis and evaluation with 64-detector row CT angiography. Radiology. 2010;256:219–28.
102. Mark DG, Hung YY, Offerman SR, et al. Nontraumatic subarachnoid hemorrhage in the setting of negative cranial computed tomography results: external validation of a clinical and imaging prediction rule. Ann Emerg Med. 2013;62:1–10.e11.
103. Backes D, Rinkel GJ, Kemperman H, Linn FH, Vergouwen MD. Time-dependent test characteristics of head computed tomography in patients suspected of nontraumatic subarachnoid hemorrhage. Stroke. 2012;43:2115–9.
104. Suarez JI, Tarr RW, Selman WR. Aneurysmal subarachnoid hemorrhage. N Engl J Med. 2006;354:387–96.
105. Chen W, Xing W, Peng Y, He Z, Wang C, Wang Q. Cerebral aneurysms: accuracy of 320-detector row nonsubtracted and subtracted volumetric CT angiography for diagnosis. Radiology. 2013;269:841–9.
106. Villablanca JP, Jahan R, Hooshi P, et al. Detection and characterization of very small cerebral aneurysms by using 2D and 3D helical CT angiography. AJNR Am J Neuroradiol. 2002;23:1187–98.
107. Pechlivanis I, Schmieder K, Scholz M, Konig M, Heuser L, Harders A. 3-Dimensional computed tomographic angiography for use of surgery planning in patients with intracranial aneurysms. Acta Neurochir (Wien). 2005;147:1045–53. discussion 1053.

108. Karamessini MT, Kagadis GC, Petsas T, et al. CT angiography with three-dimensional techniques for the early diagnosis of intracranial aneurysms. Comparison with intra-arterial DSA and the surgical findings. Eur J Radiol. 2004;49:212–23.
109. Machida H, Takeuchi H, Tanaka I, et al. Improved delineation of arteries in the posterior fossa of the brain by model-based iterative reconstruction in volume-rendered 3D CT angiography. AJNR Am J Neuroradiol. 2013;34:971–5.
110. Ramasundara S, Mitchell PJ, Dowling RJ. Bone subtraction CT angiography for the detection of intracranial aneurysms. J Med Imaging Radiat Oncol. 2010;54:526–33.
111. Thines L, Dehdashti AR, Howard P, et al. Postoperative assessment of clipped aneurysms with 64-slice computerized tomography angiography. Neurosurgery. 2010;67:844–53. discussion 853–4.
112. Wallace RC, Karis JP, Partovi S, Fiorella D. Noninvasive imaging of treated cerebral aneurysms, Part II: CT angiographic follow-up of surgically clipped aneurysms. AJNR Am J Neuroradiol. 2007;28:1207–12.
113. Pfefferkorn T, Crassard I, Linn J, Dichgans M, Boukobza M, Bousser MG. Clinical features, course and outcome in deep cerebral venous system thrombosis: an analysis of 32 cases. J Neurol. 2009;256:1839–45.
114. Leach JL, Fortuna RB, Jones BV, Gaskill-Shipley MF. Imaging of cerebral venous thrombosis: current techniques, spectrum of findings, and diagnostic pitfalls. Radiographics. 2006;26 Suppl 1:S19–41. discussion S42–3.
115. Bousser MG, Ferro JM. Cerebral venous thrombosis: an update. Lancet Neurol. 2007;6:162–70.
116. Linn J, Pfefferkorn T, Ivanicova K, et al. Noncontrast CT in deep cerebral venous thrombosis and sinus thrombosis: comparison of its diagnostic value for both entities. AJNR Am J Neuroradiol. 2009;30:728–35.
117. Masuhr F, Mehraein S, Einhaupl K. Cerebral venous and sinus thrombosis. J Neurol. 2004;251:11–23.
118. Dior U, Shelef I, Joshua B, Gluck O, Puterman M. Arachnoid granulation masquerading as lateral sinus vein thrombosis. Isr Med Assoc J. 2012;14:198–9.
119. Choi HJ, Cho CW, Kim YS, Cha JH. Giant arachnoid granulation misdiagnosed as transverse sinus thrombosis. J Korean Neurosurg Soc. 2008;43:48–50.
120. Ayanzen RH, Bird CR, Keller PJ, McCully FJ, Theobald MR, Heiserman JE. Cerebral MR venography: normal anatomy and potential diagnostic pitfalls. AJNR Am J Neuroradiol. 2000;21:74–8.
121. Widjaja E, Griffiths PD. Intracranial MR venography in children: normal anatomy and variations. AJNR Am J Neuroradiol. 2004;25:1557–62.
122. Wetzel S, Boos M, Bongartz G, Radu EW. Selection of patients for carotid thromboendarterectomy: the role of magnetic resonance angiography. J Comput Assist Tomogr. 1999;23 Suppl 1:S91–4.
123. Gratama van Andel HA, van Boven LJ, van Walderveen MA, et al. Interobserver variability in the detection of cerebral venous thrombosis using CT venography with matched mask bone elimination. Clin Neurol Neurosurg. 2009;111:717–23.
124. Gupta RK, Bapuraj JR, Khandelwal N, Khurana D. Prognostic indices for cerebral venous thrombosis on CT perfusion: a prospective study. Eur J Radiol. 2014;83:185–90.
125. Einhaupl K, Stam J, Bousser MG, et al. EFNS guideline on the treatment of cerebral venous and sinus thrombosis in adult patients. Eur J Neurol. 2010;17:1229–35.
126. Ducros A. Reversible cerebral vasoconstriction syndrome. Lancet Neurol. 2012;11:906–17.
127. Ducros A, Boukobza M, Porcher R, Sarov M, Valade D, Bousser MG. The clinical and radiological spectrum of reversible cerebral vasoconstriction syndrome. A prospective series of 67 patients. Brain. 2007;130:3091–101.
128. Mawet J, Boukobza M, Franc J, et al. Reversible cerebral vasoconstriction syndrome and cervical artery dissection in 20 patients. Neurology. 2013;81:821–4.
129. Robert T, Kawkabani Marchini A, Oumarou G, Uske A. Reversible cerebral vasoconstriction syndrome identification of prognostic factors. Clin Neurol Neurosurg. 2013;115:2351–7.

130. Berlit P. Diagnosis and treatment of cerebral vasculitis. Ther Adv Neurol Disord. 2010;3:29–42.
131. Kraemer M, Berlit P. Systemic, secondary and infectious causes for cerebral vasculitis: clinical experience with 16 new European cases. Rheumatol Int. 2010;30:1471–6.
132. Birnbaum J, Hellmann DB. Primary angiitis of the central nervous system. Arch Neurol. 2009;66:704–9.
133. de Boysson H, Zuber M, Naggara O et al. Revised primary angiitis of the central nervous system: description of the first 52 adults enrolled in the french COVAC' cohort. Arthritis Rheum 2014.
134. Kronenburg A, Braun KP, van der Zwan A, Klijn CJ. Recent advances in Moyamoya disease: pathophysiology and treatment. Curr Neurol Neurosci Rep. 2014;14:423.
135. Scott RM, Smith ER. Moyamoya disease and Moyamoya syndrome. N Engl J Med. 2009;360:1226–37.
136. Zhang J, Wang J, Geng D, Li Y, Song D, Gu Y. Whole-brain CT perfusion and CT angiography assessment of Moyamoya disease before and after surgical revascularization: preliminary study with 256-slice CT. PLoS One. 2013;8:e57595.
137. Dupas B, Gayet-Delacroix M, Villers D, Antonioli D, Veccherini MF, Soulillou JP. Diagnosis of brain death using two-phase spiral CT. AJNR Am J Neuroradiol. 1998;19:641–7.
138. Frampas E, Videcoq M, de Kerviler E, et al. CT angiography for brain death diagnosis. AJNR Am J Neuroradiol. 2009;30:1566–70.
139. Shankar JJ, Vandorpe R. CT perfusion for confirmation of brain death. AJNR Am J Neuroradiol. 2013;34:1175–9.
140. Sawicki M, Bohatyrewicz R, Safranow K, et al. Dynamic evaluation of stasis filling phenomenon with computed tomography in diagnosis of brain death. Neuroradiology. 2013;55:1061–9.

Intravenous Flat Panel Detector CT Angiography for the Assessment of Intracranial Arteries

Jin Pyeong Jeon and Seung Hun Sheen

Introduction

Atherosclerotic intracranial arterial stenosis is an important cause of ischemic stroke [1, 2]. Main predictor of vulnerable intracranial stenosis includes high severity (>70 % luminal narrowing), extent of disease (number of intracranial stenosis), disease progression, and presence of symptomaticity [2]. Although cerebral angiography is the most accurate method for estimating stenosis, procedural complications and invasive nature can be concerns. Accordingly, noninvasive methods such as magnetic resonance angiography (MRA), computed tomography angiography (CTA), and transcranial Doppler (TCD) have been used alternatively.

Intravenous flat panel detector CT (IV FDCT) angiography is an emerging technology for obtaining CT-like images from C-arm biplane angiography system. Various terminologies have been used such as C-arm cone-beam CT (CBCT) [3], flat panel detector CT (FPCT) [4, 5], and angiographic CT, although each definition is somewhat different [6]. IV FDCT has been increasingly studied from technical characteristics in comparison with CT to cerebral hemodynamics in acute stroke models [4, 6–8]. In this chapter, we reviewed IV FDCT in depicting intracranial arteries from its image acquisition and clinical applications to its limitations.

J.P. Jeon, M.D.
Department of Neurosurgery, Hallym University College of Medicine, Chuncheon, South Korea

S.H. Sheen, M.D. (✉)
Department of Neurosurgery, Bundang Jesaeng Hospital, Seoul, South Korea
e-mail: nssheen@gmail.com

R. Trivedi et al. (eds.), *3D Imaging Technologies in Atherosclerosis*,
DOI 10.1007/978-1-4899-7618-5_5

Technology of IV FDCT Systems

IV FDCT systems include X-ray source and detector, mechanical setup, and image reconstruction [9]. In early stage, image intensifiers were used for making CT-like images from C-arm system. However, technical limitations such as low dynamic range and distorted image and high-contrast vessel image mainly based on intra-arterial injection contributed to low use of IV FDCT in the clinical circumstances [9]. On the contrary, flat panel detector allows for better image description including soft-tissue demarcation due to its high dynamic range and higher dose efficiency. Because signal response of flat detector illustrates a linear correlation to a function of dose, high dynamic range can allow a wide range of dose requirement without risking wrong exposure. For generating vascular image, high dynamic range is more suitable from fluoroscopy of approximately 10 nGy to DSA of approximately 5 μGy [10]. Two elements, thickness of the screen and spatial resolution, are important issues for generating high-quality images [10]. Screen thickness can increase X-ray absorption; however, it can also decrease spatial resolution. During the conversion of X-ray quanta to electrical signals, light diffusion can occur. Two flat detector technologies, direct or indirect conversion of X-ray to electrical signals, are present. Although a direct converter can inhibit decrease in spatial resolution than that of an indirect converter, it is particularly adaptable to mammography due to low-lying K-edge [10, 11]. An indirect converter has been widely used for angiography and fluoroscopy. Especially needle-type phosphor-structured screen was superior to unstructured screen in increasing spatial resolution, because light can be guided by the needle [9].

The image parameters and dosimetry of the IV FDCT are summarized in Table 1 [12]. The acquisition mode parameters are somewhat different among the institutions. White et al. [12] used 10-s high-dose acquisition mode than 20-s mode for routine practice. They thought that 10-s high dose had a similar image noise (1.00

Table 1 Imaging and dosimetry parameters of the IV FDCT [12]

	10-s acquisition		20-s acquisition
	Low dose	High dose	High dose
Rotation times (s)	10	10	20
Rotation angle (°)	219	219	219
Increment	0.8	0.8	0.4
No. of frames	273	273	538
$CTDI_{vol}$ (mGy)	12.3	35.1	59.5
DAP (μGy m^2)	856	2,382	4,289
Effective dose (mSv)			
E_{dip} method	0.4	1.1	1.9
DAP method	0.24	0.67	1.2

DAP dose area product, *CTDI* CT dose index, E_{dip} effective dose conversion factor

vs. 0.74) and nonuniformity (HU) (−4.0 vs. −3.8) compared to those of 20-s acquisition mode. However, images with 20-s acquisition mode are better than those with 10-s mode in general although it requires higher dose and longer reconstruction time [12], 20-s acquisition mode was done in our institution. Contrast agent of 80 mL mixed with saline of 40 mL was injected through an anterior cubital vein with a flow rate of 5 mL/s. Then IV FDCT images were obtained according to the following parameters: 0.4 increment, 200° total angle, 538 total projections, 20-s rotation, and 18-s X-ray time delay with a radiation dose of 35 mGy (manufacturer's information) [13]. 30 × 40 cm detector which can cover a nontruncated volume about 22 cm in plane matrix size and 16 cm in *z*-direction was used [7]. Postprocessing of the rotational image data to a volume dataset is done using a Leonardo DynaCT dedicated workstation equipped with InSpace 3D software (Siemens, Erlangen, Germany) [7, 13]. A volume dataset about 400–500 sections with a 512×512 matrix with single-section thickness ranges from 0.2 to 0.3 mm can be made [7]. The images given as maximum-intensity-projection images in the axial, coronal, and sagittal planes with various section thicknesses can be reconstructed for analysis. In addition, volume-rendering technique (VRT) images also can be reconstructed.

Clinical Applications

Evaluation of Atherosclerotic Intracranial Arterial Stenosis

Accurate assessment of atherosclerotic major intracranial stenosis in terms of severity and stenosis length is important for early detection and its proper treatment. The requirements of the ideal noninvasive test for measuring intracranial stenosis is as follows: (1) good depiction of lesions including stenosis severity and length, and occlusion level; (2) a shorter canning time; (3) good delineation of calcification in the arterial wall; and (4) subsequent endovascular treatment after symptomatic stenosis in emergent situation. IV FDCT has shown to have a good depiction of lesion location and collateral circulation in the single acquisition. Jeon et al. [13] reported that IV FDCT showed a sensitivity of 97.6 %, specificity of 96.9 %, and negative predictive value (NPV) of 96.9 % for identifying stenosis ≥50 % with DSA as the reference value. For detecting stenosis ≥70 %, in particular, a sensitivity of 91.9 %, specificity of 98.2 %, and NPV of 97.4 were estimated. Good correlation of the measuring stenosis severity between the two tests was observed according to direction (horizontal segments vs. vertical segments) and circulation (anterior circulation vs. posterior circulation) [13]. Length discrepancy (IV FDCT–DSA, in millimeters) was more pronounced in higher stenosis, but the result was not statistically significant [13]. Such a discrepancy could be originated from the difference in hemodynamics and attenuation of the contrast agents. Assessment of stenosis length after the point of maximal

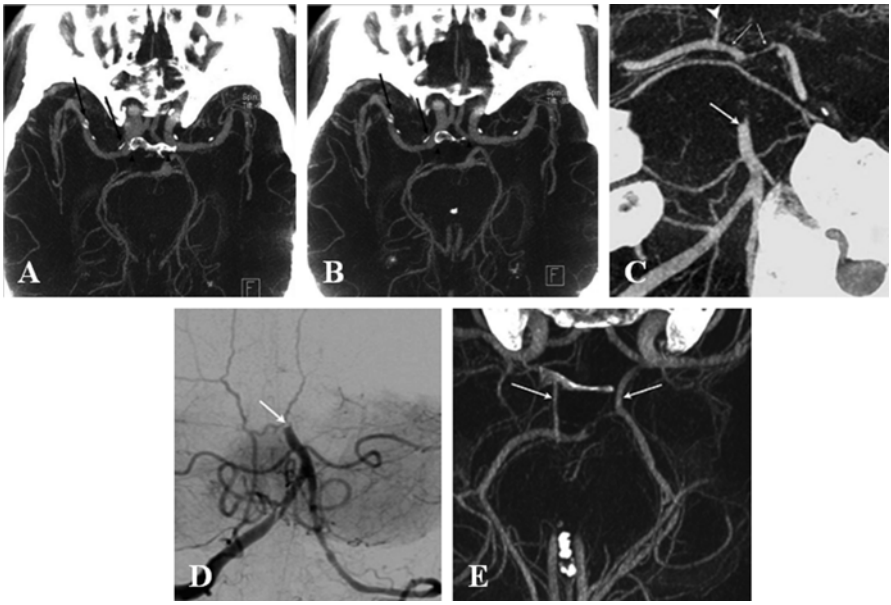

Fig. 1 IV FDCT MIP axial images show a clear depiction of the vascular lumen from circumferential calcification (*arrows*) without superimposition of bone (*arrowheads*) (**a** and **b**) [13]. IV FDCT MPR coronal image (**c**) reveals the occlusion of the middle third of the basilar artery (*arrow*) which is consistent with that of DSA (**d**). The right posterior communicating artery (*arrowhead*) and both P1 are well visualized. IV FDCT MPR axial image shows clear depiction of the both posterior communicating artery (*arrows*) [16]

narrowing could be influenced by the flow velocity and stenosis severity [13, 14]. In addition, diluted contrast agent of the IV FDCT may fill the vessel lumen more uniformly than DSA due to their similarity of attenuation values for contrast agents and blood [15].

IV FDCT can allow information on various vascular territories and collateral flow in a single acquisition [16]. Additionally, clear visualization of the calcification of the arterial wall, which can be of limited value in the DSA images, can be obtained (Fig. 1a, b). Because calcification of the arterial wall can be related to incomplete stent deploy [17, 18], an accurate detection of calcification is necessary for selecting treatment methods [19]. Blanc et al. [16] and Riedel et al. [20] reported that IV FDCT shows good depiction of occlusion level, clot length, collateral vessels, and patency of anterior and posterior communicating arteries in a single acquisition (Fig. 1c, d, f). Relative complete filling of the collateral vessels and reconstructed images in various planes in IV FDCT allows better depiction of the arteries beyond the occlusion level, clot length, and stenosis nature than DSA [16], which leads to decreased amount of contrast and radiation dose [14]. IV FDCT can

also be conducted to exclude intracranial hemorrhage in patients suspected of acute cerebral infarction. Because attenuation difference is 10 HU in IV FDCT [7, 21], it can clearly depict hemorrhage lesion before intra-arterial thrombolysis [22]. Because acute ischemic stroke has a 6-h therapeutic time window for intra-arterial thrombolysis [23], timely assessment of the stenosis nature and subsequent treatment is important to obtain good neurologic outcomes [8, 24]. Therefore, in particular, IV FDCT can be useful for early diagnosis of acute cerebral infarct and its subsequent treatment.

Role of IV FDCT in Endovascular Procedure

Advances in microcatheter and balloon technologies have increased an incidence of endovascular treatment and its success rate in patients with symptomatic intracranial stenosis. However, procedural complications such as hemorrhage, vessel dissection, and infarction can occur. In particular, symptomatic intracranial hemorrhage has been reported with a range from 1.1 to 15.4 % [22, 23, 25] and can lead to neurological deficit. Accordingly, early detection is important to avoid poor neurologic outcome during the periprocedural period. In such circumstances, IV FDCT can allow real-time monitor on complications in the same angiosuite without patient transfer [14, 26]. Karman et al. [14] reported that IV FDCT was feasible to detect or exclude suspected procedure-related complications. White et al. [12] reported that IV FDCT was a substantial factor in decision making for 40.9 % of patients during the peri-endovascular period. In their study, IV FDCT provided clear depiction of the extensive leakage of the contrast media through perforation site by microcatheter, enlarged ventricle size, and presence of hemorrhage. Accordingly, prompt detection of adverse events and subsequent appropriate management can be achieved on the same angiotable.

IV FDCT can also be used as a follow-up tool for stent-implanted arteries. The use of intracranial stent placement for atherosclerotic stenosis has been increasingly reported [27, 28]. Intracranial stents require low-profile system and adequate radial strength with high flexibility [18]. Accordingly, high spatial resolution and a lower susceptibility artifact of the radiologic test as well as sufficient radiopacity of the stents are necessary to obtain information on the stent position and arterial wall clearly in the follow-up test. IV FDCT allows stent position and cross-sectional images within the stent with a good spatial resolution of approximately 0.1 mm. Spatial resolution can be influenced by pixel binning as well as focal spot size and reconstruction methods [10]. In general pixel binning, combination of a cluster of pixels into a single pixel can decrease spatial resolution. Kalender et al. [9] demonstrated better spatial resolution of the IV FDCT compared to multi-slice spiral CT (MSCT) by comparing modulation transfer time (MTF) and visual estimate of bar pattern phantom according to different pixel binning [18]. Ebrahimi et al. [5] investigated stent conformity in curved vascular models among studies of IV FDCT,

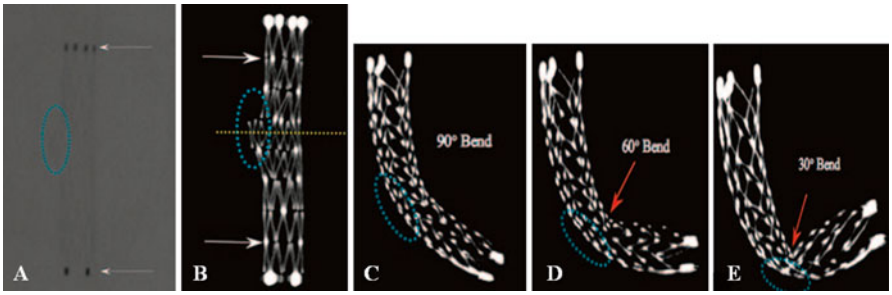

Fig. 2 Comparison of stent conformity in curved vascular models among IV FDCT and digital radiography (DR) in an in vitro study. Although the proximal and distal marker of the stent (**a**, *arrows*), Neuroform 2, is well visualized by DR images, stent cells and struts are poorly described. IV FDCT MIP image shows clear depiction of the stent architecture such as struts and connectors (*arrows*). Cross-sectional image (*yellow-dotted line*) can provide the protrusion of the stent through a hole (*dotted blue circle*) (**b**) In simulated cases over an 8-mm hole (*dotted blue circle*), flattering of the Enterprise stent as an increase in bending is clearly shown (**c**–**e**)

DSA, and digital radiography. In their study, IV FDCT provided more clear visualization of stent deployment and adverse stent mechanics such as increased cell opening and strut prolapse than digital radiography or DSA (Fig. 2). Nevertheless, IV FDCT can offer increased noise level and decreased low-contrast resolution than MSCT. Kalender et al. [9] showed the different ability to detect low-contrast details according to noise and dose. Reconstructed images from high spatial resolution can make images with high noise, which can decrease low-contrast detectability. When increasing dose, improvement of noise level and low-contrast detectability can be observed. Accordingly, technical advances in enhancing low-contrast resolution are necessary in IV FDCT.

Consensus over a contrast protocol in stent implantation in human intracranial arteries remains undetermined. Patel et al. [3] optimized a contrast protocol in stent-implanted swine model. The protocol was as follows: (1) 20 % of iodinated contrast (iopamidol 51 %, Isovue; 250 mg/mL iodine concentration) in normal saline; (2) 2-s time delay; and (3) velocity of 3.0 mL/s for 23 s at the common carotid artery in the anterior circulation or 2.0 mL/s for 23 s at the vertebral artery in the posterior circulation. Nevertheless, optimal contrast attenuation in stented arterial segment in human has not been clearly established.

An Estimate of Cerebral Perfusion by IV FDCT

Beyond identification of anatomical information on the intracranial stenosis, identification of brain perfusion abnormalities is also important to select revascularization methods. Recently, the feasibility of IV FDCT in measuring cerebral blood volume (CBV) or cerebral blood flow (CBF) has been studied. Struffert

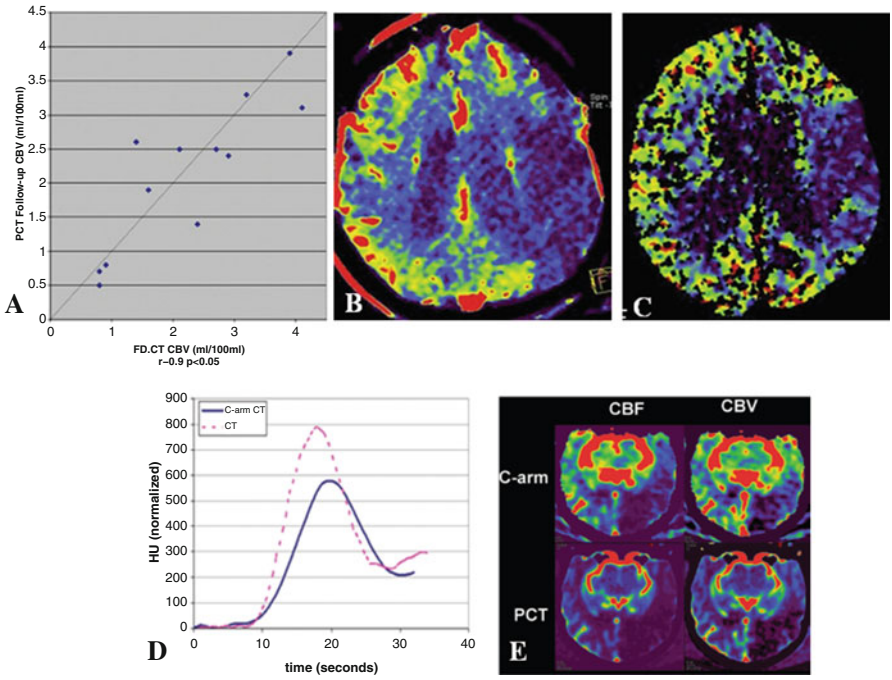

Fig. 3 Cerebral perfusion imaging by IV FDCT. A high correlation between abnormal CBV lesion on IV FDCT and stroke volume on follow-up multisection CT (MSCT) was observed in the oligemic areas (**a**–**c**). Overestimation of the CBV and CBF by IV FDCT is observed due to the difference in arterial input function (AIF) measurement compared with that in perfusion CT (**d** and **e**)

et al. [4] compared CBV lesion between IV FDCT and MSCT in patients with acute MCA occlusions. Because FDCT CBV map can be calculated only under the steady-state condition of contrast medium in the brain parenchyma, "bolus watching" method was used during the acquisition [4, 29]. A high correlation between abnormal CBV lesion on IV FDCT and stroke volume on follow-up MSCT was observed in the oligemic areas in the initial image (Fig. 3a–c). In addition, IV FDCT and perfusion CT showed comparable absolute CBV. Royalty et al. [30] compared IV FDCT and perfusion CT in measuring CBV and CBF in canine stroke model. The perfusion acquisition protocol of IV FDCT which was used was as follows: (1) seven 200° rotations over 2.8 s with a 1.5-s pause between rotations; (2) 133 projections at about 60 projections per second during rotation; (3) 70 kVp and 1.2 μGy/frame dose level in each projection; and (4) mainly 5-s X-ray time delay [30]. High levels of interobserver agreement for detecting ischemic lesion and perfusion mismatch between CBV and CBF in IV FDCT were observed. Nevertheless, technical limitations of IV FDCT include lower temporal resolution than conventional perfusion CT and low-contrast

resolution. The lower temporal resolution of the IV FDCT attributes to the broader time attenuation curve with lower peak, in particular voxels that are arteries. Accordingly, overestimated CBV and CBF can be achieved (Fig. 3d, e) [30]. The lower temporal resolution could be improved by increasing rotation speed of C-arm or a steady state of contrast enhancement within the brain parenchyma [30, 31]. A protocol for the fastest commercial C-arm rotation is over 6 s of a temporal sampling rate [30]. Although Royalty et al. [30] showed an increased temporal sampling rate of 4.3 s, consistent overestimation of the CBV and CBF still remains. Accordingly, further study on the temporal sampling rate-lowering algorithm is necessary to obtain perfusion parameters which are compatible perfusion CT. A steady state of contrast enhancement can be obtained by increase in duration of contrast injection [31]. However, optimal contrast dose and injection route have not been well established in IV FDCT. In addition, consensus on the X-ray time delay remains undetermined. As a result, future work on the optimal value of contrast dose, injection route, and X-ray time delay should be studied together.

Cerebral Aneurysm

IV FDCT has not been routinely used for the diagnosis of aneurysm in clinical circumstances. However, studies about the efficacy of IV FDCT for following secured aneurysm have been carried out. Psychogios et al. [32] reported that larger clip size, multiple clips, and clip direction were associated with image degradation obtained by IV FDCT. In particular, long axis of clip which was placed parallel or perpendicular to the rotational axis can cause insufficient images for interpretation. Because 30 % of the images were unsuitable for interpretation, they did not recommend IV FDCT as a routine test for following post-clipped aneurysm such as parent artery patency and the presence of residual neck. Regarding evaluation of aneurysm after endovascular treatment, IV FDCT cannot routinely replace the role of DSA in detecting residual neck [6]. Large coil mass also causes an amorphous signal within the coil mass; accurate detection of residual filling could not be accomplished by IV FDCT [6]. Although they reported that IV FDCT allows slight superiority in depicting aneurysms after stent remodeling in comparison to time-of-flight MRA [6], its superiority can be limited in aneurysms over 10 mm in diameter due to beam-hardening artifacts of the stent [33]. Nevertheless, the feasibility of IV FDCT in detecting vasospasm remains undetermined. Images of IV FDCT which are reconstructed in various directions could allow the information on the presence of vasospasm and its severity in a single acquisition (Fig. 4). Accordingly, study about the usefulness of IV FDCT in estimating vasospasm is needed further.

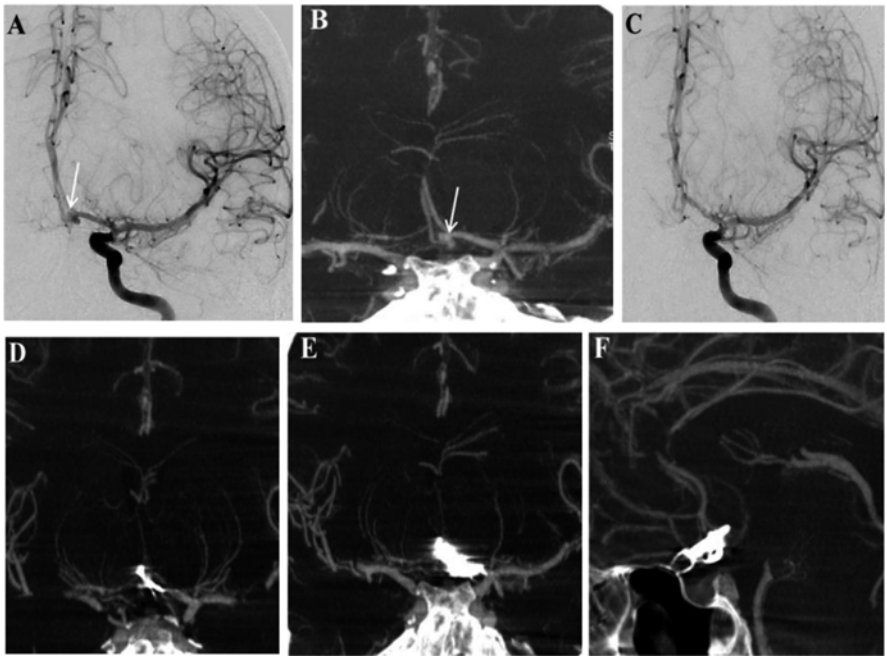

Fig. 4 IV FDCT for the assessment of vasospasm after aneurysm clipping. A 22-year-old male was transferred for subarachnoid hemorrhage. Initial DSA and IV FDCT reveal aneurysmal dilatation (*arrow*) of the anterior communicating (A-com) artery (**a** and **b**). On the 5 days after operation, confused mentality with increased transcranial Doppler velocity was observed. DSA shows no significant luminal narrowing of the vessels compared with those of initial images of DSA (**c**). Selective coronal and sagittal IV FDCT MIP images demonstrate no significant vasospasm which is consistent with DSA (**d**–**f**) [34]

Limitations

The major limitations of IV FDCT include radiation dose and metal artifact and motion artifact. Patel el al. [3] obtained images of IV FDCT with a radiation dose of 49 mGy. Bai et al. [35] reported that IV FDCT generates images with lesser effective radiation dose of 1.18 mSv than multi-slice CT of 1.89 mSv. Prell et al. [36] proposed metal artifact reduction methods. They showed that combination procedures of initial correction of 3D linear interpolation and subsequent attenuation-normalization methods using a multilevel segmentation provided metal artifact-reduced images. Motion artifact also can develop in patients with poor compliance. Because motion artifact can increase with scanning time, methods to increase rotation speed and decrease angular sampling are required to reduce motion artifact. Other limitations of the IV FDCT are cone beam artifacts due to wide cone angle, filed-of-view truncation,

streaking artifacts due to angular undersampling in projection image, and inefficient scatter artifact reduction. Accordingly, technical advances to decrease such limitations are necessary further.

Conclusions

IV FDCT angiography is a feasible method for depicting intracranial arteries with DSA as the reference value. Surely, we do not aim here to advocate superiority of IV FDCT than conventional CT as a routine diagnostic test. IV FDCT can provide information on the stenosis nature such as stenosis severity, occlusion level, clot length, and collateral vessels in the single acquisition. In addition, prompt endovascular treatment and real-time monitoring of the complications during the peri-procedural period can be done, which would be especially beneficial for patients with acute ischemic stroke. IV FDCT also allows clear depiction of the stented arteries than conventional CT due to its high spatial resolution. However, absence of the comparative analyses for measuring intracranial stenosis with other tests such as CTA and MRA can be a limitation. Technical advances also should be achieved further to reduce overestimation of perfusion parameters, beam-hardening effect, and metal and motion artifact to generate high-quality images.

Acknowledgement We would like to thank Sung-Eun Kim and YoungHo Kim (Siemens) for help with the data collection and valuable contribution to the image preparation.

References

1. Wong KS, Li H. Long-term mortality and recurrent stroke risk among Chinese stroke patients with predominant intracranial atherosclerosis. Stroke. 2003;34:2361–6.
2. Arenillas JF. Intracranial atherosclerosis: current concepts. Stroke. 2011;42:S20–3.
3. Patel NV, Gounis MJ, Wakhloo AK, Noordhoek N, Blijd J, Babic D, et al. Contrast-enhanced angiographic cone-beam CT of cerebrovascular stents: Experimental optimization and clinical application. AJNR Am J Neuroradiol. 2011;32:137–44.
4. Struffert T, Deuerling-Zheng Y, Engelhorn T, Kloska S, Golitz P, Kohrmann M, et al. Feasibility of cerebral blood volume mapping by flat panel detector CT in the angiography suite: first experience in patients with acute middle cerebral artery occlusions. AJNR Am J Neuroradiol. 2012;33:618–25.
5. Ebrahimi N, Claus B, Lee CY, Biondi A, Benndorf G. Stent conformity in curved vascular models with simulated aneurysm necks using flat-panel ct: an in vitro study. AJNR Am J Neuroradiol. 2007;28:823–9.
6. Buhk JH, Kallenberg K, Mohr A, Dechent P, Knauth M. Evaluation of angiographic computed tomography in the follow-up after endovascular treatment of cerebral aneurysms–a comparative study with DSA and TOF-MRA. Eur Radiol. 2009;19:430–6.
7. Psychogios MN, Buhk JH, Schramm P, Xyda A, Mohr A, Knauth M. Feasibility of angiographic CT in peri-interventional diagnostic imaging: a comparative study with multidetector CT. AJNR Am J Neuroradiol. 2010;31:1226–31.

8. Struffert T, Deuerling-Zheng Y, Kloska S, Engelhorn T, Strother CM, Kalender WA, et al. Flat detector ct in the evaluation of brain parenchyma, intracranial vasculature, and cerebral blood volume: a pilot study in patients with acute symptoms of cerebral ischemia. AJNR Am J Neuroradiol. 2010;31:1462–9.
9. Kalender WA, Kyriakou Y. Flat-detector computed tomography (FD-CT). Eur Radiol. 2007;17:2767–79.
10. Spahn M. Flat detectors and their clinical applications. Eur Radiol. 2005;15:1934–47.
11. Stone MF, Zhao W, Jacak BV, O'Connor P, Yu B, Rehak P. The x-ray sensitivity of amorphous selenium for mammography. Med Phys. 2002;29:319–24.
12. White PM, Gilmour JN, Weir NW, Innes B, Sellar RJ. AngioCT in the management of neurointerventional patients: a prospective, consecutive series with associated dosimetry and resolution data. Neuroradiology. 2008;50:321–30.
13. Jeon JS, Sheen SH, Hwang GJ, Kim HC, Kwon BJ. Feasibility of intravenous flat panel detector ct angiography for intracranial arterial stenosis. AJNR Am J Neuroradiol. 2013;34:129–34.
14. Kamran M, Nagaraja S, Byrne JV. C-arm flat detector computed tomography: the technique and its applications in interventional neuro-radiology. Neuroradiology. 2010;52:319–27.
15. Jou LD, Mohamed A, Lee DH, Mawad ME. 3D rotational digital subtraction angiography may underestimate intracranial aneurysms: findings from two basilar aneurysms. AJNR Am J Neuroradiol. 2007;28:1690–2.
16. Blanc R, Pistocchi S, Babic D, Bartolini B, Obadia M, Alamowitch S, et al. Intravenous flat-detector CT angiography in acute ischemic stroke management. Neuroradiology. 2012;54:383–91.
17. Nonaka T, Oka S, Miyata K, Mikami T, Koyanagi I, Houkin K, et al. Prediction of prolonged postprocedural hypotension after carotid artery stenting. Neurosurgery. 2005;57:472–7. discussion 472–477.
18. Benndorf G, Strother CM, Claus B, Naeini R, Morsi H, Klucznik R, et al. Angiographic CT in cerebrovascular stenting. AJNR Am J Neuroradiol. 2005;26:1813–8.
19. Jeon JS, Sheen SH, Kim HC. Intravenous flat-detector computed tomography angiography for high-grade carotid stenosis. J Comput Assist Tomogr. 2013;37:242–6.
20. Riedel CH, Jensen U, Rohr A, Tietke M, Alfke K, Ulmer S, et al. Assessment of thrombus in acute middle cerebral artery occlusion using thin-slice nonenhanced computed tomography reconstructions. Stroke. 2010;41:1659–64.
21. Daly MJ, Siewerdsen JH, Moseley DJ, Jaffray DA, Irish JC. Intraoperative cone-beam CT for guidance of head and neck surgery: assessment of dose and image quality using a c-arm prototype. Med Phys. 2006;33:3767–80.
22. Furlan A, Higashida R, Wechsler L, Gent M, Rowley H, Kase C, et al. Intra-arterial prourokinase for acute ischemic stroke. The proact II study: a randomized controlled trial. Prolyse in acute cerebral thromboembolism. JAMA. 1999;282:2003–11.
23. del Zoppo GJ, Higashida RT, Furlan AJ, Pessin MS, Rowley HA, Gent M. Proact: a phase II randomized trial of recombinant pro-urokinase by direct arterial delivery in acute middle cerebral artery stroke. Proact investigators. Prolyse in acute cerebral thromboembolism. Stroke. 1998;29:4–11.
24. Jansen O, Schellinger P, Fiebach J, Hacke W, Sartor K. Early recanalisation in acute ischaemic stroke saves tissue at risk defined by MRI. Lancet. 1999;353:2036–7.
25. Akins PT, Amar AP, Pakbaz RS, Fields JD, Investigators S. Complications of endovascular treatment for acute stroke in the swift trial with solitaire and merci devices. AJNR Am J Neuroradiol. 2014;35:524–8.
26. Heran NS, Song JK, Namba K, Smith W, Niimi Y, Berenstein A. The utility of dynact in neuroendovascular procedures. AJNR Am J Neuroradiol. 2006;27:330–2.
27. Buhk JH, Lingor P, Knauth M. Angiographic CT with intravenous administration of contrast medium is a noninvasive option for follow-up after intracranial stenting. Neuroradiology. 2008;50:349–54.

28. Suh DC, Kim JK, Choi JW, Choi BS, Pyun HW, Choi YJ, et al. Intracranial stenting of severe symptomatic intracranial stenosis: results of 100 consecutive patients. AJNR Am J Neuroradiol. 2008;29:781–5.
29. Bley T, Strother CM, Pulfer K, Royalty K, Zellerhoff M, Deuerling-Zheng Y, et al. C-arm CT measurement of cerebral blood volume in ischemic stroke: an experimental study in canines. AJNR Am J Neuroradiol. 2010;31:536–40.
30. Royalty K, Manhart M, Pulfer K, Deuerling-Zheng Y, Strother C, Fieselmann A, et al. C-arm CT measurement of cerebral blood volume and cerebral blood flow using a novel high-speed acquisition and a single intravenous contrast injection. AJNR Am J Neuroradiol. 2013;34:2131–8.
31. Wintermark M, Smith WS, Ko NU, Quist M, Schnyder P, Dillon WP. Dynamic perfusion CT: optimizing the temporal resolution and contrast volume for calculation of perfusion ct parameters in stroke patients. AJNR Am J Neuroradiol. 2004;25:720–9.
32. Psychogios MN, Wachter D, Mohr A, Schramm P, Frolich AM, Jung K, et al. Feasibility of flat panel angiographic ct after intravenous contrast agent application in the postoperative evaluation of patients with clipped aneurysms. AJNR Am J Neuroradiol. 2011;32:1956–62.
33. Richter G, Engelhorn T, Struffert T, Doelken M, Ganslandt O, Hornegger J, et al. Flat panel detector angiographic CT for stent-assisted coil embolization of broad-based cerebral aneurysms. AJNR Am J Neuroradiol. 2007;28:1902–8.
34. Jeon JP, Sheen SH, Cho YJ. Intravenous flat-detector computed tomography angiography for symptomatic cerebral vasospasm following aneurysmal subarachnoid hemorrhage. Scientific World Journal. 2014:315960.
35. Bai M, Liu B, Mu H, Liu X, Jiang Y. The comparison of radiation dose between c-arm flat-detector CT (dynact) and multi-slice CT (MSCT): a phantom study. Eur J Radiol. 2012; 81:3577–80.
36. Prell D, Kyriakou Y, Struffert T, Dorfler A, Kalender WA. Metal artifact reduction for clipping and coiling in interventional c-arm CT. AJNR Am J Neuroradiol. 2010;31:634–9.

Basic Principles of Magnetic Resonance Imaging

Martin J. Graves and Chengcheng Zhu

Introduction

Magnetic resonance imaging (MRI) is a non-invasive method of mapping structure and various aspects of function within the body. It uses non-ionising electromagnetic radiation and is without known exposure-related hazard. It employs alternating magnetic fields in the radiofrequency (RF) part of the electromagnetic spectrum together with carefully controlled magnetic field gradients in order to produce high quality cross-sectional images of the body in any plane. It is primarily used to portray the distribution of hydrogen nuclei and parameters relating to their physical surroundings in water and lipids. MRI has advanced dramatically over the last 40 years, from showing great potential to being the primary investigation for many clinical conditions.

The phenomenon of "nuclear induction", later to be termed Nuclear Magnetic Resonance, was described separately but almost simultaneously in 1946 by Purcell [1] working at Harvard and Bloch [2] at Stanford. Following its discovery NMR was, and continues to be, used extensively for studying the properties of matter at the molecular level using the technique of NMR spectroscopy.

NMR imaging was not developed until 1973 when Paul Lauterbur [3] demonstrated a method of spatial localisation by applying a linearly varying magnetic field across an inanimate object. Human in vivo images were first published in the late 1970s by Mansfield and Maudsley [4], Damadian et al. [5] and Hinshaw et al. [6].

M.J. Graves, Ph.D., FIPEM (✉)
Department of Radiology, Cambridge, University Hospitals NHS Trust,
Hills Road, Cambridge, CB2 0QQ, UK
e-mail: mjg40@cam.ac.uk

C. Zhu, Ph.D.
VA Medical Center, University of California in San Francisco,
4150 Clement Street, San Francisco, CA 94121, USA

R. Trivedi et al. (eds.), *3D Imaging Technologies in Atherosclerosis*,
DOI 10.1007/978-1-4899-7618-5_6

In applications to medicine, the term "nuclear" has been dropped leaving it as Magnetic Resonance or MR imaging.

Magnetic resonance is a phenomenon whereby the nuclei of certain atoms, when placed in a magnetic field, absorb and emit energy at a specific radiofrequency (RF). Nuclei suitable for MRI are those that have an odd number of protons and/or neutrons, which means they have an overall nuclear charge. They also exhibit the property of nuclear spin. The combination of charge and spin causes these nuclei to exhibit a magnetic moment, i.e. we can think of them as behaving like microscopic bar magnets. Almost all clinical MR images are produced using the simplest of all nuclei, that of hydrogen, which comprises a single proton. Hydrogen is present in virtually all biological material and exhibits relatively high MR sensitivity.

Nuclear Magnetisation

If we place a subject into a strong uniform static magnetic field (B_0) we can consider that the magnetic moments of all the protons experience a force tending to line them up either with the direction of B_0, similar to the way a compass needle aligns along the direction of magnetic north, or in the opposite direction, equivalent to a compass needle pointing south. Due to their intrinsic thermal energy, there are a slightly greater number of protons that align "north" compared to "south". In the human body there are a huge number of protons and even in a single imaging voxel this difference, known as the nuclear polarisation, comprises hundreds of trillions of protons all of which act together to form what is known as a net, or bulk, magnetisation which is aligned along the "north" direction. In MRI we usually denote the "north" direction as the longitudinal z-direction.

This net magnetisation also exhibits the phenomenon of precession, i.e. the vector can be considered to rotate about the B_0 direction. The magnetisation precesses at a fixed frequency defined as the product of the gyromagnetic constant and the static magnetic field strength. For protons the gyromagnetic constant is 42.57 MHz/T, so that at a typical clinical MRI system field strength of 1.5 T, the precessional frequency, often known as the Larmor frequency, is 63.85 MHz, which is in the radiofrequency (RF) range of the electromagnetic spectrum. Since the net magnetisation is aligned along the same direction as B_0 it is necessary to rotate the magnetisation away from this z-direction into the transverse (x–y) plane. This rotation can be achieved by the application of an external magnetic field at 90° to the z-direction that is also alternating at the Larmor frequency. An RF magnetic field is created by an alternating current circulating through a transmitter "coil" of wire surrounding the body. This requirement for the external magnetic field to rotate at the same frequency as the natural precessional frequency of the net magnetisation explains the "resonance" part of nuclear magnetic resonance, i.e. the net magnetisation can only be rotated by an external magnetic field that is resonant with the natural frequency.

The net magnetisation will rotate whilst the external magnetic field is applied, so only relatively short "pulses" of RF magnetisation are required to rotate the net

magnetisation. In MRI we typically talk about 90° excitation pulses that rotate the longitudinal magnetisation from the z-direction into the transverse plane and 180° pulses that can either invert the magnetisation, or rotate any existing transverse magnetisation by 180° within the plane.

Relaxation

Immediately following the application of the excitation RF pulse, the net magnetisation, which is now in the transverse plane, rotates about the z-direction. This precessing magnetisation can induce a voltage and hence a current in a receiver "coil". The receiver coil maybe the same as the transmitter coil but is usually a separate, anatomically closely fitting, coil or array of coils. Over a timescale of milliseconds the individual nuclei that make up this net magnetisation, start to dephase with respect to each other. This dephasing is caused by the magnetic moments of individual nuclei (spin-spin interactions) affecting the local Larmor frequency as well as the fact that the static magnetic field is not perfectly uniform. This non-uniformity is caused by both engineering limitations in the magnet itself as well as differences in the magnetic behaviour of tissues. The effect of this dephasing is that the net magnetisation decays, or more correctly relaxes, which can be detected as a decreasing voltage in the receiver coil. This relaxation of the transverse magnetisation can be considered, to a first order, as an exponential with a time constant known as T_2^*. It is possible to eliminate the effects of the static and tissue-induced magnetic field non-uniformities to leave only the decay due to spin–spin interactions. This is achieved by applying a second RF pulse after a period of dephasing τ. This pulse duration and amplitude is such that it has the effect of rotating the magnetisation 180° in the transverse plane. This effectively reverses the dephasing causing the individual nuclei to rephase. After a further time period τ the nuclei come back into phase, forming what is known as a "spin-echo" signal (Fig. 1). This echo forms a period 2τ, known as the echo time (TE), after the initial excitation pulse. The application of this 180° refocusing pulse will eliminate the dephasing caused by the static and tissue-induced magnetic field non-uniformities but cannot eliminate the desirable, in terms of image contrast, T_2-*induced* spin–spin dephasing. Since different tissues exhibit different spin–spin interactions, differential T_2 relaxation is an important contrast mechanism in MRI.

The effect of the RF pulse is to increase the energy of the spin system and once the pulse has been switched off the magnetisation returns to thermal equilibrium, i.e. it realigns along the z-direction. Whilst T_2 relaxation does not involve any energy loss, only dephasing of the individual spins, in order to return to thermal equilibrium the spin system needs to give up its energy to the surrounding macromolecular environment, often referred to as the lattice. This energy loss results in an exponential recovery of the magnetisation along the z-direction. This process is known as longitudinal relaxation and is exponential with a time constant of T_1. Again since different tissues interact with the lattice differently, differential T_1 relaxation is an additional MRI contrast mechanism. Since it is only possible to detect signal in the

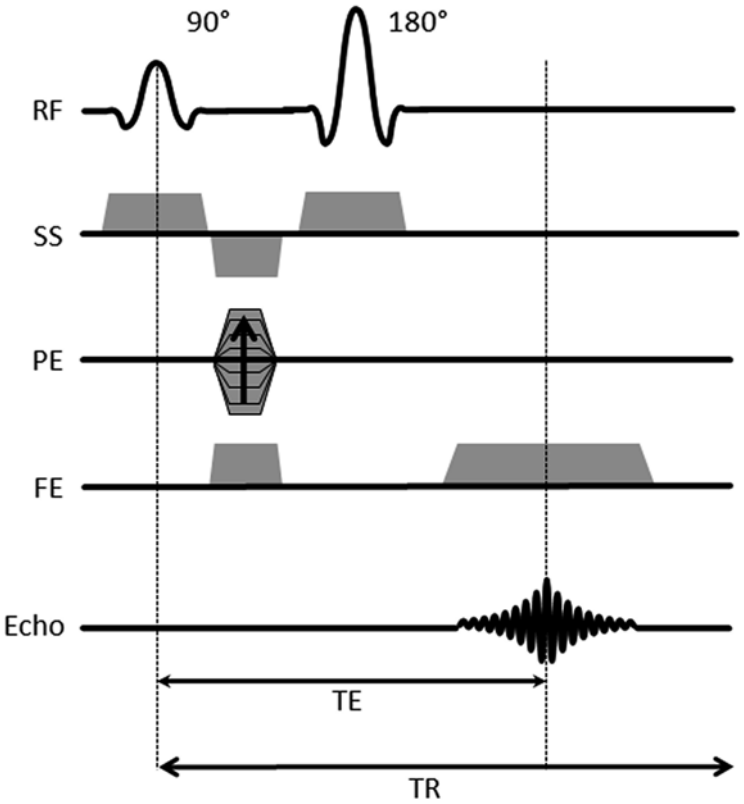

Fig. 1 Spin echo pulse sequence. *RF* radiofrequency, *SS* slice selection, *PE* phase encoding, *FE* frequency encoding, *TE* echo time, *TR* repetition time

transverse plane, T_1 contrast is achieved by altering the period between subsequent excitation pulses, known as the repetition time (TR). The TR affects how much longitudinal relaxation occurs, so that the subsequent excitation pulse will rotate the differentially recovered magnetisation into the transverse plane. If the TE is kept short then the signal that is detected will largely represent the T_1 relaxation and not any subsequent T_2 transverse relaxation. The difficulty in completely eliminating T_2 relaxation from T_1 images (which would require TE to be zero), or T_1 relaxation from T_2 images (which would require TR to be infinite), results in the images generally being referred to as either T_1- or T_2-weighted. The use of a very short TE with a very long TR can minimise both T_2 and T_1 effects respectively resulting in proton-density weighted images. Figure 2 shows how the transverse (M_{xy}) decays as a function of TE and the longitudinal (M_z) magnetisation recovers as a function of TR for the three main contrast weightings. Example images from a patient with a large lipid core containing plaque are shown to demonstrate the multiple contrast weightings.

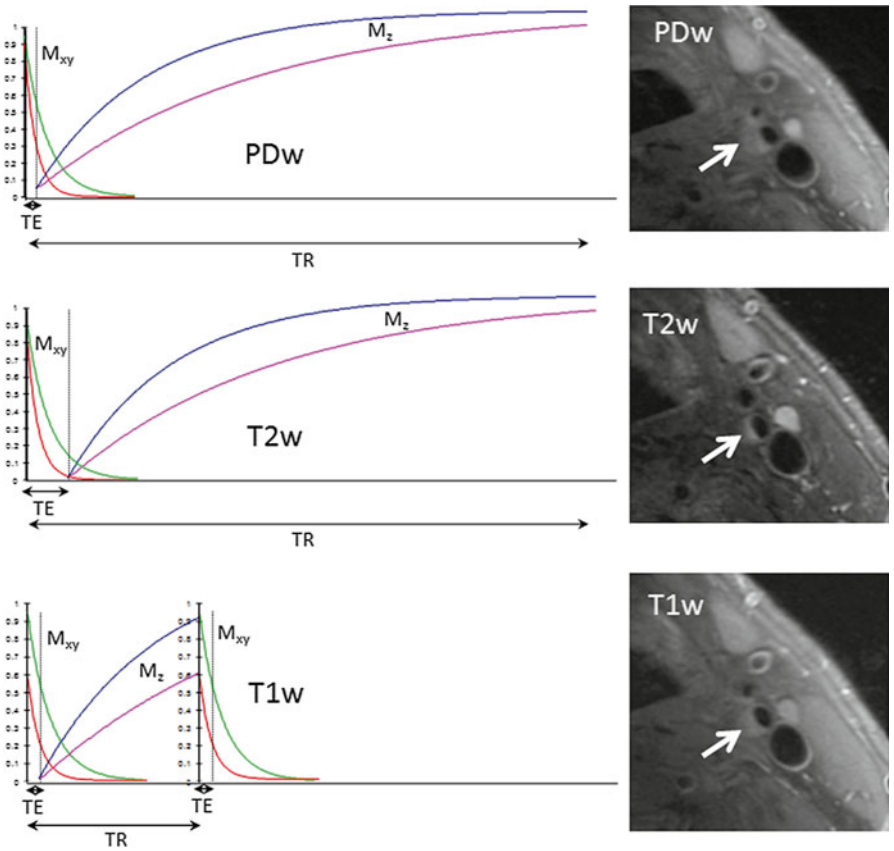

Fig. 2 Proton density (PD), T_2 and T_1 weighted contrast for two different tissue types with example carotid images from a patient with a plaque comprising a large lipid core and fibrous cap *(arrows)*. *TE* echo time, *TR* repetition time. M_{xy} transverse magnetisation, M_z longitudinal magnetisation

Spatial Localisation

The wavelength of the RF in the body at 1.5 T is typically around 50 cm and is therefore on a scale of the object being imaged, unlike for example X-rays. It is necessary therefore to use a spectroscopic technique in order to achieve an acceptable spatial resolution. In MRI magnetic field gradients are used to spatially encode the NMR signal, followed by an appropriate mathematical process to reconstruct the images. The magnetic field gradients are created by additional coils of wire inside the MRI magnet. These gradient coils create a linear variation in magnetic field with position inside the magnet. These gradient fields are superimposed upon the static magnetic field causing a linear variation in Larmor frequency with position. Spatial localisation of the MRI signal requires the application of three orthogonal gradient fields

that are applied, together with the RF pulses at different time points. The combination of RF and gradient pulses are known as a pulse sequence which fulfils the dual requirement of rotating the magnetisation, via the RF pulses, to achieve the desired contrast whilst effectively changing the precessional frequency, via the gradient pulses, to achieve spatial localisation of the signal.

In a standard MRI pulse sequence there are three basic steps in spatial localisation; slice selection, phase encoding and frequency encoding. Slice selection requires that the RF pulses be applied simultaneously with a gradient pulse in one of the three orthogonal directions in order to rotate a thin section of magnetisation by the desired angle. This slice-selection (SS) gradient pulse causes the magnetisation to precess at a positionally dependent frequency in the slice selection direction. The application of an RF pulse at a frequency that matches the precessional frequency at the desired slice location will result in the magnetisation in that location being excited, i.e. rotated. In practice the RF pulse actually excites a small range of precessional frequencies centred about this location so that a desired thickness, e.g. 5 mm, of magnetisation will be excited. The SS gradient is applied for the same duration as the RF pulse in order to rotate the magnetisation by the desired angle, typically 90° in order to create a detectable signal into the transverse plane as described above. Once this "slice" of magnetisation has been rotated into the transverse plane it is necessary to spatially encode the signal within the slice plane using a two-step process. Firstly a phase-encoding (PE) gradient pulse is applied in one of the two in-plane directions. Similar to slice selection this PE gradient pulse causes the magnetisation to precess at a positionally dependent frequency along the PE direction. When the gradient pulse is switched off the spins return to the nominal frequency but retain a relative phase shift with respect to each other. This phase shift constitutes a "pseudo-frequency" along the PE direction. Finally the frequency encoding (FE) gradient is applied along the other in-plane direction. The timing of this gradient pulse is such that it is centred about the time when the echo signal is formed, i.e. TE. The frequency encoding gradient also induces a positionally dependent frequency along the FE direction. The echo signal is digitised in the presence of this gradient and stored in the memory of the reconstruction computer.

The whole pulse sequence is then repeated every TR period. However, with each repetition the amplitude of the PE gradient is changed, so that a different "pseudo-frequency" is induced in the transverse magnetisation prior to the frequency encoding process. Each digitised echo signal, with its own PE gradient-induced phase shift is stored in computer memory. Typically the PE gradient will be applied 256 times in a standard MRI acquisition and each echo will comprise 256 samples. This will result in a two-dimensional (2D) raw data matrix of 256×256 samples. Since the spatial information in the images is encoded in the raw data as frequencies the image can be reconstructed by application of an inverse 2D Fourier transformation to the raw data. This method of image acquisition is termed "spin-warp" and was originally developed at the University of Aberdeen by Edelstein and co-workers [7].

Depending upon the choice of TE and TR the reconstructed images will be proton-density, T_2 or T_1 weighted. The spatial resolution in the PE direction will be determined by the number of different PE gradient amplitudes applied and the

operator chosen field-of-view that controls the maximum PE gradient amplitude. Since in a basic pulse sequence only one PE gradient is applied per TR the product of the TR and the number of PE steps equals the minimum scan time, e.g. a TR of 3,000 ms multiplied by 256 gradient steps will result in a minimum acquisition time of 12 min and 48 s. The spatial resolution in the FE direction is determined by the number of samples in each echo and the operator chosen field-of-view that controls the FE gradient amplitude.

MRI Hardware

An MRI system comprises four main components. The first is an appropriate magnet to generate the strong static magnetic field (B_0), which is required to induce the nuclear polarisation. The second is a radiofrequency (RF) system that generates the required alternating magnetic field (B_1), at the Larmor frequency and also detects the weak MR signal being returned from the patient. The third component is the gradient system that generates the required linear magnetic field variations that are superimposed upon B_0 and are used to spatially encode the MR signal. The gradient and whole-body RF coils are concentrically positioned inside the bore of the magnet. Figure 3 shows a schematic cross section through a superconducting MRI system. Finally the fourth component consists of a number of computers that are used to provide the user interface, generate the digital representations of the RF and gradient pulses, and also perform the mathematical operations, e.g. Fourier transformation, required to reconstruct an image from the digitised signals returned from the patient.

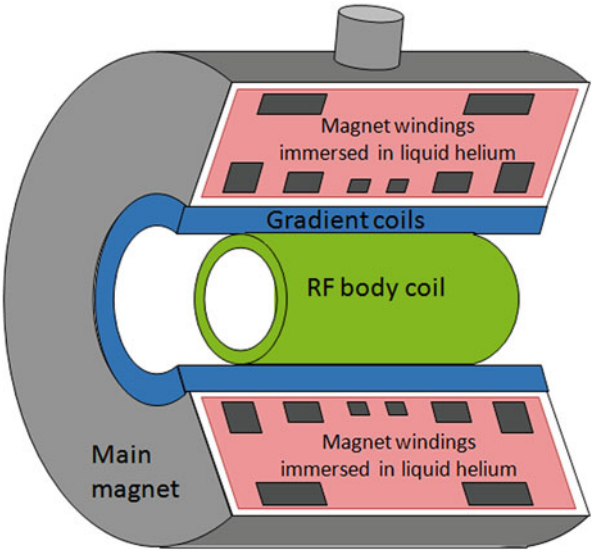

Fig. 3 Cross section through a superconducting MRI system. The figures shows (1) the main magnet windings that generate the static magnetic field, (2) the gradient coils that generate the linear magnetic field variations required for spatial localisation and (3) the radiofrequency (RF) body coil used for transmission of the RF pulses

Magnets

The requirements for the static field are that it should be reasonably strong, stable and uniform. Magnetic field strength or, more accurately, "magnetic flux density", is measured in the SI derived unit of tesla (symbol T). Whilst it is certainly true that bigger is not necessarily better, there is an approximately linear increase in signal-to-noise ratio (SNR) with increasing field strength. Over the last 30 years of MRI various technologies and designs have been used to create magnets of an appropriate configuration that a human body can be placed inside. These designs have various trade-offs in terms of field strength as well as stability, uniformity and patient acceptance. It was not until the development of superconducting magnet technology that higher field strengths could be achieved. Typical clinical superconducting MRI systems are available at 1.0 T, 1.5 T and 3.0 T, having Larmor frequencies of 42, 64 and 128 MHz, respectively. Most vendors have also developed 7.0 T whole body systems for research purposes, with even higher field strengths, e.g. 11.7 T being custom-developed. Superconducting magnets generate their magnetic field by circulating an electric current through solenoidal coils of niobium-titanium (NbTi) filaments embedded in a copper matrix. At temperatures below approximately 10 K NbTi becomes superconducting, which means it has zero electrical resistance and current will circulate indefinitely without an external power supply. Practically, a superconducting MRI magnet comprises a steel cryostat with the superconducting coils immersed in liquid helium at 4.2 K (−269 °C or −452 °F). Whilst iron-cored or permanent magnet designs can have a C or H-shape and may therefore appear more patient friendly, superconducting MRI system cryostats are most commonly shaped like a cylindrical tube with the patient placed inside the central bore. In addition to the patient, the gradient and the RF body coil are also positioned inside the bore, although hidden from the patient behind fibre-glass covers. Although the diameter of the cryostat bore is approximately 100 cm, once these additional coils are installed the patient accessible bore is reduced to approximately 60 cm. However, in response to demands for improved patient acceptance as well as an increasingly bariatric population, manufacturers have introduced systems to allow 70 cm or greater patient apertures as well as reducing overall magnet lengths.

Whilst a strong, but not necessarily very uniform, B_0 is required to achieve a good nuclear polarisation, an extremely high uniformity is required to perform spatial localisation. The uniformity of B_0 is usually defined as the variation of the field within a spherical volume of a given diameter which, for a 1.5 T magnet would typically be less than 1 part per million (ppm) over a 40 cm diameter spherical volume. Further improvements can be achieved over smaller volumes by a process known as "shimming", which is often automatically performed by the system for each body part imaged. In addition the field must be temporally very stable, with a typical superconducting magnet having a stability of better than 0.1 ppm/h.

Whilst the signal-to-noise ratio increases with field strength, often allowing higher spatial resolution, higher magnetic fields, e.g. 3 T and above, also bring additional challenges. These include: a lengthening in T_1 relaxation times resulting in poorer T_1-weighted image contrast; increased magnetic susceptibility-gradient

effects that can cause signal dropout and localised geometric non-linearity; increased artefacts associated with involuntary motion, physiological flow and variation in the uniformity of RF excitation.

Magnets also have an associated fringe-field that needs to be considered when siting the system. Most superconducting magnets are now actively shielded which means they have a separate set of superconducting coils inside the cryostat positioned outside the main magnet coils, in which the current flows in the opposite direction, reducing the magnitude and effect of the external magnetic field on the surrounding environment. However, due to siting space limitations, occasionally additional passive magnetic shielding in the scan room wall(s) may be required.

In addition all MR systems must be situated within a six-sided RF-shielded examination room with conductive metal lining, usually made of copper or aluminium through which external RF electromagnetic interference will not pass.

Gradients

Linear magnetic field gradients are created by additional coils of wire which are positioned inside the magnet bore, adjacent to the liquid helium cryostat in a cylindrical superconducting system. These coils are designed to provide gradients in the three orthogonal physical directions *x*, *y* and *z*. The effective fulcrum point of each of the three gradients is at the centre of the magnet bore, known as the isocentre. Gradient pulses are trapezoidal in shape since it takes time for the gradient field to ramp up to the desired amplitude and then ramp down again. Gradient performance is defined by the maximum achievable amplitude of the gradient in mTm^{-1}; typically in the range 30–50 mTm^{-1} and the time take to ramp up and down the waveform, known as the rise-time; typically in the range 200–1000 μs. Higher gradient amplitudes allow the system to achieve thinner slices or smaller fields-of-view, whilst shorter rise-times allow shorter TEs, echo-spacings or repetition times. Depending upon the desired imaging plane the required logical gradient pulses: slice-selection, phase and frequency encoding, are played out on the appropriate physical *x*, *y* and *z* gradients, with a mixed combination for oblique imaging.

Gradient switching is accountable for the characteristic knocking noise heard during MRI. As the coils lie within strong static magnetic fields and currents in the coils are pulsed, the coil windings experience a Lorenz force which causes flexion, albeit of very small amplitude, of the gradient coils resulting in acoustic noise. The gradient switching also induces currents in the magnet cryostat, known as eddy currents. These currents decay with time but also cause their own magnetic fields, which can cause image artefacts. Gradient coils are themselves actively shielded by a second set of outer coils to minimise the induction of unwanted eddy currents.

Gradient coils require high currents and voltages in order to produce field variations over the size of the human body. Hence amplifiers are needed to convert the digital waveforms into gradient pulses. Most of this power is dissipated as heat and the gradient coils and often the amplifiers require water-cooling.

Radiofrequency

The RF transmitter creates shaped pulses, centred at the Larmor frequency, which can be used to tip the net magnetisation. The RF pulse waveform is amplified and applied to the transmitter coil. Most commonly this is a large diameter coil, known as the body coil, which is located just inside the gradient coil assembly. Whilst the MR signal received back from the patient can be detected by the body coil, its large size means that the SNR would be relatively poor. In order to maximise SNR, a separate receiver coil is often positioned closely to the anatomy of interest, hence the large number of anatomically optimised receiver coils available (e.g. head, spine, shoulder and knee). In recent years most receiver coils have been constructed from arrays of smaller coil elements. The idea is that smaller coils have a better SNR but a limited field-of view (FOV). Careful combination of multiple coils in a matrix configuration gains the advantage of small coil SNR but with a larger FOV. The signal from each individual coil element is amplified and then digitised in preparation for reconstruction. To minimise noise induced in the receiver chain, detected signal digitisation occurs in close proximity to the RF receiver coil(s). Although the signal is centred on the Larmor frequency the MRI encoding process only involves a small range of frequencies typically in the range ±16 to ±250 kHz, known as the readout bandwidth. Part of the receiver processing is to extract this small readout bandwidth before passing the digitised signals from each coil to the reconstruction hardware. Figure 4 shows a dedicated four element receiver coil for high resolution imaging of the carotid arteries.

Fig. 4 A dedicated four-element receiver coil for bilateral high resolution imaging of the carotid arteries. The images in Figs. 7, 8 and 9 were acquired using this coil

A complication of higher field MR systems is that the power required to achieve a given flip angle is proportional to the square of the frequency. For example a 180° pulse at 3 T requires four times the power than at 1.5 T. With RF power deposition restricted for safety reasons it may be necessary to use fewer RF pulses or longer TRs at 3 T. A further issue at high B_0 is that the wavelength of the RF pulses starts to become comparable with the size of the patient. These effects become more problematic with increasing bore diameter and now most 70 cm 3.0 T systems employ dual channel transmit systems that attempt to mitigate this effect.

Computers

MRI systems utilise a number of computers to control the various sub-systems. The operators console computer (often termed the "host") manages the graphical user interface (GUI) and converts the desired MR parameters, e.g. pulse sequence, slice thickness, FOV and bandwidth into digital representations of the RF and gradient pulses needed to achieve these parameters. Separate computers then manage the timing of these pulses together with other inputs, e.g. ECG triggering. The reconstruction computer takes the digitised data from the receiver coils and performs the necessary mathematical steps required to reconstruct the final image. The reconstructed images are then passed back to the operator's console computer for image display, any further post processing and ultimately archiving to the local Picture Archiving and Communications System (PACS).

Pulse Sequences

The two most basic classes of MRI pulse sequence are spin echo and gradient echo. The spin echo sequence, as already described above (Fig. 1), comprises a 90° excitation pulse followed a time τ later by a 180° refocusing pulse leading to the formation of an echo signal at a time $TE = 2\tau$ after the initial excitation pulse. The signal decay during TE is dependent upon T_2 relaxation. The gradient echo sequence (Fig. 5) does not use a refocusing pulse; instead the echo is formed by a negative-polarity gradient that forcibly dephases the magnetisation before the positive-polarity frequency encoding gradient refocuses the echo. In this case, since the dephasing caused by the static and tissue-induced magnetic field non-uniformities are not eliminated the signal decay is dependent upon T_2^* relaxation.

Gradient echo sequences also generally use excitation flip angles less than 90° combined with very short TRs, thereby achieving very short acquisition times. Gradient echo sequences also yield a very high signal from moving magnetisation, such as in blood, and are routinely used for obtaining MR angiograms, these techniques are commonly referred to as time-of-flight (TOF) methods.

Proton density or T_2-weighted spin echo sequences are quite slow due to the necessity to have a long TR to allow complete recovery of the longitudinal magnetisation

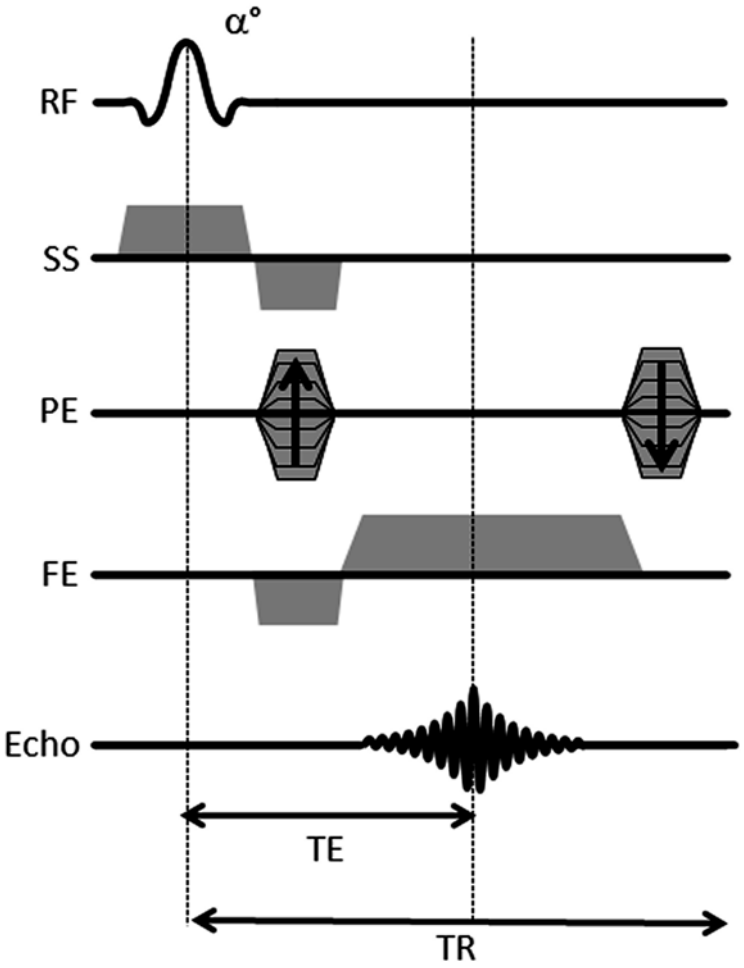

Fig. 5 Gradient echo pulse sequence. *RF* radiofrequency, *SS* slice selection, *PE* phase encoding, *FE* frequency encoding, *TE* echo time, *TR* repetition time

before the next excitation pulse. These long scan times led to the development of Fast or Turbo Spin Echo (FSE/TSE) sequences, originally called Rapid Acquisition with Relaxation Enhancement (RARE) [8]. These sequences are a modification of the standard spin echo sequence whereby multiple refocusing pulses are used to create multiple echo signals during the T_2 decay (Fig. 6). However, each echo is individually phase encoded so that it can be used in the same raw data array, e.g. if 16 refocusing pulses are used then each of the 16 echoes can be used resulting in a factor of 16 reduction in overall scan time. This method has had a significant impact on reducing MRI acquisition times.

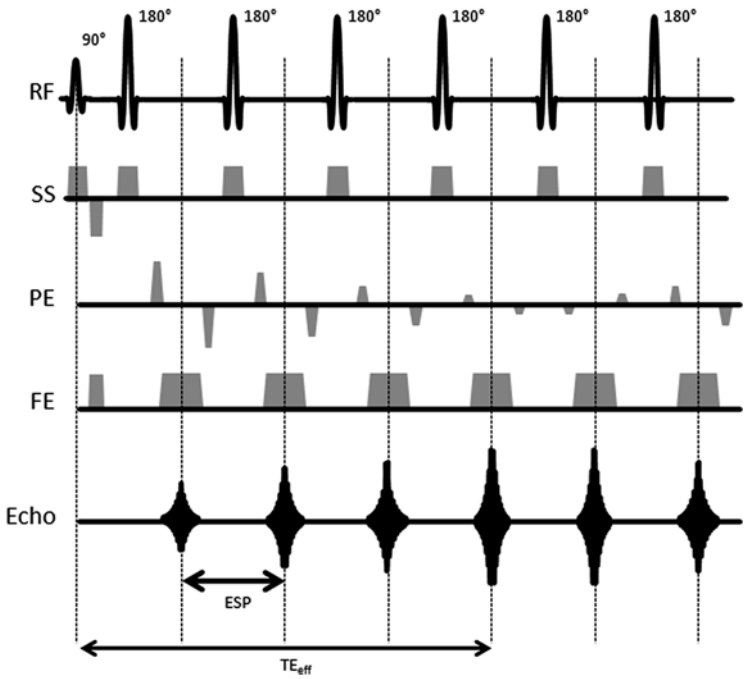

Fig. 6 Fast Spin echo pulse sequence. *RF* radiofrequency, *SS* slice selection, *PE* phase encoding, *FE* frequency encoding, TE_{eff} effective echo time, *ESP* echo spacing

MR images are usually acquired as multiple 2D slices that encompass the anatomy of interest. Whilst these images have relatively good in-plane resolution they have relatively large section thickness, i.e. several times the in-plane resolution, in order to maintain an acceptable signal-to-noise ratio (SNR). It is possible to acquire true three-dimensional (3D) volumetric data with near isotropic spatial resolution by acquiring data using 3D MRI techniques. These methods involve exciting a large slab of tissue, as opposed to individual 2D slices, and then performing an additional phase-encoding in the slice selection direction. By applying a range of slice-selection encoding gradients in the same way as the in-plane phase encoding gradients it is possible to achieve a 3D array of raw data which, after 3D Fourier transformation, yields a set of thin contiguous slices. If the voxels are near isotropic then the images can be reformatted into any plane to optimally demonstrate the pathology.

Vessel Wall Imaging

The main challenge in obtaining high quality images of the vessel wall using MRI is to obtain a sufficiently good SNR. The SNR in MRI is proportional to the size of the imaging voxel therefore high resolution images require good SNR. Due to their

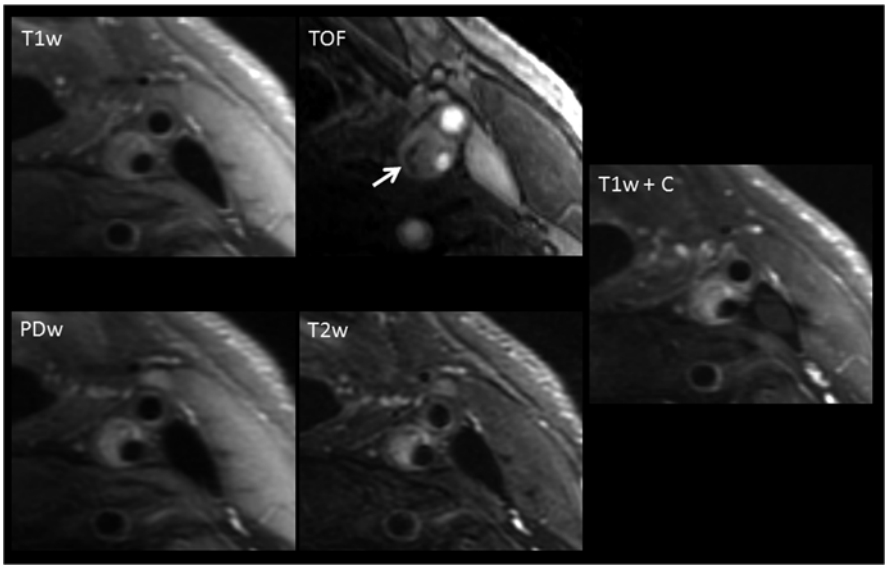

Fig. 7 Multi-contrast 2D acquisition in a patient with a heavily calcified plaque. The calcification is best seen as a hypointense region on the time of-flight (TOF) image (*arrow*)

relatively superficial location it is possible to obtain very high quality images of the carotid vessel wall particularly with the use of dedicated RF receiver coils that are positioned very closely to the subject's neck [9].

In order to achieve a relatively short imaging time, FSE sequences are routinely used for morphological imaging; however, the multiple refocusing pulses often result in variable signal intensities from blood depending upon the flow rate. This can lead to problems in separating slow flow effects from vessel wall pathology such as atheromatous plaques. Various schemes have therefore been developed to suppress the signal from flowing blood without adversely affecting the tissue contrast in the vessel wall. These include techniques such as Double Inversion Recovery (DIR) [10], Motion-Sensitised-Driven-Equilibrium (MSDE) [11] and Delay Alternating with Nutation for Tailored Excitation (DANTE) [12] pulse sequences that are played out just before the imaging sequences, i.e. as preparation schemes. Since MRI can provide multiple contrast weightings, e.g. blood-suppressed T1w, PDw and T2w using FSE acquisitions and bright-blood TOF sequences it is possible to classify the various plaque constituents, e.g. lipid-rich necrotic core (LRNC), fibrous tissue, calcification and thrombus [14]. The use of standard gadolinium-based MRI contrast agents can also help improve tissue differentiation, particularly in the identification of the LRNC [15]. Clinical examples of blood suppressed multi-contrast images obtained in a patient with a heavily calcified plaque are shown in Fig. 7. Images from a patient with plaque containing a large lipid core are shown

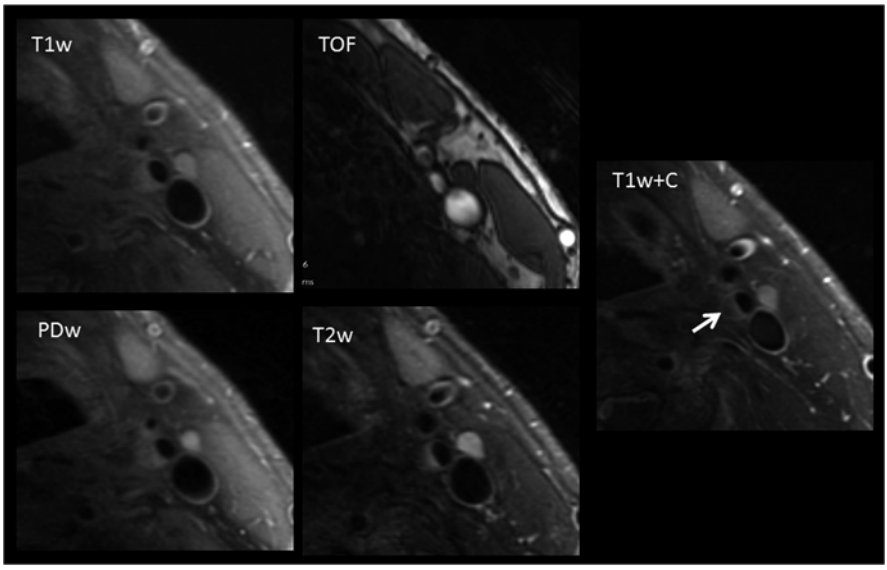

Fig. 8 Multi-contrast 2D acquisition in a patient with a plaque containing a large lipid core, best seen on the T1w image post contrast (T1w + C) (*arrow*), with a fibrous cap

in Fig. 8. Recent developments in three-dimensional (3D) acquisition techniques allow high quality blood-suppressed imaging of the vessel wall with near isotropic sub-millimetre voxel sizes [13]. A clinical example of a 3D FSE acquisition with 0.6 mm isotropic resolution is shown in Fig. 9.

MRI techniques can also be used to perform functional imaging of the vessel wall. One approach is to perform Dynamic Contrast Enhanced (DCE)-MRI. This technique use repeated, i.e. dynamic, imaging of the vessel wall during the first pass of a gadolinium-based MRI contrast agent. The gadolinium shortens the T_1 relaxation time of blood and nearby tissues resulting in a signal hyper-enhancement, particularly during the first pass of the agent. This has been used to visualise and quantify the uptake of contrast agent into the vasa vasorum [16].

Imaging of the coronary arteries presents a number of additional challenges in comparison to the carotid. Firstly the vessels are much smaller and are located more centrally, i.e. further away from the RF receiver coil. This means that the relative resolution of the images is quite poor. In addition cardiac and respiratory motion means that sophisticated techniques are required to "gate" the acquisitions so that data is only acquired during relatively quiescent periods of both cardiac and respiratory motion. Whilst there has been good progress in recent years in obtaining coronary angiograms using MRI [17], and possibly quantifying coronary artery wall thickness [18], currently coronary plaque classification is in its infancy.

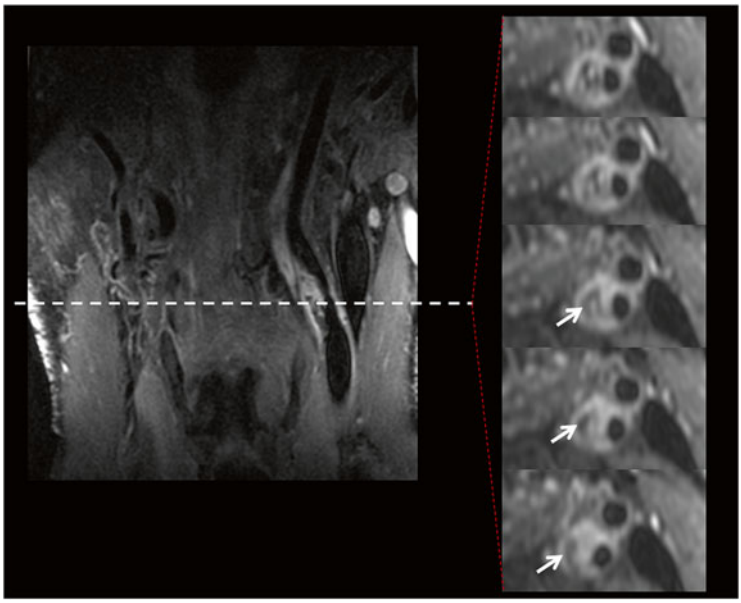

Fig. 9 Coronal 3D post-contrast T1w fast spin echo acquisition acquired with 0.6 mm isotropic resolution. Axial reformats are also shown demonstrating a large lipid core (*arrow*)

References

1. Purcell EM, Torrey HC, Pound RV. Resonance absorption by nuclear magnetic moments in a solid. Phys Rev. 1946;69:37–8.
2. Bloch F, Hansen WW, Packard M. Nuclear induction. Phys Rev. 1946;69:127.
3. Lauterbur PC. Image formation by induced local interactions: examples employing nuclear magnetic resonance. Nature. 1973;242:190–1.
4. Mansfield P, Maudsley AA. Planar spin imaging by NMR. J Phys C Solid State Phys. 1976;9:L409–12.
5. Damadian R, Goldsmith M, Minkoff L. NMR in cancer: XVI. Fonar image of the live human body. Physiol Chem Phys. 1977;9:97–100.
6. Hinshaw WS, Bottomley PA, Holland GN. Radiographic thin-section image of the wrist by nuclear magnetic resonance. Nature (London). 1977;270:722–3.
7. Edelstein WA, Hutchison JMS, Johnson G, Redpath TW. Spin warp NMR imaging and application to human whole-body imaging. Phys Med Biol. 1980;25:751–6.
8. Hennig J, Nauerth A, Friedburg H. RARE imaging: a fast imaging method for clinical MR. Magn Reson Med. 1986;3:823–33.
9. Hayes CE, Mathis CM, Yuan C. Surface coil phased arrays for high-resolution imaging of the carotid arteries. J Magn Reson Imaging. 1996;6:109–12.
10. Simonetti OP, Finn JP, White RD, Laub G, Henry DA. "Black blood" T2-weighted inversion-recovery MR imaging of the heart. Radiology. 1996;199:49–57.
11. Wang J, Yarnykh VL, Hatsukami T, Chu B, Balu N, Yuan C. Improved suppression of plaque-mimicking artifacts in black-blood carotid atherosclerosis imaging using a multislice motion-sensitized driven-equilibrium (MSDE) turbo spin-echo (TSE) sequence. Magn Reson Med. 2007;58:973–81.

12. Li L, Miller KL, Jezzard P. DANTE-prepared pulse trains: a novel approach to motion-sensitized and motion-suppressed quantitative magnetic resonance imaging. Magn Reson Med. 2012;68:1423–38.
13. Koktzoglou I, Chung YC, Carroll TJ, Simonetti OP, Morasch MD, Li D. Three-dimensional black-blood MR imaging of carotid arteries with segmented steady-state free precession: initial experience. Radiology. 2007;243:220–8.
14. Cai JM, Hatsukami TS, Ferguson MS, Small R, Polissar NL, Yuan C. Classification of human carotid atherosclerotic lesions with in vivo multicontrast magnetic resonance imaging. Circulation. 2002;106:1368–73.
15. Cai J, Hatsukami TS, Ferguson MS, et al. In vivo quantitative measurement of intact fibrous cap and lipid-rich necrotic core size in atherosclerotic carotid plaque: comparison of high-resolution, contrast-enhanced magnetic resonance imaging and histology. Circulation. 2005;112:3437–44.
16. Kerwin WS, O'Brien KD, Ferguson MS, Polissar N, Hatsukami TS, Yuan C. Inflammation in carotid atherosclerotic plaque: a dynamic contrast-enhanced MR imaging study. Radiology. 2006;241:459–68.
17. Nezafat R, Manning WJ. Coronary artery disease: high field strength coronary MRA–ready for prime time? Nat Rev Cardiol. 2009;6:676–8.
18. Miao C, Chen S, Macedo R, et al. Positive remodeling of the coronary arteries detected by magnetic resonance imaging in an asymptomatic population: MESA (Multi-Ethnic Study of Atherosclerosis). J Am Coll Cardiol. 2009;53:1708–15.

MR Imaging of Vulnerable Carotid Atherosclerotic Plaques

Chin Lik Tan, Rohitashwa Sinha, Karol Budohoski, and Rikin A. Trivedi

Introduction

Carotid artery atherosclerosis has long been recognised as a major cause of cerebral ischaemia and infarction, with about 30 % of ischaemic strokes attributable to carotid artery disease [1]. Traditionally, the risk of cerebrovascular event was believed to be related to the luminal stenosis brought about by the atherosclerotic plaque [2]. This formed the basis for risk stratification and decision-making on surgical treatment for patients with carotid plaques, even up until today. An analysis of data pooled from several major randomised controlled trials, including European Carotid Surgery Trial (ECST), North American Symptomatic Carotid Endarterectomy Trial (NASCET) and Veterans' Affairs Trial, showed that only patients with severe carotid stenosis, i.e. 70–99 %, were able to derive a significant benefit from a carotid endarterectomy operation [3]. Those with moderate stenosis (50–69 %) or near-occlusion only obtained a marginal benefit from surgery [3]. In the asymptomatic population, current practice is informed by two major trials, the Asymptomatic Carotid Atherosclerosis Study (ACAS) and the Asymptomatic Carotid Surgery Trial (ACST). Together they demonstrated that carotid endarterectomy significantly reduced the risk of strokes at 5 years and 10 years in those with severe narrowing of the carotid arteries (≥60–70 %) [4–6].

More recent research suggests that luminal stenosis may not be the primary contributor to the development of cerebral ischaemic events. Studies from coronary arterial atherosclerosis found that large plaques may be able to dilate vessel walls without causing significant narrowing of the lumen [7]. Meanwhile, many patients with neurological symptoms attributable to internal carotid artery atherosclerosis demonstrated only a moderate degree of internal carotid artery stenosis [8].

C.L. Tan • R. Sinha • K. Budohoski • R.A. Trivedi (✉)
Department of Neurosurgery, Addenbrooke's Hospital, Box 167, Cambridge CB2 0QQ, UK
e-mail: rikin.trivedi@addenbrookes.nhs.uk

R. Trivedi et al. (eds.), *3D Imaging Technologies in Atherosclerosis*,
DOI 10.1007/978-1-4899-7618-5_7

Instead, attention is now directed towards elucidating the characteristics of atherosclerotic plaques. Histological analysis of plaques causing ischaemic stroke or transient ischaemic attacks (TIAs) revealed the different types of lesions which can occur on carotid plaques, which more accurately and sensitively reflect disease progression [9, 10]. Certain features were regularly observed on plaques which have caused ischaemic events, i.e. "vulnerable plaques"; and they define the criteria used to identify plaques at high risk for developing complications including thrombosis, rupture and embolisation [11, 12]. The major criteria for high-risk plaques include active inflammation within the plaque, a thin cap with a large lipid-rich necrotic core, endothelial denudation with superficial platelet aggregation, fissured plaque and severe stenosis (>90 %), while the minor criteria include superficial calcified nodules, yellow colour on angioscopy, intra-plaque haemorrhage, endothelial dysfunction and expansive remodeling [11, 12].

However, specimens for histological studies can only be obtained during invasive therapeutic procedures or post-mortem, thus limiting its usage as an investigative tool preoperatively. One way to circumvent this problem is the use of imaging techniques which are sufficiently sensitive to provide information about the plaque characteristics. This is aided by the fact that carotid arteries lie rather superficially and are relatively immobile. The most promising candidate at the moment is magnetic resonance imaging (MRI) due to its many advantages over other modalities such as ultrasound, computed tomography (CT) or digital subtraction angiography (DSA). It provides images of high spatial resolution for soft tissues, is non-invasive and involves no ionising radiation. Various components within an atherosclerotic artery can be distinguished relatively more easily with MRI, as it allows the acquisition and combination of multi-contrast images. In addition, MRI appears to be capable of identifying features associated with vulnerable plaques, which correlate strongly with subsequent histological analysis [13–16].

Table 1 compares the characteristics of vulnerable plaques that can be obtained using different imaging techniques [17]. Different MRI sequences or modalities

Table 1 Imaging modalities available to assess atherosclerotic carotid plaque characteristics

Plaque characteristic	MRI	CT	US	PET	SPECT	DSA
Active inflammation	✓	x	x	✓	x	x
Thin FC with large LRNC	✓	✓	x	x	x	x
FC disruption	✓	x	x	x	✓	x
Severe stenosis	✓	✓	✓	x	x	✓
Intra-plaque haemorrhage	✓	x	x	x	x	x
Expansive remodelling	✓	x	✓	x	x	x
Superficial calcified nodules	✓	✓	x	x	x	x
Yellow colouring on angioscopy	x	x	x	x	x	x
Endothelial dysfunction	✓	x	x	✓	x	x

MRI magnetic resonance imaging, *CT* computed tomography, *US* ultrasonography, *PET* positron emission tomography, *SPECT* single-photon emission computed tomography, *DSA* digital subtraction angiography

have been employed successfully to image the various characteristics of vulnerable plaques. A recent meta-analysis found that the presence of intra-plaque haemorrhage, lipid-rich necrotic core and thinning/rupture of the fibrous cap as detected using MRI is associated with increased risk of stroke or TIA [18]. Nevertheless, MRI also has its shortcomings, which may limit its wider use. It is expensive and requires highly trained staff. Patients with metallic implants are an absolute contraindication. There is also a long image acquisition time, which can pose problems in imaging stroke patients with impaired neurological status.

Fibrous Cap

The atherosclerotic plaque is covered by a fibrous cap, which consists of a mixture of endothelial cells, collagen fibres and matrix glycoproteins overlying the lipid-rich core (Fig. 1) [19]. A thin fibrous cap has been shown to be associated with higher risks of plaque rupture [10, 11, 20, 21]. Thin or ruptured fibrous cap detected using carotid MRI, in turn, is correlated with ipsilateral ischaemic event [22]. Using a three-dimensional multiple overlapping thin-slab angiography protocol, one group categorised fibrous cap into (1) intact and thick, (2) intact and thin and (3) ruptured, and demonstrated that these findings correlated closely (89 %) with histological assessment [23]. Multi-sequence, high-resolution MRI used to quantify fibrous cap and lipid core thickness also showed strong agreement with histological results, and the fibrous cap-to-lipid core thickness ratio was suggested as a method for characterising vulnerable plaques in vivo [24]. Similarly, in vivo high-resolution contrast-enhanced MRI (CEMRI) was found to provide moderate-to-good measurements of the length and area of intact fibrous cap and lipid-rich necrotic core [25]. In a study of asymptomatic patients with <50 % carotid stenosis, men were shown to have a higher level of thin or ruptured fibrous cap and a larger percentage volume of lipid-rich necrotic core, as compared to women, reflecting the higher risk of subsequent stroke in the former [26]. Treatment of carotid stenosis patients with an anti-platelet agent, cilostazol, was found to significantly increase the percentage of fibrous component in a plaque while simultaneously decreasing the percentage of lipid and haemorrhagic components [27]. These studies provided good evidence that MR imaging of atherosclerotic plaques offers a non-invasive but accurate means of quantifying the fibrous cap.

Disruption of the fibrous cap, e.g. rupture or ulceration, is often seen in histopathological specimens from patients with previous TIA or stroke [28, 29]. This is mainly caused by the pulsatile force imposed by the arterial blood on the atherosclerotic plaque during the cardiac cycle, which leads to fibrous cap fatigue, and subsequent rupture [30]. High-resolution MRI was used to identify ruptured fibrous cap, which was shown to be associated with recent TIA or stroke [16]. In patients who had suffered a stroke, the presence of a thin or ruptured fibrous cap is associated with higher risk of recurrence [31]. Hatsukami et al. successfully used MRI to detect ruptured plaques to a high degree of consistency with histological findings [23].

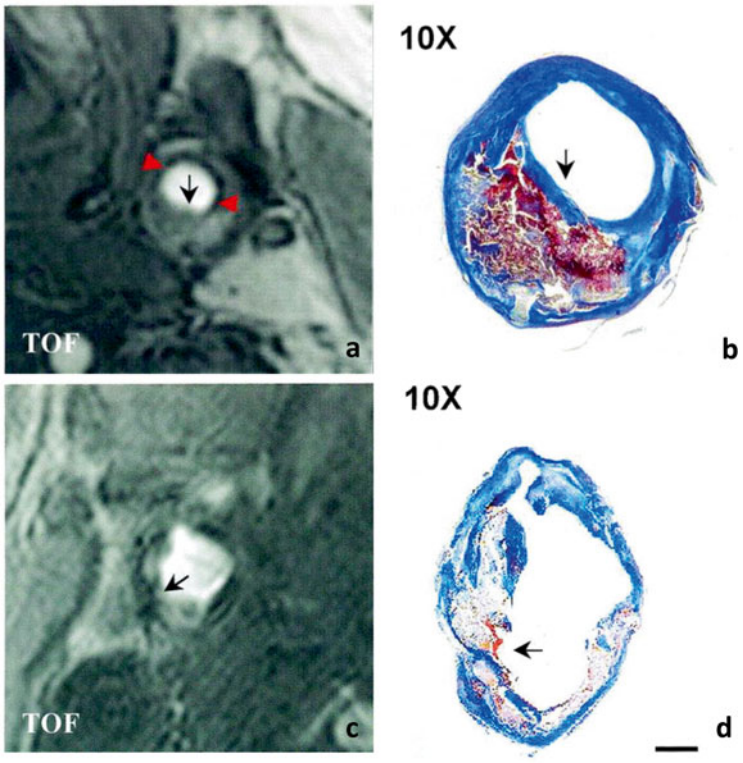

Fig. 1 Comparison of carotid atherosclerotic plaques with intact and ruptured fibrous caps. MRI TOF image of an atherosclerotic plaque with intact fibrous cap (**a**) shows a hypointense band (*red arrowheads*) lining most of the luminal surface except over the bulk of the plaque (*black arrow*). TOF image of a heavily calcified plaque with ruptured fibrous cap (**c**) shows a discontinuous hypointense band surrounding the lumen (*arrow*). Mallory's trichrome-stained sections of the corresponding plaques (**b** and **d**) show a large necrotic core with overlying intact (**b**) or ruptured (**d**) fibrous cap (*arrow*) (scale bar 1 mm). *Adapted from Yuan* et al. *(2002)* Circulation *105:181–185*

Multi-sequence cross-sectional MRI has been used to detect ulceration of carotid atherosclerotic plaques [32, 33]. This technique can be further improved by the addition of longitudinal black-blood MR angiography which enhances the ability to identify plaque ulceration [34]. Nevertheless, it must be borne in mind that the spatial resolution of MRI is lower than the histological definition of a thin fibrous cap, thus limiting its ability to accurately determine the thickness of these caps [25].

Lipid-Rich Necrotic Core

The size of the lipid-rich necrotic core of an atherosclerotic plaque can also determine its vulnerability. This is believed to be due to the combined effect of hypoxia and necrosis in the lipid core and the accompanying neovascularisation, which

promote intra-plaque haemorrhage, which itself is a contributor to the development of vulnerable plaque. The size of lipid-rich necrotic core and % wall volume are plaque characteristics associated with cerebral infarction [35]. A multicentre cross-sectional study using multi-contrast MRI identified the maximum proportion of the arterial wall occupied by the lipid-rich necrotic core as the strongest predictor of intra-plaque haemorrhage [36]. This has potential to be used as a risk-stratifying strategy. Meanwhile, Young et al. performed echo-planar diffusion-weighted imaging sequence along with standard MRI to generate apparent diffusion coefficient (ADC) maps for patients with confirmed moderate-to-severe carotid artery stenosis. They found that quantitative ADC values correlated well with histological examination, with heavier lipid staining corresponding to low ADC values [37]. In addition, they also showed that DWI can be used to differentiate lipid-rich necrotic core from fibrous cap [37]. A recent prospective study calculated the carotid atherosclerosis score (CAS) based on maximal wall thickness and % lipid-rich necrotic core, and found a significant increasing relationship with disrupted luminal surface and plaque progression, features characteristic of a vulnerable plaque [38].

Multi-contrast MRI has also been utilised as an outcome measure for a study investigating the effect of lipid-lowering therapy on carotid atherosclerotic plaque [39]. By following up patients on atorvastatin monotherapy or in combination with other lipid-lowering drugs annually, the authors demonstrated that intensive lipid-lowering therapy significantly decreased the volume and percentage of arterial wall occupied by lipid-rich necrotic core. This lipid-depleting effect was observed after 1 year of treatment and preceded the regression of the plaque itself [39]. Sun et al., meanwhile, showed that short-term (mean 6.9 months) changes in the characteristics or composition of lipid-rich necrotic core can be followed up using serial MRI of the carotid artery, and demonstrated that the progression of lipid-rich necrotic core can be affected by intra-plaque haemorrhage [40].

Vessel Wall Thickness

Arteries may also undergo expansive remodelling, whereby atherosclerotic plaques progress by pushing the vessel wall outwards, rather than causing narrowing of the lumen, making it difficult to be identified using methods such as DSA [7]. A study looking at the impact of simvastatin showed that the lipid-lowering therapy significantly decreased vessel wall thickness and vessel wall area at 12 months, 18 months and 24 months, as assessed by black-blood fast spin-echo MRI [41, 42]. However, further investigations revealed that this effect was not dependent on the dose of the simvastatin used, with both high-dose (80 mg/day) and low-dose (20 mg/day) patients demonstrating similar improvements in vessel wall thickness and area [43]. Another group compared the utility of MRI-derived plaque volume and two-dimensional ultrasound intima-media thickness (IMT) of the carotid plaque in patients on 6-month statin therapy. They found that while IMT did not detect any changes, measurements from MRI showed a significant reduction in plaque volume,

highlighting the advantages of MRI over ultrasound in assessing the response to treatment in patients with atherosclerotic diseases [44].

A recent phase 2b, multicentre clinical trial investigating the effect of dalcetrapib on atherosclerosis used multiple non-invasive imaging modalities, including MRI, CT and PET, as its primary end points looking at vessel structure and inflammation [45]. MRI was used to assess vessel area, wall area, wall thickness and normalised wall index after 24 months of treatment. It was found that MRI-derived change in total vessel area was reduced in patients who were given dalcetrapib, who also did not show progression of carotid plaques [45]. A prospective cohort study on the natural history of carotid and femoral atherosclerosis also employed high-resolution MRI as its non-invasive tool assessing lumen area, vessel area and vessel wall area [46]. The authors reported a progressive decrease in lumen area accompanied by an increased vessel wall area, while the vessel area remained unchanged [46].

Intra-plaque Haemorrhage

The chronic inflammatory process taking place within an atherosclerotic plaque can lead to neovascularisation. These newly formed vessels tend to be weak and fragile, and may rupture easily leading to haemorrhage into the plaque. Recurrent intra-plaque haemorrhage then further perpetuates the inflammatory process, resulting in a vicious cycle. The ability of MRI to detect intra-plaque haemorrhage depends on the degradation of haemorrhage into hemosiderin and ferritin, two major iron-storing proteins in the bloodstream. Haemorrhage appears as a high signal on T1-weighted sequences and low signal on T2-weighted sequences.

The prevalence of intra-plaque haemorrhage as identified by MRI of the carotid artery was significantly higher in symptomatic, compared to asymptomatic, patients [47]. MRI-defined intra-plaque haemorrhage is a strong independent predictor of recurrent ischaemic events and strokes in symptomatic patients with significant carotid stenosis (>50 %) [48]. Atherosclerotic plaques undergo a significantly higher progression rate following the development of intra-plaque haemorrhage, suggesting that early identification of intra-plaque haemorrhage may be clinically useful in ensuring optimal management of patients [49]. Following a stroke, patients with MRI-detected intra-plaque haemorrhage have a higher risk of suffering from a recurrence [31]. Using magnetisation transfer (MT) magnetic resonance (MR) to calculate the magnetisation transfer ratio (MTR), Qiao et al. were able to distinguish low-protein areas from high-protein areas within a plaque, which has different MTRs. Furthermore, they showed that old and recent intra-plaque haemorrhages displayed higher MTR compared to fresh haemorrhage, providing a novel avenue for detecting these vulnerable plaques [50]. The location of haemorrhage can also be identified more precisely with a high-resolution MRI, in distinguishing intra-plaque haemorrhage from juxtaluminal haemorrhage [51]. As mentioned earlier, treatment with an anti-platelet agent cilostazol significantly reduced the percent area occupied by the haemorrhagic component within a carotid atherosclerotic

plaque [27]. In patients with severe carotid stenosis (>50 %) who are also symptomatic, MRI-detected plaque haemorrhage occurs less frequently in females compared to males [52].

Improvements in MRI technology also helped to promote the feasibility of identifying intra-plaque haemorrhage. Magnetisation-prepared rapid acquisition gradient-echo (RAGE) was shown to be highly sensitive and specific in detecting intra-plaque haemorrhage, with a high signal-to-noise ratio [53]. One group developed a novel slab-selective phase-sensitive inversion-recovery (SPI) technique which demonstrated a superior ability to detect intra-plaque haemorrhage, with significantly improved intra-plaque haemorrhage-wall contrast-to-noise ratio and blood suppression efficiency compared to traditional methods [54].

Inflammation

Atherosclerosis is essentially a chronic inflammatory process affecting the tunica intima of the arteries [55]. There is an influx of inflammatory cells including macrophages, neutrophils, T lymphocytes and B lymphocytes into the intima, along with the production and release of a variety of pro-inflammatory factors [55, 56]. This, coupled with the associated neovascularisation, is implicated in the development of vulnerable plaques. Therapies targeting the inflammatory process are also beginning to be used in the treatment of atherosclerosis.

The accumulation of activated macrophages indicates areas of active inflammation. MRI can be utilised to identify these areas, which in turn may suggest increased vulnerability of an atherosclerotic plaque [57, 58]. One technique that has been used is ultra-small superparamagnetic iron oxide (USPIO)-enhanced MRI, in which the USPIO acts as a non-gadolinium-based contrast agent that is selectively taken up by activated macrophages in areas of inflammation. Accumulation of USPIO in macrophages was clearly detected in almost all (10/11) of the patients in one in vivo study, which correlated with ruptured or rupture-prone atherosclerotic plaques [59]. Trivedi et al. subsequently characterised the time frame of USPIO-enhanced MRI signal, demonstrating that the optimal window for detection was 24–36 h post-infusion of contrast (Fig. 2) [60]. USPIO-enhanced MRI of the carotid artery has also been tested as an outcome measure for the effect of lipid-lowering agents on atherosclerotic plaques in a clinical trial (ATHEROMA). The authors showed that treating patients with known carotid plaques with high-dose (80 mg/day) atorvastatin significantly reduced USPIO-defined inflammation, from as early as 6 weeks after starting treatment [61]. This highlights the potential of USPIO-enhanced MRI as a novel imaging modality in assessing plaque vulnerability and the effectiveness of medical therapies.

A further study demonstrated an association between USPIO-enhanced MRI signal and biomechanical stress, suggesting a complex interaction between different risk factors in contributing to the vulnerability of atherosclerotic plaques [62]. On the other hand, there appears to be no correlation between inflammation as detected

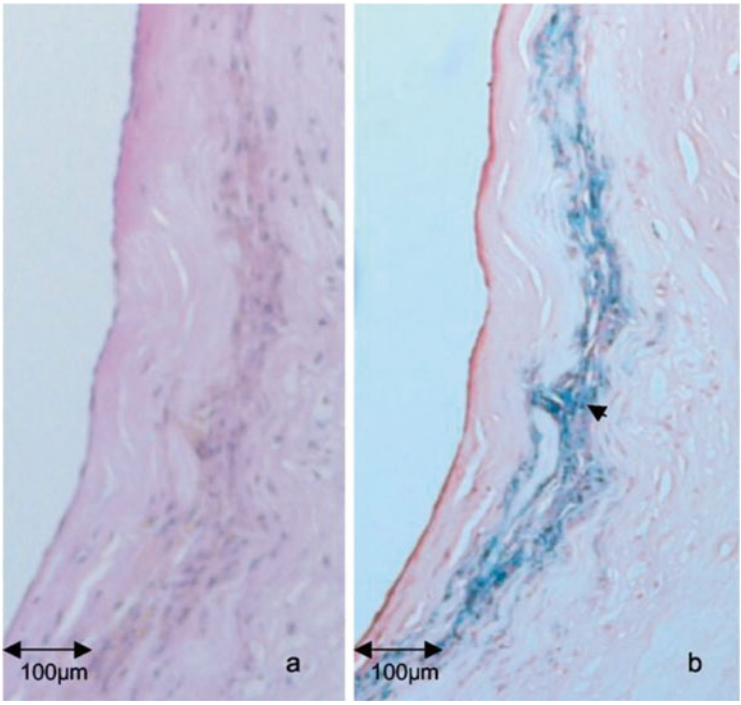

Fig. 2 Co-localisation of USPIO with areas of high macrophage content in the fibrous cap of an atherosclerotic plaque. H&E (**a**) and Perls staining (**b**) on a section of atherosclerotic plaque shows areas of USPIO accumulation co-localising with areas of high macrophage content in the fibrous cap region at high power (*arrow*). *Adapted from Trivedi* et al. *(2004)* Stroke *35:1631–1635*

by USPIO-enhanced signal change and luminal stenosis [63]. However, plaques that have undergone intra-plaque haemorrhage also had higher levels of macrophage and lymphoid cells, suggesting a link between intra-plaque haemorrhage and inflammation [64].

Another feature of inflammation in atherosclerosis is neovascularisation, whereby new, weak and fragile vessels encroach into the areas affected, increasing the risk of intra-plaque haemorrhage. A direct correlation exists between the extent of microvasculature within a plaque and the risk of intra-plaque haemorrhage and subsequent rupture [65, 66]. To visualise these new vessel formation in atherosclerotic plaques, dynamic contrast-enhanced MRI (DCE-MRI), a technique originally developed for neuro-oncology is beginning to be used. DCE-MRI of the human carotid arteries demonstrated a hyperintense outer rim surrounding the vessel, indicating angiogenesis of the wall itself, which was thicker in older patients [67]. DCE-MR angiography, meanwhile, provided a highly accurate image of the areas around the atherosclerotic plaque, including plaque morphology and the thickened arterial wall [68].

Kinetic modelling is used to analyse the images obtained, providing information about the different tissues imaged. In the case of microvasculature formation around the atherosclerotic plaque, two main parameters are used, i.e. fractional plasma volume (V_p) and transfer constant of the contrast agent (K^{trans}). They represent the intravascular and extravascular spaces, respectively. V_p correlates well with histological findings of neovascularisation, and is believed to represent the actual microvascular volume [69, 70]. In contrast, K^{trans} reflects the permeability of the microvasculature, and correlates with the accumulation of macrophages within the plaque [70].

MRI contrast agents generally elicit a non-specific signal enhancement in tissues. Major studies are under way to discover more specific markers which can accurately identify lipid components [28, 71], thrombus [72], inflammatory mediators [73–75] and apoptotic cells [76]. A study using gadolinium-enhanced MRI on carotid plaque revealed an association between contrast enhancement and characteristics of a vulnerable plaque, including neovascularisation and macrophage infiltration [77].

Biomechanical Stress

Local mechanical loading can lead to the formation of intraluminal thrombus as well as plaque haemorrhage. This is mainly due to an increased stretch force causing the rupture of neovessels, resulting in the formation of intra-plaque haemorrhage [78]. Arteries under constant biomechanical stress due to hyperkinetic or turbulent flow, such as those undergoing chronic inflammation from atherosclerosis, have a higher tendency to rupture [79]. Arteries with high stiffness as measured by aortic pulse wave velocity were associated with the presence of an atherosclerotic plaque, as well as the characteristic features of a vulnerable plaque such as intraplaque haemorrhage [80].

Significant differences in plaque stress were observed between the diseased and non-diseased segments of the artery [81]. Similarly, carotid plaques in symptomatic patients, especially those suffering from recurrent TIAs, tend to be under a higher biomechanical stress, when compared to asymptomatic ones (Fig. 3) [81]. High-resolution MRI performed on stroke or TIA patients showed that haemorrhagic plaques tended to have higher biomechanical stresses than non-haemorrhagic ones [82, 83]. Measurements of arterial distensibility have also been used to detect carotid stenosis (>15 %) resulting from atherosclerotic plaques [84]. In this study, significantly higher distensibility was detected in the common segment of the carotid artery compared to the internal carotid segment in healthy patients, whereas no segmental differences in distensibility were seen in the disease population [84].

Aggressive lipid-lowering treatment with high-dose (80 mg/day) atorvastatin was shown to result in a significant reduction in arterial wall strain and stiffness, as well as increase in distensibility and compliance coefficients [85, 86].

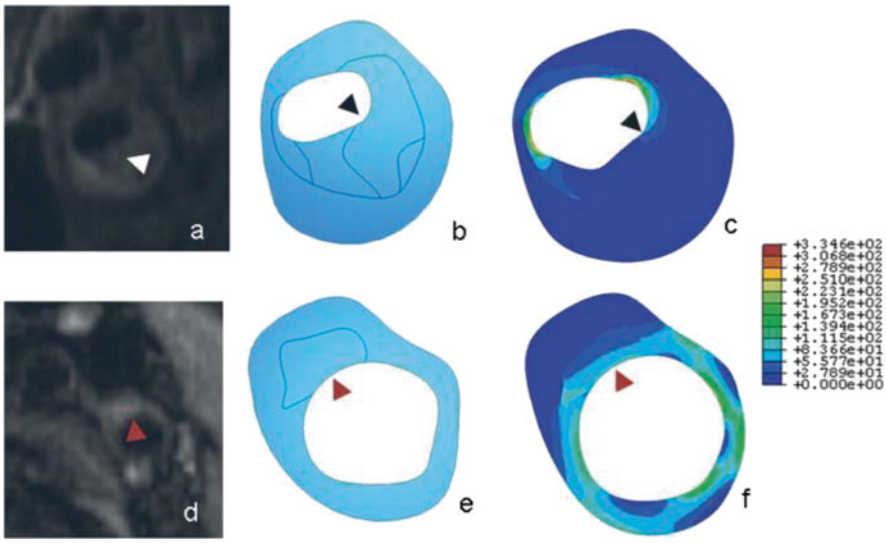

Fig. 3 Comparison of stress maps of atherosclerotic plaques between symptomatic (**a**–**c**) and asymptomatic individuals (**d**–**f**). Magnetic resonance images (**a** and **d**), geometry delineations (**b** and **e**) and stress maps (**c** and **f**) for symptomatic (**a**–**c**) and asymptomatic (**d**–**f**) individuals. The symptomatic plaque (**a**–**c**) is more stenotic and has a large lipid core (*arrowhead*), with higher peak stresses in distinct foci while the asymptomatic plaque (**d**–**f**) is predominantly fibrous (*arrowhead*). *Adapted from Trivedi* et al. *(2007)* J Neurosurg *107:536–542*

Conclusion

Since the shift of focus on the pathophysiology of atherosclerosis from luminal stenosis to the characteristics of carotid plaque, much effort has been put in to find ways of elucidating the plaque components non-invasively. Features associated with a vulnerable plaque, i.e. one at a high risk of resulting in an ischaemic event, such as thin fibrous cap, large volume of lipid-rich necrotic core, intra-plaque haemorrhage and active inflammation, have all been effectively imaged using MRI. However, many of those experiments were only at a preliminary stage, and further studies involving larger populations are warranted. With further validation and additional supporting evidence, it is likely that MRI will become the frontline investigative tool for imaging carotid atherosclerotic plaques, including for diagnosis, surveillance and follow-up post-treatment.

References

1. Levy EI, Mocco J, Samuelson RM, Ecker RD, Jahromi BS, Hopkins LN. Optimal treatment of carotid artery disease. J Am Coll Cardiol. 2008;51:979–85.
2. Fisher M. Occlusion of the internal carotid artery. AMA Arch Neurol Psychiatry. 1951;65:346–77.

3. Rothwell PM, Eliasziw M, Gutnikov SA, Fox AJ, Taylor DW, Mayberg MR, Warlow CP, Barnett HJ. Analysis of pooled data from the randomised controlled trials of endarterectomy for symptomatic carotid stenosis. Lancet. 2003;361:107–16.
4. Executive Committee for the Asymptomatic Carotid Atherosclerosis Study. Endarterectomy for asymptomatic carotid artery stenosis. JAMA. 1995;273:1421–8.
5. Halliday A, Mansfield A, Marro J, Peto C, Peto R, Potter J, Thomas D, MRC, Asymptomatic Carotid Surgery Trial (ACST) Collaborative Group. Prevention of disabling and fatal strokes by successful carotid endarterectomy in patients without recent neurological symptoms: randomised controlled trial. Lancet. 2004;363:1491–502.
6. Halliday A, Harrison M, Hayter E, Kong X, Mansfield A, Marro J, Pan H, Peto R, Potter J, Rahimi K, Rau A, Robertson S, Streifler J, Thomas D, Asymptomatic Carotid Surgery Trial (ACST) Collaborative Group. 10-year stroke prevention after successful carotid endarterectomy for asymptomatic stenosis (ACST-1): a multicentre randomised trial. Lancet. 2010; 376:1074–84.
7. Glagov S, Weisenberg E, Zarins CK, Stankunavicius R, Kolettis GJ. Compensatory enlargement of human atherosclerotic coronary arteries. N Engl J Med. 1987;316:1371–5.
8. Brown PB, Zwiebel WJ, Call GK. Degree of cervical carotid artery stenosis and hemispheric stroke: duplex US findings. Radiology. 1989;170:541–3.
9. Stary HC, Chandler AB, Glagov S, Guyton JR, Insull Jr W, Rosenfeld ME, Schaffer SA, Schwartz CJ, Wagner WD, Wissler RW. A definition of initial, fatty streak, and intermediate lesions of atherosclerosis. A report from the Committee on Vascular Lesions of the Council on Arteriosclerosis, American Heart Association. Circulation. 1994;89:2462–78.
10. Stary HC, Chandler AB, Dinsmore RE, Fuster V, Glagov S, Insull Jr W, Rosenfeld ME, Schwartz CJ, Wagner WD, Wissler RW. A definition of advanced types of atherosclerotic lesions and a histological classification of atherosclerosis. A report from the Committee on Vascular Lesions of the Council on Arteriosclerosis, American Heart Association. Circulation. 1995;92:1355–74.
11. Naghavi M, Libby P, Falk E, Casscells SW, Litovsky S, Rumberger J, Badimon JJ, Stefanadis C, Moreno P, Pasterkamp G, Fayad Z, Stone PH, Waxman S, Raggi P, Madjid M, Zarrabi A, Burke A, Yuan C, Fitzgerald PJ, Siscovick DS, de Korte CL, Aikawa M, Airaksinen KE, Assmann G, Becker CR, Chesebro JH, Farb A, Galis ZS, Jackson C, Jang IK, Koenig W, Lodder RA, March K, Demirovic J, Navab M, Priori SG, Rekhter MD, Bahr R, Grundy SM, Mehran R, Colombo A, Boerwinkle E, Ballantyne C, Insull Jr W, Schwartz RS, Vogel R, Serruys PW, Hansson GK, Faxon DP, Kaul S, Drexler H, Greenland P, Muller JE, Virmani R, Ridker PM, Zipes DP, Shah PK, Willerson JT. From vulnerable plaque to vulnerable patient: a call for new definitions and risk assessment strategies: part II. Circulation. 2003;108:1772–8.
12. Naghavi M, Libby P, Falk E, Casscells SW, Litovsky S, Rumberger J, Badimon JJ, Stefanadis C, Moreno P, Pasterkamp G, Fayad Z, Stone PH, Waxman S, Raggi P, Madjid M, Zarrabi A, Burke A, Yuan C, Fitzgerald PJ, Siscovick DS, de Korte CL, Aikawa M, Juhani Airaksinen KE, Assmann G, Becker CR, Chesebro JH, Farb A, Galis ZS, Jackson C, Jang IK, Koenig W, Lodder RA, March K, Demirovic J, Navab M, Priori SG, Rekhter MD, Bahr R, Grundy SM, Mehran R, Colombo A, Boerwinkle E, Ballantyne C, Insull Jr W, Schwartz RS, Vogel R, Serruys PW, Hansson GK, Faxon DP, Kaul S, Drexler H, Greenland P, Muller JE, Virmani R, Ridker PM, Zipes DP, Shah PK, Willerson JT. From vulnerable plaque to vulnerable patient: a call for new definitions and risk assessment strategies: part I. Circulation. 2003;108:1664–72.
13. Stemme S, Faber B, Holm J, Wiklund O, Witztum JL, Hansson GK. T lymphocytes from human atherosclerotic plaques recognize oxidized low density lipoprotein. Proc Natl Acad Sci U S A. 1995;92:3893–7.
14. Saam T, Hatsukami TS, Takaya N, Chu B, Underhill H, Kerwin WS, Cai J, Ferguson MS, Yuan C. The vulnerable, or high-risk, atherosclerotic plaque: noninvasive MR imaging for characterization and assessment. Radiology. 2007;244:64–77.
15. Trivedi RA, Gillard JH, Kirkpatrick PJ. Modern methods for imaging carotid atheroma. Br J Neurosurg. 2008;22:350–9.

16. Yuan C, Zhang SX, Polissar NL, Echelard D, Ortiz G, Davis JW, Ellington E, Ferguson MS, Hatsukami TS. Identification of fibrous cap rupture with magnetic resonance imaging is highly associated with recent transient ischemic attack or stroke. Circulation. 2002;105:181–5.
17. Sinha R, Budohoski KP, Young VEL, Trivedi RA. Magnetic resonance imaging of vulnerable carotid plaques. In: Saba L et al., editors. Multi-modality atherosclerosis imaging and diagnosis. New York: Springer; 2014. p. 107–19.
18. Gupta A, Baradaran H, Schweitzer AD, Kamel H, Pandya A, Delgado D, Dunning A, Mushlin AI, Sanelli PC. Carotid plaque MRI and stroke risk: a systematic review and meta-analysis. Stroke. 2013;44:3071–7.
19. Berliner JA, Navab M, Fogelman AM, Frank JS, Demer LL, Edwards PA, Watson AD, Lusis AJ. Atherosclerosis: basic mechanisms. Oxidation, inflammation, and genetics. Circulation. 1995;91(9):2488–96.
20. Saam T, Ferguson MS, Yarnykh VL, Takaya N, Xu D, Polissar NL, Hatsukami TS, Yuan C. Quantitative evaluation of carotid plaque composition by in vivo MRI. Arterioscler Thromb Vasc Biol. 2005;25:234–9.
21. Virmani R, Narula J, Farb A. When neoangiogenesis ricochets. Am Heart J. 1998;136:937–9.
22. Takaya N, Yuan C, Chu B, Saam T, Underhill H, Cai J, Tran N, Polissar NL, Isaac C, Ferguson MS, Garden GA, Cramer SC, Maravilla KR, Hashimoto B, Hatsukami TS. Association between carotid plaque characteristics and subsequent ischemic cerebrovascular events: a prospective assessment with MRI–initial results. Stroke. 2006;37:818–23.
23. Hatsukami TS, Ross R, Polissar NL, Yuan C. Visualization of fibrous cap thickness and rupture in human atherosclerotic carotid plaque in vivo with high-resolution magnetic resonance imaging. Circulation. 2000;102:959–64.
24. Trivedi RA, U-King-Im JM, Graves MJ, Horsley J, Goddard M, Kirkpatrick PJ, Gillard JH. MRI-derived measurements of fibrous-cap and lipid-core thickness: the potential for identifying vulnerable carotid plaques in vivo. Neuroradiology. 2004;46:738–43.
25. Cai J, Hatsukami TS, Ferguson MS, Kerwin WS, Saam T, Chu B, Takaya N, Polissar NL, Yuan C. In vivo quantitative measurement of intact fibrous cap and lipid-rich necrotic core size in atherosclerotic carotid plaque: comparison of high-resolution, contrast-enhanced magnetic resonance imaging and histology. Circulation. 2005;112:3437–44.
26. Ota H, Reeves MJ, Zhu DC, Majid A, Collar A, Yuan C, DeMarco JK. Sex differences of high-risk carotid atherosclerotic plaque with less than 50% stenosis in asymptomatic patients: an in vivo 3T MRI study. AJNR Am J Neuroradiol. 2013;34:1049–1055, S1.
27. Yamaguchi M, Sasaki M, Ohba H, Mori K, Narumi S, Katsura N, Ohura K, Kudo K, Terayama Y. Quantitative assessment of changes in carotid plaques during cilostazol administration using three-dimensional ultrasonography and non-gated magnetic resonance plaque imaging. Neuroradiology. 2012;54:939–45.
28. Chen W, Vucic E, Leupold E, Mulder WJ, Cormode DP, Briley-Saebo KC, Barazza A, Fisher EA, Dathe M, Fayad ZA. Incorporation of an apoE-derived lipopeptide in high-density lipoprotein MRI contrast agents for enhanced imaging of macrophages in atherosclerosis. Contrast Media Mol Imaging. 2008;3:233–42.
29. Spagnoli LG, Mauriello A, Sangiorgi G, Fratoni S, Bonanno E, Schwartz RS, Piepgras DG, Pistolese R, Ippoliti A, Holmes Jr DR. Extracranial thrombotically active carotid plaque as a risk factor for ischemic stroke. JAMA. 2004;292:1845–52.
30. Huang Y, Teng Z, Sadat U, He J, Graves MJ, Gillard JH. In vivo MRI-based simulation of fatigue process: a possible trigger for human carotid atherosclerotic plaque rupture. Biomed Eng Online. 2013;12:36.
31. Kwee RM, van Oostenbrugge RJ, Mess WH, Prins MH, van der Geest RJ, ter Berg JW, Franke CL, Korten AG, Meems BJ, van Engelshoven JM, Wildberger JE, Kooi ME. MRI of carotid atherosclerosis to identify TIA and stroke patients who are at risk of a recurrence. J Magn Reson Imaging. 2013;37:1189–94.
32. Chu B, Ferguson MS, Underhill H, Takaya N, Cai J, Kliot M, Yuan C, Hatsukami TS. Images in cardiovascular medicine. Detection of carotid atherosclerotic plaque ulceration, calcification, and thrombosis by multicontrast weighted magnetic resonance imaging. Circulation. 2005;112(1):e3–4.

33. Chu B, Yuan C, Takaya N, Shewchuk JR, Clowes AW, Hatsukami TS. Images in cardiovascular medicine. Serial high-spatial-resolution, multisequence magnetic resonance imaging studies identify fibrous cap rupture and penetrating ulcer into carotid atherosclerotic plaque. Circulation. 2006;113(12):e660–1.
34. Yu W, Underhill HR, Ferguson MS, Hippe DS, Hatsukami TS, Yuan C, Chu B. The added value of longitudinal black-blood cardiovascular magnetic resonance angiography in the cross sectional identification of carotid atherosclerotic ulceration. J Cardiovasc Magn Reson. 2009;11:31.
35. Zhao H, Zhao X, Liu X, Cao Y, Hippe DS, Sun J, Li F, Xu J, Yuan C. Association of carotid atherosclerotic plaque features with acute ischemic stroke: a magnetic resonance imaging study. Eur J Radiol. 2013;82:e465–70.
36. Underhill HR, Hatsukami TS, Cai J, Yu W, DeMarco JK, Polissar NL, Ota H, Zhao X, Dong L, Oikawa M, Yuan C. A noninvasive imaging approach to assess plaque severity: the carotid atherosclerosis score. AJNR Am J Neuroradiol. 2010;31:1068–75.
37. Young VE, Patterson AJ, Sadat U, Bowden DJ, Graves MJ, Tang TY, Priest AN, Skepper JN, Kirkpatrick PJ, Gillard JH. Diffusion-weighted magnetic resonance imaging for the detection of lipid-rich necrotic core in carotid atheroma in vivo. Neuroradiology. 2010;52:929–36.
38. Xu D, Hippe DS, Underhill HR, Oikawa-Wakayama M, Dong L, Yamada K, Yuan C, Hatsukami TS. Prediction of high-risk plaque development and plaque progression with the carotid atherosclerosis score. JACC Cardiovasc Imaging. 2014;7(4):366–73. pii: S1936-878X(13)00900-5.
39. Zhao XQ, Dong L, Hatsukami T, Phan BA, Chu B, Moore A, Lane T, Neradilek MB, Polissar N, Monick D, Lee C, Underhill H, Yuan C. MR imaging of carotid plaque composition during lipid-lowering therapy a prospective assessment of effect and time course. JACC Cardiovasc Imaging. 2011;4:977–86.
40. Sun J, Balu N, Hippe DS, Xue Y, Dong L, Zhao X, Li F, Xu D, Hatsukami TS, Yuan C. Subclinical carotid atherosclerosis: short-term natural history of lipid-rich necrotic core–a multicenter study with MR imaging. Radiology. 2013;268:61–8.
41. Corti R, Fayad ZA, Fuster V, Worthley SG, Helft G, Chesebro J, Mercuri M, Badimon JJ. Effects of lipid-lowering by simvastatin on human atherosclerotic lesions: a longitudinal study by high-resolution, noninvasive magnetic resonance imaging. Circulation. 2001;104:249–52.
42. Corti R, Fuster V, Fayad ZA, Worthley SG, Helft G, Smith D, Weinberger J, Wentzel J, Mizsei G, Mercuri M, Badimon JJ. Lipid lowering by simvastatin induces regression of human atherosclerotic lesions: two years' follow-up by high-resolution noninvasive magnetic resonance imaging. Circulation. 2002;106:2884–7.
43. Corti R, Fuster V, Fayad ZA, Worthley SG, Helft G, Chaplin WF, Muntwyler J, Viles-Gonzalez JF, Weinberger J, Smith DA, Mizsei G, Badimon JJ. Effects of aggressive versus conventional lipid-lowering therapy by simvastatin on human atherosclerotic lesions: a prospective, randomized, double-blind trial with high-resolution magnetic resonance imaging. J Am Coll Cardiol. 2005;46:106–12.
44. Migrino RQ, Bowers M, Harmann L, Prost R, LaDisa Jr JF. Carotid plaque regression following 6-month statin therapy assessed by 3T cardiovascular magnetic resonance: comparison with ultrasound intima media thickness. J Cardiovasc Magn Reson. 2011;13:37.
45. Fayad ZA, Mani V, Woodward M, Kallend D, Abt M, Burgess T, Fuster V, Ballantyne CM, Stein EA, Tardif JC, Rudd JH, Farkouh ME, Tawakol A. Safety and efficacy of dalcetrapib on atherosclerotic disease using novel non-invasive multimodality imaging (dal-PLAQUE): a randomised clinical trial. Lancet. 2011;378:1547–59.
46. Bianda N, Di Valentino M, Periat D, Segatto JM, Oberson M, Moccetti M, Sudano I, Santini P, Limoni C, Froio A, Stuber M, Corti R, Gallino A, Wyttenbach R. Progression of human carotid and femoral atherosclerosis: a prospective follow-up study by magnetic resonance vessel wall imaging. Eur Heart J. 2012;33:230–7.
47. Millon A, Mathevet JL, Boussel L, Faries PL, Fayad ZA, Douek PC, Feugier P. High-resolution magnetic resonance imaging of carotid atherosclerosis identifies vulnerable carotid plaques. J Vasc Surg. 2013;57:1046–1051.e2.

48. Hosseini AA, Kandiyil N, Macsweeney ST, Altaf N, Auer DP. Carotid plaque hemorrhage on magnetic resonance imaging strongly predicts recurrent ischemia and stroke. Ann Neurol. 2013;73:774–84.
49. Sun J, Underhill HR, Hippe DS, Xue Y, Yuan C, Hatsukami TS. Sustained acceleration in carotid atherosclerotic plaque progression with intraplaque hemorrhage: a long-term time course study. JACC Cardiovasc Imaging. 2012;5:798–804.
50. Qiao Y, Hallock KJ, Hamilton JA. Magnetization transfer magnetic resonance of human atherosclerotic plaques ex vivo detects areas of high protein density. J Cardiovasc Magn Reson. 2011;13:73.
51. Kampschulte A, Ferguson MS, Kerwin WS, Polissar NL, Chu B, Saam T, Hatsukami TS, Yuan C. Differentiation of intraplaque versus juxtaluminal hemorrhage/thrombus in advanced human carotid atherosclerotic lesions by in vivo magnetic resonance imaging. Circulation. 2004;110:3239–44.
52. Kandiyil N, Altaf N, Hosseini AA, MacSweeney ST, Auer DP. Lower prevalence of carotid plaque hemorrhage in women, and its mediator effect on sex differences in recurrent cerebrovascular events. PLoS One. 2012;7, e47319.
53. Ota H, Yarnykh VL, Ferguson MS, Underhill HR, Demarco JK, Zhu DC, Oikawa M, Dong L, Zhao X, Collar A, Hatsukami TS, Yuan C. Carotid intraplaque hemorrhage imaging at 3.0-T MR imaging: comparison of the diagnostic performance of three T1-weighted sequences. Radiology. 2010;254:551–63.
54. Wang J, Ferguson MS, Balu N, Yuan C, Hatsukami TS, Bornert P. Improved carotid intraplaque hemorrhage imaging using a slab-selective phase-sensitive inversion-recovery (SPI) sequence. Magn Reson Med. 2010;64:1332–40.
55. Frostegård J. Immunity, atherosclerosis and cardiovascular disease. BMC Med. 2013;11:117.
56. Libby P. Inflammation in atherosclerosis. Arterioscler Thromb Vasc Biol. 2012;32:2045–51.
57. Schmitz SA, Coupland SE, Gust R, Winterhalter S, Wagner S, Kresse M, Semmler W, Wolf KJ. Superparamagnetic iron oxide-enhanced MRI of atherosclerotic plaques in Watanabe hereditable hyperlipidemic rabbits. Invest Radiol. 2000;35:460–71.
58. Schmitz SA, Taupitz M, Wagner S, Wolf KJ, Beyersdorff D, Hamm B. Magnetic resonance imaging of atherosclerotic plaques using superparamagnetic iron oxide particles. J Magn Reson Imaging. 2001;14:355–61.
59. Kooi ME, Cappendijk VC, Cleutjens KB, Kessels AG, Kitslaar PJ, Borgers M, Frederik PM, Daemen MJ, van Engelshoven JM. Accumulation of ultrasmall superparamagnetic particles of iron oxide in human atherosclerotic plaques can be detected by in vivo magnetic resonance imaging. Circulation. 2003;107:2453–8.
60. Trivedi RA, U-King-Im JM, Graves MJ, Cross JJ, Horsley J, Goddard MJ, Skepper JN, Quartey G, Warburton E, Joubert I, Wang L, Kirkpatrick PJ, Brown J, Gillard JH. In vivo detection of macrophages in human carotid atheroma: temporal dependence of ultrasmall superparamagnetic particles of iron oxide-enhanced MRI. Stroke. 2004;35:1631–5.
61. Tang TY, Howarth SP, Miller SR, Graves MJ, Patterson AJ, U-King-Im JM, Li ZY, Walsh SR, Brown AP, Kirkpatrick PJ, Warburton EA, Hayes PD, Varty K, Boyle JR, Gaunt ME, Zalewski A, Gillard JH. The ATHEROMA (Atorvastatin Therapy: Effects on Reduction of Macrophage Activity) Study. Evaluation using ultrasmall superparamagnetic iron oxide-enhanced magnetic resonance imaging in carotid disease. J Am Coll Cardiol. 2009;53:2039–50.
62. Tang TY, Howarth SP, Li ZY, Miller SR, Graves MJ, U-King-Im JM, Trivedi RA, Walsh SR, Brown AP, Kirkpatrick PJ, Gaunt ME, Gillard JH. Correlation of carotid atheromatous plaque inflammation with biomechanical stress: utility of USPIO enhanced MR imaging and finite element analysis. Atherosclerosis. 2008;196:879–87.
63. Tang TY, Howarth SP, Miller SR, Graves MJ, U-King-Im JM, Li ZY, Walsh SR, Patterson AJ, Kirkpatrick PJ, Warburton EA, Varty K, Gaunt ME, Gillard JH. Correlation of carotid atheromatous plaque inflammation using USPIO-enhanced MR imaging with degree of luminal stenosis. Stroke. 2008;39:2144–7.
64. Altaf N, Akwei S, Auer DP, MacSweeney ST, Lowe J. Magnetic resonance detected carotid plaque hemorrhage is associated with inflammatory features in symptomatic carotid plaques. Ann Vasc Surg. 2013;27:655–61.

65. Mofidi R, Crotty TB, McCarthy P, Sheehan SJ, Mehigan D, Keaveny TV. Association between plaque instability, angiogenesis and symptomatic carotid occlusive disease. Br J Surg. 2001;88:945–50.
66. Moreno PR, Purushothaman KR, Fuster V, Echeverri D, Truszczynska H, Sharma SK, Badimon JJ, O'Connor WN. Plaque neovascularization is increased in ruptured atherosclerotic lesions of human aorta: implications for plaque vulnerability. Circulation. 2004;110:2032–8.
67. Aoki S, Aoki K, Ohsawa S, Nakajima H, Kumagai H, Araki T. Dynamic MR imaging of the carotid wall. J Magn Reson Imaging. 1999;9:420–7.
68. Aoki S, Nakajima H, Kumagai H, Araki T. Dynamic contrast-enhanced MR angiography and MR imaging of the carotid artery: high-resolution sequences in different acquisition planes. AJNR Am J Neuroradiol. 2000;21(2):381–5.
69. Kerwin W, Hooker A, Spilker M, Vicini P, Ferguson M, Hatsukami T, Yuan C. Quantitative magnetic resonance imaging analysis of neovasculature volume in carotid atherosclerotic plaque. Circulation. 2003;107:851–6.
70. Kerwin WS, O'Brien KD, Ferguson MS, Polissar N, Hatsukami TS, Yuan C. Inflammation in carotid atherosclerotic plaque: a dynamic contrast-enhanced MR imaging study. Radiology. 2006;241:459–68.
71. Briley-Saebo KC, Shaw PX, Mulder WJ, Choi SH, Vucic E, Aguinaldo JG, Witztum JL, Fuster V, Tsimikas S, Fayad ZA. Targeted molecular probes for imaging atherosclerotic lesions with magnetic resonance using antibodies that recognize oxidation-specific epitopes. Circulation. 2008;117:3206–15.
72. Spuentrup E, Botnar RM, Wiethoff AJ, Ibrahim T, Kelle S, Katoh M, Ozgun M, Nagel E, Vymazal J, Graham PB, Gunther RW, Maintz D. MR imaging of thrombi using EP-2104R, a fibrin-specific contrast agent: initial results in patients. Eur Radiol. 2008;18:1995–2005.
73. Laitinen I, Saraste A, Weidl E, Poethko T, Weber AW, Nekolla SG, Leppanen P, Yla-Herttuala S, Holzlwimmer G, Walch A, Esposito I, Wester HJ, Knuuti J, Schwaiger M. Evaluation of alphavbeta3 integrin-targeted positron emission tomography tracer 18F-galacto-RGD for imaging of vascular inflammation in atherosclerotic mice. Circ Cardiovasc Imaging. 2009;2:331–8.
74. Mulder WJ, Strijkers GJ, Briley-Saboe KC, Frias JC, Aguinaldo JG, Vucic E, Amirbekian V, Tang C, Chin PT, Nicolay K, Fayad ZA. Molecular imaging of macrophages in atherosclerotic plaques using bimodal PEG-micelles. Magn Reson Med. 2007;58:1164–70.
75. Nahrendorf M, Jaffer FA, Kelly KA, Sosnovik DE, Aikawa E, Libby P, Weissleder R. Noninvasive vascular cell adhesion molecule-1 imaging identifies inflammatory activation of cells in atherosclerosis. Circulation. 2006;114:1504–11.
76. Lancelot E, Amirbekian V, Brigger I, Raynaud JS, Ballet S, David C, Rousseaux O, Le Greneur S, Port M, Lijnen HR, Bruneval P, Michel JB, Ouimet T, Roques B, Amirbekian S, Hyafil F, Vucic E, Aguinaldo JG, Corot C, Fayad ZA. Evaluation of matrix metalloproteinases in atherosclerosis using a novel noninvasive imaging approach. Arterioscler Thromb Vasc Biol. 2008;28:425–32.
77. Millon A, Boussel L, Brevet M, Mathevet JL, Canet-Soulas E, Mory C, Scoazec JY, Douek P. Clinical and histological significance of gadolinium enhancement in carotid atherosclerotic plaque. Stroke. 2012;43:3023–8.
78. Teng Z, He J, Degnan AJ, Chen S, Sadat U, Bahaei NS, Rudd JH, Gillard JH. Critical mechanical conditions around neovessels in carotid atherosclerotic plaque may promote intraplaque hemorrhage. Atherosclerosis. 2012;223:321–6.
79. Kaazempur-Mofrad MR, Isasi AG, Younis HF, Chan RC, Hinton DP, Sukhova G, LaMuraglia GM, Lee RT, Kamm RD. Characterization of the atherosclerotic carotid bifurcation using MRI, finite element modeling, and histology. Ann Biomed Eng. 2004;32:932–46.
80. Selwaness M, van Den Bouwhuijsen Q, Mattace-Raso FU, Verwoert GC, Hofman A, Franco OH, Witteman JC, van der Lugt A, Vernooij MW, Wentzel JJ. Arterial stiffness is associated with carotid intraplaque hemorrhage in the general population: The Rotterdam Study. Arterioscler Thromb Vasc Biol. 2014;34(4):927–32.

81. Trivedi RA, Li ZY, U-King-Im J, Graves MJ, Kirkpatrick PJ, Gillard JH. Identifying vulnerable carotid plaques in vivo using high resolution magnetic resonance imaging-based finite element analysis. J Neurosurg. 2007;107:536–42.
82. Huang X, Teng Z, Canton G, Ferguson M, Yuan C, Tang D. Intraplaque hemorrhage is associated with higher structural stresses in human atherosclerotic plaques: an in vivo MRI-based 3D fluid-structure interaction study. Biomed Eng Online. 2010;9:86.
83. Sadat U, Teng Z, Young VE, Li ZY, Gillard JH. Utility of magnetic resonance imaging-based finite element analysis for the biomechanical stress analysis of hemorrhagic and non-hemorrhagic carotid plaques. Circ J. 2011;75:884–9.
84. Canton G, Hippe DS, Sun J, Underhill HR, Kerwin WS, Tang D, Yuan C. Characterization of distensibility, plaque burden, and composition of the atherosclerotic carotid artery using magnetic resonance imaging. Med Phys. 2012;39:6247–53.
85. Li ZY, Tang TY, Jiang F, Zhang Y, Gillard JH. Reduction in arterial wall strain with aggressive lipid-lowering therapy in patients with carotid artery disease. Circ J. 2011;75:1486–92.
86. Sadat U, Howarth SP, Usman A, Taviani V, Tang TY, Graves MJ, Gillard JH. Effect of low-and high-dose atorvastatin on carotid artery distensibility using carotid magnetic resonance imaging -a post-hoc sub group analysis of ATHEROMA (Atorvastatin Therapy: Effects On Reduction Of Macrophage Activity) Study. J Atheroscler Thromb. 2013;20(1):46–56.

Cardiovascular Magnetic Resonance Imaging of Coronary Arteries

Vassilios Vassiliou, James H.F. Rudd, Rene Botnar, and Gerald Greil

Introduction

Over the last few decades, there has been an increased emphasis and focus on identification, prevention, and treatment of coronary artery disease (CAD) by both national and international societies and medical communities [1]. Despite this increased attention CAD remains globally the most common cause of death: an estimated 7.3 million people died from CAD in 2008, a number projected to double by 2030 [2, 3].

Dr. Rudd is part-supported by the NIHR Cambridge Biomedical Research Centre.

V. Vassiliou (✉)
CMR Unit and Biomedical Research Unit, Royal Brompton Hospital and Imperial College, London SW3 6NP, UK
e-mail: v.vassiliou@rbht.nhs.uk

J.H.F Rudd
Cambridge University and Honorary Consultant Cardiologist, Addenbrooke's Hospital, Cambridge CB2 0QQ, UK
e-mail: jhfr2@cam.ac.uk

R. Botnar
Division of Imaging Science and Biomedical Engineering, The Rayne Institute, King's College London, St Thomas' Hospital, 4th Floor, Lambeth Wing, London SE1 7EH, UK
e-mail: rene.botnar@kcl.ac.uk

G. Greil
Division of Imaging Science and Biomedical Engineering, The Rayne Institute, King's College London, St Thomas' Hospital, 4th Floor, Lambeth Wing, London SE1 7EH, UK

Congenital Cardiac MRI Imaging Service, S. Thomas' Hospital/Evelina Children's Hospital, London, UK
e-mail: gerald.greil@kcl.ac.uk

R. Trivedi et al. (eds.), *3D Imaging Technologies in Atherosclerosis*,
DOI 10.1007/978-1-4899-7618-5_8

Investigating patients with risk factors for CAD or any anginal symptoms remains challenging: The correct diagnosis needs to be established to allow modification of pharmacotherapy and guide intervention. However, the risk of harming the patients needs to be minimized. In the US alone, 16,300,000 patients have CAD, leading to approximately 715,000 heart attacks annually and an estimated CAD-related cost of $109 billion annually [4, 5]. There are more than 1,000,000 cardiac catheterizations performed in the US annually. Up to 40 % of them identify no significant CAD [6]. This implies that 400,000 patients are exposed unnecessarily to the risks of diagnostic coronary angiography. This results in an increase of morbidity and mortality for these patients, which includes vascular side effects, accumulation of radiation dose and, rarely, stroke, myocardial infarction (MI), or coronary artery dissection. An alternative approach that could minimize these risks, but at the same time provide equal sensitivity and specificity in identifying CAD, would be of high clinical value.

In this chapter the various imaging modalities for investigating patients with suspected CAD or other coronary anomalies are reviewed.

Imaging Modalities for Investigating Patients with Suspected Coronary Artery Disease

When reviewing patients with suspected CAD, clinicians must decide whether the combination of risk factors for an individual patient (such as hypertension, hypercholesterolemia, diabetes, smoking, obesity, and a family history of CAD) and a possible history of chest pain potentially indicating significant CAD would merit initiation of pharmacotherapy and further investigation. The benefits of any potential imaging tests must be balanced against the risks associated with each procedure, for that particular patient. In this section the commonly used imaging tests for investigating patients with suspected CAD are discussed.

Invasive Diagnostic Coronary Angiography

For more than 50 years diagnostic coronary angiography has remained the “gold standard” test for identifying significant epicardial CAD. As an invasive procedure it is still inconvenient for the patients, has the potential for morbidity and mortality, and involves significant costs and exposure to radiation (ranging from 2.3 to 22.7 mSv with a mean of 7 mSv) [7].

Rare risks include coronary artery dissection, stroke, myocardial infarction (MI), radial or femoral dissection, aorto-venous fistulae, retroperitoneal bleeding and significant bruising, and the potential need for blood transfusion. When diagnostic angiography identifies significant lumen narrowing of the coronary arteries

(>50 % of the vessel diameter) this can lead to significant change in pharmacotherapy and/or intervention both of which can improve symptoms and prognosis. In the 40 % of patients with no significant CAD using luminography with cardiac catheterization the therapeutic consequences remain unclear. Some of these patients have no CAD and have undergone an invasive test unnecessarily. However, it is increasingly understood that visualization of just the coronary lumen could underestimate the burden of atherosclerosis in the wall of the vessel. The absence of significant lumen narrowing based on the results of coronary angiogram and the resulting halt of medical therapy could have adverse implications in the long-term outcome of these patients. The ideal test would therefore be a low risk noninvasive radiation-free test, which will identify major epicardial vessel disease and early coronary vessel wall atherosclerosis.

Computed Tomography Coronary Angiography

Computed tomography coronary angiography (CTCA) is a noninvasive method currently used mainly for delineating coronary artery lumen in patients with known or suspected coronary artery disease. Patients require intravenous peripheral cannulation for contrast injection. A heart rate below 70 bpm is beneficial for image quality and reduction of radiation dose with current state of the art scanners. This is often achieved with intravenous administration of beta blockers. With new optimized protocols and prospective ECG triggering, a relatively lower dose of radiation of 3.4 ± 1.4 mSv [8] is required (equivalent to just under 2 years background radiation for a person living in the United Kingdom). However this still confers a risk of neoplasia of 0.13–0.16 % (i.e. approximately 1 in 650 patients will develop a cancer as a result of this test) [9], making this method less appropriate for screening and assessing patients at low cardiac risk. Finally, coronary calcification and arrhythmia can impair image quality, and arrhythmia is frequently found both in patients with suspected coronary artery disease but particularly in an aging population.

Cardiovascular Magnetic Resonance in the Assessment of Atherosclerosis

Cardiovascular magnetic resonance (CMR) enables a comprehensive evaluation of patients with suspected or known coronary artery disease. This method can provide information regarding cardiac anatomy as well as myocardial function, viability, and perfusion (Figs. 1–3). Non-significant CAD can be ruled out with a high level of security [10]. CMR can also visualize the coronary artery lumen and vessel wall. Coronary vessel wall imaging may also allow early detection of atherosclerosis, prior to acute myocardial infarction.

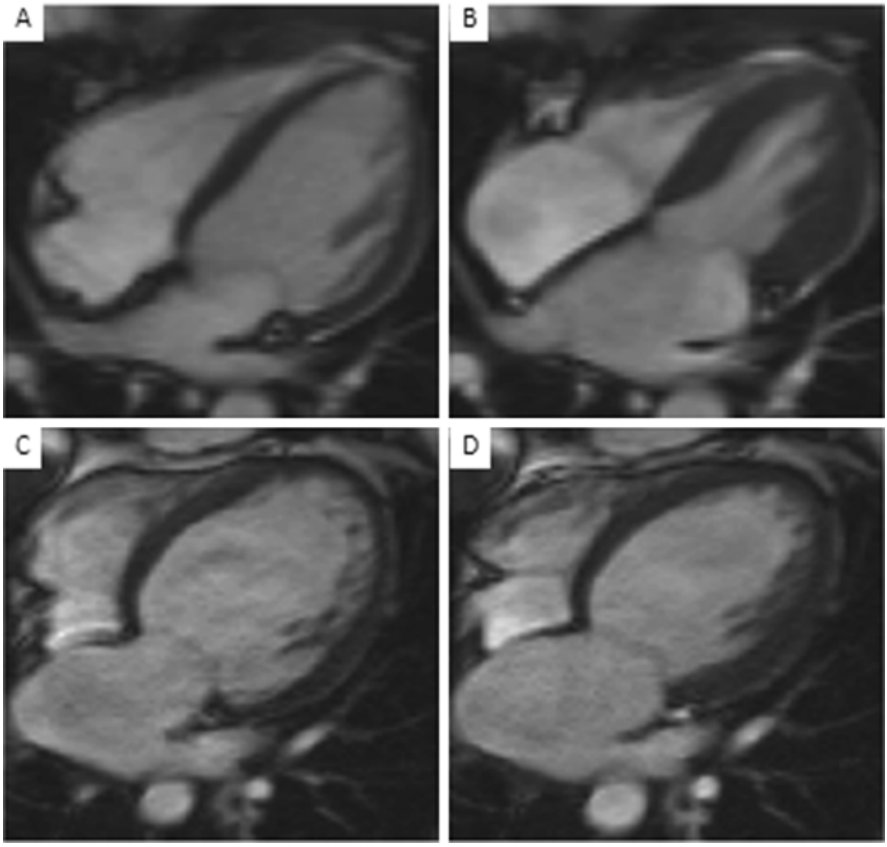

Fig. 1 CMR provides an excellent modality for delineating cardiac anatomy and function. (**a**) represents a four-chamber view of a normal heart in diastole and (**b**) in systole. (**c**, **d**) represent images in diastole and systole from a patient with ischemic cardiomyopathy and impaired ejection fraction

This early identification allows guiding of pharmacotherapy at a very early stage, offering the opportunity of halting the rate of progression of atherosclerosis and even potentially reversing its burden [11]. Hence, in addition to the relevant anatomical and functional information which can be acquired in a single, safe, noninvasive, and radiation-free examination, CMR has the potential of visualizing the coronary artery lumen and wall to identify early signs of atherosclerosis. However, there are challenges in imaging the coronary artery lumen and wall, limiting the use of CMR in clinical practice at present.

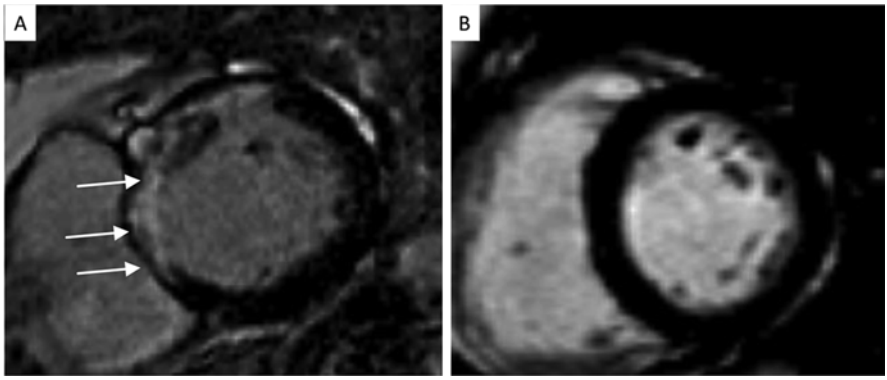

Fig. 2 Following administration of the paramagnetic contrast agent containing gadolinium, areas of myocardial enhancement (*white area* shown by *white arrows*) can be identified representing myocardial fibrosis (scarring). Such areas represent not viable myocardium, which will not benefit from revascularization of the coronary artery supplying blood to this area. Image (**a**) is from a patient with 3-vessel CAD. The area supplied by the left anterior descending (LAD) coronary artery is not viable (*white arrows*), therefore LAD revascularization will not be beneficial. Image (**b**) is from a patient with 3-vessel CAD as well where there is no late Gadolinium enhancement (LGE). The myocardium is viable and revascularization can be recommended

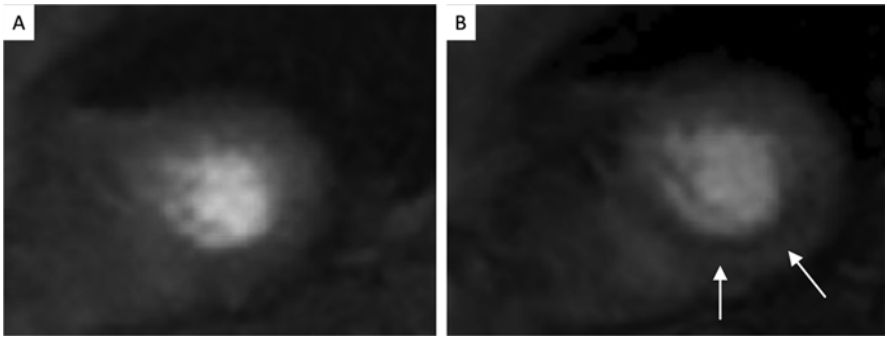

Fig. 3 Images taken from the same patient at rest (**a**, on the *left*) and following stress using adenosine (**b**, on the *right*). The *black area* on the *right* represents a perfusion abnormality indicating reversible ischemia in the right coronary artery (RCA) territory

Challenges in Undertaking Coronary Magnetic Resonance Angiography

Since the first studies on the use of coronary MRA (CMRA) [12–15] there have been significant technical advancements, leading to better imaging quality with reduced scanning time. However, movement of the coronary arteries due to cardiac and respiratory motion introduces motion artifacts. Reduction of these artifacts is crucial due to the small and tortuous caliber of the coronary vessels. The following section describes some of the challenges associated with coronary MRA.

Cardiac Motion: Coronary Movement in Systole and Diastole

An ideal subject for visualization using magnetic resonance is something that remains still during the entire acquisition time. In humans for example the upper and lower limbs can be very still and allow for good visualization. The coronary arteries are small, often tortuous, and they are displaced during the cardiac cycle. This leads to significant motion artifacts when trying to visualize the coronaries and the vessel wall. For optimal results, any CMR sequences aimed at visualizing the heart and the coronaries in particular need to take this into consideration. Synchronizing image acquisition to the ECG (R-wave) corresponding to the times of minimal displacement is therefore mandatory for successful coronary artery imaging with CMR. Coronary artery motion is minimal during end-systole and mid-diastole and previous research has shown the advantage of acquiring image data during both rest periods [16]. The specific advantages of both techniques are illustrated in Table 1.

The optimal trigger delay and the length of the acquisition window vary with the patient's heart rate. The rest period should be identified for each patient from a high-temporal resolution cine scan usually as a four chamber view performed shortly before the coronary scan [17]. Real time arrhythmia rejection algorithms that facilitate only the inclusion of regular heartbeats within certain limits might further improve image quality for MRA angiography [18, 19].

Table 1 Comparison of cardiac imaging in end-systole and mid-diastole in an attempt to image the heart in minimal displacement during the cardiac cycle

Comparison of cardiac imaging with cardiovascular magnetic resonance aiming for minimal displacement	
During end-systolic rest	*During mid-diastolic rest*
Advantages	*Advantages*
Heart rate variability less important	Longer acquisition window
Larger diameter of the venous vessels (if this information required)	Higher signal when gradient echo sequences used
Disadvantages	*Disadvantages*
Shorter acquisition window	Heart rate variability has higher potential to affect image quality

Respiratory Motion

Another major problem for cardiac imaging with CMR is the displacement of the heart during respiration. It can often reach a distance that can be ten-fold higher than the coronary artery diameter. Synchronization of the image acquisition with the respiratory cycle is therefore mandatory. Several methods have been used to minimize this respiratory motion. Initial approaches for visualizing the proximal native coronary arteries used two-dimensional breath-holding or averaging techniques and mid- or late-diastolic image acquisition with average 6–8 phase encoding lines acquired during each cardiac cycle. However, the main drawback of such techniques was that a long breath-hold of up to 20 s was required for each image slice, which is not easily achieved by every patient. Furthermore, even if patients can initially manage a 20 s breath-hold to complete the MRA an average of 25 slices are required per patient. This can be very tiring and it is therefore common to see the quality of breath-holding decreasing towards the end of the examination, leading to misregistration artifacts between successive breath-holds, degrading the overall image quality. Currently breath-holds for high-resolution three-dimensional datasets are too long and imaging results were rather disappointing. Currently a prospective real-time navigator of the diaphragm is most commonly used and successful technique for coronary lumen and vessel wall imaging.

To compensate in part for this problem, Ehman and Felmee [20] first proposed the use of respiratory MR navigators to remove the time constraint of a breath-hold. The MR navigator (typically an one-dimension pencil beam) is usually placed on the dome of the right hemidiaphragm [21] (Fig. 4). Data are only accepted if the diaphragm-lung interface is within a user-defined window (usually up to 8 mm), preferably positioned around the end-expiratory interface position. If the navigator signal falls outside this predefined window, data is rejected and needs to be reacquired in the following cycle. This results generally in a gating efficiency of around 40–60 %, which means that a large proportion of the scanning time is actually not used [22, 23]. To improve this shortcoming several new self gating navigator approaches have been developed to

1. Directly measure the motion of the heart.
2. Account for the 3D motion of the heart (food-head, left-right, and posterior-anterior).
3. Achieve 100 % scan efficiency by applying more sophisticated motion correction methods including 3D rigid body or 3D affine.

Other approaches included scanning the patient in prone position [24] and the use of thoracic or abdominal bandings [25].

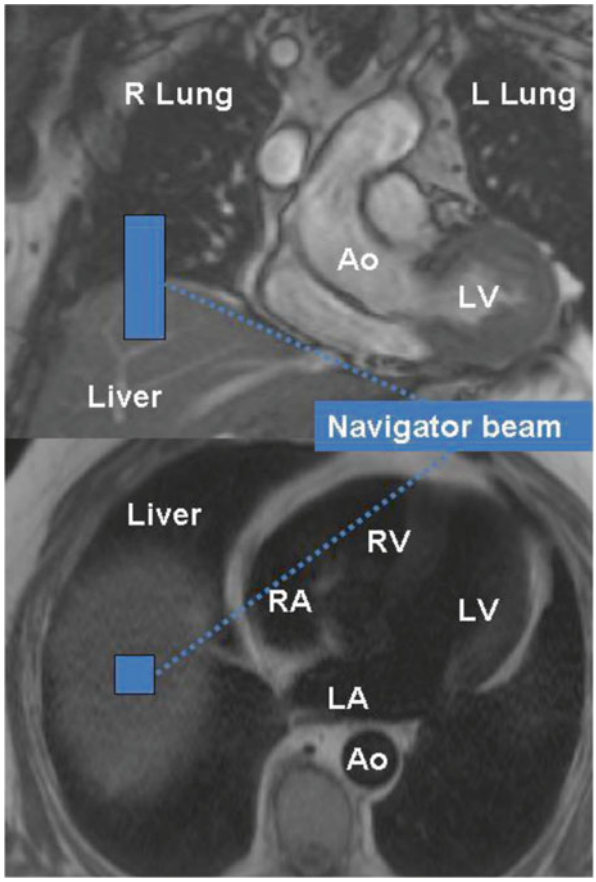

Fig. 4 Using scout images the position of the respiratory navigator can be planned. A pencil beam (one-dimensional navigator) is usually placed on the dome of the right hemi-diaphragm (heart in the left chest). Using the respiratory navigator a three-dimensional volume covering the whole heart can be acquired in a free breathing subject. *R Lung* right lung, *L Lung* left lung, *Ao* aorta, *LV* left ventricle, *RV* right ventricle, *LA* left atrium, *RA* right atrium

Cardiovascular Magnetic Resonance Sequences

Image quality for coronary MRA was significantly improved using two-dimensional gradient echo techniques (Edelman [26] and Manning [27]). Sixteen heartbeats were required initially in order to acquire one slice during a single breath-hold, which meant that most patients would tire towards the end of the test. Following the introduction of navigator techniques as described above, three-dimensional imaging covering the whole heart became feasible. Due to its ease to use, this is now the preferred approach in the clinical arena. Several modifications are currently available. The most widely accepted is a T2 preparation technique in combination with a three-dimensional gradient echo (at 3 T) or steady-state free-precession (SSFP) technique (at 1.5 T). Steady-state free-precession sequences are usually preferred at 1.5 T. Although possible at 3 T, the use of SSFP sequences is currently limited by the prolongation of repetition times, increased sensitivity of off-resonance and the

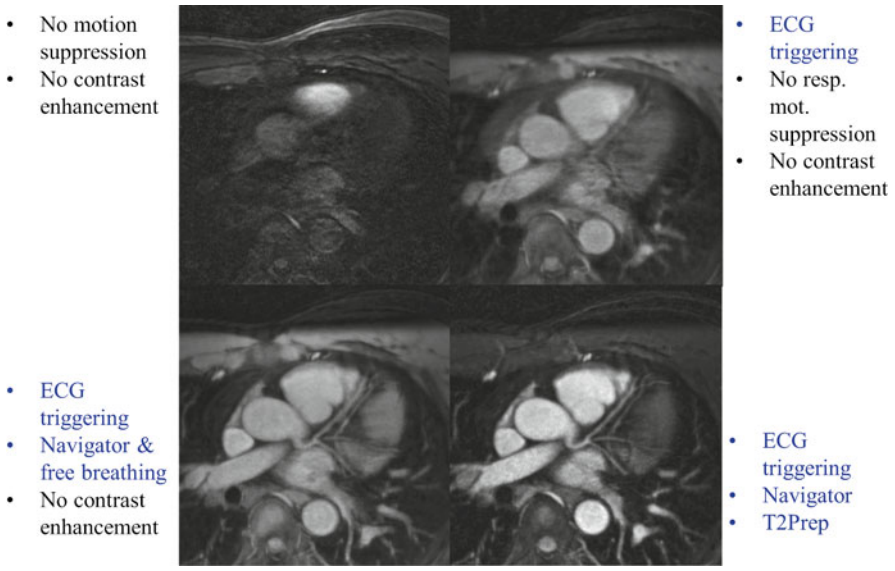

Fig. 5 Progressive improvement in the image quality can be noticed by adding ECG triggering, then a respiratory navigator followed by T2 preparation. (Image courtesy of Matthias Stuber, Professor and Director CVMR/CIBM/CHUV, University of Lausanne, Switzerland)

need for higher flip angles. T2-preparation and fat suppression techniques are now preferred for noncontrast-enhanced imaging of the coronary artery lumen. The epicardial fat can cause artifacts and fat suppression techniques reduce the signal generated by the epicardial fat tissue, making the lumen of the coronaries more visible [26, 28]. T2-preparation techniques improve the contrast between the coronary lumen and the underlying myocardium [29] as although blood and myocardium have similar T1, they have different T2. Additionally T2-preparation suppresses deoxygenated venous blood leading to better visualization of coronary arteries. An example of the currently most commonly used technique is shown in Fig. 5.

Contrast Agents for Coronary Angiography

The currently most commonly used type of contrast agents in CMR are nonspecific and distribute in the extracellular space. These are used for first pass contrast-enhanced angiography, perfusion imaging, and late gadolinium enhancement (LGE) imaging of the myocardium [30]. Other types of contrast agents include intravascular targeted [31] and blood pool iron contrast agents (fast and slow blood pool clearance). Each contrast agents has specific characteristics, which needs to be encountered for its clinical use. It is very important to choose the sequence design appropriately for the clinical question and the contrast agent used [31].

On a practical level the ultimate decision depends on the clinical question for the individual patient, balancing the luminographic information required against the vessel wall and myocardial information required. For example, extracellular contrast agents quickly extravasate into the interstitial space, and while they provide excellent detection of scar tissue by LGE (indicating previous myocardial infarction, Fig. 2a), diffuse fibrosis by T1 mapping and viability of the myocardium (suggesting that the muscle is still alive and that myocardial function is likely to improve following revascularization, Fig. 2b), they are suboptimal for coronary artery lumen imaging due to their rapid clearance. Blood-pool contrast agents on the other hand, offer the highest contrast between the vessel lumen and the surrounding tissues but might provide less information regarding late Gadolinium enhancement (LGE). Contrast agents with low albumin-binding properties have the potential for combined coronary artery and infarct imaging This is due to their prolonged retention time in blood and their higher relaxivities thereby improving coronary artery imaging while maintaining a good late enhancement for fibrosis and viability assessment [32]. Intravascular contrast agents are best used for coronary artery lumen imaging with an inversion prepulse instead of a T2-preparation prepulse [33, 34] The diagnostic value of this approach in patients with coronary artery disease still needs to be evaluated in larger clinical studies.

Are We Ready for Coronary Magnetic Resonance Angiography to Enter Routine Clinical Use?

The advances in coronary lumen and vessel wall imaging currently allow clinical applications in selected patient groups [35] (Figs. 6–8). This includes patients with Kawasaki disease [36–38] and imaging the origins and course of the coronary vessels in patients of different age groups for diagnosis and planning of interventional procedures.

Equally the origins of the coronary vessels can also be visualized in every patient, if needed [16]. When trying to visualize the mid- or the distal segment of a vessel, however, imaging quality is often less optimal. Images of the right and left coronary arteries are usually of better quality than those of the circumflex coronary artery as demonstrated in Fig. 6. This is because the circumflex artery tends to run in the direct vicinity of the myocardium and great cardiac vein and is further away from the CMR receiver coils. Previous studies have shown that the mean length of arteries that could be seen with coronary MRA is about 80 mm for the right coronary, 50 mm for the left anterior descending and 40 mm of the circumflex coronary artery [39] (Fig. 8).

However, coronary MRA is currently not a standard clinical tool in patients with coronary artery disease. This is due to relatively lengthy acquisition times, limited spatial resolution, and being dependent on a regular heart rate in a cooperative patient. Significant further improvements regarding faster acquisition times and more time efficient data acquisition techniques may bring coronary MRA into

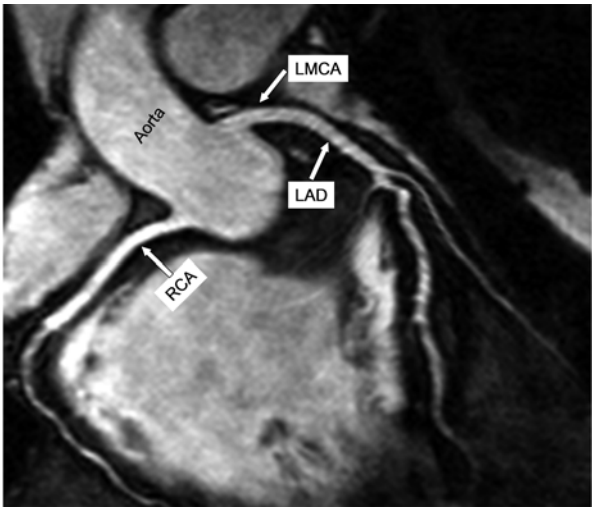

Fig. 6 In this healthy subject the proximal origin and course of the right coronary artery, left main coronary artery, and left anterior descending coronary artery are well visualized and seen to be free of any significant disease [6]. Please note that the vessel wall is imaged using the same CMR sequence (see Fig. 7). *RCA* right coronary artery, *LMCA* left main coronary artery, *LAD* left anterior descending coronary artery

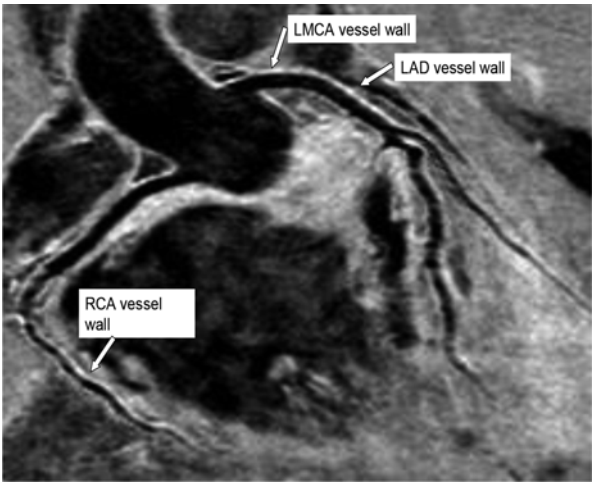

Fig. 7 CMR imaging from the same healthy subject as shown in Fig. 6, with emphasis on imaging of the coronary wall, confirming no significant atherosclerotic process in the wall of the vessel [6]. The same CMR sequence can be used to visualize both the coronary lumen (Fig. 6) and coronary wall (Fig. 7)

clinical practice together with myocardial perfusion imaging and LGE as a reliable and safe alternative for invasive and x-ray-dependent coronary artery angiography in the cardiac catheterization laboratory.

At present current clinical applications are listed below:

1. *Coronary artery origin anomalies*

Coronary MRA can provide excellent delineation of the origin and proximal course of both the right and the left coronary arteries including children and young adults [16]. This is particularly helpful in the evaluation of young patients with chest pain and/or syncope, where the anomalous coronary origin needs to be excluded as an

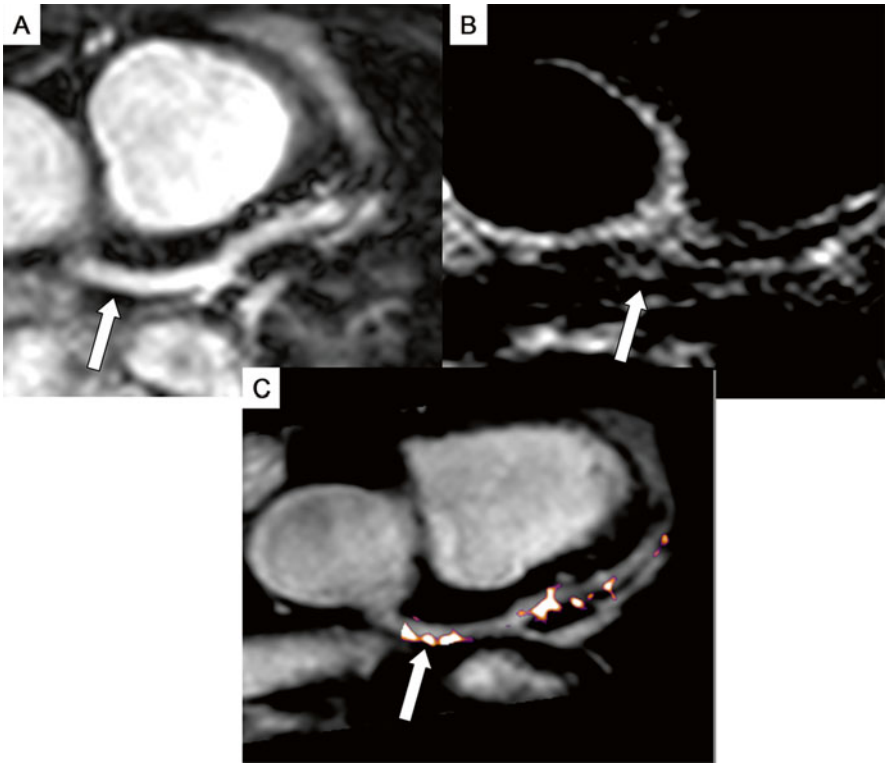

Fig. 8 CMRA shows the left main coronary artery (*arrow*) and the left anterior descending. (**b**) demonstrates late gadolinium enhancement (LGE) in the vessel wall (*arrow*) and (**c**) shows the result of superimposing image (**a**) and (**b**). This combines coronary artery anatomy as well as vessel wall imaging with LGE in one image. (Image adapted with permission from reference [35])

alternative to computed tomography and invasive coronary angiography [40] (Fig. 9).

2. *Coronary artery aneurysms*
   - Patients with vasculitis such as patients with Kawasaki disease need life-long follow-up and carry higher risk when investigated with invasive x-ray-dependent coronary angiography. Sometimes these patients develop extensive coronary artery aneurysms with the risk of coronary artery stenosis and thrombosis within the coronary artery aneurysm. Coronary MRA is accepted as a valuable alternative to follow-up coronary artery aneurysms location and extension noninvasively without the use of x-ray radiation [36–38] (Fig. 10).

3. *Coronary bypass graft assessment*

In patients following coronary artery bypass graft surgery (CABG) anginal chest pain is a common finding, both soon after CABG but more commonly a few years later. Frequently prior operation notes are not available and thus the luminal integ-

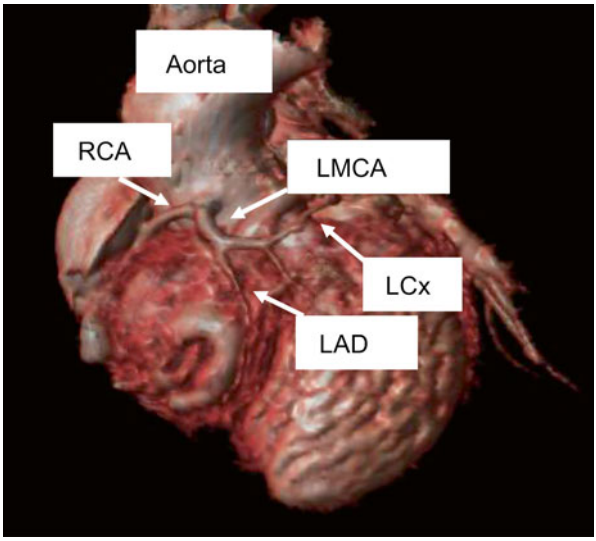

Fig. 9 This CMRA image shows a single coronary artery in a 3-year-old patient with a hypoplastic right ventricle. The left main coronary artery (LMT) arises from the right coronary artery (RCA). *Ao* aorta, *LAD* left anterior descending artery, *LCX* left circumflex coronary artery, *LV* left ventricle, *RV* right ventricle. (Image adapted with permission from reference [40])

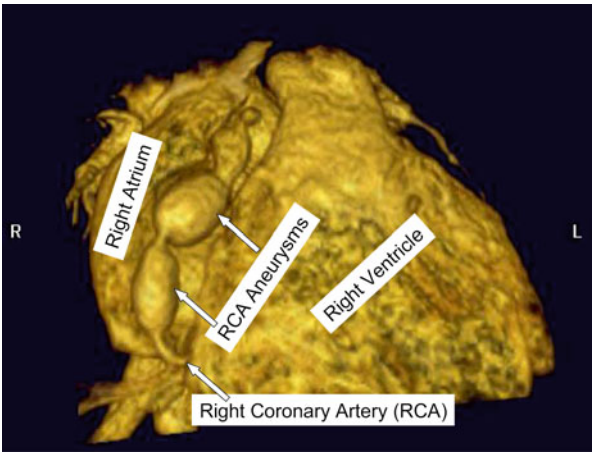

Fig. 10 Multiple aneurysms of the right coronary artery are shown in an 8-year-old patient with Kawasaki disease using volume rendering of a free breathing respiratory navigator-gated and ECG-triggered isotropic, whole-heart, 3D steady-state-free-precession magnetic resonance dataset. *RCA* right coronary artery. (Image adapted with permission from reference [36])

rity of the grafts needs to be assessed. Coronary MRA may provide a road map prior to cardiac catheterization angiography to describe the number and location of arterial and venous grafts used. Bypass grafts however have certain distinct characteristics differentiating them from the coronary arteries, actually making them ideal for visualization with CMR: they are usually much larger compared to native arteries and they typically have a rather straight and (sometimes) known course. Furthermore, they tend to remain in an almost stationary position with each successive cardiac cycle. With spin and gradient echo techniques and the use of contrast agents, the sensitivity in identifying a blood signal inside a graft approaches 95–100 % [41–43]. The major limitation in graft imaging with CMR lies in the metallic clips frequently

used (particularly for left and right internal mammary grafts), which causes signal voids and susceptibility artifacts, sometimes preventing a full assessment of their anatomy. To fill this gap subsequent coronary angiography or aortography can be targeted to the remaining questions. This will reduce the time in the cardiac catheterization laboratory, radiation exposure, and risk associated with invasive angiography.

4. *Patients with a dilated heart*
   When faced with a patient with a dilated heart, it is not clear whether this phenotype relates to ischemic cardiomyopathy or dilated non-ischemic cardiomyopathy. Traditionally such patients undergo invasive angiography or Computed Tomography coronary angiography to exclude coronary artery disease. However, it has been recently proposed [44] that coronary MRA in conjunction with late gadolinium enhancement and perfusion imaging of the myocardium is sufficient to establish the diagnosis without the need of further anatomical coronary tests.

Conclusion

In clinical cardiology the role of cardiac magnetic resonance is a well established tool for diagnosis and monitoring of cardiac anatomy, function, viability, and perfusion. Even though coronary MRA technology has improved significantly in the last few years, it is not used routinely at present in clinical practice. However, coronary MRA plays an important role for diagnosis and follow-up of specific coronary lesions, such as patients with vasculitis e.g. patients after Kawasaki disease. Coronary artery aneurysm location and size can be assessed with this technology radiation free and noninvasively which is very important in pediatric patients. Coronary MRA also allows visualization of coronary artery origins and course, which allows clarification of unclear chest pain in children and young adults. It also provides additional support for planning complex congenital heart surgery. Further improvements in motion compensation and more time efficient acquisition and reconstruction techniques make it more likely that coronary MRA will play an increasingly important role in the clinical routine of cardiac disease in the future.

References

1. Perk J, De Backer G, Gohlke H, et al. The fifth joint task force of the European Society of Cardiology and other societies on cardiovascular disease prevention in clinical practice. Eur Heart J. 2012;33:1635–701.
2. Global status report on non-communicable diseases 2010. Geneva, World Health Organization, 2011
3. Mathers CD, Loncar D. Projections of global mortality and burden of disease from 2002 to 2030. PLoS Med. 2006;3, e442.

4. Heidenreich PA, Trogdon JG, Khavjou OA, et al. Forecasting the future of cardiovascular disease in the United States: a policy statement from the American Heart Association. Circulation. 2011;123:933–44.
5. Chiribiri A, Ishida M, Nagel E, Botnar RM. Coronary imaging with cardiovascular magnetic resonance: current state of the art. Prog Cardiovasc Dis. 2011;54:240–52.
6. Patel MR, Peterson ED, Dai D, et al. Low diagnostic yield of elective coronary angiography. N Engl J Med. 2010;362:886–95.
7. Bashore TM, Balter S, Barac A, et al. 2012 American College of Cardiology Foundation/ Society for Cardiovascular Angiography and Interventions expert consensus document on cardiac catheterization laboratory standards update: a report of the American College of Cardiology Foundation Task Force on Expert Consensus documents developed in collaboration with the Society of Thoracic Surgeons and Society for Vascular Medicine. J Am Coll Cardiol. 2012;59:2221–305.
8. Efstathopoulos EP, Pantos I, Thalassinou S, Argentos S, Kelekis NL, Zograpfos T, Panayiotakis G, Katritsis DG. Patients radiation doses in Cardiac Computed Tomography: comparison of published results with prospective and retrospective acquisition. Radiat Prot Dosimetry. 2011;148:83–91.
9. Huda W, Schoepf UJ, Abro JA, Mah E, Costello P. Radiation-related cancer risk in a clinical patient population undergoing cardiac CT. Am J Roentgenol. 2011;196:159–65.
10. Greenwood JP, Maredia N, Younger JF, et al. Cardiovascular magnetic resonance and single-photon emission computed tomography for diagnosis of coronary heart disease (CE-MARC): a prospective trial. Lancet. 2012;379:453–60.
11. Nissen SE, Tuzcu EM, Schoenhagen P, Brown BG, Ganz P, Vogel RA, Crowe T, Howard G, Cooper CJ, Brodie B, Grines CL, DeMaria AN. REVERSAL Investigators. Effect of intensive compared with moderate lipid-lowering therapy on progression of coronary atherosclerosis: a randomized controlled trial. JAMA. 2004;291:1071–80.
12. Botnar RM, Stuber M, Danias PG, Kissinger KV, Manning WJ. Improved coronary artery definition with T2-weighted, free-breathing, three-dimensional coronary MRA. Circulation. 1999;99:3139–48.
13. Kim WY, Danias PG, Stuber M, et al. Coronary magnetic resonance angiography for the detection of coronary stenosis. N Engl J Med. 2001;345:1863–9.
14. Paulin S, von Schulthess GK, Fossel E, Krayenbuehl HP. MR imaging of the aortic root and proximal coronary arteries. AJR Am J Roentgenol. 1987;148:665–70.
15. Edelman RR, Manning WJ, Burstein D, Paulin S. Coronary arteries: breath-hold MR angiography. Radiology. 1991;181:641–3.
16. Uribe S, Hussain T, Valverde I, et al. Congenital heart disease in children: coronary MR angiography during systole and diastole with dual cardiac phase whole-heart imaging. Radiology. 2011;260:232–40.
17. Kim WY, Stuber M, Kissinger KV, et al. Impact of bulk cardiac motion on right coronary MR angiography and vessel wall imaging. J Magn Reson Imaging. 2001;14:383–90.
18. Jahnke C, Paetsch I, Nehrke K, et al. A new approach for rapid assessment of the cardiac rest period for coronary MRA. J Cardiovasc Magn Reson. 2005;7:395–9.
19. Tangcharoen T, Jahnke C, Koehler U, et al. Impact of heart rate variability in patients with normal sinus rhythm on image quality in coronary magnetic angiography. J Magn Reson Imaging. 2008;28:74–9.
20. Ehman RL, Felmlee JP. Adaptive technique for high-definition MR imaging of moving structures. Radiology. 1989;173:255–63.
21. Wang Y, Riederer SJ, Ehman RL. Respiratory motion of the heart: kinematics and the implications for the spatial resolution in coronary imaging. Magn Reson Med. 1995;33:713–9.
22. Danias PG, Stuber M, Botnar RM, et al. Relationship between motion of coronary arteries and diaphragm during free breathing: lessons from real-time MR imaging. AJR Am J Roentgenol. 1999;172:1061–5.
23. Nagel E, Bornstedt A, Schnackenburg B, et al. Optimization of realtime adaptive navigator correction for 3D magnetic resonance coronary angiography. Magn Reson Med. 1999; 42:408–11.

24. Huber S, Bornstedt A, Schnackenburg B, et al. The impact of different positions and thoracial restrains on respiratory induced cardiac motion. J Cardiovasc Magn Reson. 2006;8:483–8.
25. Sakuma H, Ichikawa Y, Chino S, et al. Detection of coronary artery stenosis with whole-heart coronary magnetic resonance angiography. J Am Coll Cardiol. 2006;48:1946–50.
26. Edelman RR, Manning WJ, Burstein D, Paulin S. Coronary arteries: breath-hold MR angiography. Radiology. 1991;181:641–3.
27. Manning WJ, Li W, Boyle NG, Edelman RR. Fat-suppressed breath-hold magnetic resonance coronary angiography. Circulation. 1993;87:94–104.
28. Li D, Paschal CB, Haacke EM, Adler LP. Coronary arteries: three-dimensional MR imaging with fat saturation and magnetization transfer contrast. Radiology. 1993;187:401–6.
29. Brittain JH, Hu BS, Wright GA, Meyer CH, Macovski A, Nishimura DG. Coronary angiography with magnetization-prepared t2 contrast. Magn Reson Med. 1995;33:689–96.
30. Regenfus M, Ropers D, Achenbach S, Kessler W, Laub G, Daniel WG, et al. Noninvasive detection of coronary artery stenosis using contrast-enhanced three-dimensional breath-hold magnetic resonance coronary angiography. J Am Coll Cardiol. 2000;36:44–50.
31. Makowski MR, Wiethoff AJ, Uribe S, et al. Congenital heart disease: cardiovascular MR imaging by using an intravascular blood pool contrast agent. Radiology. 2011;260:680–8.
32. Laurent S, Elst LV, Muller RN. Comparative study of the physicochemical properties of six clinical low molecular weight gadolinium contrast agents. Contrast Media Mol Imaging. 2006;1:128–37.
33. Goldfarb JW, Edelman RR. Coronary arteries: breath-hold, gadolinium-enhanced, three-dimensional MR angiography. Radiology. 1998;206:830–4.
34. Stuber M, Botnar RM, Danias PG, et al. Contrast agent–enhanced, free-breathing, three-dimensional coronary magnetic resonance angiography. J Magn Reson Imaging. 1999; 10:790–9.
35. Hussain T, Fenton M, Peel SA, et al. Detection and grading of coronary allograft vasculopathy in children with contrast enhanced magnetic resonance imaging of the coronary vessel wall. Circ Cardiovasc Imaging. 2013;8:66–70.
36. Greil GF, Seeger A, Miller S, et al. Coronary magnetic resonance angiography and vessel wall imaging in children with Kawasaki disease. Pediatr Radiol. 2007;37:666–73.
37. Greil GF, Stuber M, Botnar RM, et al. Coronary magnetic resonance angiography in adolescents and young adults with Kawasaki disease. Circulation. 2002;105:908–11.
38. Mavrogeni S, Papadopoulos G, Hussain T, Chiribiri A, Botnar R, Greil GF. The emerging role of cardiovascular magnetic resonance in the evaluation of Kawasaki disease. Int J Cardiovasc Imaging. 2013;29(8):1787–98.
39. Chiribiri A, Botnar RM, Nagel E. Magnetic resonance angiography: where are we today? Curr Cardiol Rep. 2013;15:328.
40. Tangcharoen T, Bell A, Hegde S, et al. Detection of coronary artery anomalies in infants and young children with congenital heart disease by using MR imaging. Radiology. 2011;259:240–7.
41. Galjee MA, van Rossum AC, Doesburg T, et al. Value of magnetic resonance imaging in assessing patency and function of coronary artery bypass grafts. An angiographically controlled study. Circulation. 1996;93:660–6.
42. Vrachliotis TG, Bis KG, Aliabadi D, et al. Contrast-enhanced breath-hold MR angiography for evaluating patency of coronary artery bypass grafts. AJR Am J Roentgenol. 1997;168: 1073–80.
43. Rubinstein RI, Askenase AD, Thickman D, et al. Magnetic resonance imaging to evaluate patency of aortocoronary bypass grafts. Circulation. 1987;76:786–91.
44. Assomull RG, Shakespeare C, Kalra PR, et al. Role of cardiovascular magnetic resonance as a gatekeeper to invasive coronary angiography in patients presenting with heart failure of unknown etiology. Circulation. 2011;124:1351–60.

MRI of Intracranial Atherosclerosis

Mark R. Radon, Maneesh Bhojak, H. Levansri D. Makalanda, and Damiano Giuseppe Barone

Introduction

MRI provides excellent demonstration of the intracranial contents, including both the brain parenchyma and, via magnetic resonance angiography (MRA) techniques, the intracranial vasculature. There has been considerable technical progress in the development of MRA which now offers a modality with high sensitivity for the detection of intracranial vascular occlusions.

In addition to being able to provide anatomical and tissue detail, magnetic resonance (MR) can also detect a variety of other physical processes. Early clinical MRI was troubled by motion effects, but by the mid-1980s these had been well characterised and a variety of techniques had been proposed to exploit these for measurement of intravascular flow [1]. Additional developments have permitted a variety of physiological measures through diffusion and perfusion-weighted imaging.

The intracranial circulation features relatively small vessels which, when diseased, can have profound clinical effects. MRI is prone to a number of technical artefacts, and sensitive to motion. As a result, intracranial vascular imaging is technically challenging. Optimal image quality requires optimised protocols and high-performance equipment. Benefits from improved signal-to-noise ratio available at higher field strengths are particularly visible in these demanding techniques (Fig. 1).

M.R. Radon (✉) • M. Bhojak
Department of Neuroradiology, The Walton Centre Foundation Trust, Liverpool, UK
e-mail: Mark.Radon@thewaltoncentre.nhs.uk

H.L.D. Makalanda
Department of Neuroradiology, Royal London Hospital, London, UK

D.G. Barone
Department of Neurosurgery, The Walton Centre Foundation Trust, Liverpool, UK

R. Trivedi et al. (eds.), *3D Imaging Technologies in Atherosclerosis*,
DOI 10.1007/978-1-4899-7618-5_9

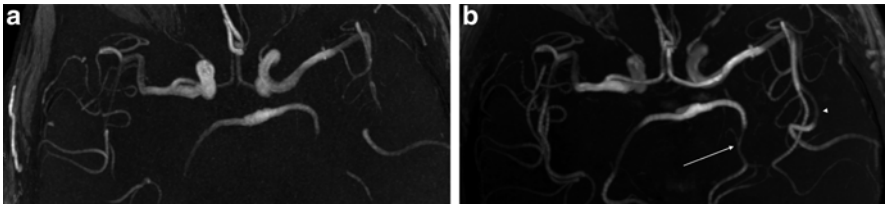

Fig. 1 Impact of field strength on imaging. (**a**) Axial maximum intensity projection (MIP) slab from 3D TOF MRA study at 1.5 T. (**b**) Axial MIP slab from 3D TOF MRA study at 3.0 T in the same patient. The higher signal-to-noise ratio enables vessels which run close to the plane of the images to be seen more clearly, particularly the posterior cerebral arteries (*arrow*) and distal M2 branch arteries (*arrowhead*)

Magnetic Resonance Techniques

Anatomical Imaging

Structural brain imaging is most useful for the detection of cerebral infarcts resulting from intracranial atherosclerotic disease (ICAD). The anatomical detail provided by MRI is considerably greater than CT and permits detection and quantitation of both acute and chronic infarcts and of white matter ischaemia. Certain patterns of ischaemic disease, such as borderzone infarction, have a correlation with patterns of vascular disease, e.g. MCA atherosclerosis [2] (Fig. 2).

A minimum structural imaging protocol is suggested to include T1, T2 fluid-attenuated inversion recovery (FLAIR) and T2-weighted imaging. Imaging planes should include the axial plane, and preferably at least one orthogonal plane. FLAIR is useful for the detection of infarcts in the periventricular white matter and within the cortex by virtue of suppression of CSF signal [3]. However, FLAIR is susceptible to a variety of artefacts and is not adequate as a sole technique.

T2*, or more recently, susceptibility-weighted imaging is commonly used in the context of acute stroke for the detection of intracranial haemorrhage (including microhaemorrhage). However, because of the sensitivity to magnetic susceptibility of this technique, it can also be used to detect intravascular thrombus/clot due to the paramagnetic properties of deoxyhemoglobin. This phenomenon has been termed the *hypointense vessel sign*, in a manner analogous to the *hyperdense artery sign* on CT [4]. In practice, the sensitivity and specificity are poor, and given the easy availability of MR angiography techniques, the value of this sign is limited.

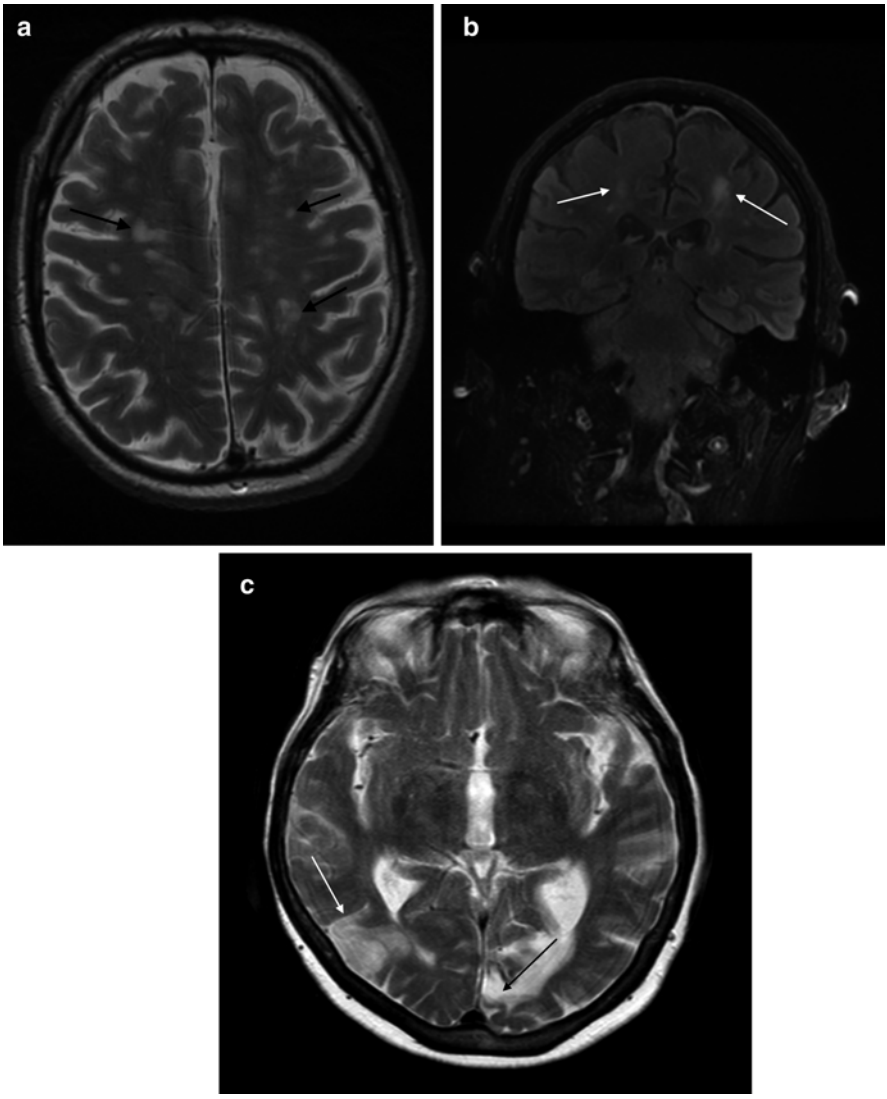

Fig. 2 Cerebral borderzone ischaemia. (**a** and **b**) T2 axial and T2 FLAIR coronal images showing ischaemic lesions (*arrows*) along the deep ACA/MCA borderzone. (**c**) T2 axial image showing right posterior MCA borderzone cortical infarction (*white arrow*) and an old left occipital lobe infarct (*black arrow*)

Physiological Imaging

Diffusion-Weighted Imaging

The development of diffusion-weighted imaging (DWI) has revolutionised the imaging of acute stroke due to very high sensitivity and specificity for cerebral infarction. The principle of DWI is the quantitation of molecular diffusion of water within tissue, which is typically performed by using an imaging sequence modified with the addition of a diffusion-sensitising gradient [5]. The underlying technique is typically an ultra-fast T2-weighted imaging sequence. The measure of diffusion sensitivity as defined by the prescribed sensitising gradient is termed the *b*-value. Much of the literature is based on imaging with *b*-value of 1,000 s/mm^2, but there has been interest in the use of higher *b*-values of up to 3,000 s/mm^2, for the detection of cerebral ischaemic lesions [6].

The resulting DWI images demonstrate loss of signal in the presence of diffusion (or bulk patient motion) giving a dark appearance. From these images may be computed a map of apparent diffusion coefficient (ADC) which represents a measure where the main structural imaging contrast (T2 effects) on the base sequence has been removed, effectively generating an image based almost solely on diffusion effects, although some contamination from non-diffusion effects such as bulk motion may remain.

Acutely infarcted and critically ischaemic brain parenchyma shows restriction of water diffusion due to cytotoxic edema. This is shown as high intensity on DWI images, and restriction of diffusion can be confirmed by corresponding low values on the ADC map (Fig. 3).

Because the white matter of the brain shows directional diffusion parameters, this technique can be extended to estimate the diffusion tensor by using multiple directional diffusion measurements, providing an estimate of the predominant direction of diffusion and its anisotropy [7]. Diffusion tensor imaging (DTI) provides a number of quantitative measures, in addition to ADC, which include the fractional anisotropy (FA) and radial and longitudinal diffusivities. The role of these additional parameters is a field of active exploration, but they may be of value in detecting chronic regional cerebral ischaemia [8].

Perfusion Imaging

The aim of perfusion-weighted imaging is the quantitation of blood flow through the cerebral tissue. The most studied method, dynamic susceptibilty contrast (DSC), utilises a bolus of an intravascular contrast agent. The contrast agent results in a quantifiable loss of signal during its passage through the intravascular space. From a curve of signal intensity, maps of cerebral blood flow and volume can be synthesised [9]. Non-contrast methods based on arterial spin labelling (ASL) have also been developed, but there are challenges and pitfalls [10].

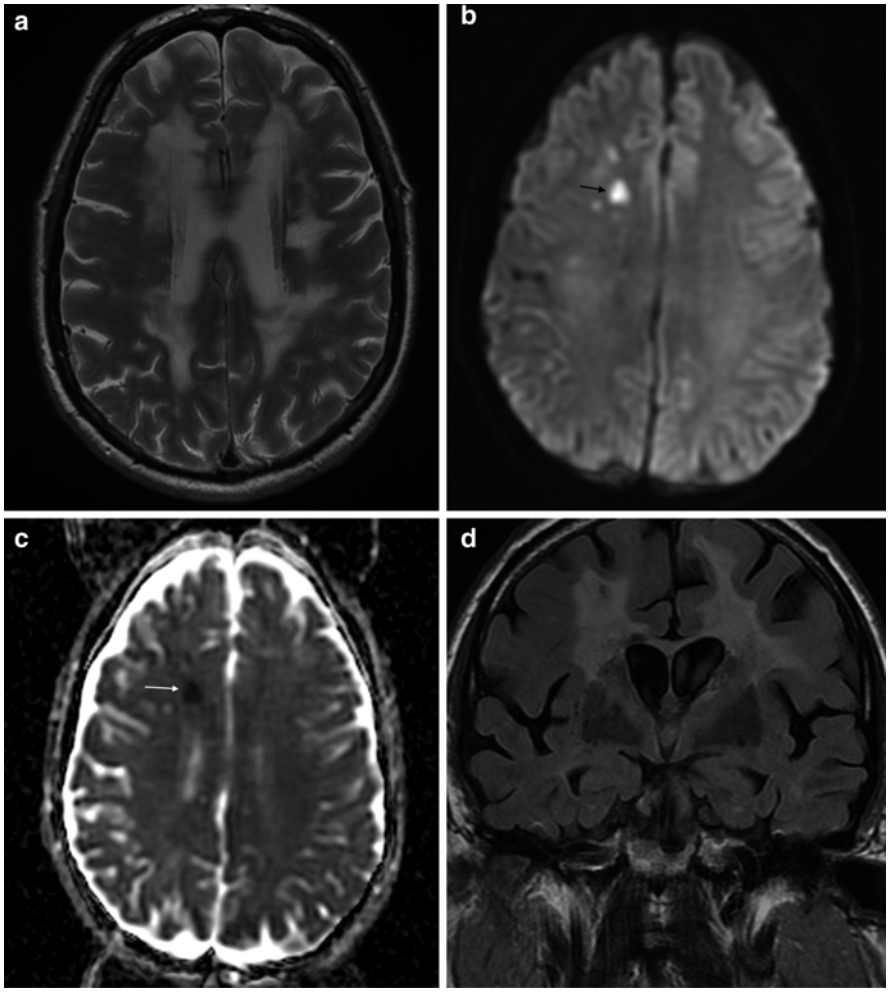

Fig. 3 Detection of acute cerebral infarction with diffusion-weighted imaging. (**a**) T2 axial imaging showing extensive, confluent white matter abnormality with a discrete left corona radiata lacunar infarct. (**b**) Diffusion-weighted imaging (DWI) shows focal hyperintensity in the right frontal white matter. (**c**) Apparent diffusion coefficient (ADC) map demonstrates low ADC, i.e. restricted diffusion, in the right frontal white matter lesion, indicating acute infarction. (**d**) Coronal T2 FLAIR image fails to distinguish the acutely infarcted region from the background of small vessel ischaemic disease

Perfusion imaging has proved useful in the context of acute stroke imaging for early prognostication and stratification for treatment by identifying tissue at risk of infarcting (the ischaemic penumbra) prior to DWI changes [11].

Outside of the acute phase, there is scope for the determination of cerebrovascular reserve. This technique is reasonably established in selecting patients for intervention in severe carotid stenosis and in Moyamoya vasculopathy. However, it has been demonstrated in the context of MCA stenosis (Fig. 4) [12].

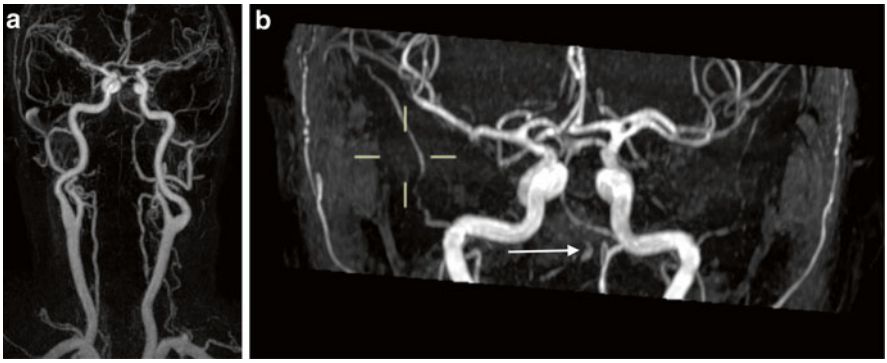

Fig. 4 Contrast-enhanced MRA. (**a**) Thick-slab MIP image from contrast-enhanced MRI of cervical and intracranial arteries. The right intracranial VA shows no opacification. (**b**) Thick-slab MIP image from 3D TOF MRA in the same patient performed at the same time as (**a**). There is high signal visible in the right VA. This was subsequently shown to be hyperintense on T1 imaging, indicating that this is intravascular thrombus, and not flow-related signal. The underlying cause in this case was thought to be arterial dissection

Vascular Imaging

There are several MRA techniques available for assessment of the intracranial arteries. Broadly, they are divisible into flow-sensitive techniques, in which image contrast is derived from the effects of bulk motion, and contrast-enhanced techniques, in which a contrast agent changes the imaging properties of the blood within the vascular lumen.

While it is unnecessary to have a detailed knowledge of the fundamental physics and techniques to interpret MRA images, appreciation of the limitations and artefacts is important to avoid error and to be able to develop and apply imaging protocols.

Time of Flight

Technical Background

Time of flight (TOF) effects alter the signal returned by flowing blood, and can commonly be seen as flow-related enhancement on conventional gradient echo (GE) T1-weighted images. Flowing blood results in bulk movement of magnetised spins. If the direction of flow is perpendicular to the plane of the imaging slice, unsaturated spins from outside of the imaging slice will replace those which have been partially saturated by the imaging sequence. In a heavily T1-weighted imaging sequence, the stationary spins have an attenuated signal due to partial saturation, whereas the moving blood returns a more intense signal.

The technique of two-dimensional GE TOF was introduced by Wehrli and Gullberg [13, 14]. Sequential axial sections acquired with this technique could be used to examine the intracranial arteries as well as the carotid bifurcations. The development of three-dimensional Fourier transform techniques permitted the acquisition of numerous thin sections, with isotropic voxel resolution. This improved resolution was of substantial benefit for assessment of the intracranial circulation when compared with 2D techniques [15]. The benefits of the reduced voxel size go beyond that of higher spatial resolution and include improved signal-to-noise ratio and reduced susceptibility effects. The 3D TOF technique represents the most commonly used technique for assessment of the intracranial arteries [16]. A variant which uses relatively thin, stacked, overlapping volumes (multiple overlapping thin-slab acquisition, MOTSA) has been the most effective in combining the technical advantages of both the 2D technique (reduced spin saturation) and 3D technique (improved SNR and resolution) [17].

Potentials, Limitations and Artefacts

Early reports of the performance of TOF MRA against intra-arterial digital subtraction angiography (IADSA) reported 100 % agreement for detection of occlusions and 61 % agreement for grade of stenosis [18], and showed sensitivity and specificity for occlusion of up 85–100 % and 95–97 %, respectively, and lower values for non-occlusive stenosis [19, 93]. A more recent, prospective, multicentre trial (SONIA) compared detection of non-occlusive stenosis by TOF MRA against the gold standard of IADSA [20]. Negative predictive value (NPV) was good (91 %), but positive predictive value (PPV) was only fair at 59 %, leading to the recommendation that a positive 3D-TOF MRA study should be followed by confirmatory testing. Smaller studies have quoted similar figures at 1.5 T [21]. At 3 T, however, both NPV and PPV are substantially increased [22], although this study examined a different population and the NPV/PPV may be confounded by different disease prevalence.

A tendency for TOF MRA to overestimate stenosis is recognised in the intracranial arteries [23]. The two most important causes are turbulent flow and slow velocity flow. Turbulent flow, resulting in disordered motion, can result in signal dropout due to intra-voxel spin dephasing, for example within the cavernous segment of the ICA [18] (Fig. 5). This problem can be exacerbated by the presentation of images in the form of maximum intensity projection (MIP) images. Review of the source images may assist in recognition of this artefact [24]. Slow flow can also result in loss of flow-related signal and this has been recognised following severe stenosis and proximal ICA stenosis [22]. However, this sign can also be used as a marker of severe stenosis [25].

As the base sequence for TOF imaging is inherently T1-weighted images, there is potential for other sources of T1 hyperintensity to be visible on TOF MRA. This can be seen in thrombus and haemorrhage, as well as fat.

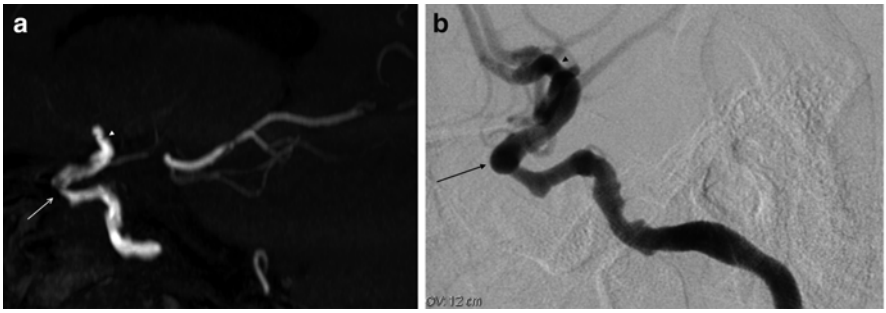

Fig. 5 TOF MRA in vascular stenosis. Sagittal thin-slab MIP projection to show the right cavernous ICA. The right carotid siphon appears critically stenosed (*arrow*) and there is irregularity of the terminal ICA (*arrowhead*). IA-DSA of the right ICA shows that the stenosis of the carotid siphon (*arrow*) and terminal ICA (*arrowhead*) are not as severe as the TOF MRA had suggested

Contrast-Enhanced MRA

Contrast-enhanced (CE) MRA utilises the paramagnetic effect of an intravenously administered gadolinium compound. The T1 shortening effect of the contrast agent results in increased signal intensity within the vessels [26].

CE MRA is technically challenging due to the requirement for rapid acquisition and precise timing so as to avoid venous enhancement. The advantage is the avoidance of saturation effects which may result in signal dropout. Time-resolved examination is also possible. Various techniques have been described to achieve this, albeit with some compromise to image resolution [27, 28].

Despite this, intracranial CE MRA has been reported to have similar diagnostic performance to 3D-TOF MRA with the benefit of faster image acquisition, which may be particularly advantageous in the acute situation, and a larger field of view which can include the extracranial arteries [29] (Fig. 4).

Disadvantages of the use of CE MRA relate primarily to the use of the contrast agent: occasional idiosyncratic/anaphylactic reactions and nephrogenic systemic fibrosis [30] are potential risks.

Early reports of the use of blood-pool contrast agents for intracranial MRA suggest that image quality can be improved and gadolinium dosage reduced [31]. Enhanced relaxivity due to macromolecular binding of the agent is thought to be a major contributor to the image quality, even during first-pass circulation [32].

The technique of CE TOF MRA provides flow-based imaging and the increased signal provided by the relaxivity contributed by the contrast agent. This technique could be of value for the assessment of stented arteries [33].

Other Vascular Imaging Techniques

There has been some interest in the technique of quantitative MRA to measure posterior circulation hemodynamics in patients with vertebrobasilar disease, where it has shown some benefit in risk stratification [34], and in the detection of in-stent restenosis [35]. However, despite initial promise of a reliable non-invasive technique, for assessment of stent patency, there has not yet been any robust independent validation of this technique.

A variety of high-resolution (HR) techniques have been described in recent years for the assessment of the intracranial arteries, including assessment of the arterial wall [36–39, 94]. These protocols have varying degrees of similarity to protocols based upon proximal ICA plaque imaging [40]. These techniques have had limited penetration into routine practice, and have not been incorporated into acute stroke/TIA imaging guidelines where established MRA techniques, potentially supplemented with perfusion imaging, are the mainstay [41].

High-resolution black-blood MRI is one technique for detection and classification of MCA stenoses [36]. The demonstration and measurement of plaque size and volume, as well as measure wall thickness, have been demonstrated together with differences between symptomatic and asymptomatic plaques [42].

Also echoing techniques in the ICA, there have also been reports of the detection of direct thrombus imaging for the identification of intraplaque haemorrhage or dissection by the presence of T1 hyperintensity within the arterial wall [43].

The disappointing results of the Stenting versus Aggressive Medical Management for Preventing Recurrent Stroke in Intracranial Arterial Stenosis (SAMMPRIS) trial [44, 45] have resulted in changes in practice away from intracranial stenting [46]. However, the SAMMPRIS trial has been criticised on a number of fronts, and there is ongoing interest in the refinement of interventional techniques and patient selection, and plaque imaging may play a role in this. Early reports of the reproducibility of these HR techniques show excellent inter- and intra-observer reliability for identification of plaques, and contrast enhancement, with substantial agreement for presence of intra-plaque haemorrhage [47]. However, future work to correlate clinical outcomes with HR imaging findings is required.

Mechanisms of Stroke

Ischaemic stroke resulting from occlusive disease of the intracranial arteries can be broadly classified according to its mechanism into thrombotic occlusions, embolic occlusions and perforator occlusions. Initially introduced as part of the TOAST study [48], this traditional classification is limited because a proportion of strokes remain unclassifiable, or represent a mixture of aetiologies. Newer classification systems, such as the Causative Classification System (CCS) [49] and ASCOD phenotypic system [50], aim to improve classification in these circumstances. The prevalence of individual subtypes is widely variable between studies, and

between populations and races [51]. Broadly, however, the relative prevalence of the major subtypes ranges between 15 and 40 % for large artery atherosclerosis, 15 and 30 % for embolic and 15 and 30 % for lacunar infarcts [52]. The coexistence of multiple mechanisms is also recognised as is the importance of factors such as cerebrovascular reserve and collateral circulation [53].

Patterns of Atherosclerosis

The most common site of intracranial atherosclerosis is the carotid siphon. However, atherosclerotic disease at this site has a relatively more benign course than extracranial carotid disease; one study found no relation between disease at the siphon and recurrent stroke following carotid endarterectomy [54, 55].

The most well-studied parts of the intracranial circulation are the MCAs and the vertebrobasilar system. In comparison, there is relatively little literature on the significance of ACA and PCA disease. This may be explained by the relatively low incidence of ACA stoke and the rarity of ACA atherosclerosis [56].

ICAD is also not a static disease. MRA has been used to define progression, demonstrating that symptomatic lesions progress in up to 29 % and regress in 15 % [57].

The clinical significance of intracranial arterial stenosis has been less well defined than that of carotid bifurcation stenosis. In part, this may be due to the difficulty of the detection of such small lesions. One early clinicopathological study [58] detected a relatively low rate of MCA atherosclerosis and attributed the primary cause to the proximal ICA. More recent studies have suggested higher rates of intracranial atherosclerosis [59] [60], and this has prompted recent commentators to suggest that this early underestimate established a precedent favouring the investigation of extracranial atherosclerosis [61].

Intracranial ICA stenosis has also been reported to have a higher incidence of borderzone infarction than extracranial ICA stenosis [62]. There has been one report that this type of pattern may be due to embolisation [63], a mechanism previously implicated in the pathophysiology of borderzone infarction [64]. However, neither pattern is specific; both patterns become more frequent as the degree of stenosis increases [65]. Another infarct pattern is the phenomenon of pure subcortical infarction (cortex sparing) in the context of MCA stenosis or occlusion [66], which if shown on structural imaging should prompt the review of vascular imaging.

MCA Atherosclerosis

Intracranial arterial stenosis has long been recognised as a risk factor of recurrent stroke [67] [68]. More recent studies have also established intracranial arterial stenosis as a risk factor for recurrent events after transient ischaemic attack (TIA) in

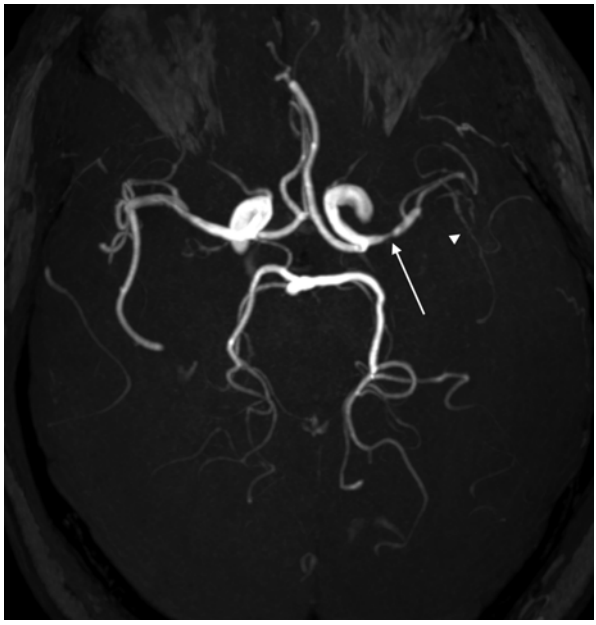

Fig. 6 MCA stenosis. (**a**) Axial thick-slab MIP projection of 3D TOF MRA. A severe stenosis of the left MCA (*arrow*) is present in this patient who presented recurrent "crescendo" left hemisphere TIAs. The more distal left MCA branches show reduced flow-related signal indicative of reduced flow (*arrowhead*)

both early (within 7 days) and late (90 days) phases [69] [70] (Fig. 6). This finding is not universal; the Trial of Cilostazol in Symptomatic Intracranial Arterial Stenosis (TOSS)-2 found instead that initial ischaemic lesion pattern was a better predictor than the presence of arterial stenosis [71]. However, the high-risk pattern of peripheral subcortical infarction may be a manifestation of severe stenosis, as turbulent blood flow may be more likely to cause plaque rupture and distal embolisation [72].

However, the symptomatology of intracranial stenosis may be different to that of extracranial stenosis: MCA stenosis-related MCA-territory ischaemic events are reported to have lower NIHSS scores than ICA disease [73] [2]. The presence of MCA stenosis has been correlated with the presence of more "central", lenticulostriate perforator territory infarction, which would not be unexpected, given the origin of these perforating branches from the M1 segment [74] (Fig. 7).

Vertebrobasilar Atherosclerosis

The vertebrobasilar system is also frequently affected by atherosclerosis, although large vessel disease is the major cause of stroke within the posterior circulation. The presence of basilar atherosclerosis is also correlated to more extensive large vessel disease and diffuse intracranial disease [75]. Atherosclerotic disease of the vertebral

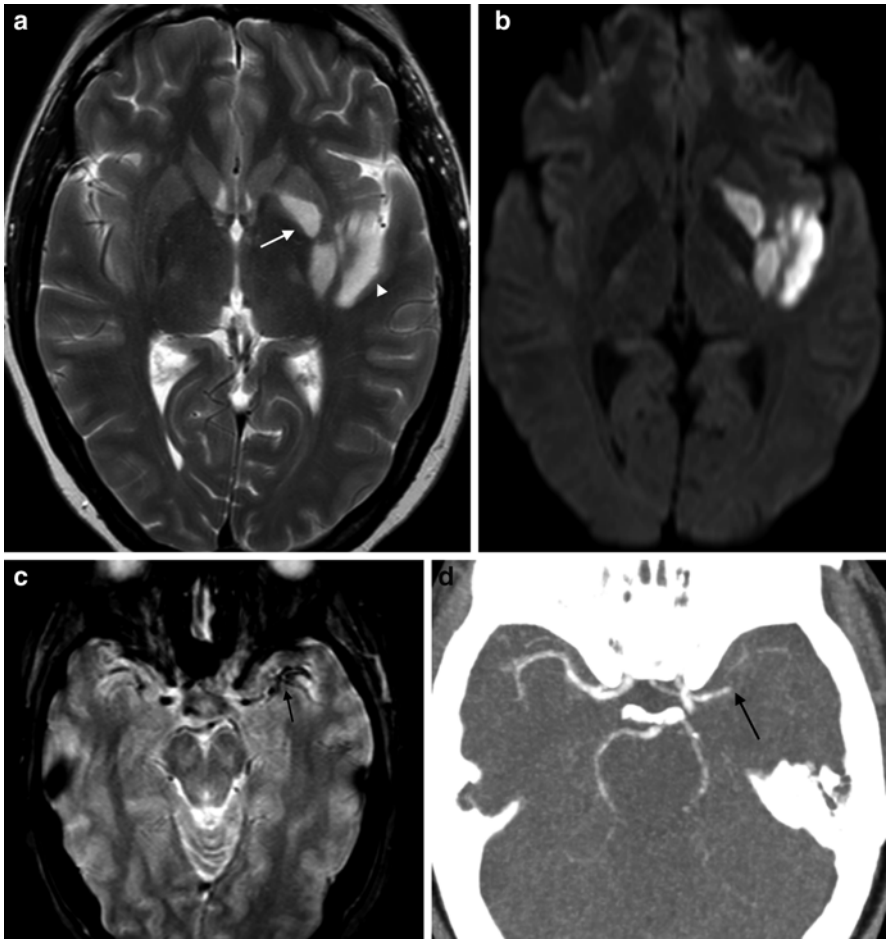

Fig. 7 MCA thrombosis. (**a**) Axial T2 image in a patient with acute right hemiparesis shows signal abnormality in the left putamen (*arrow*) and left insula cortex (*arrowhead*). (**b**) DWI shows hyperintensity in congruent regions, indicating acute infarction. (**c**) Axial T2* imaging shows hypointensity of the left M1 and M2 branches. Magnetic susceptibility due to deoxyhemoglobin in thrombus results in "blooming" and signal dropout. (**d**) CT angiogram confirms occlusion of the left M1

arteries is most commonly extracranial. However, intracranial VA disease (Fig. 8) is well recognised and can result in occlusion of medullary branches with subsequent infarction [76].

However, the branch vessels of the vertebrobasilar system, most importantly, the posterior inferior cerebellar arteries, superior cerebellar and posterior cerebral arteries, may also be affected by emboli. In the presence of atherosclerotic (both intra- and extracranial) disease, there may be artery-to-artery embolisation [77].

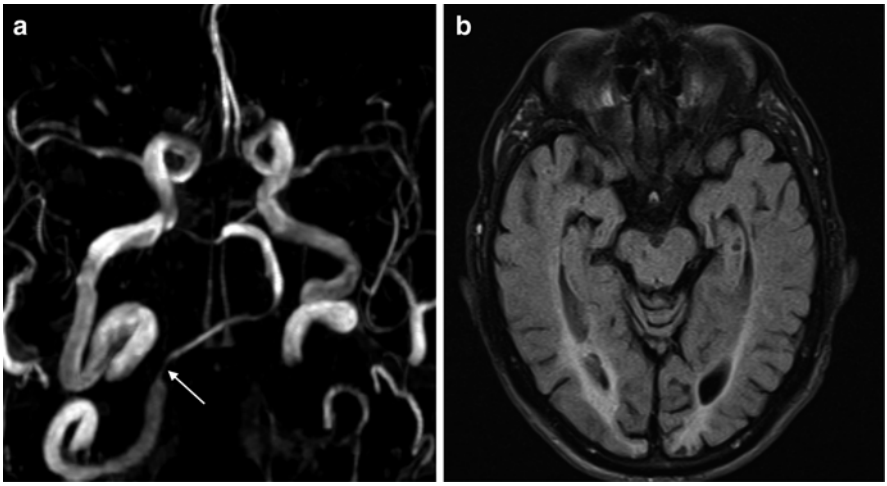

Fig. 8 Vertebral artery stenosis. (**a**) Oblique MIP image from TOF MRA shows severe stenosis of the right intracranial VA (*arrow*). The left VA (not shown) is hypoplastic. (**b**) Axial FLAIR image shows bilateral infarction of the medial occipital lobes

The mid segment of the basilar artery (BA) is a common site for atherosclerosis. Ischaemia may occur due to haemodynamic insufficiency, occlusion or distal embolisation. Basilar perforator branch occlusion is also a relatively common pattern of infarction. The imaging pattern in this case is of a lacunar infarct within the brainstem (often unilateral), commonly in the pons (Fig. 9). As is the case with VA disease, artery-to-artery embolisation is common, and distal emboli can be shown.

PCA atherosclerosis has been scantily described in the literature, but has been implicated in recurrent TIA [78] and midbrain/thalamic (perforator) infarction [79].

Diffuse Atherosclerosis

Intracranial atherosclerosis, like atherosclerosis in general, is frequently multifocal. Asymptomatic lesions can be found in up to 41 % of patients with symptomatic intracranial atherosclerosis [80] (Fig. 9). The presence of multiple MRA-defined stenoses worsens prognosis in the acute phase and predicts a higher stroke recurrence rate [81] [82] (Fig. 10).

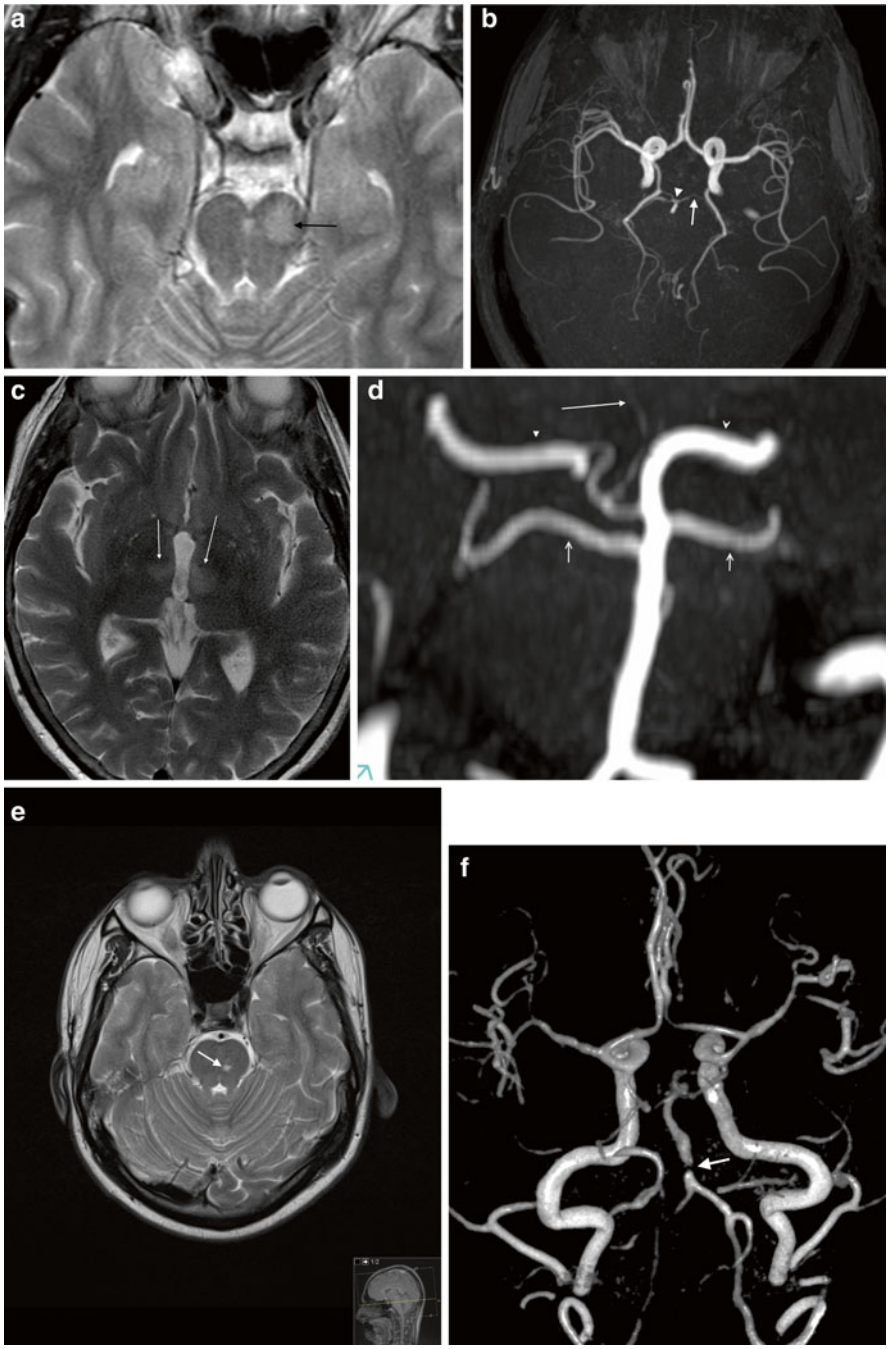

Fig. 9 Basilar perforator branch occlusion. (**a**) Axial T2 image showing acute infarct in the left of the midbrain (*arrow*). (**b**) Axial MIP of 3D TOF MRA shows a congenitally hypoplastic left P1 (*arrow*) and irregularity of the basilar tip. Perforator branches arise from the P1 segments and P2 segments. Embolisation to one of these vessels is thought to be the cause in this patient. (**c**) Axial T2 image in a different patient showing bilateral medial thalamic infarction, due to occlusion of a developmental variant of a PCA perforator branch (the artery of Percheron).

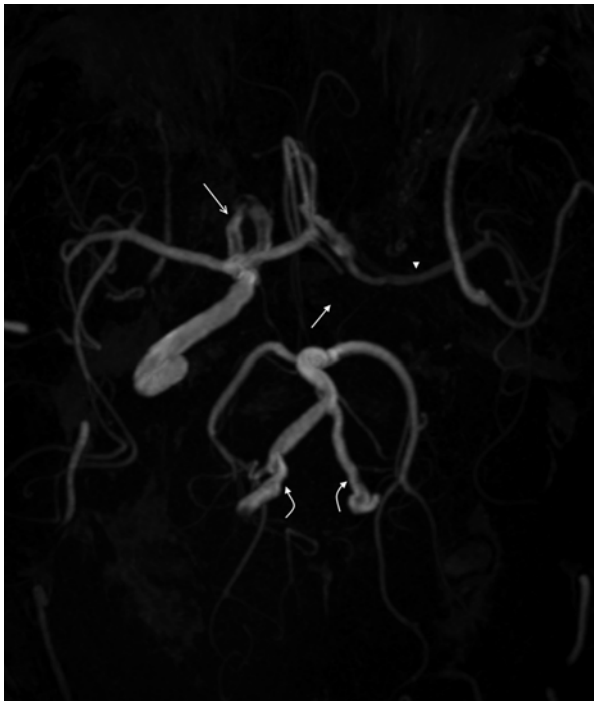

Fig. 10 Diffuse intracranial atherosclerosis. Axial projection MIP from 3D TOF MRA. The left ICA is completely occluded at the skull base and its flow-related signal is absent (*filled arrow*). There is considerable irregularity and appearance of severe stenosis of the right ICA siphon (*open arrow*). There is also considerable irregularity of the intradural vertebral arteries (*curved arrows*). The left MCA shows low-intensity flow-related signal, in keeping with slow flow secondary to the ICA occlusion (*arrowhead*). There is cross flow across the anterior communicating artery

Mimics and Other Causes of Intracranial Arterial Stenosis

There are a variety of non-atherosclerotic causes of intracranial arterial stenosis, and these should not be forgotten in the workup of the patient with stenosis on imaging.

Arterial Dissection

Intracranial arterial dissection is an uncommon condition, with prevalence of approximately 12 % in patients with symptomatic cerebrovascular dissection (the remainder having extracranial dissection) [83]. Unlike extracranial dissections,

Fig. 9 (continued) (**d**) Coronal MIP of TOF MRA in a different patient shows the artery of Percheron arising from a single P1 (*right*) to supply both medial thalami (*arrow*). The right P2 segment (*arrowhead*) is shown with dominant supply from the posterior communicating artery. The left PCA is supplied primarily from the basilar (*open arrowhead*). The superior cerebellar arteries are shown arising from just below the basilar tip (*open arrows*). (**e**) Axial T2 image showing a small lacunar pontine infarct (*arrow*). (**f**) Volume-rendered/shaded image from TOF MRA showing mid basilar stenosis (*arrow*)

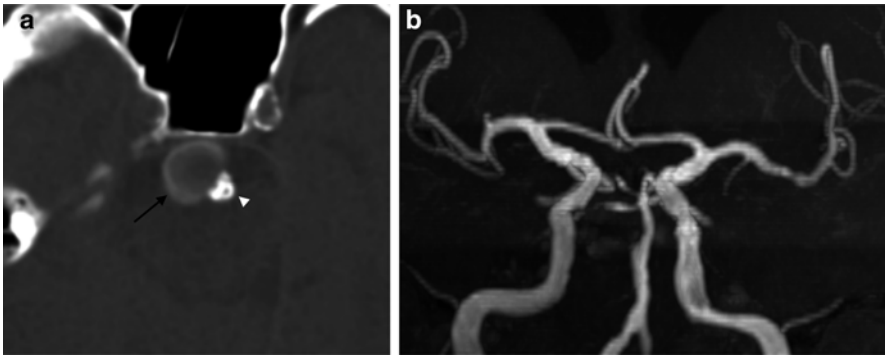

Fig. 11 Basilar artery dissection. (**a**) Unenhanced axial CT image shows densely calcified atherosclerotic involvement of the basilar artery (*arrowhead*) with a partially thrombosed dissecting aneurysm sac (*arrow*). (**b**) Coronal MIP from TOF MRA. The aneurysm sac is poorly shown, but the basilar artery is moderately stenosed at the site of the dissection, and there is widespread vascular irregularity consistent with diffuse atherosclerosis

intracranial dissections are more likely to result in dissecting aneurysm formation and subarachnoid haemorrhage (SAH) [84]. The most common locations are the terminal ICA, proximal MCA and VA.

Four major clinical syndromes have been described in the VA: aneurysm formation (Fig. 11), subintimal dissection and perforator occlusion, SAH and chronic dissection with recurrent TIA or stroke [64].

Inflammatory Vasculitis

There are numerous immunologic and inflammatory angiitis disorders.

Primary angiitis of the CNS (PACNS) is an extremely rare disorder, but the diagnosis should not be neglected as immunosuppressive treatment may alter the prognosis. While ischaemia is the underlying pathophysiology as a cause of stroke PACNS accounted for only 0.15 % of cases of stroke in one large series [85].

Imaging features are variable, and include variable patterns of infarction, and intracerebral or subarachnoid haemorrhage. Angiographic findings are often normal, but abnormalities include “beading” (multifocal narrowing in a vessel) in a variety of patterns and distributions, single regions of stenosis and collateral flow [86]. However, even IA DSA has limited sensitivity, with the role of MRA not well defined.

Polyarteritis nodosa (PAN) and Takayasu’s arteritis (TA) can give similar findings, with TA tending to affect larger and extracranial vessels [87].

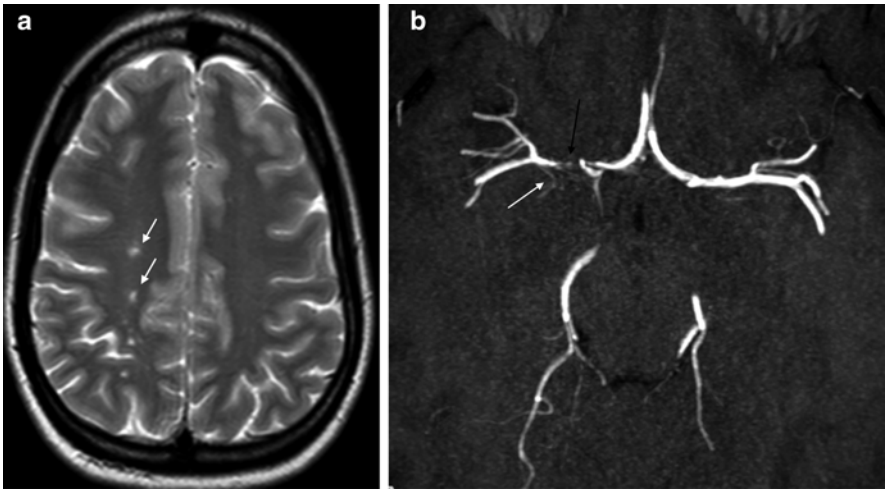

Fig. 12 Moyamoya syndrome. (**a**) T2 axial image in a young woman who presented with transient weakness of the left hand. Several small foci of white matter abnormality are shown along the ACA/MCA borderzone, suggestive of ischaemic lesions. (**b**) Thin-slab MIP projection of TOF MRA. The right M1 is severely stenosed and virtually occluded (*black arrow*). A number of thread-like collateral vessels (Moyamoya vessels) are present within the Sylvian fissure (*white arrow*)

Moyamoya

Moyamoya (MM) is an uncommon condition of unknown cause, which results in progressive stenosis and occlusion of the terminal ICA and proximal MCA/ACA. Moyamoya syndrome is the term given to a Moyamoya-like vascular disorder associated with another disease condition, of which numerous have been described [88] (Fig. 12). Presentation may be with SAH or ischaemic symptoms.

Diagnosis has historically required IA DSA evidence of bilateral terminal ICA occlusion or stenosis, the presence of collateral basal vessels and external carotid or posterior circulation collaterals. Contemporary MRA is capable of demonstrating these features. HR MRI has recently been reported as possibly discriminating between MM and atherosclerosis [89].

Miscellaneous Conditions

Numerous additional conditions have been reported as causing intracranial stenoses or vasospasm, which may need to be considered in the clinical context. These include radiation injury, such as may follow treatment of cervical or intracranial tumors [90], vasospastic disorders (reversible cerebral vasoconstriction syndromes) [91] and drugs of abuse, particularly cocaine [92].

Conclusion

MRA provides the most important diagnostic information for the diagnosis and prognostication in ICAD. However, familiarity with structural imaging and the common patterns of disease are needed for the interpretation of a complete study. The high sensitivity of DWI for acute ischaemia has revolutionised stroke diagnosis, and the use of perfusion imaging now plays an important role in determining the choice of treatment. Greater recognition of the radiation burden of CT may place a greater role on MRI perfusion imaging. HR MRI techniques for plaque assessment still need to be validated in large studies but have shown significant promise in detecting and classifying atherosclerotic disease and may have a role in guiding interventional treatment in the future.

References

1. Axel L. Blood flow effects in magnetic resonance imaging. Magn Reson Annu. 1986;237–44.
2. Lee P, Oh S, Bang O, et al. Infarct patterns in atherosclerotic middle cerebral artery versus internal carotid artery disease. Neurology. 2004;62(8):1291–6.
3. Brant-Zawadzki M, Atkindson D, Detrick M, et al. Fluid attenuated inversion recovery (FLAIR) for assessment of cerebral infarction. Initial clinical experience in 50 patients. Stroke. 1996;27:1187–91.
4. Chalela J, Haymore J, Ezzeddine M, et al. The hypointense MCA sign. Neurology. 2002;58:1470.
5. Stejskal E, Tanner J. Spin diffusion measurements: spin echos in the presence of a time-dependent field gradient. J Chem Phys. 1965;42:288–92.
6. Kim H, Choi C, Lee D et al. High-b-value diffusion-weighted MR imaging of hyperacute ischemic stroke at 1.5 T. AJNR. 2005;26(2):208-15.
7. Mukherjee P, Chung SW. Berman JI, et a. Diffusion tensor MR imaging and fiber tractography: technical considerations AJNR. 2008;29:843–52.
8. Meng X, Jun C, et al. High b-value diffusion tensor imaging of the remote white matter and white matter of obstructive unilateral cerebral arterial regions. Clin Radiol. 2013;68: 815–22.
9. Belliveau JW, Rosen BR, Kantor HL, et al. Functional cerebral imaging by susceptibility-contrast NMR. Magn Reson Med. 1990;538–46.
10. Golay X, Petersen E. Arterial spin labeling: benefits and pitfalls of high magnetic field. Neuroimaging Clin N Am. 2006;16(2):259–68.
11. Beaulieu C, de Crespigny A, Tong D, et al. Longitudinal magnetic resonance imaging study of perfusion and diffusion in stroke: evolution of lesion volume and correlation with clinical outcome. Ann Neurol. 1999;46:568–78.
12. Kim H, Kim T, Ryu S, et al. Acetazolamide-challenged perfusion magnetic resonance imaging for assessment of cerebrovascular reserve capacity in patients with symptomatic middle cerebral artery stenosis: comparison with technetium-99 m-hexamethylpropyleneamine oxime single-photon emis. Clin Imaging. 2011;35:413–20.
13. Wehrli F et al. Time-of-flight MR flow imaging: selective saturation recovery with gradient refocusing. Radiology. 1987;241–246.
14. Gullberg G et al. MR Vascular imaging with a fast gradient refocusing pulse sequence and reformatted images from transaxial sections. Radiology. 1987;241–246.

15. Marchal G et al. Intracranial vascular lesions: optimization and clinical evaluation of three dimensional time-of-flight MR angiography. Radiology. 1990;443–448.
16. Pedraza S. Comparison of preperfusion and postperfusion magnetic resonance angiography in acute stroke. Stroke. 2004;2105–2110.
17. Blatter DD et al. Cerebral MR angiography with multiple overlapping thin slab acquisition. Part II. Early clinical experience. Radiology. 1992;379–389.
18. Heiserman JE et al. Intracranial vascular stenosis and occlusion: evaluation with three-dimensional time-of-flight MR angiography. Radiology. 1992;185(3).
19. Stock KW, Radue EW, Jacob AL, et al. Intracranial arteries: prospective blinded comparative study of MR angiography and DSA in 50 patients. Radiology. 1995;195:451–56.
20. Feldmann E. ea. The Stroke Outcomes and Neuroimaging of Intracranial Atherosclerosis (SONIA) trial. Neurology. 2007;68(24):2099–106.
21. Bash J et al. Intracranial vascular stenosis and occlusive disease: evaluation with CT angiography, MR angiography, and digital subtraction angiography. AJNR. 2005;26:1012–21.
22. Choi CG et al. Detection of Intracranial Atherosclerotic Steno-Occlusive Disease with 3D Time-of-Flight Magnetic Resonance Angiography with Sensitivity Encoding at 3 T. AJNR. 2007;28:439–46.
23. Sadikin C et al. The current role of 1.5 T non-contrast 3D time-of-flight magnetic resonance angiography to detect intracranial steno-occlusive disease. J Formos Med Assoc. 2007;106(9):691–9.
24. Korogi Y, Takahashi M, Nakagawa T, et al. Intracranial vascular stenosis and occlusion: MR angiographic findings. AJNR. 1997;18:135–43.
25. Leng X, Wong KS, Soo Y, Leung T, Zou X, et al. Magnetic Resonance Angiography Signal Intensity as a Marker of Hemodynamic Impairment in. PLoS ONE. 2013;8(11), e80124.
26. Zhang HL, Maki JH, Prince MR. 3D contrast enhanced MR angiography. J Magn Reson Imaging. 2007;25:13–25.
27. Cashen TA, Carr JC, Shin W, et al. Intracranial time resolved contrast enhanced MR angiography at 3 T. AJNR. 2006;27:822–9.
28. Turski PA, Korosec FR, Carroll TJ, et al. Contrast enhanced magnetic resonance angiography of the carotid bifurcation using the time resolved imaging contrast kinetics (TRICKS) technique. Top Magn Reson Imaging. 2001;12:175–81.
29. Alfke J, Jensen U, Pool C, et al. Contrast-enhanced magnetic resonance angiography in stroke diagnostics: additional information compared with time-of-flight magnetic resonance angiography? Clin Neuroradiol. 2011;21(1):5–10.
30. Medicines and Healthcare products Regulatory Agency. Gadolinium-containing contrast agents: new advice to minimise the risk of nephrogenic systemic fibrosis. [Internet]. 2010 [cited 2014 Jan]. Available from: http://www.mhra.gov.uk/Safetyinformation/DrugSafetyUpdate/CON087741.
31. S. Dehkharghani JKaAMS. Improved Quality and Diagnostic Confidence Achieved by Use of dose-reduced Gadolinium Blood-Pool agents for Time-resolved intracranial MR angiography. AJNR. 2013.
32. Rohrer M. BHMJea. Comparison of magnetic properties of MRI contrast media solutions at different magnetic field strengths Invest Radiol. 2005;40:715–24.
33. Lovblad K, Yilmaz H, Chouiter A, et al. Intracranial aneurysm stenting: follow-up with MR angiography. J Magn Reson Imaging. 2006;24(2):418–22.
34. Amin-Hanjani S, Du X, Zhao M, et al. Use of Quantitative Magnetic Resonance Angiography to Stratify Stroke Risk in Symptomatic Vertebrobasilar Disease. Stroke. 2005;36:1140–11475.
35. Prabhakaran S, Warrior L, Wells K, et al. The utility of quantitative magnetic resonance angiography in the assessment of intracranial in-stent stenosis. Stroke. 2009;40(3):991–3.
36. Ryu CW, Jahng GH, Kim EJ, et al. High resolution wall and lumen MRI of the middle cerebral arteries at 3 tesla. Cerebrovasc Dis. 2009;27(5):433–42.
37. Ma N, Jiang WJ, Lou X, et al. Arterial remodeling of advanced basilar atherosclerosis: a 3-Tesla MRI study. Neurology. 2010;75:253–58.

38. Xu WH, Li ML, Gao S, et al. In vivo high-resolution MR imaging of symptomatic and asymptomatic middle cerebral artery atherosclerotic stenosis. Atherosclerosis. 2010; 212:507–11.
39. Klein IF, Lavallee PC, Touboul PJ, et al. In vivo middle cerebral artery plaque imaging by high-resolution MRI. Neurology. 2006;67:327–29.
40. Saam T, Cai J, Ma L, et al. Comparison of Symptomatic and Asymptomatic Atherosclerotic Carotid Plaque Features with in Vivo MR Imaging. Radiology. 2006;240(2):464–72.
41. Wintermark M, Sanelli P, Albers G, et al. Imaging Recommendations for Acute Stroke and Transient Ischemic Attack Patients: A Joint Statement by the American Society of Neuroradiology, the American College of Radiology, and the Society of NeuroInterventional Surgery. AJNR. 2013;34:E117–127.
42. Chung GH, Kwak HS, Hwang SB, Jin GY. High resolution MR imaging in patients with symptomatic middle cerebral artery stenosis. Eur J Radiol. 2012;81:4069–74.
43. Turan TN, Bonilha L, Morgan PS, et al. Intraplaque hemorrhage in symptomatic intracranial atherosclerotic disease. J Neuroimaging. 2011;21:E159–61.
44. Chimowitz MI, Lynn MJ, Derdeyn CP, et al. Stenting versus aggressive medical therapy for intracranial arterial stenosis. N Engl J Med. 2011;365:993–1003.
45. Deryden C, Chimowitz M, Lynn M, et al. Aggressive medical treatment with or without stenting in high-risk patients with intracranial artery stenosis (SAMMPRIS): the final results of a randomised trial. Lancet. 2014;383(9914):333–41.
46. Zaidatt O, Castonguay A, Nguyen T et al. Impact of SAMMPRIS on the future of intracranial atherosclerotic disease management: polling results from the ICAD symposium at the International Stroke Conference. J Neurointerv Surg. 2013.
47. Yang W, Huang B, Liu X, et al. Reproducibility of high-resolution MRI for the middle cerebral artery plaque at 3 T. Eur J Radiol. 2014;83(1):e49–55.
48. Adams HP. BBKLea. Classification of subtype of acute ischaemic stroke definitions for use in a multicentre clinical trial TOAST. Trial of Org 10172 in Acute Stroke Treatment. Stroke. 1993;24:35–41.
49. Ay H, Benner T, Arsava EM, Furie KL, et al. A computerized algorithm for etiologic classification of ischaemic stroke: the Causative Classification of Stroke System. Stroke. 2007;38:2979–84.
50. Amarenco P, Bogousslavsky J, Caplan LR, et al. The ASCOD phenotyping of ischemic stroke (Updated ASCO Phenotyping). Cerebrovasc Dis. 2013;36(1):1–5.
51. White H. BABWCea. Ischemic stroke subtype incidence among whites, blacks and Hispanics: The northern Manhattan study. Circulation. 2005;111:1327–31.
52. Lee LJ. KCAJea. Impact on stroke subtype diagnosis of early diffusion-weighted magnetic resonance imaging and magnetic resonance angiography Stroke. 2000;31:1081–9.
53. Derdeyn C, Powers W, Grubb Jr R. Hemodynamic effects of middle cerebral artery stenosis and occlusion. AJNR. 1998;19(8):1463–9.
54. Roederer GO. LYCAea. Is siphon disease important in predicting outcome of carotid endarterectomy? Arch Surg. 1983;10:1177–81.
55. Fredericks R. TTLDTB. Implications of the angiographic string sign in carotid atherosclerosis. Stroke. 1990;21(3):476–9.
56. Gacs G, Fox A, Barnett H, Vinuela F. Occurrence and mechanisms of occlusion of the anterior cerebral artery. Stroke. 1983;14:952–9.
57. Kwon S, Cho Y, Koo J, et al. Cilostazol prevents the progression of the symptomatic intracranial arterial stenosis: the multicenter double-blind placebo controlled trial of cilostazol in symptomatic intracranial arterial stenosis. Stroke. 2005;36:782–6.
58. Lhermitte F, Gautier JC, Derouesne C, et al. Ischemic accidents in the middle cerebral artery territory: a study of the causes in 122 cases. Arch Neurol. 1968;19:248–56.
59. Mazighi M, Labreuche J, Gongora-Rivera F, et al. Autopsy prevalence of intracranial atherosclerosis in patients with fatal stroke. Stroke. 2008;39:1142–47.

60. Klein IF, Labreuche J, Lavallee PC, et al. Is moderate atherosclerotic stenosis in the middle cerebral artery a cause of or a coincidental finding in ischemic stroke? Cerebrovasc Dis. 2010;29:140–5.
61. Degnan AJ, Gallagher G, Teng Z, et al. MR Angiography and Imaging for the Evaluation of Middle Cerebral Artery Atherosclerotic Disease. AJNR. 2012;33:1427–35.
62. Chen H, Hong H, Liu D, et al. Lesion patterns and mechanism of cerebral infarction caused by severe atherosclerotic intracranial internal carotid artery stenosis. J Neurol Sci. 2011;307(1-2):79–85.
63. Min W, Park K, Kim Y, et al. Atherothrombotic middle cerebral artery territory infarction: topographic diversity with common occurrence of concomitant small cortical and subcortical infarcts. Stroke. 2000;31:2055–61.
64. Caplan L, Hennerici M. Impaired clearance of emboli (washout) is an important link between hypoperfusion, embolism and ischemic stroke. Arch Neurol. 1998;55:1475–82.
65. Khan M, Rasheed A, Hashmi S, et al. Stroke radiology and distinguishing characteristics of intracranial atherosclerotic disease in native South Asian Pakistanis. Stroke: Int J; 2013.
66. Adams H, Demasio H, Putman S, Demasia A. Middle cerebral artery occlusion as a cause of isolated subcortical infarction. Stroke. 1983;14:948–52.
67. Hinton RC. MJARea. Symptomatic middle cerebral artery stenosis Ann neurol. 1979;5:152–7.
68. Adams H, Gross C. Embolism distal to stenosis of the middle cerebral artery. Stroke. 1981 Dec;228–229.
69. Ssi-Yan-Kai G, Nasr N, Faury A, et al. Intracranial Artery Stenosis or Occlusion Predicts Ischemic Recurrence after Transient Ischemic Attack. AJNR. 2013;34:185–90.
70. Coutts SB, Simon JE, Eliasziw M, et al. Triaging transient ischemic attack and minor stroke patients using acute magnetic resonance imaging. Ann Neurol. 2005;57:848–54.
71. Jung J, Kang D, Koo J, et al. Predictors of Recurrent Stroke in Patients With Symptomatic Intracranial Arterial Stenosis. Stroke. 2012;43:2785–7.
72. Ogata J, Masuda J, Yutani C, Yamaguchi T. Mechanisms of cerebral artery thrombosis: a histopathological analysis on eight necropsy cases. J Neurol Neurosurg Psychiatry. 1994;57:17–21.
73. Chen XY, Wong KS, Lam WW, et al. Middle cerebral artery atherosclerosis: histological comparison between plaques associated with and not associated with infarct in a postmortem study. Cerebrovasc Dis. 2008;25:74–80.
74. Cho H, Roh H, Moon W, Kim H. Perforator territory infarction in the lenticulostriate arterial territory: mechanisms and lesion patterns based on the axial location. Eur Neurol. 2010;63(2):107–15.
75. Voetsch B, DeWitt D, Pessin M, Caplan L. Basilar Artery Occlusive Disease in the New England Medical Center Posterior Circulation Registry. Arch Neurol. 2004;61:496–504.
76. Kim J. Pure lateral medullary infarction: clinical-radiological correlation of 130 acute, consecutive patients. Barin. 2003;126:1864–72.
77. Pessin M, Daneault N, Kwan E, et al. Local embolism from vertebral artery occlusion. Stroke. 1988;19:112–5.
78. Kim J. Pure or predominantly sensory transient ischemic attacks associated with posterior cerebral artery stenosis. Cerebrovasc Dis. 2002;14:136–8.
79. Kim J, Kim J. Pure midbrain infarction: clinical, radiological and pathophysiological findings. Neurology. 2005;64:1227–32.
80. Mazighi M, Tanasescu R, Ducrocq X, et al. Prospective study of symptomatic atherothrombotic intracranial stenoses: the GESICA study. Neurology. 2006;66:1187–91.
81. Asil T, Balci K, Uzunca I, et al. Six-month follow-up study in patients with symptomatic intracranial arterial stenosis. J Clin Neurosci. 2006;13(9):913–6.
82. Kate M, Sylaja P, Kesavadas C, Thomas B. Imaging and Clinical Predictors of Unfavorable Outcome in Medically Treated Symptomatic Intracranial Atherosclerotic Disease. J Stroke Cerebrovasc Dis. 2013.

83. Pelkonen O, Tikkakoski T, Leinonen S, et al. Intracranial arterial dissection. Neuroradiology. 1998;40:442–7.
84. Yonas H, Agamanolid S, Takaoka Y, White R. Dissecting intracranial aneurysms. Surg Neurol. 1977;8:407–15.
85. Wiszniewska M, Devuys G, Bogousslavsky J. Giant cell arteritis as a cause of first-ever stroke. Cerebrovasc Dis. 2007;24(2-3):226–30.
86. Alhalabi M, Moore P. Serial angiography in isolated angiitis of the central nervous system. Neurology. 1994;44(7):1221–6.
87. Cantu C, Pineda C, Baringarrementeria F, et al. Noninvasive cerebrovascular assessment of Takayasu arteritis. Stroke. 2000;31(9):2197–202.
88. Scott R, Smith E. Moyamoya disease and Moyamoya syndrome. N Engl J Med. 2009;360:1226–37.
89. Kim Y, Lee D, Kwon J, et al. High resolution MRI difference between Moyamoya disease and intracranial atherosclerosis. Eur J Neurol. 2013;20(9):1311–8.
90. Kang J, Kwon S, Kim J. Radiation induced angiopathy in acute stroke patients. J Stroke Cerebrovasc Dis. 2002;11:315–9.
91. Calabrese L, Dodick D. Schwedt. Singhal A Narrative review: reversible cerebral vasoconstriction syndromes Ann Intern Med. 2007;146:34–44.
92. Kaye B, Fainstat M. Cerebral vasculitis associated with cocaine abuse. JAMA. 1987;258:2104–6.
93. Korogi Y, Takahashi M, Mabuchi N, et al. Intracranial vascular stenosis and occlusion: diagnostic accuracy of three-dimensional, Fourier transform, time-of-flight MR angiography. Radiology. 1994;193:187–93.
94. Yasaka M, Yamaguchi T, Shichiri M. Distribution of Atherosclerosis and Risk Factors in Atherothrombotic Occlusion. Stroke. 1993;24:206–11.

Evolving Technologies in MR and PET for Imaging Atherosclerosis

Maciej Jakuciński, Karol P. Budohoski, Victoria E.L. Young, Peter J. Kirkaptrick, Mirosław Ząbek, and Leszek Królicki

Introduction

Atherosclerosis is a progressive and chronic inflammatory condition of the cardiovascular. Atherosclerotic changes that lead to significant complications are most commonly located in the coronary and carotid arteries. Studies show that the frequency of clinical events does not correlate well with the degree of vascular stenosis in the affected territory. Data from patients with myocardial infarction showed that only 22 % of patients presenting with STEMI had >70 % occlusion of the related artery [1]. Similarly, like most patients who have a myocardial infarction do not report any symptoms of ischemia prior to the event, in most cases a history of a transient ischemic attack (TIA) is not present in most cases of stroke. This indicates that the pathophysiology of the condition is likely to have a greater impact on the outcome of the disease than the degree of stenosis.

Rothwell et al. [2], in an analysis of pooled data from the three major randomized controlled trials of CEA for symptomatic patients [European Carotid Surgery Trial

M. Jakuciński, M.D. • M. Ząbek, M.D., Ph.D. • L. Królicki, M.D., Ph.D.
Department of Radiology, Mazowiecki Szpital Brodnowski, Warsaw, Poland

K.P. Budohoski, M.D. (✉)
Division of Neurosurgery, Department of Clinical Neurosciences, Addenbrooke's Hospital, University of Cambridge, Cambridge, UK
e-mail: kpb26@cam.ac.uk

V.E.L. Young, M.D., Ph.D.
Department of Radiology, University of Cambridge, Cambridge, UK

P.J. Kirkaptrick, M.D., F.R.C.S.(SN), FMedSci
Division of Neurosurgery, Department of Clinical Neurosciences, Addenbrooke's Hospital, University of Cambridge, Cambridge, UK

R. Trivedi et al. (eds.), *3D Imaging Technologies in Atherosclerosis*,
DOI 10.1007/978-1-4899-7618-5_10

(ECST), North American Symptomatic Carotid Endarterectomy Trial (NASCET), and Veterans' Affairs Trial], demonstrated that a significant benefit from surgery can only be achieved in patients with severe stenosis (70–99 %), with an absolute risk reduction (ARR) of ipsilateral stroke within the next 5 years of 16 % [2]. A marginal benefit was observed in symptomatic patients with moderate stenosis (50–69 %) with an ARR of 4.6 % [2]. For asymptomatic patients combined data from the Asymptomatic Carotid Atherosclerosis Study (ACAS) and the Asymptomatic Carotid Surgery Trial (ACST) demonstrated that patients who benefited from surgical treatment were those who had a significant narrowing of ≥70 %. The decrease of 5-year stroke risk was shown to be from 11.5 to 6 % [3, 4].

Classical angiography allows for the interpretation of the degree of stenosis, but is unable to measure other important parameters, such as inflammation within the plaque or the structure of the atherosclerotic plaque. Furthermore, adaptive outward arterial remodeling may lead to the formation of large plaques without significant luminal narrowing and this cannot be adequately assessed using DSA alone [5].

In approximately 70 % of patients the cause of an infarct is a plaque rupture resulting in blood clot formation with or without embolization [6]. In the remaining patients with acute vascular events, intraluminal thrombosis may be precipitated by plaque erosion with endothelial dysfunction and denuding, as well as the influence of distorted anatomy due to the formation of calcified nodules [6–12].

Histological studies have been used to characterize plaque morphology and identify vulnerable atheromatous disease (Table 1) [10, 11]. As understanding of the morphology has increased, there has been a shift of interest toward identifying the characteristics of the carotid arterial wall on imaging, which may play a part in risk assessment, especially for the asymptomatic patients.

Various underlying mechanisms which can cause mechanical failure of the fibrous cap, leading to plaque rupture, have been suggested, including biomechanical stress [13–15], hemorrhage within the plaque [10, 16, 17], inflammation within

Table 1 Criteria for defining vulnerable plaques and diagnostic imaging methods [8]

Type of criteria	Criterion	Imaging
Major	Active inflammation	CE-MRI, USPIO-MRI, FDG-PET
	Thin FC with large LRNC	MRI, CE-MRI, CT
	FC disruption	MRI, CE-MRI, SPECT
	Severe stenosis	MRA, CTA, B-mode ultrasonography
Minor	IPH	MRI, CT
	Expansive remodeling	MRI
	Superficial calcified nodules	MRI, CT
	Endothelial dysfunction	–

LRNC lipid-rich necrotic core, *MRI* magnetic resonance imaging, *CE-MRI* contrast-enhanced MRI, *USPIO-MRI* ultra-small super-paramagnetic iron oxide-enhanced MRI, *FDG-PET* fluorodeoxyglucose positron emission tomography, *CT* computed tomography, *SPECT* single-photon emission computed tomography

the plaque with an influx of macrophages [18–20], destruction of the fibrous cap by proteolytic enzymes such as matrix metalloproteinases (MMPs) [21], and apoptotic cell death of fibrous cap fibroblasts [18–20].

PET Imaging of the Vulnerable Plaque

PET and SPECT studies allow for the analysis of atherosclerotic plaque composition by imaging the inflammatory process, apoptosis, and metabolism of lipids.

The risk of plaque rupture and thrombus formation depends not only on the thickness of the fibrous cap surrounding the plaque, but also on the composition/state, e.g., the presence of lipid and the inflammation initiated by macrophages [8–11]. The inflammatory process is linked to plaque instability and the risk of acute vascular events. Among the effects, inflammation leads to enzymatic damage and subsequent rupture of the fibrous cap.

Due to the active inflammation, macrophages are of interest in monitoring atherosclerosis. They have a significant glycolytic activity, which can be imaged in PET after the administration of 18FDG [22]. 18FDG is a glucose analog, which is carried by the same transport mechanisms, and is subsequently transformed in the Krebs cycle, taking part in the first step, phosphorylation, only. As a result, the uptake of 18FDG is directly proportional to the glucose transport mechanisms and the activity of hexokinase and therefore the metabolic activity of the tissue.

18F-FDG-PET studies were introduced into clinical practice over 20 years ago and are most commonly used to evaluate neoplastic and inflammatory diseases. Tawakol et al. showed that the degree of 18FDG uptake strictly correlates with the presence of macrophages in the plaque (Fig. 1) [22]. The technique potentially allows for diagnosis of inflammatory vascular lesions, as well as treatment monitoring.

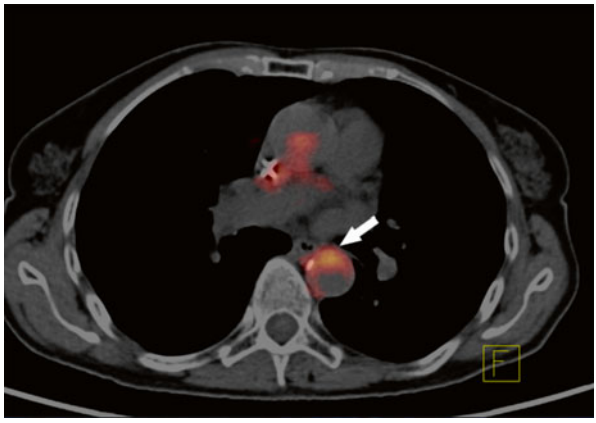

Fig. 1 18FDG-PET/CT of the thoracic aorta. Accumulation of 18FDG in the aortic wall (*white arrow*) signifies an active inflammatory process in the atherosclerotic plaque

PET has greatly improved after the introduction of hybrid PET/CT [23]. The CT imaging allows for an analysis of density of the surrounding tissue, which is then used to correct the attenuation phenomenon. The second advantage of this technique is image fusion from the two modalities, allowing good anatomical correlation, some assessment of plaque structure, as well as information on the metabolic activity. PET also allows for the evaluation of structures in multiple vascular territories at once, which is advantageous in this systemic disease. Studies have shown that inflammatory changes in atherosclerotic plaques are located diffusely throughout the vascular system. If a plaque is demonstrated to have inflammatory changes, it is common for the morphological changes to be present in other plaques to a similar degree. The presence of a plaque in one carotid artery is often connected with a contralateral, but is more commonly associated with plaques located within the same anatomical area. It has been shown that the uptake of 18FDG in atherosclerotic plaques does not correlate with the degree of calcification. This suggests that calcification is the final step in the disease process and is a more stable state. This observation shows the potential role of functional studies in disease work-up. The systemic nature of the disease can also be determined as illustrated with the increased 18FDG uptake in the area of atherosclerotic carotid plaques of patients who have had a previous myocardial infarction and a higher concentration of serum inflammatory markers (including matrix metalloproteinase (MMP 3 and MMP 9) and C-reactive protein (CRP)).

PET/CT allows for the evaluation of the effectiveness of new generation drugs, which reduce plaque inflammation in some way, by examining their effect on plaque stabilization. Tahara et al. [24] studied the effect of simvastatin on the degree of 18FDG uptake in atherosclerotic plaques in two patient groups: those treated with simvastatin vs. low-cholesterol diet alone (overall population 43 patients). Measuring the 18FDG uptake values before treatment and at 3 months, the18F-FDG uptake in atherosclerotic plaque was markedly smaller in patients treated with simvastatin compared to diet alone, with an added correlation of decreased 18FDG uptake with higher high-density lipoprotein (HDL) levels. Lee et al. [25] established that PET allows for objective conclusions of the effect of lifestyle on disease progression. Prior to the observational period, 362 anatomical areas with increased 18FDG uptake were identified in a cohort of 60 patients. After 17 months the number of areas of increased uptake reduced to 124. The authors also evaluated the whole body 18FDG index. After lifestyle changes, the index decreased from 1.39 to 0.53, which correlated with a decreased total and low-density lipoprotein (LDL) cholesterol concentration. This data illustrates that PET is a useful tool in the study of disease progression, as well as the effectiveness of drugs and lifestyle modification in progression. Fayad et al. [26] used 18FDG-PET/CT combined with MR to study the effect of dalcetrapib on plaque morphology. Dalcetrapib modulates cholesteryl ester transfer protein (CETP) activity to raise HDL cholesterol. The authors were able to demonstrate that PET as well as MRI are acceptable techniques to evaluate drug effectiveness. Furthermore, they have shown that dalcetrapib acts positively on the structure and functional parameters of vessel wall plaques.

Cardiac

Patients with a myocardial infarction do not always demonstrate significant coronary stenosis. However, histological assessment of plaques has often demonstrated features of instability, suggesting that modalities, such as PET, may be helpful in identifying this cohort of patients. A limitation to this method in coronary imaging is the physiological high uptake of 18FDG in myocardial tissue. If the patient was well prepared, with a low-carbohydrate, high-fat meal, myocardial suppression of 18FDG uptake was enhanced allowing for proper evaluation of atherosclerotic plaques in coronary arteries. Wykrzykowska et al. [27] used the diet patient preparation before a PET study, which was correlated to coronary angiography and the results suggested that increased 18FDG uptake matched disease identified on angiography, although the results were not significant in this small study (15 patients had 18FDG-positive coronary vessels).

MRI and the Vulnerable Plaque

MRI is as an established imaging modality for plaque morphology and stenosis evaluation. The technique does not require ionizing radiation, provides high-resolution images, and using multiple sequences can evaluate disease characteristics. The use of different sequences allows for evaluation of plaque structure [28], without the need of intravenous contrast, although this further enhances the technique [29, 30]. It is possible to assess the fibrous cap, lipid-rich necrotic core, or possible intraplaque hemorrhage. In contrast, calcification may be more difficult to analyze.

Plaque Hemorrhage

One of the most common risk factors correlating with a high risk of clinical sequelae is plaque hemorrhage [31, 32]. The reason of bleeding is unclear, but most probably it is caused by fragile neovessels within the plaque [33, 34]. Without proper smooth muscle cell support and with a leaky endothelium it is common for them to rupture and cause a hemorrhage [35, 36]. Bleeding causes an increase in size of the plaque, with extravasated blood having a pro-inflammatory effect, leading to accumulation of macrophages which produce proteases, and a positive feedback loop is created of inflammation and neovascularization [33, 34]. This in turn causes degradation of the fibrous cap. MRI allows for the identification of methemoglobin (which can be used as an endogenous contrast for MRI imaging), among other hemorrhage types, in the area of an atherosclerotic plaque. Methemoglobin has paramagnetic properties and is best identified with a high signal on T1-weighted (T1 W) images. This phenomenon has a high sensitivity and specificity for identifying recent intraplaque hemorrhage [37, 38]. High signal on both spin echo and time-of-flight (TOF) gradient echo T1-weighted images were noted by Yuan et al. [39]. MR imaging with

Table 2 Stages of intraplaque hemorrhage

Stage of hemorrhage	Characteristics		
		MRI	
	Histology	T_1W/TOF	T_2W/PDw
Fresh (Type I)	Intact RBC with intracellular methemoglobin	Hyperintense	Isointense
Recent (Type II)	Lytic RBC with extracellular methemoglobin	Hyperintense	Hyperintense
Old	Amorphemosid	Hypointense	Hypointense

RBC red blood cells, *T1W* T1 weighted, *TOF* time of flight, *T2W* T2 weighted, *PDw* proton density weighted [36, 40]

T1-weighted/TOF and T2-weighted/proton density (PD)-weighted sequences can now be used to date the intraplaque hemorrhage (Table 2) [36, 40]. Moody et al. proposed an MR sequence used for direct thrombus imaging—magnetization-prepared rapid acquisition with gradient echo (MP-RAGE)—to image lower-limb deep venous thrombosis [41], which was later modified for plaque imaging, providing sensitive but low-resolution imaging of plaque hemorrhage [42].

The concurrent use of angio-MR (MRA) and plaque analysis is also being developed. Yoo et al. used the maximum intensity projection (MIP) of TOF MRA showing the presence of juxtaluminal hyperintensities indicating plaque hemorrhage [43]. Another imaging method that has been applied is based on phase-sensitive reconstruction of an inversion recovery (IR)-prepared sequence that is timed to produce strongly negative signals in the vessel lumen and strongly positive signals in the vulnerable plaque. One of the difficulties in combining angiography and plaque morphology imaging has been getting good angiographic coverage; for clinical purposes carotid angiography is performed from the aortic arch to the circle of Willis while most plaque imaging is performed with dedicated high-resolution coils over the carotid bifurcation providing great detail of the plaque but limited angiographic coverage if the coil is not changed for a more standard array.

The assessment of intraluminal bleeding, also known as juxtaluminal hemorrhage, is an important sign of plaque vulnerability. This has mostly been studied in small patient groups, but they provide a strong indication of the importance of this feature. Takaya et al. [12] showed that the presence of juxtaluminal hemorrhage is associated with a cerebral infarction in 67 % of non-symptomatic patients with 50–79 % carotid artery stenosis.

Plaque Morphology

Another factor determining the development of complications is the size (and volume) of a plaque.

Arterial expansive remodeling is a process whereby growth of the plaque is not reflected in the narrowing of the arterial lumen [5]. This process has been implicated

in plaque vulnerability by disguising large lesions [44, 45]. Such lesions may not manifest themselves in angiography, despite extensive atherosclerotic changes. Numerous studies confirm that there are no clear relationship between the size of a plaque and the degree of vessel stenosis [46]. Volume assessment of a vulnerable plaque is difficult to image well. MRI is a potentially useful method for assessment of the extent of this phenomenon as it allows for simultaneous imaging of both the arterial lumen and wall [47, 48]. The most frequently used sequences are black-blood fast spin echo sequences [44, 47, 49, 50]. Corti et al. [49, 51] studied the effects of simvastatin lipid-lowering therapy on human atherosclerotic lesions (aortic and carotid lesions) demonstrated by changes in both vessel wall thickness (VWT) and vessel wall area (VWA), which are often used as surrogate markers of expansive remodeling. Reductions in both parameters were statistically significant at 12, 18, and 24 months after initiation of the treatment regime.

There are however limitations to MRI for measuring these parameters. Artifacts associated with blood flow and the partial volume effect due to an obliquity of the vessel wall can reduce the accuracy of defining the boundaries of the vessel wall. When using inflow-dependent blood suppression techniques errors are encountered when there is slow or recirculating flow within the imaging slab, which may be as high as 50 %. New imaging methods for inflow-independent blood suppression and 3D imaging to minimize partial volume effects are implemented. 3D sequences additionally improved signal-to-noise ratios, increased longitudinal coverage, improved resolution especially in the through-plane direction, and provided greater acquisition efficiency. The through-plane resolution is important because volumes need to be calculated with larger slice thicknesses making the results less accurate.

To assess the plaque burden it is necessary to accurately define the external and internal walls of the vessel wall; traditionally this has been done by an experienced observed, but a number of software packages have been developed to automate this time-consuming task [52].

Fibrous Cap and Lipid-Rich Necrotic Core

Fibrous cap thickness and lipid-rich necrotic core size are two most readily available parameters from high-resolution MRI, which potentially may give additional information regarding the stability of a carotid atheromatous plaque (Fig. 2) [53, 54]. Mostly histological studies have shown that one of the most common phenotypes of plaques prone to rupture is a thin fibrous cap overlying a large lipid-rich necrotic core [6, 9, 10, 55]. Sequences used to image the FC and LRNC rely on the ability of cholesterol esters, which are the predominant component of lipid-rich necrotic core to shorten T2 relaxation time.

The result is a hypointense area on T_2W images representing lipid-rich necrotic core. High intraobserver agreement was noted for the identification of lipid-rich necrotic core and moderate agreement for fibrous cap. Furthermore the accuracy of feature identification on imaging was validated against histology with good results.

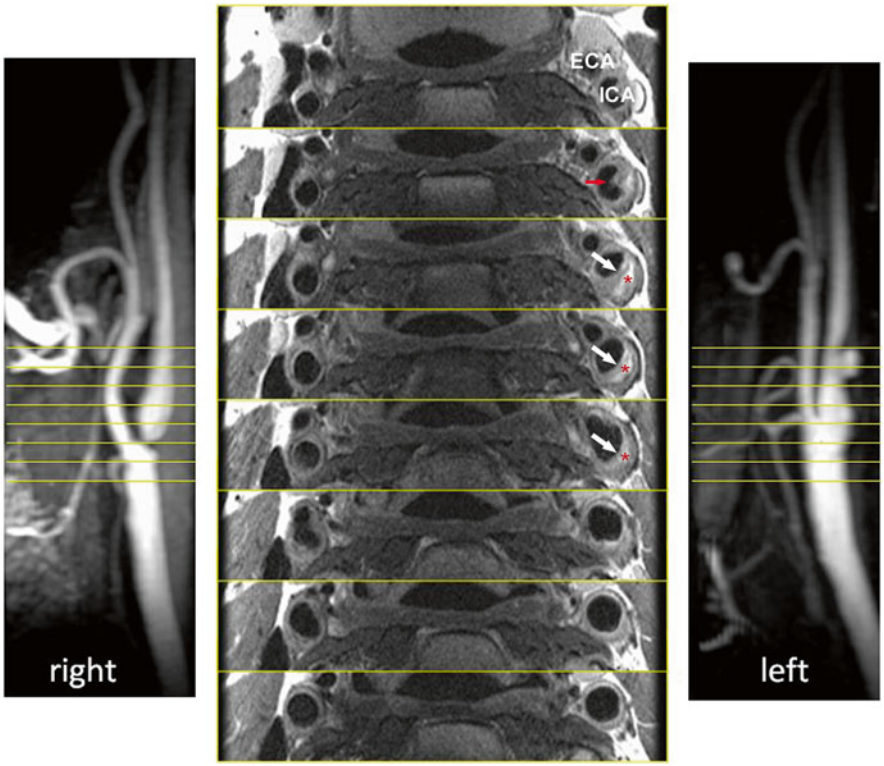

Fig. 2 Plaque morphology. Sequential images of an atherosclerotic plaque within the left internal carotid artery. The typical morphological components are seen, including the lipid-rich necrotic core (*red asterisk*), the fibrous cap (*white arrow*), and a possible site of ulceration (*red arrow*). ECA—external carotid artery; ICA—internal carotid artery

Hatsukami et al. [56] performed an analysis of the ability of high-resolution MRI to distinguish between differences in fibrous cap thickness and rupture. They used 3D multiple overlapping thin-slab angiography (MOTSA) sequence to identify thick, thin, and ruptured plaques. Results showed an 89 % agreement with histological assessment. Trivedi et al. [57] performed a study of carotid plaque composition with emphasis on depicting lipid-rich necrotic core and fibrous cap ($n=40$) using 2D, blood-suppressed, fast spin echo, T_2W MRI sequences. A high interobserver agreement was reported between subsequent MRI measurements as well as between MRI and histology. Cai et al. [53] used CE-MRI to measure the dimensions of fibrous cap and lipid-rich necrotic core in intact plaques. Sequences included DIR T_1W, TOF, and proton density-weighted (PDw). Measurements obtained from CE-MRI were compared with those from T2 W MRI and histological findings. A good correlation with histology of both measures (fibrous cap and lipid-rich necrotic core) was observed.

It has been shown in prospective studies that plaque ulceration and thrombosis are more common in patients who are symptomatic [58, 59]. In symptomatic patients, a minimum cap thickness under 200 microns was associated with an odds ratio of 5.0 for the presence of fibrous cap rupture [60]. Studies on case series have shown that it is possible to identify fibrous cap disruption of carotid plaques using multisequence MRI with black- and bright-blood sequences [61]. It has to be noted, though, that the histological definition of a thin FC (<250 microns [56]) is below the spatial resolution of conventional MRI. Therefore the plaque can be classified as [17]:

- Thick fibrous cap—fibrous cap is clearly visible on contrast-enhanced (CE)-T1W as being between the LRNC and the vessel lumen.
- Thin fibrous cap—fibrous cap not evident on CE-T1W as being between the LRNC and the vessel lumen.
- Ruptured fibrous cap—fibrous cap absent on all imaging sequences.

Superficial calcified nodules were first reported in coronary arteries, and then subsequently in carotid arteries as well [6]. In the classification of atherosclerotic lesions proposed by the American Heart Association (AHA), plaques with superficial calcifications are classified as lesions Type Vb [56]. Later in a modification to the AHA classification [6] these lesions have been classified as a "calcified nodule" and described as an eruptive nodular calcification with underlying fibrocalcific plaque. The second element is calcification—calcified nodules protruding into the lumen can lead to thrombus formation [73]. Calcified nodules are distinguished from most plaque calcifications, which are separated from the lumen by fibrous tissue and may be indicative of stable lesions [62]. An in vivo MRI study on 123 patients was able to visualize, using fast spin echo multi-contrast imaging, calcifications with a sensitivity of 76 %, specificity of 86 %, and a good intraobserver agreement [55]. However, this analysis was performed without regard to the location of calcified nodules. Juxtaluminal nodules, which are associated with a greater risk of rupture however, are more difficult to visualize than those located deeper within the plaque because they appear as a hypointense signal on T_1W, T_2W and TOF images and are not easily distinguishable from the lumen. This limitation, however, can be overcome by an addition of bright-blood sequences to the imaging, making the hypointense calcification clearly different from the hyperintense signal of blood on TOF [63].

Recently Underhill et al. [17] proposed a risk assessment system for patients with carotid atheroma based solely on MRI characteristics. The system was designed to aid in objective and uniform, noninvasive stratification of patients' risk arising from their plaque burden. Additionally the authors aimed to define features of carotid plaques, which may precede the development of fibrous cap rupture and plaque hemorrhage. The classification system was named the Carotid Atherosclerosis Score (CAS) (Fig. 3). Despite being histologically validated, CAS was based on cross-sectional data and will need to undergo a series of prospective studies in order to compare its predictive value against the degree of stenosis seen on angiography.

Table 3 presents the summary of the various characteristics of carotid plaques and the MRI sequences best used for their evaluation.

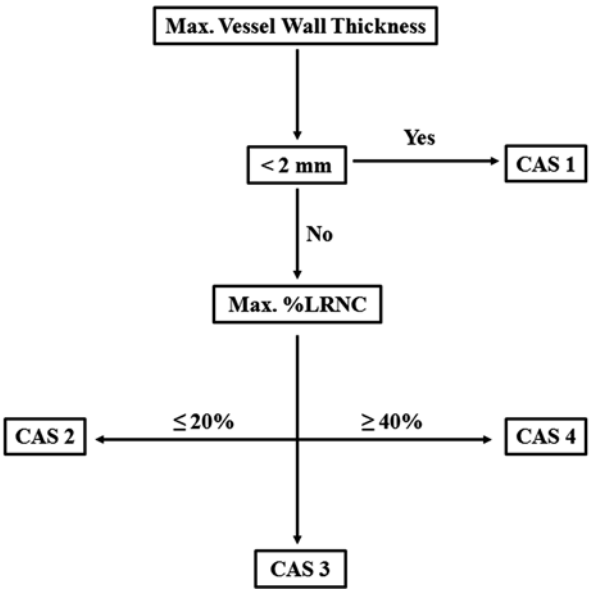

Fig. 3 Carotid atherosclerosis score. CAS 1: low risk; CAS 2: medium-low risk; CAS 3: low-high risk; CAS 4: high-risk plaques. Max % LRNC-maximum percentage of plaque wall occupied by LRNC. Adapted from Underhill et al. [17]. LRNC—lipid-rich necrotic core

Future Directions of MR Imaging

Contrast-enhanced MRI (CE-MRI) of atherosclerosis is a developing area. It is commonly used to image the neovascularization of atherosclerotic plaques, which is thought to represent active inflammation. Gadolinium-based contrast media are used for their T1 shortening ability. Accumulation of the media leads to signal increase on T1-weighted (T_1W) sequences. By using gadolinium chelates it is possible to investigate late-phase enhancement, which is a surrogate of contrast diffusion to the extracellular compartment, and observe the diffusion of contrast over time. For both CE-MRI and DCE-MRI the choice of image acquisition is essential. Care needs to be taken to sufficiently suppress the blood signal to allow clear visualization of the vessel wall. This can be achieved by using black-blood T_1W sequences with either double inversion-recovery (DIR) [64] or more recently proposed quadruple inversion-recovery (QIR) [65]. For dynamic contrast-enhanced MRI, on the other hand, a sequence which does not suppress blood is sometimes used, e.g., spoiled gradient-recalled echo (SPGR) T_1W.

Another solution that has been used is T2-shortening contrast agents such as ultra-small super-paramagnetic particles of iron oxide (USPIOs), which have been studied both in vitro and in vivo. The agent undergoes phagocytosis by macrophages leading to a low-intensity signal in the plaque directly proportional to the amount of macrophages [66]. The T2 effect creates a hypointense area on conventional spin echo (SE) MR sequences. Because of a T2* sensitivity of gradient echo (GE) sequences, they are more sensitive to USPIO effects than spin echo sequences

Table 3 MRI characteristics of carotid plaques

	Appearance of plaque components				
Technique	LRNC	FC	Thrombus	IPH	Calcifications
SE T2W	Hypointense	Hyperintense	Hyperintense	Hypointense	Dark
FSE T2W	Hypointense	Hyperintense	–	Hypointense	Dark
FSE PDW	Hypointense	Isointense	–	Isointense	Dark
DIR FSE T1W	Isointense	Hyperintense	–	Hyperintense	Dark
DIR FSE T2W	Hyperintense/isointense	Isointense	–	Hyperintense	Dark
DIR FSE PDW	Hyperintense/Isointense	Hyperintense	–	Hyperintense	Dark
3D TOF	Isointense	Hypointense	–	Hyperintense	
3D EPI T1W with IR	Hypointense	Isointense	–	Hyperintense	Dark

DIR double inversion-recovery, *EPI* echo planar imaging, *FC* fibrous cap, *FSE* fast spin echo, *IPH* intraplaque hemorrhage, *IR* inversion recovery, *LRNC* lipid-rich necrotic core, *PDW* proton density weighted, *SE* spin echo, *TE* echo time, *T1W*, *T2W*, *TOF* time of flight

but may be subject to poorer image quality [67]. There is also an interesting study with a fibrin-targeted contrast agent which allows for the assessment of thrombus formation [68].

It was proposed that tensile wall stress and wall shear stress may be responsible for progression as well as rupture of atherosclerotic lesions [69]. Stress can be measured in carotid arteries using MR imaging as a basis, with the aid of finite element analysis (FEA) [70]. Stress modeling using FEA has been validated against histological findings using excised atherosclerotic plaques [71]. U-King-Im et al. [71] confirmed that high-resolution MR-derived 2D geometrical arterial models can be used to perform FEA. Trivedi et al. [15] have expanded on this work and performed an MRI-based FEA to predict the differences in plaque tensile stress for symptomatic and asymptomatic patients with carotid atherosclerosis.

Studies have used an atherosclerotic targeting contrast agent (ATCA) in which gadolinium-containing endohedrals were functionalized and formulated into liposomes with CD36 ligands intercalated into the lipid bilayer. ATCA is specifically internalized by CD36 receptors on atherosclerotic plaque providing enhanced visualization of lesions under physiological conditions. ATCA may become a new tool for physicians to noninvasively detect atherosclerotic disease [72].

Furthermore, continued advances in radiofrequency hardware have resulted in an increase in the operating field strength from 1.5 T to 3 T and even 7 T. At 3 T an approximately twofold increase in signal-to-noise ratio can be obtained, resulting in a fourfold reduction in scanning time or a significant increase in temporal resolution.

It is important to note that MRI and PET are able to visualize different aspects of the disease process, making them complementary to each other in the evaluation of vulnerability of the plaque. Saito et al. demonstrated the complementary use of the techniques in plaque evaluation, with a high lipid content, the presence of blood in MRI imaging, and an inflammatory process in PET being important [73].

References

1. Ambrose JA et al. Angiographic progression of coronary artery disease and the development of myocardial infarction. J Am Coll Cardiol. 1988;12(1):56–62.
2. Rothwell PM et al. Analysis of pooled data from the randomised controlled trials of endarterectomy for symptomatic carotid stenosis. Lancet. 2003;361(9352):107–16.
3. Endarterectomy for asymptomatic carotid artery stenosis. Executive Committee for the Asymptomatic Carotid Atherosclerosis Study. JAMA, 1995. **273**(18): p. 1421-8.
4. Halliday A et al. Prevention of disabling and fatal strokes by successful carotid endarterectomy in patients without recent neurological symptoms: randomised controlled trial. Lancet. 2004;363(9420):1491–502.
5. Glagov S et al. Compensatory enlargement of human atherosclerotic coronary arteries. N Engl J Med. 1987;316(22):1371–5.
6. Virmani R et al. Lessons from sudden coronary death: a comprehensive morphological classification scheme for atherosclerotic lesions. Arterioscler Thromb Vasc Biol. 2000;20(5):1262–75.

7. Imparato AM, Riles TS, Gorstein F. The carotid bifurcation plaque: pathologic findings associated with cerebral ischemia. Stroke. 1979;10(3):238–45.
8. Naghavi M et al. From vulnerable plaque to vulnerable patient: a call for new definitions and risk assessment strategies: part I. Circulation. 2003;108(14):1664–72.
9. Naghavi M et al. From vulnerable plaque to vulnerable patient: a call for new definitions and risk assessment strategies: part II. Circulation. 2003;108(15):1772–8.
10. Stary HC et al. A definition of advanced types of atherosclerotic lesions and a histological classification of atherosclerosis. A report from the Committee on Vascular Lesions of the Council on Arteriosclerosis, American Heart Association. Circulation. 1995;92(5):1355–74.
11. Stary HC et al. A definition of initial, fatty streak, and intermediate lesions of atherosclerosis. A report from the Committee on Vascular Lesions of the Council on Arteriosclerosis, American Heart Association. Circulation. 1994;89(5):2462–78.
12. Takaya N et al. Association between carotid plaque characteristics and subsequent ischemic cerebrovascular events: a prospective assessment with MRI–initial results. Stroke. 2006; 37(3):818–23.
13. Tang D et al. Steady flow and wall compression in stenotic arteries: a three-dimensional thick-wall model with fluid-wall interactions. J Biomech Eng. 2001;123(6):548–57.
14. Tang TY et al. Correlation of carotid atheromatous plaque inflammation using USPIO-enhanced MR imaging with degree of luminal stenosis. Stroke. 2008;39(7):2144–7.
15. Trivedi RA et al. Identifying vulnerable carotid plaques in vivo using high resolution magnetic resonance imaging-based finite element analysis. J Neurosurg. 2007;107(3):536–42.
16. Nighoghossian N, Derex L, Douek P. The vulnerable carotid artery plaque: current imaging methods and new perspectives. Stroke. 2005;36(12):2764–72.
17. Underhill HR et al. A noninvasive imaging approach to assess plaque severity: the carotid atherosclerosis score. AJNR Am J Neuroradiol. 2010;31(6):1068–75.
18. Garcia de Tena J. Inflammation, atherosclerosis, and coronary artery disease. N Engl J Med. 2005;353(4):429–30. author reply 429–30.
19. Hansson GK. Inflammation, atherosclerosis, and coronary artery disease. N Engl J Med. 2005;352(16):1685–95.
20. Kriszbacher I, Koppan M, Bodis J. Inflammation, atherosclerosis, and coronary artery disease. N Engl J Med. 2005;353(4):429–30. author reply 429–30.
21. Newby AC. Dual role of matrix metalloproteinases (matrixins) in intimal thickening and atherosclerotic plaque rupture. Physiol Rev. 2005;85(1):1–31.
22. Tawakol A et al. In vivo 18F-fluorodeoxyglucose positron emission tomography imaging provides a noninvasive measure of carotid plaque inflammation in patients. J Am Coll Cardiol. 2006;48(9):1818–24.
23. Rudd JH et al. Imaging atherosclerotic plaque inflammation with [18F]-fluorodeoxyglucose positron emission tomography. Circulation. 2002;105(23):2708–11.
24. Tahara N et al. Simvastatin attenuates plaque inflammation: evaluation by fluorodeoxyglucose positron emission tomography. J Am Coll Cardiol. 2006;48(9):1825–31.
25. Lee SJ et al. Reversal of vascular 18F-FDG uptake with plasma high-density lipoprotein elevation by atherogenic risk reduction. J Nucl Med. 2008;49(8):1277–82.
26. Fayad ZA et al. Safety and efficacy of dalcetrapib on atherosclerotic disease using novel non-invasive multimodality imaging (dal-PLAQUE): a randomised clinical trial. Lancet. 2011;378(9802):1547–59.
27. Wykrzykowska J et al. Imaging of inflamed and vulnerable plaque in coronary arteries with 18F-FDG PET/CT in patients with suppression of myocardial uptake using a low-carbohydrate, high-fat preparation. J Nucl Med. 2009;50(4):563–8.
28. Yuan C et al. MRI of atherosclerosis in clinical trials. NMR Biomed. 2006;19(6):636–54.
29. Kerwin WS et al. Inflammation in carotid atherosclerotic plaque: a dynamic contrast-enhanced MR imaging study. Radiology. 2006;241(2):459–68.
30. Zhao X et al. Minimization of MR contrast weightings for the comprehensive evaluation of carotid atherosclerotic disease. Investig Radiol. 2010;45(1):36–41.

31. Altaf N et al. Carotid intraplaque hemorrhage predicts recurrent symptoms in patients with high-grade carotid stenosis. Stroke. 2007;38(5):1633–5.
32. Singh N et al. Moderate carotid artery stenosis: MR imaging-depicted intraplaque hemorrhage predicts risk of cerebrovascular ischemic events in asymptomatic men. Radiology. 2009;252(2):502–8.
33. Kolodgie FD et al. Intraplaque hemorrhage and progression of coronary atheroma. N Engl J Med. 2003;349(24):2316–25.
34. Doyle B, Caplice N. Plaque neovascularization and antiangiogenic therapy for atherosclerosis. J Am Coll Cardiol. 2007;49(21):2073–80.
35. Virmani R, Narula J, Farb A. When neoangiogenesis ricochets. Am Heart J. 1998; 136(6):937–9.
36. Takaya N et al. Presence of intraplaque hemorrhage stimulates progression of carotid atherosclerotic plaques: a high-resolution magnetic resonance imaging study. Circulation. 2005;111(21):2768–75.
37. Ota H et al. Carotid intraplaque hemorrhage imaging at 3.0-T MR imaging: comparison of the diagnostic performance of three T1-weighted sequences. Radiology. 2010;254(2):551–63.
38. Qiao Y et al. Identification of intraplaque hemorrhage on MR angiography images: a comparison of contrast-enhanced mask and time-of-flight techniques. AJNR Am J Neuroradiol. 2011;32(3):454–9.
39. Yuan C et al. In vivo accuracy of multispectral magnetic resonance imaging for identifying lipid-rich necrotic cores and intraplaque hemorrhage in advanced human carotid plaques. Circulation. 2001;104(17):2051–6.
40. Chu B et al. Hemorrhage in the atherosclerotic carotid plaque: a high-resolution MRI study. Stroke. 2004;35(5):1079–84.
41. Moody AR et al. Lower-limb deep venous thrombosis: direct MR imaging of the thrombus. Radiology. 1998;209(2):349–55.
42. Moody AR et al. Characterization of complicated carotid plaque with magnetic resonance direct thrombus imaging in patients with cerebral ischemia. Circulation. 2003;107(24): 3047–52.
43. Yim YJ et al. High signal intensity halo around the carotid artery on maximum intensity projection images of time-of-flight MR angiography: a new sign for intraplaque hemorrhage. J Magn Reson Imaging. 2008;27(6):1341–6.
44. Corti R et al. Effects of aggressive versus conventional lipid-lowering therapy by simvastatin on human atherosclerotic lesions: a prospective, randomized, double-blind trial with high-resolution magnetic resonance imaging. J Am Coll Cardiol. 2005;46(1):106–12.
45. Saam T et al. The vulnerable, or high-risk, atherosclerotic plaque: noninvasive MR imaging for characterization and assessment. Radiology. 2007;244(1):64–77.
46. Zhao XQ et al. MR imaging of carotid plaque composition during lipid-lowering therapy a prospective assessment of effect and time course. JACC Cardiovasc Imaging. 2011;4(9): 977–86.
47. Lima JA et al. Statin-induced cholesterol lowering and plaque regression after 6 months of magnetic resonance imaging-monitored therapy. Circulation. 2004;110(16):2336–41.
48. Yarnykh VL, Yuan C. Multislice double inversion-recovery black-blood imaging with simultaneous slice reinversion. J Magn Reson Imaging. 2003;17(4):478–83.
49. Corti R et al. Effects of lipid-lowering by simvastatin on human atherosclerotic lesions: a longitudinal study by high-resolution, noninvasive magnetic resonance imaging. Circulation. 2001;104(3):249–52.
50. Yonemura A et al. Effect of lipid-lowering therapy with atorvastatin on atherosclerotic aortic plaques detected by noninvasive magnetic resonance imaging. J Am Coll Cardiol. 2005;45(5):733–42.
51. Corti R et al. Lipid lowering by simvastatin induces regression of human atherosclerotic lesions: two years' follow-up by high-resolution noninvasive magnetic resonance imaging. Circulation. 2002;106(23):2884–7.

52. Mani V et al. Cardiovascular magnetic resonance parameters of atherosclerotic plaque burden improve discrimination of prior major adverse cardiovascular events. J Cardiovasc Magn Reson. 2009;11:10.
53. Cai J et al. In vivo quantitative measurement of intact fibrous cap and lipid-rich necrotic core size in atherosclerotic carotid plaque: comparison of high-resolution, contrast-enhanced magnetic resonance imaging and histology. Circulation. 2005;112(22):3437–44.
54. Cai JM et al. Classification of human carotid atherosclerotic lesions with in vivo multicontrast magnetic resonance imaging. Circulation. 2002;106(11):1368–73.
55. Saam T et al. Quantitative evaluation of carotid plaque composition by in vivo MRI. Arterioscler Thromb Vasc Biol. 2005;25(1):234–9.
56. Hatsukami TS et al. Visualization of fibrous cap thickness and rupture in human atherosclerotic carotid plaque in vivo with high-resolution magnetic resonance imaging. Circulation. 2000;102(9):959–64.
57. Trivedi RA et al. MRI-derived measurements of fibrous-cap and lipid-core thickness: the potential for identifying vulnerable carotid plaques in vivo. Neuroradiology. 2004;46(9): 738–43.
58. Fisher M et al. Carotid plaque pathology: thrombosis, ulceration, and stroke pathogenesis. Stroke. 2005;36(2):253–7.
59. Spagnoli LG et al. Extracranial thrombotically active carotid plaque as a risk factor for ischemic stroke. JAMA. 2004;292(15):1845–52.
60. Redgrave JN et al. Critical cap thickness and rupture in symptomatic carotid plaques: the oxford plaque study. Stroke. 2008;39(6):1722–9.
61. Chu B et al. Magnetic [corrected] resonance imaging [corrected] features of the disruption-prone and the disrupted carotid plaque. JACC Cardiovasc Imaging. 2009;2(7):883–96.
62. Virmani R et al. Histopathology of carotid atherosclerotic disease. Neurosurgery. 2006;59(5 Suppl 3):S219–27. discussion S3–13.
63. Kampschulte A et al. Differentiation of intraplaque versus juxtaluminal hemorrhage/thrombus in advanced human carotid atherosclerotic lesions by in vivo magnetic resonance imaging. Circulation. 2004;110(20):3239–44.
64. Simonetti OP et al. "Black blood" T2-weighted inversion-recovery MR imaging of the heart. Radiology. 1996;199(1):49–57.
65. Yarnykh VL, Yuan C. T1-insensitive flow suppression using quadruple inversion-recovery. Magn Reson Med. 2002;48(5):899–905.
66. Tang TY et al. Iron oxide particles for atheroma imaging. Arterioscler Thromb Vasc Biol. 2009;29(7):1001–8.
67. Bulte JW et al. Relaxometry and magnetometry of the MR contrast agent MION-46L. Magn Reson Med. 1999;42(2):379–84.
68. Spuentrup E et al. Molecular magnetic resonance imaging of coronary thrombosis and pulmonary emboli with a novel fibrin-targeted contrast agent. Circulation. 2005;111(11):1377–82.
69. Kaazempur-Mofrad MR et al. Characterization of the atherosclerotic carotid bifurcation using MRI, finite element modeling, and histology. Ann Biomed Eng. 2004;32(7):932–46.
70. Baldewsing RA et al. Finite element modeling and intravascular ultrasound elastography of vulnerable plaques: parameter variation. Ultrasonics. 2004;42(1–9):723–9.
71. U-King-Im JM, Li ZY, Trivedi RA, Howarth S, Graves MJ, Kirkpatrick PJ, et al. Correlation of shear stress with carotid plaque rupture using MRI and finite element analysis. J Neurol. 2006;253(3):379–81.
72. Dellinger A et al. Functionalization of gadolinium metallofullerenes for detecting atherosclerotic plaque lesions by cardiovascular magnetic resonance. J Cardiovasc Magn Reson. 2013;15:7.
73. Saito H et al. Validity of dual MRI and F-FDG PET imaging in predicting vulnerable and inflamed carotid plaque. Cerebrovasc Dis. 2013;35(4):370–7.